STUDY OF SINTERING BEHAVIOURS AND MECHANICAL PROPERTIES OF BARIUM STRONTIUM COBALT IRON OXIDE CERAMICS

A thesis submitted to The University of Manchester for the degree

of **Doctor of Philosophy**

in the Faculty of Engineering and Physical Sciences

2016

Li Wang

School of Materials

List of Contents

Word Counts: 50960

List of Figures

Chapter 1

Chapter 2

Chapter 3

Chapter 4

Chapter 5

List of Tables

Chapter 2

Chapter 3

Chapter 4

Chapter 5

List of Publications

Li Wang *et al.* Characterisation of microstructure and hardness of perovskite-structured $Ba_{0.5}Sr_{0.5}Co_{0.8}Fe_{0.2}O_{3-\delta}$ under different sintering conditions. **Journal of the European Ceramic Society**. http://dx.doi.org/10.1016/j.jeurceramsoc.2016.02.010, article in press 2016

Li Wang *et al.* Microstructure and mechanical properties of $Ba_{0.5}Sr_{0.5}Co_{0.8}Fe_{0.2}O_{3-\delta}$ perovskite-structured oxides doped with different contents of Ni. **Materials Science & Engineering A**. 658 (2016) 280-288

Li Wang *et al*. A case study of the effect of Ni substitution on the sintering behaviours of $Ba_{0.5}Sr_{0.5}Co_{0.8}Fe_{0.2}O_{3-\delta}$ oxygen transport membranes. **Ceramics International**. 2016, under review.

Li Wang *et al*. Fracture strength and Weibull analysis of $Ba_{0.5}Sr_{0.5}Co_{0.8}Fe_{0.2}O_{3-\delta}$ evaluated by biaxial and uniaxial bending tests. **Journal of the American Ceramic Society.** 2016, under review.

Abstract

Study of sintering behaviours and mechanical properties of Barium Strontium Cobalt Iron Oxide Ceramics

Li Wang

The University of Manchester for the degree of Doctor of Philosophy in the Faculty of Engineering and Physical Sciences

2016

The thesis studies the sintering behaviours and mechanical properties of perovskite-structured $Ba_{0.5}Sr_{0.5}Co_{0.8}Fe_{0.2}O_{3-\delta}$ (BSCF) ceramics. The sintering behaviours of BSCF are studied by sintering BSCF powder using a series of sintering temperatures and dwell times. Under all circumstances, only a cubic perovskite structure is identified in as-sintered samples. The relative density of BSCF increases with increasing sintering temperature and dwell time, but shows a more significant increase with increasing temperature. While the grain size increases with increasing sintering temperature and dwell time, it is found that the increasing temperature contributes much more significantly than increasing dwell time in grain growth. The shape of grain size distribution profile is independent of sintering temperature and dwell time, but the profile shifts with different sintering conditions. The grain maintains an aspect ratio of 1.8 irrespective of sintering conditions. Similar findings are also made on the Ni-doped BSCF, but it is found that Ni doping inhibits the grain growth and retards the densification of BSCF while it has little influence on the grain size distributions and grain aspect ratio distributions. The grain growth exponent (n) and apparent activation energy (Q) are also systematically studied. It is found that grain boundary diffusion is the dominant controlling mechanism for BSCF while both grain boundary and lattice diffusions are the equally dominant controlling mechanisms for BSCF-Ni8. The fracture stress of BSCF is measured by both three-point and ring-on-ring bending tests at room and high temperatures. The fracture stress determined by three-point bending tests is consistently higher than that value measured by ring-on-ring tests for a given temperature. By utilising Weibull statistics a close prediction is made of the three-point values from the ring-on-ring values. Compared with the Young's modulus of BSCF obtained from three-point bending tests between RT and 800 ℃, the values determined from ring-on-ring tests shows a fairly good agreement. However, the Young's modulus measured by both bending tests is lower than that value determined by micro-indentation tests. Hardness and fracture toughness are independent of grain size and grain orientation. Porosity is the dominant factor in Young's modulus, hardness and fracture toughness of BSCF. The intrinsic hardness, intrinsic Young's modulus and intrinsic fracture toughness of BSCF are also determined. The subcritical crack growth (SCG) of BSCF is also studied using constant load method at RT and constant stress rate method at 800 ℃. It is found that that BSCF is not susceptible to SCG at RT but becomes relatively sensitive to SCG at 800 ℃. The results are subsequently used as a basis for a strength–probability–time (SPT) lifetime prediction. Ni doping increases the Young's modulus, hardness and fracture toughness of BSCF determined micro-indentation tests at RT. Both hardness and Young's modulus show a non-monotonic trend with Ni doping content, which is attributed to the porosity and secondary phase. The intrinsic hardness, intrinsic Young's modulus and intrinsic fracture toughness of 8 mol% Ni-doped BSCF are determined. Dopants have little influence on grain orientation and the distribution of grain boundary misorientation angles of BSCF.

Declaration

No portion of the work referred to in this thesis has been submitted in support of an application for another degree or qualification of this or any other university or other institute of learning.

Copyright Statement

Acknowledgement

First of all I would like to acknowledge my ex-supervisor Dr. Colin Leach for his guidance, patience and encouragement as I started to do the research. Even when he was in the hospital, he also sent the emails to me and offered some valuable suggestions and advice. And I also would like to thank my supervisor Dr. David Hall and co-supervisor Prof. Brian Derby, who helped me throughout the whole thesis with valuable comments. This is not to forget the present Dr. Liang Qiao.

I would like to acknowledgement the staff of the material department who offered their time and expertise to help me to use the facilities on the right route. Particularly I would like to thank: Mrs. Olwen Richert, Mr. Stuart Morris, Mr. Michel Faulkner, Dr. Chris Wilkins, Mr. John Goodier, Mr. Andy Forrest, Mr. Andy Wallwork, Mr. Ken Gyves, Dr. John Warren, and Mr. Gary Harrison.

I would like to thank my colleagues who have offered their help, suggestions, advice and encouragement and who have so kindly shared their research results, including Dr. Colin Norman and Dr. Huanghai Lu. And I am also appreciated of my best friends, Dr. Rui Dou, Mr. Yizhe Li, Dr. Mingwen Bai, and Mr. Chun Li. I am particularly grateful to Dr. Ying Chen who always drags me out of the morass of despair when unexpected difficulties arise in the course of my experiments. He could be sent for whenever needed. Absolutely, this is not to forget his wife Dr. Yu Dang. I am grateful to have so many friends who care about me, and I would like to give many thanks to them in person.

I would like to express my gratitude to my wife Ms. Youyou Zhao for her love, encouragement, patience, support and understanding. Without her, I could not successfully go through a rough patch of my life. Every time I could not hold on, she always stays by my side and encourages me to keep plugging away.

Last but not least, I would like to thank Beijing Julong Company for its financial support, and absolutely thank my parents for their never-ending love and support. This is not to forget the love and encouragement of my elder sister and younger brother.

List of Nomenclature

Acronyms

BSCF	$Ba_{0.5}Sr_{0.5}Co_{0.8}Fe_{0.2}O_{3-\delta}$
CCS	CO_2 capture and storage
CCU	CO_2 capture and utilisation
EBSD	Electron Backscattered Diffraction
EDX	energy-dispersive X-ray spectroscopy
fcc	face-centred cubic
FIB	focused ion beam
IPF	inverse pole figure
ISE	indentation size effect
MIEC	mixed ionic and electronic conducting
MSA	Minimum Solid Area
ND	normal direction
PSA	Pressure swing adsorption
RD	rolling direction
RT	room temperature
SCG	subcritical crack growth
SEM	Scanning electron microsocpe
SOFC	Solid oxide fuel cell
SPT	strength–probability–time
TD	transverse direction
TEC	thermal expansion coefficient
TEM	Transmission electron microscopy
TG	thermogravimetry
XRD	X-ray diffraction

Symbols

n	grain growth exponent
μ_0	the chemical potential gradient
a	the lattice parameter
t	tolerance factor
γ_s	the specific surface energy

A	the total pore/solid interfacial area
γ_{GB}	the grain boundary energy
R_p	the radius of curvature of pores
R_G	the radius of curvature of grains
x	the radius of the neck
R	the radius of the spherical particle
K	a constant dependent on temperature
t	sintering time
η	viscosity
b	Burgers Vector
D_g	grain boundary diffusivity
k	Boltzmann's constant
T	absolute temperature
P	vapour pressure
ρ	theoretical density
M	molecular weight
D_v	volume diffusivity
Ω	atomic volume
D_s	surface diffusivity
M_{gb}	grain boundary mobility
εm	energy barrier
a	atomic spacing
v	the atomic vibration frequency
D_0	the initial average grain size
n	the kinetic grain growth exponent
Q	the apparent activation energy
R	the gas constant
T	the absolute temperature
E	Young's modulus
σ	the applied stress
ε	the strain
F	the load
L	the distance between the two support points
b	the width of the specimen
h	the thickness of the specimen
d	the central deflection of the specimen
t_h	the specimen thickness
v	the Poisson ratio
r_1	the radius of the loading ring
r_2	the radius of the supporting ring

r_3	the radius of the specimen
E_i	the Young's modulus of the indenter
v_s	the Poisson's ratio of the tested sample
v_i	the Poisson's ratio of the tested samples and indenter
E_r	the reduced modulus
β	indenter constant
S	the maximum slope of the load-displacement curve
A_p	the projected contact area at applied load
E_0	the Young's modulus of the fully dense material
P	volume fraction of the porosity
b	an empirical constant
Hv	Vickers hardness
α	indenter geometry
n	the Meryer coefficient
H_0	the indentation hardness value corresponding to a specimen with zero porosity
b	a material dependence constant
X_0	the distance between atoms in equilibrium.
F	the probability of failure
σ_m	reference maximum stress in the stressed solid
m	Weibull modulus
σ_0	characteristic strength
V_{eff}	effective stress volume
σ_f	the measured fracture stress
C_0	the crack length
K_{IC}	fracture toughness
v	crack growth rate
K	the stress intensity factor
Y	crack shape factor
n	slow crack growth parameter
T_m	absolute melting temperature
p	the inverse grain size exponent
m	the oxygen partial pressure exponent
n	the stress exponent
D	Grain size

Chapter 1 Introduction

1.1 General background

The rapid development of our economic society is coupled with an increase in the requirement for worldwide energy. In the next few decades, the demand for worldwide energy will be expected to reach more than 35 trillion kilowatt-hours[1]. This energy consumption will be two orders of magnitude higher than that in 2008[2]. One of the most broadly consumed resources of energy production remains fossil fuels. However, there are two main drawbacks of fossil fuels[1]. One is that fossil fuels are finite resources. The other is that extensive consumption of fossil fuels brings about environmental pollution, such as nitrogen oxide, sulphur dioxide and chemical vapours. In order to overcome these problems, we can enhance the efficiency of combustion and reduce the emission of greenhouse gases (CO_2, NO_x, SO_x) [2]. The utilisation of pure oxygen to combust fossil fuels obtains a better thermal efficiency and a reduction in the emission of greenhouse gases, because there is no need to separate toxic nitrogen oxides from the exhaust gases and saves the energy that would be used to heat the inert nitrogen. Additionally, it can increase the flame temperature thereby increasing the thermal efficiency. Therefore, there is a constant increase in demand for pure oxygen [2].

1.2 Introduction of pure oxygen production and CO_2 capture

1.2.1 Oxygen production

Oxygen, a major raw material used extensively in many advanced industries, is the

second largest volume of chemical produced worldwide[3]. Pure oxygen is widely applied in chemical synthesis, power station and steel manufacturing [4-6]. There is a hundred-billion-dollar market for oxygen consumption annually in the world[2]. Because air is the main source of oxygen production, any reduction in the cost of the separation of oxygen from air becomes more important. Currently, there are two main methods for producing oxygen in industry. One is cryogenic distillation of liquid air[7]; the other is pressure swing adsorption[6].

1.2.1.1 Cryogenic distillation method

The cryogenic distillation method exploits the different boiling points of oxygen and nitrogen. This method for oxygen production is applied in industry on a large scale, in total producing over 1 million tonnes of oxygen every year[3]. Although this method has been advancing over the past century, it has been struggling to reduce the energy requirements for the compression and cooling processes. For this reason, cryogenic oxygen is not affordable for low-cost, next-generation energy production or other oxygen-intensive industries.

1.2.1.2 Pressure swing adsorption

Pressure swing adsorption (PSA) is a technology that can be used to separate oxygen from air under pressure according to oxygen's affinity for an adsorbent material. This system has the characteristics of versatility and easy of operation, but it also has its limitations. The purity of the oxygen produced by pressure swing adsorption is under 95% while the rest is essentially argon[6]. Additionally, it also consumes a large amount of energy.

Although the two methods described above are widely used to produce oxygen, the

drawbacks are efficiency limitations, high energy consumption, and impurity. Therefore, more cost-effective and environmentally-friendly methods have been sought. Among these methods, mixed ionic and electronic conducting (MIEC) ceramic membranes have been proposed for use in oxygen separation due to their higher efficiency and purity of product than the conventional techniques[3].

1.2.2 CO_2 capture

It is popularly believed that CO_2 capture is an effective solution to CO_2 emissions[8]. Currently there are two methods of CO_2 capture: CO_2 capture and storage (CCS), and CO_2 capture and utilisation (CCU) [8]. It is well-known that fossil fuelled plants are the largest point sources of CO_2[8]. Therefore, it is urgent to develop different methods to capture CO_2, including pre-combustion, post-combustion, and oxyfuel[9]. As for oxyfuel, pure oxygen is utilised for fossil fuel combustion. In this way, nitrogen (78% in the air) can be avoided from the combustion, and CO_2 and H_2O as main products in the flue gases can be easily separated by condensation as shown in Figure 1.1

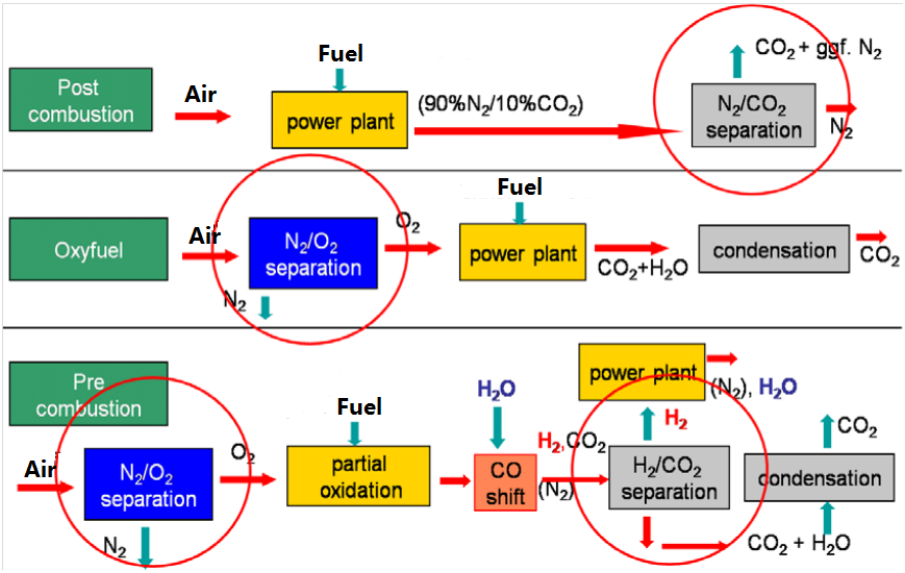

Figure 1.1 Schematic diagram of possible separation processes in fossil power plants[9]

1.3 Introduction to MIEC ceramic membranes

Mixed ionic and electronic conducting (MIEC) ceramic membranes can produce oxygen with 100% purity in theory [10] and have the potential to lower the cost of oxygen production in comparison with the traditional methods (e.g. cryogenic distillation)[7]. These membranes possess the ability to conduct both oxygen ions and electrons simultaneously. When they are exposed to an oxygen pressure gradient, oxygen is allowed to move through the membranes. Although these MIEC membranes have not been used commercially, the Department of Energy in the United States has successfully designed an Intermediate Scale Test Unit on the basis of ceramic membranes, which produced oxygen with 100 tonnes-per-day in late 2013 [11]. Based on this intermediate unit, a larger plant will be designed to produce oxygen up to 2000 tonnes-per-day in 2020, and MIEC membranes are expected to have the ability to realise the industrial production of oxygen[11].

Because of high oxygen permeability [12-14], the perovskite oxide $Ba_{0.5}Sr_{0.5}Co_{0.8}Fe_{0.2}O_{3-\delta}$ is one of the most promising materials for application as dense ceramic MIEC membranes. In real applications, MIEC membranes are operated at high temperature and are exposed to a high oxygen pressure gradient between feed and permeate side. Besides high oxygen permeability, the MIEC membranes must maintain their geometrical and structural stability for a long time under these severe conditions. Therefore, mechanical properties need to be assessed. Additionally, their sintering behaviours are also required to be investigated, because mechanical properties and oxygen permeability depend on the microstructure of the membranes.

1.4 Objectives of this study

The aims of this study are to characterise mixed ionic and electronic conducting (MIEC) membranes which are potentially applied in the area of oxygen separation in industry. As an oxygen separation membrane material used at high temperature (800 ℃), high oxygen permeability and long-term mechanical integrity are two of the most important desirable properties which highly depend on microstructures (e.g. density and grain size) and compositions (e.g. concentration of dopants). Therefore, the first objective of this thesis is to study the microstructures and mechanical properties of the BSCF and how they evolve with a variety of sintering conditions. The second objective is to study the effect of Ni doping on the microstructures and the mechanical properties of BSCF.

1.5 Thesis outline

Chapter 2 is a literature review of perovskite-structured materials, with a focus on sintering behaviours, mechanical properties and failure mechanisms.

Chapter 3 presents the experimental procedures and characterisation methods

Chapter 4 concentrates on the sintering behaviours of BSCF, including powder characterisation, phase identification, relative density, grain growth and grain size distribution as well; focuses on the mechanical properties of BSCF determined by various methods, the evaluation of slow crack growth and lifetime prediction at RT and 800 ℃; presents the effect of different Ni doping levels on the sintering behaviours of BSCF, including phase identification, grain growth, porosity and pore evaluation; and studies the mechanical properties of Ni-doped BSCF, including hardness, Young's modulus and fracture toughness.

Chapter 5 shows a study of grain orientation of BSCF with different dopants using an EBSD technique.

Chapter 6 describes conclusions obtained from the results and gives suggestions for future work

Chapter 2 Literature review

2.1 Requirement of oxygen transport membranes

As a membrane applied in industry, it is expected to meet several essentially desirable requirements. Firstly, the materials need to exhibit high oxygen permeation. To be more specific, the oxygen permeation of these materials can be over 10^{-8} mol $s^{-1}cm^{-2}$ at elevated temperature. Secondly, chemical and structural stabilities in long term operation are also essential at elevated temperature. Thirdly, the thermal expansion of membranes requires compatibility with metallic substrates at elevated temperature. Lastly, it is warranted for the membranes to keep good comprehensive mechanical properties to resist failure and maintain mechanical integrity due to the stress induced by the presence of an oxygen partial pressure gradient across the membrane at high temperature.

2.2 Materials of choice

Among many structures available for oxygen transport membranes, most of the best compounds with regard to oxygen permeation properties show either a perovskite or fluorite crystal structure[15].

2.2.1 Fluorite structure

The ideal fluorite structure is shown in Figure 2.1. It is composed of anions in simple cubic packing with half of the interstices occupied by cations[16]. The unit cell is based on the face-centred cubic (fcc) packing of the cations[16]. A notable feature is the large

void in the centre of the unit cell[16]. Solid solution such as $(ZrO_2)_x(CaO)_{1-x}$ with fluorite structure possesses high electrical conductivity, mainly because of oxygen ion movement[12]. It has been reported that X-ray studies show that the oxygen vacancy in a solid solution of a composition is attributed to having cations fill all the cation sites while oxygen ion lattice sites are vacant[12].

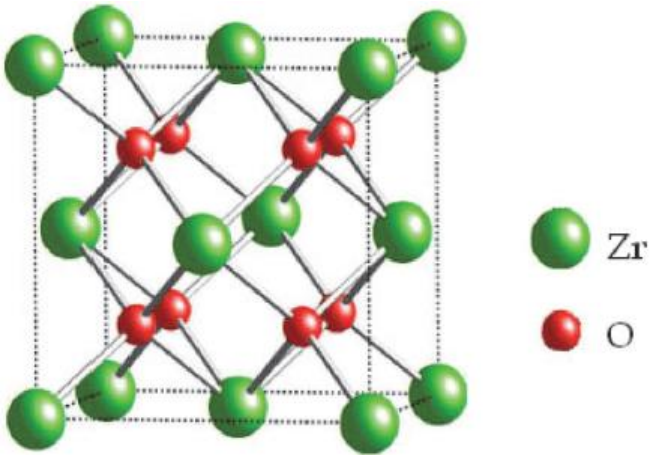

Figure 2.1 Unit cell of zirconium fluorite [17]

2.2.2 Perovskite structure

Perovskite is defined as a group of compounds for a particular mineral with the formula $ABO_3(^{XII}A^{2+}\,^{VII}B^{4+}O^{2-}{}_3$; A=rare earth metal ions; B=transition metal ions)[18]. The ideal perovskite crystal structure is depicted in Figure 2.2.

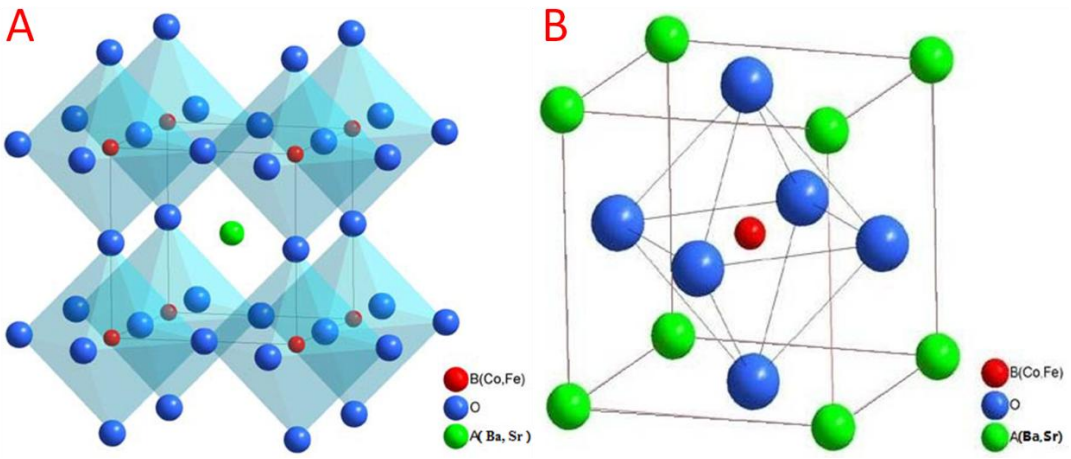

Figure 2.2 Ideal perovskite structure ABO_3[19]: (A) A-ions cube centred; (B) B-ions cube centred

A^{2+} unites with O^{2-} to shape a cubic structure and the smaller radius more greatly electric charged B^{4+} occupies octahedral interstices. Each A^{2+} is surrounded by twelve equidistant O^{2-} ; O^{2-} is encircled by four A^{2+} and eight O^{2-}; B^{4+} is octahedrally coordinated to six O^{2-} and locates the centre of the cube[20, 21]. The angles between the six equal B-O bonds are 90 ¶[21]. With regard to the ideal cubic symmetry, the atoms are assumed to be closely packed and it can be stated that:

$$2(R_A + R_O) = \sqrt{2}a \tag{2.1}$$

$$2(R_B + R_O) = a \tag{2.2}$$

where R_A, R_B, and R_O are the radii of *A*, *B* and *O* atoms, respectively; *a* is the lattice parameter. Combining the Equations (2.1) and (2.2), it can be obtained by the following equation:

$$(R_A + R_O) = \sqrt{2}(R_B + R_O) \tag{2.3}$$

In terms of the integrity of cubic symmetry, tolerance factor (*t*) is defined by Goldschmidt:

$$t = \frac{R_A + R_O}{\sqrt{2}(R_B + R_O)} \tag{2.4}$$

In order to maintain the perovskite structure, the tolerance factor (*t*) is controlled between 0.8 and 1. The ideal cubic perovskite structure is preserved when the tolerance factor is approximate to 1. The value of t considerably smaller than 1 results in distorting the cubic structure, whereas t notably greater than 1 induces a phase transformation[20, 22].

2.2.3 $Ba_{0.5}Sr_{0.5}Co_{0.8}Fe_{0.2}O_{3-\delta}$

The variants of $Ba_xSr_{1-x}Co_yFe_{1-y}O_{3-\delta}$ are the most promising oxygen separation MIEC materials [23, 24]. It has been reported that BSCF originated from $SrCoO_{3-\delta}$ considered

as a fundamental perovskite-structured parent compound[21]. To be more specific, BSCF was modified from $SrCo_{1-y}Fe_yO_{3-\delta}$[25], which was first suggested as a potential application of oxygen transport membrane[24]. In terms of the crystal structure of $SrCoO_{3-\delta}$, it has been expected to have high oxygen permeability, because nearly one-six of its oxygen lattice site is vacant and the bond strength of Co-O is relative weak thereby favouring the transport of oxygen ions and electrons[26, 27]. However, considerable oxygen permeation of $SrCoO_{3-\delta}$ only can be achieved at high temperature (over 900 ℃)[26]. When cooling to certain critical temperatures, its oxygen permeability dramatically decreases because the high oxygen permeability can be only achieved in the cubic structure and there is a phase transition from cubic to hexagonal between 800 ℃ and 900 ℃[26, 27].

Many research groups have investigated the oxygen permeation of the doped $A_xSr_{1-x}Co_{1-y}B_yO_{3-\delta}$ systems on the basis of $SrCoO_{3-\delta}$[28-34]. Teraoka *et al*.[35] have found the compound $SrCo_{0.8}Fe_{0.2}O_{3-\delta}$ (x=0, y=0.2) shows the highest oxygen permeation rate. However, $SrCo_{0.8}Fe_{0.2}O_{3-\delta}$ exhibits poor mechanical integrity and phase instability, because the small radius of Sr results in the tolerance factor less than 1. From the point of maintaining the cubic symmetry, large atoms doped in A site can be realised according to the Goldschmidt Equation (2.4). In this way, Shao *et al*.[14] have substituted a series of Ba with different composition for the smaller radius Sr and have acquired the best one with half substitution of Sr by Ba to maintain the cubic stability[14]. It has been demonstrated [36-38] that $Ba_{0.5}Sr_{0.5}Co_{0.8}Fe_{0.2}O_{3-\delta}$ membranes are capable of retaining cubic structure up to 1000 ℃ even under low oxygen partial pressure and possess high concentration of oxygen vacancies distributed randomly.

2.3 Transport mechanism

MIEC membranes are used in separating oxygen from air by means of lattice diffusion of oxygen ions[39]. The driving force for oxygen permeation is provided by chemical potential gradient or electric potential gradient, e.g. the differential oxygen partial pressure between the feed and sweep sides of the membranes[40]. The oxygen transport mechanisms of the MIEC membranes are schematically displayed in Figure 2.3

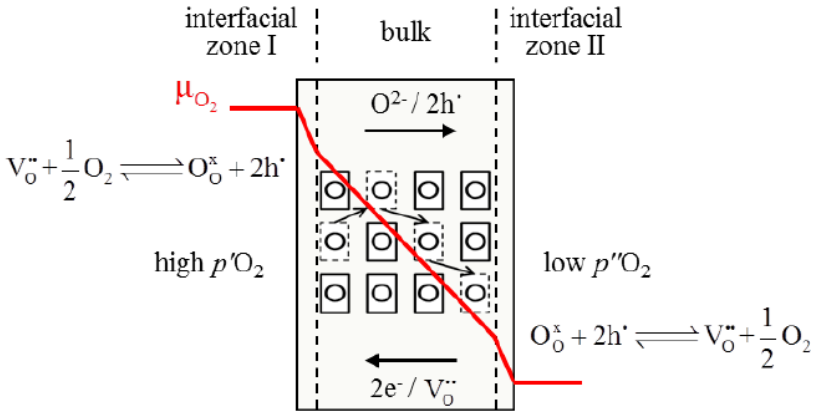

Figure 2.3 Schematic principle of the process of oxygen transport through a perovskite-structured membrane[41]. μ_0 is the chemical potential gradient between the feed side with high oxygen partial pressure $P_{O_2}{}'$ and the sweep side with low oxygen partial pressure $P_{O_2}{}''$; $h^{\cdot}$ is electron hole.

The oxygen transport across the MIEC membranes involves three successive processes[12, 41]:

(i) the surface-exchange reaction on the interface I under high oxygen partial pressure on the feed side; dissociating of an oxygen molecule and combining with electrons to form O^{2-};

(ii) the diffusion of charged ions (O^{2-}) and electrons/electron holes in the bulk;

(iii) the surface-exchange reaction on the interface II under low oxygen partial pressure on the sweep side; combination of oxygen ions and electron holes to form oxygen.

It is apparent that oxygen transport through a MIEC membrane is basically limited by two factors, e.g. surface-exchange resistance on both interfaces of the membrane and the diffusion kinetics within the bulk [42-44]. The overall permeation rate is determined by the slowest process of oxygen transport[12].

2.4 Oxygen permeability data for perovskite-structured materials

Table 2.1 Oxygen permeation flux data for perovskite-structured materials

Materials	Temperature(℃)	J_{O_2} (mol s^{-1} cm^{-2})	Shape	Thickness (mm)	References
$Ba_{0.5}Sr_{0.5}Co_{0.8}Fe_{0.2}O_{3-\delta}$	850-900	9×10^{-8} to 1.6×10^{-6}	Disk	1.8	[24]
	800-900	7×10^{-7} to 2.3×10^{-6}	Tube	1.5	[45]
	850-950	1.4×10^{-6} to 13.3×10^{-6}	Tube	0.22	[46]
$Ba_{0.5}Sr_{0.5}Zn_{0.2}Fe_{0.8}O_{3-\delta}$	800-975	1.1×10^{-6} to 2.6×10^{-6}	Disk	1.45	[47]
$La_{0.6}Sr_{0.4}Co_{0.2}Fe_{0.8}O_{3-\delta}$	850-900	4×10^{-8} to 1.0×10^{-7}	Tube	0.22	[34]
$La_{0.6}Sr_{0.4}Co_{0.4}Fe_{0.6}O_{3-\delta}$	1000-1100	2.5×10^{-8} to 1.3×10^{-7}	Disk	1	[48]
$La_{0.6}Sr_{0.4}Co_{0.8}Fe_{0.2}O_{3-\delta}$	860	4.6×10^{-7}	Disk	1.5	[34]
$La_{0.6}Sr_{0.4}Co_{0.8}Ni_{0.2}O_{3-\delta}$	860	1.1×10^{-6}	Disk	1.5	[49]
$La_{0.6}Sr_{0.4}Co_{0.8}Mn_{0.2}O_{3-\delta}$	860	3.7×10^{-7}	Disk	1.5	[49]
$La_{0.8}Sr_{0.2}Co_{0.3}Ga_{0.7}O_{3-\delta}$	700-1000	2.3×10^{-7} to 1.1×10^{-6}	Disk	0.5	[50]
$La_{0.6}Sr_{0.4}Ga_{0.7}Ni_{0.3}O_{3-\delta}$	700-1000	2.6×10^{-7} to 1.0×10^{-6}	Disk	0.5	[50]
$SrCoO_{3-\delta}$	850-1000	0 to 3.4×10^{-7}	Disk	1	[29]
$SrCo_{0.8}Fe_{0.2}O_{3-\delta}$	850-870	1.7×10^{-7} to 5.4×10^{-7}	Disk	1	[35]

Table 2.1 shows the oxygen permeation flux data for some perovskite-structured materials. Although $SrCo_{0.8}Fe_{0.2}O_{3-\delta}$ exhibits a similar oxygen permeation flux as $Ba_{0.5}Sr_{0.5}Co_{0.8}Fe_{0.2}O_{3-\delta}$ at the same temperature, it also displays chemical instability [23, 51]. Additionally, $La_{1-x}Sr_xCo_{1-y}Fe_yO_{3-\delta}$ shows good chemical stability at high

temperature, but it exhibits much lower oxygen permeation flux than that of $Ba_{0.5}Sr_{0.5}Co_{0.8}Fe_{0.2}O_{3-\delta}$[12, 52, 53].

2.5 Sintering of ceramics

Sintering refers to a process of the bonding of particles by molecular or atomic attraction and forming a solid mass, possibly causing densification and recrystallisation by transport of powders under the heat treatment below the melting point of a material[16]. Therefore, sintering is considered as a diffusive process[54, 55], with a rate determined by two factors. One is temperature which controls the diffusion rate, and the other is powder particle size which controls the length scale for diffusion[56].

2.5.1 General background

With regard to the process of sintering, it reduces the surface area of the powder compact. The driving force for sintering is the decrease in the total surface energy $\Delta(\gamma_s A)$[57], which can be expressed as the following equation[58, 59]:

$$\Delta(\gamma_s A) = \gamma_s \Delta A + A \Delta \gamma_s \tag{2.5}$$

where γ_s is the specific surface energy and A is the total pore/solid interfacial area.

The changes in the interfacial energy and interfacial area are caused by densification and grain coarsening (grain growth), respectively. During the sintering, replacing the solid/pore interfaces (surfaces) by solid/solid interfaces (grain boundaries) can result in a decrease in interfacial energy[60]. This process gives rise to densification and it decreases the total pore volume. To be more specific, the pores at the beginning tend to change shape and form isolated spheres or channels, but the size of pores does not change as shown in Figure 2.4. During the densification stage, both the shape and the

size of the pores change; the shape becomes more spherical and the diameter reduces as sintering proceeds [16].

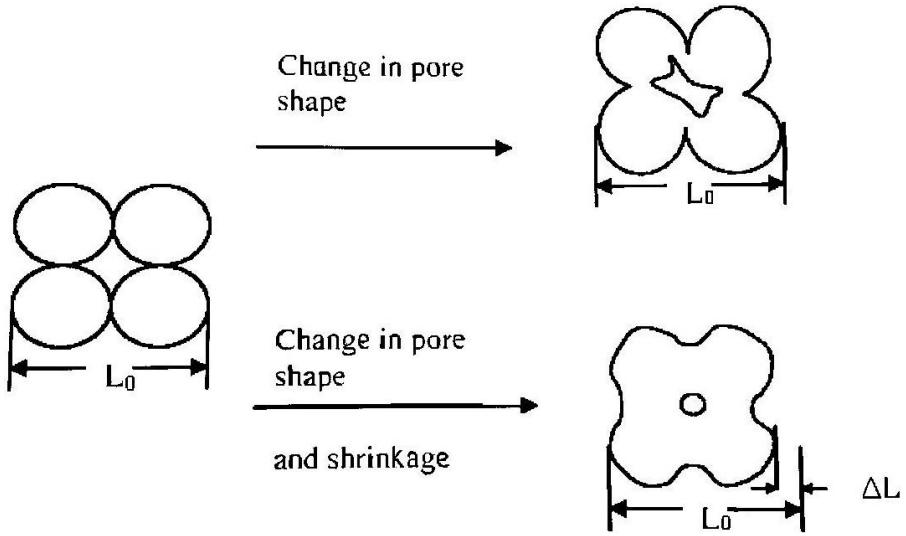

Figure 2.4 Schematic sketch of sintering about particle compacts related to only change in pore shape and linked to changes in both pore shape and shrinkage[16].

The sintering stress, σ_s, is defined as the equal external stress that can result in the same densification strain rate as the internal driving force[61]. The sintering stress which can be proportional to the strain rate ratio and nearly independent of sintered density and temperature[61] for a grain-pores system[62, 63], is developed from the Young-Laplace equation as follows[64]:

$$\sigma_S = \frac{2\gamma_S}{R_P} + \frac{2\gamma_{GB}}{R_G} \tag{2.6}$$

where γ_s is the surface energy; γ_{GB} is the grain boundary energy; R_P and R_G are the radii of curvature of pores and grains, respectively. According to Equation (2.6), sintering stress is inversely proportional to the initial radii of curvature of pores and grains. Microscopically, the change in free energy between the neck and the surface of the particle can influence mass transport. If the particle size becomes relatively small (its curvature is high), the sintering stress can be of a great magnitude. Therefore, most ceramic sintering technology basically depends on the fine-particle raw materials, because surface energy becomes much higher when the radius of curvature is kept under

a few micrometres[16].

2.5.1.1 Neck growth

Kuczynski[58] first reported the two-sphere sintering model as shown in Figure 2.5 and investigated neck growth rate for six different types of mass transport mechanisms and obtained the following equation[58]:

$$(\frac{x}{R})^{\alpha} = K\frac{t}{R^{m}} \tag{2.7}$$

where x and R are the radii of the neck and the spherical particle, respectively; K is a constant dependent on temperature; t is sintering time; α and m are exponents depending on the mechanism of mass transport and the values of these two exponents are shown in Table 2.2. As a consequence of these equations, neck growth is also strongly dependent on sintering temperature, dwell time and particle size.

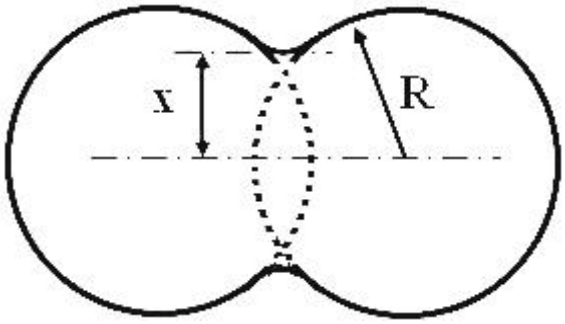

Figure 2.5 Schematic of the two-sphere model[62]

Table 2.2 the values of α, m and K depending on the mechanisms of mass transport [16, 58, 60, 62, 65]

Mechanism of mass transport	α	m	K
Viscous flow	2	1	$3\gamma/\eta$
Plastic flow	2	1	$9\pi\gamma bD_g/kT$
Evaporation-condensation	3	2	$(3P\gamma/\rho 2)(\pi/2)1/2(M/kT)3/2$
Lattice diffusion	5	3	$80\gamma D_v\Omega/kT$
Grain boundary diffusion	6	4	$20\delta D_g\gamma\Omega/kT$
Surface diffusion	7	4	$56D_s\gamma\Omega 4/3/kT$

where γ is surface energy; η viscosity; b Burgers Vector; D_g grain boundary diffusivity;

k Boltzmann's constant; *T* absolute temperature; *P* vapour pressure; ρ theoretical density; *M* molecular weight; D_v volume diffusivity; Ω atomic volume; D_s surface diffusivity.

2.5.1.2 Grain growth

There are two categories of mass transport. One is parallel to grain boundaries, which can control the process of densification. The other is perpendicular to grain boundaries, which can dominate the process of grain growth and cause coarsening of the microstructure[58, 59]. During the sintering, it is widely recognised that grain growth competes with densification. Therefore, designed ceramics with controlled microstructure and properties can be realised by control of the competition between grain growth and compact densification. During the process of grain growth, larger grains swallow up the adjacent smaller grains. In other words, small grains disappear and large grains become larger.

In Burke's and Turnbull's equation of grain growth[66, 67], the rate of grain growth $\frac{dD}{dt}$ is correlated with the average diameter of grain curvature. This curvature is inversely proportional to the grain diameter[66, 68]:

$$\frac{dD}{dt} = M_{gb}\,\frac{\eta}{D} \tag{2.8}$$

The result of this equation is the parabolic law of grain growth [67]

$$D^2 - {D_0}^2 = 2M_{gb}\,\eta t \tag{2.9}$$

The rate of grain growth is controlled by the grain boundary mobility M_{gb}, the dwell time *t* and the surface tension η.

2.5.1.3 Grain boundary mobility

The grain boundary mobility M_{gb}, can be analysed from the atomic scale. In a cubic

lattice, the atoms need to overcome the energy barrier ε_m when the atom migrates from one grain to another[58]

$$M_{gb} = \frac{va^4}{\kappa T} exp(-\frac{\varepsilon_m}{\kappa T}) \quad (2.10)$$

where M_{gb} is grain boundary mobility, a atomic spacing, ε_m energy barrier, v the atomic vibration frequency. Equation (2.10) suggests that grain boundary mobility depends on atomic vibration frequency, energy barrier and atomic spacing as well. These three different parameters are strongly influenced by point defects. In addition, these point defects are induced by impurities or dopants[69].Therefore, the grain boundary mobility can be affected by point defects, including doping and vacancies [70].

2.5.2 Sintering behaviours of $Ba_{0.5}Sr_{0.5}Co_{0.8}Fe_{0.2}O_{3-\delta}$ membranes

As mentioned previously, BSCF materials can be used as cathodes for SOFC [25] or as oxygen permeation membranes[71]. However, microstructural requirements for these two applications are different. Specifically, BSCF materials as cathodes of SOFC need a porous microstructure in order to increase the reaction area[72] while dense microstructures are required for oxygen permeation membranes in order to maintain a physical barrier to gas flow [12]. It has been reported that grain size positively affects the permeation rate of BSCF [45, 73], because the grain boundary inhibits the transport of oxygen ions[31]. In other words, the oxygen ions transport along the grain boundary slower than through the grain lattice. Therefore, the oxygen permeation flux increases with increasing grain size of membranes since there are fewer grain boundaries when the membrane consists of larger grains[45].

As mentioned above, microstructure can significantly affect the functional properties of

BSCF. Normally, microstructure entirely depends on the sintering conditions (atmosphere, time, temperature, heating and cooling rate) and methods (hot isostatic pressing, spark plasma sintering) as well as dopants. Therefore, the required microstructure of BSCF can be realised by changes in the sintering process and dopants. With respect to the current work, the changes in sintering temperature and dwell time as well as dopants are discussed below.

2.5.2.1 Densification

2.5.2.1.1 Effect of sintering temperature on density of BSCF

It is well-known that the density of the membranes increases with increasing sintering temperature in a certain range[16]. For $Ba_{0.5}Sr_{0.5}Co_{0.8}Fe_{0.2}O_{3-\delta}$ (BSCF) [13, 45, 74], the relative density can reach a value in the range from 90% to 95% when the sintering temperature is between 1000 ℃ and 1100 ℃ for 5 hours. It has been reported [13, 74] that BSCF sintered at 1100 ℃ has a relative density of 95% as shown in Figure 2.6. When the sintering temperature increases up to 1150 ℃, the relative density of BSCF will decrease slightly. According to Baumann *et al*.[13], although the presence of cobalt oxide cannot be identified by XRD, it has been found to exist at grain boundaries by TEM when the sintering temperature reaches 1150 ℃, suggesting that BSCF sintered at 1150 ℃ is decomposed, which explains the slight decrease in the relative density of BSCF due to oxygen released from the lattice. The associated defect reaction can be written in the Kroger-Vink notation as[16]

$$O_O^X + 2M_M^{\cdot} \overset{Heating}{\longleftrightarrow} \frac{1}{2}O_2 \uparrow + V_O^{\cdot\cdot} + 2M_M^X \tag{2.11}$$

where *M* refers to Fe or Co.

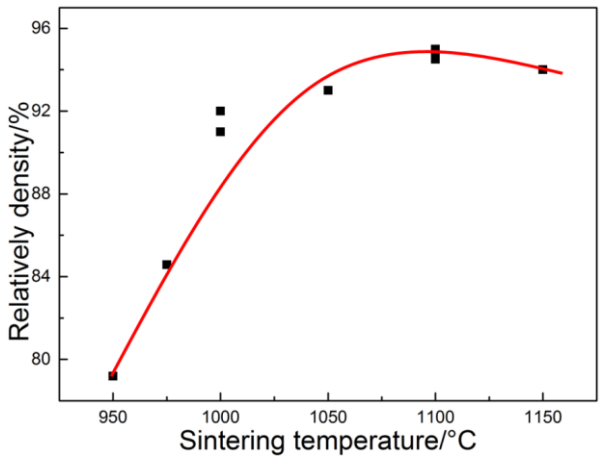

Figure 2.6 The relative density of BSCF as a function of sintering temperature. The data points were obtained from the references [13, 74]. The line is a guide to the eye.

2.5.2.1.2 Effect of dwell time on BSCF density

Dwell time also influences the relative density of BSCF membranes. For short dwell time, the influence is more significant; however, it becomes less significant as time increases beyond 10 hours as shown in Figure 2.7. Other workers[74] have also reported that the relative density remains constant after holding 10 hours and further increase in dwell time shows little influence on the relative density.

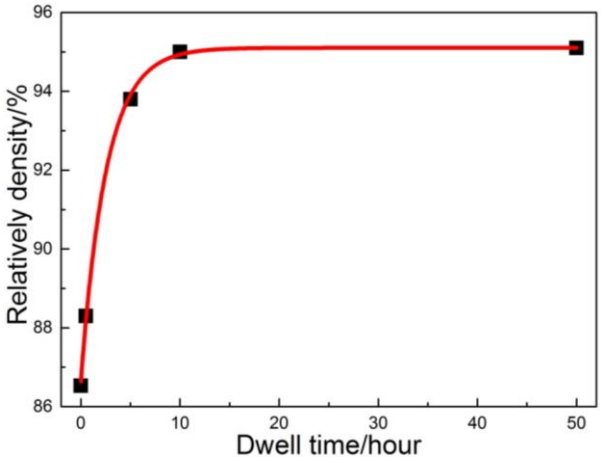

Figure 2.7 The relative density of BSCF as a function of dwell time. The data points were obtained from the references[13, 74]. The line is a guide to the eye.

2.5.2.1.3 Effect of doping on BSCF density

2.5.2.1.3.1. General mechanisms of increasing density

There are several explanations to the promoting influence of foreign cations on ceramic sintering. The first possible reason is that a secondary phase forms along the grain boundary which is generated by diffusion of low valence ions from the lattice to the grain boundary during sintering, and produces more oxygen vacancies within the grain lattice, thereby increasing the diffusion of host ions [75, 76]. The second possible reason is that the formation of secondary phase with a lower melting point becomes a liquid phase thereby promoting sintering [75, 77].

2.5.2.1.3.2. General mechanism of inhibiting density

There are also several explanations for the inhibiting effect of dopants on ceramic densification. One is that large cations can segregate strongly to the grain boundaries and restrict the diffusion of ions along grain boundaries thereby reducing grain boundary diffusivity and decreasing the densification rate[78]. Another is that secondary phase exists along the grain boundary and exerts an effective drag on the mobility of the grain boundary, thereby reducing the densification[79]. A third possible reason is the change in the controlling mechanism of densification from grain boundary diffusion to lattice diffusion [80]

2.5.2.1.3.1. Mechanism of the effect of doping on BSCF density

Studies [81-83] have reported that doping can affect the density of BSCF as well. It has been found that incorporating Cu^{2+}, Cr^{2+}, Mn^{2+}, Mg^{2+} dopants into the BSCF lattice increases the relative density, compared with pure BSCF sintered at the same conditions. This phenomenon has also been observed in other perovskite-structured materials[84].

In the case of Cu-doped BSCF, Zhao *et al*. [85] have proposed that the promoting effect of Cu dopant on the sintering of perovskite membranes can be ascribed to the formation of liquid phase CuO. With respect to Cr and Mn doping, it has been shown that these dopants improve the mobility of the A-site cation, which increases the densification of BSCF[82]. Mg-doped BSCF, introduces more oxygen vacancies, promoting cation diffusion [86]thereby increasing densification of BSCF.

However, it has been found that, Na^{+}, K^{+}, Al^{3+} and Zr^{4+} doped into BSCF lattice decrease the relative density, compared with pure BSCF sintered at the same conditions[82]. It suggests that Na^{+} or K^{+} dopant into A-site of BSCF membranes restrains the diffusion of the A-site cations during the sintering process[82]. In the case of Al-doped BSCF, Al doping inhibited the densification of BSCF, because additional phases ($BaAl_2O_4$ and $Ba_3Al_2O_6$) detected by XRD drag (pinning) the motion of grain boundary[81]. This phenomenon was also found in other Al-doped perovskite-structured materials [87, 88]. As for Zr^{4+}-doped into B-site of BSCF membranes, it has been observed by TEM [83] that small crystallites [$(Ba,Sr)ZrO_3$] form along grain boundary and inhibit the mass transport through the grain boundary thereby reducing the density.

2.5.2.2 Grain growth

2.5.2.2.1 Effect of sintering temperature and dwell time on membrane grain growth

Grain size of ceramics can be realised by controlling the sintering temperature and dwell time. Normally, grain size increases with increasing the sintering temperature and/or prolonging the dwell time[89]. Grain growth in BSCF has not been widely investigated. The isothermal rate of grain growth can be expressed by the

phenomenological kinetic grain growth equation[90]:

$$D^n - D_0{}^n = tK_0 exp(-\frac{Q}{RT}) \quad (2.12)$$

where D (μm) is average grain size at the time t; D_0 is the initial average grain size; n is the kinetic grain growth exponent, K_0 is a constant, Q is the apparent activation energy (kJ/mol); R is the gas constant, 8.314 J/mol·K; T is the absolute temperature (K). When the value of grain growth exponent is 2, the driving force for grain growth is the local curvature of the grain boundary[68]. Since research studies of the grain growth exponent in BSCF are quite limited[91], the grain growth parameters of other perovskite-structured oxides are listed in Table 2.3.

Table 2.3 Grain growth parameters of perovskite-structured materials

Perovskite materials	Grain growth exponent(n)	Activation energy Q(kJ/mol)	References
$BaTiO_3$	5	586-800	[92, 93]
$Ba_xSr_{1-x}TiO_3$(x=0.25,0.50,0.75)	/	580-791	[94]
$PrBaCoO_{5+\delta}$	3	530-560	[95]
$ZnTiO_3$	/	327	[96]
$SrTiO_3$	2	870	[97]
$SrCo_{0.8}Fe_{0.2}O_{3-\delta}$	2.5	/	[91]
$La_{0.5}Sr_{0.5}FeO_{3-\delta}$	/	385	[98]
$La_{0.6}Sr_{0.4}Co_{0.8}Fe_{0.2}O_{3-\delta}$	/	501.3	[99]
$Ba_{0.5}Sr_{0.5}Co_{0.8}Fe_{0.2}O_{3-\delta}$	3.1	/	[91]

/ Not provided by references

It is clear that the grain growth exponents of most perovskite materials are between 2 and 5. They do not follow the classic parabolic law of grain growth. Many reasons were raised to explain the deviations from the ideal grain growth, including the effect of pores or impurities which influence the grain growth kinetics[68]. As shown in Table 2.3, the activation energy for grain growth of these perovskite-structure materials is in the range from 300 to 800 kJ/mol.

Figure 2.8 shows Arrhenius profiles for grain growth of BSCF. Although there is no

direct data about the activation energy of grain growth of BSCF from the references, it can be calculated from the relevant data and is calculated to be from 372 to 741 kJ/mol, which is consistent with the data of other perovskite-structured materials in Table 2.3.

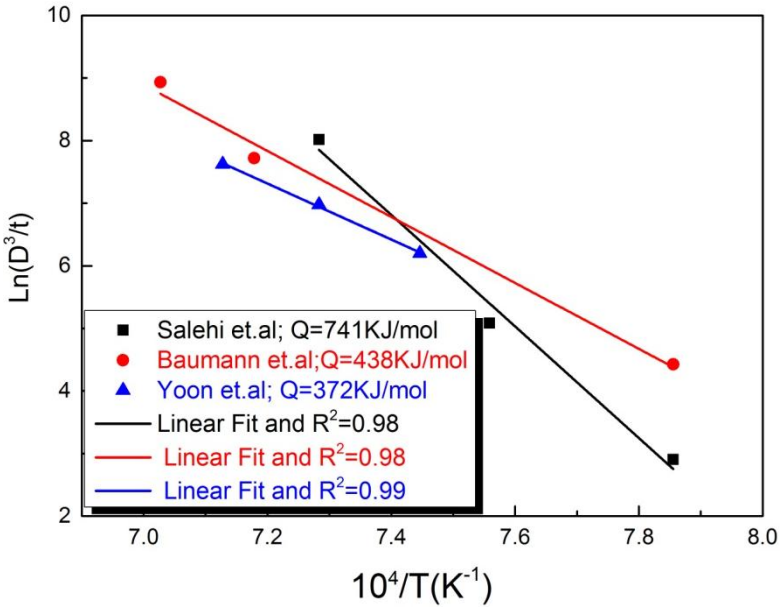

Figure 2.8 Arrhenius profiles for grain growth of BSCF. The data points were obtained from the references [13, 100, 101].

2.5.2.2.2 Effect of doping on BSCF grain growth

Doping is widely used to control grain growth in BSCF as well. It has been found that Cu^{2+} and Zn^{2+} can promote grain growth of BSCF[81]. The promoting effect of Cu^{2+} on BSCF can be attributed to the formation of A-site cation-deficient BSCF and the existence of liquid phase sintering, whereas the promoting effect of Zn^{2+} on BSCF sintering may be mainly because of the formation of A-site cation-deficient BSCF[81]. It has been reported that Zr^{4+}[102] can suppress grain growth, because secondary phases at the grain boundaries inhibit material transport through the grain boundaries and block the grain growth of the BSCF[102].

2.5.2.3 Mechanism of densification and grain growth of BSCF

As discussed above, it is difficult to clearly determine which one mechanism controls the sintering process of BSCF. According to the value of the grain growth exponent of BSCF (n=3.1), it does not follow the classic parabolic law of grain growth. Pores are reasonably believed to be the dominant factor for the higher grain growth exponent. Although there is no direct data about the activation energy of grain growth of BSCF, it can be fitted from the relevant data and is calculated to be from 372 to 741 kJ/mol as shown in Figure 2.9. It can be concluded that cations are the rate-controlling species of grain growth rather than oxygen ions, because the activation energy for oxygen ion diffusion (45-105 kJ/mol [103, 104]) is much lower than that for grain growth of BSCF, According to the studies performed by Lein *et al*.[104, 105], the diffusion of Sr/La in $La_{0.5}Sr_{0.5}Co_{0.8}Fe_{0.2}O_{3-\delta}$ has been observed to be slower than that of Co/Fe and the activation energy for Sr/La diffusion is 619 kJ/mol. Therefore, in terms of BSCF, it can be speculated that the Ba/Sr diffusion can be the rate-controlling species during the sintering process.

2.6 Mechanical properties of $Ba_{0.5}Sr_{0.5}Co_{0.8}Fe_{0.2}O_{3-\delta}$ membranes

Beside the functional performance for $Ba_{0.5}Sr_{0.5}Co_{0.8}Fe_{0.2}O_{3-\delta}$ (BSCF) membranes, good mechanical properties are also necessary in real applications. In terms of structural performance, a big challenge for BSCF is to keep chemical and structural stability not only at high operating temperature (around 800 ℃), but also under pressure gradients across the membrane and chemical or thermal strains[106]. Therefore, the understanding of mechanical properties becomes indispensable for an evaluation of

structural reliability of membranes in service. Fundamental mechanical characteristics including Young's modulus, hardness, fracture stress, and fracture toughness need to be evaluated.

2.6.1 Young's modulus

The Young's modulus, an important parameter, is used to analyse and model the mechanical property of materials, associated with stress development, deformation, and failure[107]. Elastic behaviour with uniaxial loading of isotropic ceramics is described by the Young's modulus, E, resistance to elastic deformation. It is the ratio of stress to strain in Hooke's law[108]:

$$E = \frac{\sigma}{\varepsilon} \tag{2.13}$$

where σ is the applied stress and ε is the strain.

Table 2.4 shows literature data about Young's moduli of BSCF and other perovskite-structured materials with different porosities by various methods at different temperatures.

Table 2.4 Literature data about Young's moduli of BSCF and other perovskite-structured materials with different porosities by various methods at different temperatures

Composition	Porosity	Grain size(μm)	Elastic modulus(GPa)	Temperature (℃)	Environment	Test methods	References
$Ba_{0.5}Sr_{0.5}Co_{0.8}Fe_{0.2}O_{3-\delta}$	4.5%	10	55	RT	In air	Micro-indentation	[109]
			40	200			
			48	RT	In air (annealed)		
			32	250			
			71.9	RT	In air	Micro-indentation	
			63.3	RT			
			53	100			
			47	200			
			55	300			
			53	400			
			52	500			
			50	700			
			49	800			
			72	RT	vacuum		

	4.5%	10.1	63	100		Ring-on-ring	[9]
			48	200			
			45	300			
			44	400			
			45	500			
			47	600			
			52	700			
			53	750			
			55	800			
	8%	26	52	RT	In air	Ring-on-ring	[110]
	9%	7	52	RT	In air	Ring-on-ring	[83]
	22%		50	RT	In air	Ring-on-ring	[111]
	27%		42				
	34%		35	RT			[83]
	38%	5	38	RT	In air	Micro-indentation	[112]
			33	RT		Ring-on-ring	
			27	200			
			27	400			

			29	600			
			27	800			
			68	RT	In air	Compressive test	[113]
			68	RT		Ring-on-ring	
			62	RT		O-ring	
			61	RT		Micro-indentation	
			30.6	900		Ring-on-ring	
	42%		22	RT	In air	Ring-on-ring	[111]
			15	200			
			17	400			
			17	600			
			17	800			
$LaFeO_3$	5%	3.3	213	RT	In air	Four-point bending	[114]
			206	800			
$LaCoO_3$	16%	2~3	47.8	RT	In air	Four-point bending	[115]
	10.2%		76	RT			[116]
			101	800			
$La_{0.8}Ca_{0.2}Co\ O_{3-\delta}$	0.15%	1~2	111.5	RT			[115]

			68	800			[116]
$La_{0.8}Sr_{0.2}Co\ O_{3-\delta}$	9.5%	2~3	64.4				[115]
$La_{0.2}Sr_{0.8}Fe_{0.6}Co_{0.4}\ O_{3-\delta}$			124	RT	In air		
$La_{0.5}Sr_{0.5}Fe_{0.5}Co_{0.5}O_{3-\delta}$	3%	0.8	115	RT	In air	Four-point bending	[117]
			160	800			
	5%	1.1	118	RT			
			169	800			
			121	1000			
$La_{0.5}Sr_{0.5}Fe_{0.75}Co_{0.25}O_{3-\delta}$	3%	1.4	115	RT			
			176	400			
			177	600			
			160	800			
$La_{0.5}Sr_{0.5}Co\ O_{3-\delta}$	1%	1.7	RT	122			
			800	157			
$La_{0.8}Sr_{0.2}Ga_{0.8}Mg_{0.2}O_{3-\delta}$	5%	9.0	RT	176		Four-point bending	[118]

According to the data about Young's moduli of other perovskite-structured materials, there are many factors affecting the Young's modulus, including composition, temperature, measurement method and porosity. With regard to compositions, the Young's modulus of $LaCoO_3$ is 83 GPa at RT[116], while the substitution of Fe with Co increases significantly the Young's modulus, and the value for $LaFeO_3$ is 213 GPa[114]. The partial substitution of La with Ca considerably enhances the Young's modulus, and the value for $La_{0.8}Ca_{0.2}CoO_3$ is 112 GPa[115]; while the partial replacement of La with Sr increases the Young's modulus slightly, to a value for $La_{0.8}Sr_{0.2}CoO_3$ of 86 GPa at room temperature[115]. Upon further replacement of La with Sr, the Young's modulus of $La_{0.5}Sr_{0.5}CoO_3$ has been obtained as 131 GPa[117], which is twice as high as the value for BSCF at room temperature. In the case of BSCF, the effects of measurement, porosity and temperature on Young's modulus are discussed in detail below.

2.6.1.1 Effect of measurement method on the Young's modulus of BSCF

Different methods for determining Young's modulus have been developed, which are based on the elastic response of the materials under loading. For brittle materials, both uniaxial and biaxial bending tests can be applied [113, 115]. These universal tests are regarded as a good representation of macroscopically destructive methods, while the micro-indentation test is also popularly utilised in determining Young's modulus as a non-destructive method[119]. The principles of these measurement techniques are reviewed and compared below

2.6.1.1.1 Uniaxial bending test

For uniaxial loading, the three-point bending test is widely used in analysing the

mechanical properties of brittle materials. A schematic diagram of the three-point bending test is shown in Figure 2.9.

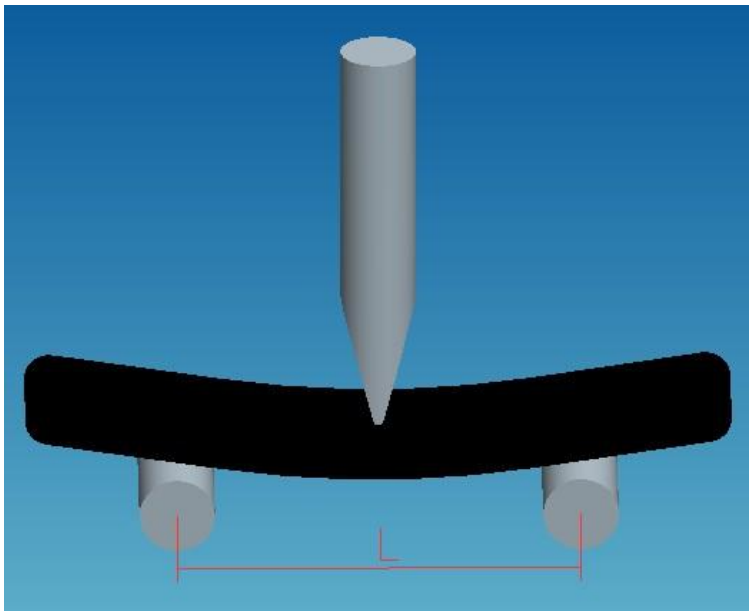

Figure 2.9 The schematic diagram of three-point bending test

The Young's modulus *E* is calculated using the following equation:

$$E = \frac{L^3 \Delta F}{4bh^3 \Delta d} \tag{2.14}$$

where *F* is the load; *L* is the distance between the two support points; *b* is the width of the specimen at the applied load; *h* is the thickness of the specimen; and *d* is the central deflection of the specimen.

The advantages of this method include easily achieved alignment and simple geometry of samples[120]. The disadvantage of this method is related to the maximum tensile stress which cannot be made vertically and laterally homogeneous[120]. In addition, this test is inherently sensitive to the defects and flaws near the specimen edge[121]. Therefore, the requirement for sample edges is to avoid any effect of cutting-induced flaws. However, there are currently no previous reports of the Young's modulus of BSCF determined by the uniaxial bending test.

2.6.1.1.2 Biaxial bending test

In terms of biaxial loading, the ring-on-ring bending test has been used in determining mechanical properties of brittle materials[122]. The schematic picture of the test is displayed in Figure 2.10:

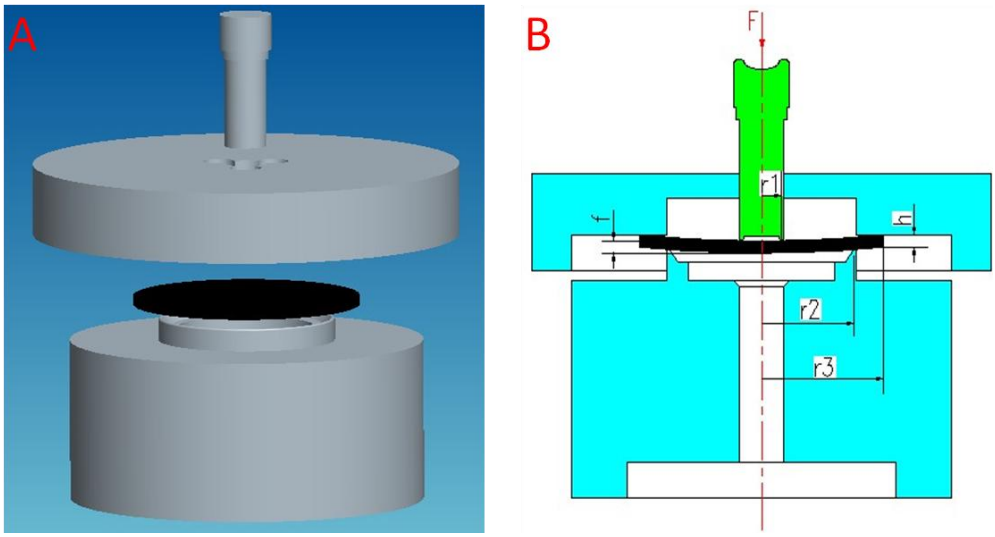

Figure 2.10 (A) Schematic representation of the ring-on-ring test; (B) Cross section

The Young's modulus *E* is calculated using the following equation:

$$E = \frac{3(1-\nu^2){r_1}^2 \Delta P}{2\pi {t_h}^3 \Delta d}\left[\left(\frac{r_2}{r_1}\right)^2 - 1 - ln\left(\frac{r_2}{r_1}\right) + \frac{1}{2}\left(\frac{1-\nu}{1+\nu}\right)\frac{({r_2}^2-{r_1}^2)^2}{{r_2}^2{r_3}^2}\right] \quad (2.15)$$

where *P* is the loading force; t_h is the specimen thickness; *d* is the central deflection of the specimen; ν is the Poisson ratio; r_1,r_2,r_3 are the radii of the loading ring, the supporting ring and the specimen, respectively[123].

This method removes the edge effect in comparison with the three-point bending test, as no stress is generated near the sample edges[121]. Particularly, the approximately constant equibiaxial and systematic maximum tensile stress occurs within the central loading area on the tensile surface[124]. However, the drawback of this method is that the stress distribution can be easily influenced by the flatness of disc-shaped samples. According to Huang *et al.*[19], the Young's modulus of BSCF determined by the

ring-on-ring method at RT was obtained as 63.3 GPa with a porosity of 4.5% while it was determined to be 52 GPa with a porosity of 8.7% by Pećanac *et al*. [125].

2.6.1.1.3 Micro-indentation test

The micro-indentation method is also widely used to determine Young's modulus. This tests can be carried out with different types of indentation tips, such as Brinell, Knoop, and Vickers[126]. For the Vickers indenter, the tip is pyramid-shaped and has 4 sides with an angle of 136 ° between opposite sides[127]. The major advantage of this technique depends on the fact that it is non-destructive and a very small surface area is used. The calculation of indentation Young's modulus E_{IT} is based on[128]:

$$E_{IT} = \frac{(1-{\nu_s}^2)}{\frac{1}{E_r}-\frac{(1-{\nu_i}^2)}{E_i}} \tag{2.16}$$

where E_i is the Young's modulus of the indenter (1141 GPa for diamond); ν_s, ν_i are the Poisson's ratio of the tested samples and indenter (0.07 for diamond), respectively. The reduced modulus E_r, which is calculated from the indentation data, is defined as:

$$E_r = \frac{\sqrt{\pi}}{2\beta}\frac{S}{\sqrt{A_p}} \tag{2.17}$$

where β is the indenter constant; S is the maximum slope of the load-displacement curve; A_p is the projected contact area at applied load[128].

Studies performed using the micro-indentation test on BSCF to determine its Young's modulus obtained higher values than those obtained from ring-on-ring bending test at room temperature, because the effective volume of the micro-indentation method is much lower than that of the biaxial bending method[19, 113]. This phenomenon is widely observed in other ceramic materials [129, 130].

2.6.1.2 Effect of porosity on the Young's modulus of BSCF

Many experimental and theoretical studies have been carried out to evaluate the influence of porosity on the Young's modulus of ceramics [131-134]. The empirical relation between porosity and Young's modulus is widely used for predicting the modulus of pore-free materials[135]:

$$E = E_0 \cdot exp(-bp) \tag{2.18}$$

where E_0 is the Young's modulus of the fully dense material, p is volume fraction of the porosity and b is an empirical constant ranging between 2 to 5. The Young's modulus-porosity relationship can also be written in a linearised form such that

$$ln(E) = -bp + ln(E_0) \tag{2.19}$$

Figure 2.11 shows the dependence of the Young's modulus of BSCF on the porosity, where the moduli were determined by the ring-on-ring bending tests and replotted from Table 2.4. The Young's modulus monotonically decreases with increasing porosity. The linear fit to Equation (2.19) yielded values of 74 GPa for E_o and 2.6 for the constant b, with a R^2 value of 0.91.

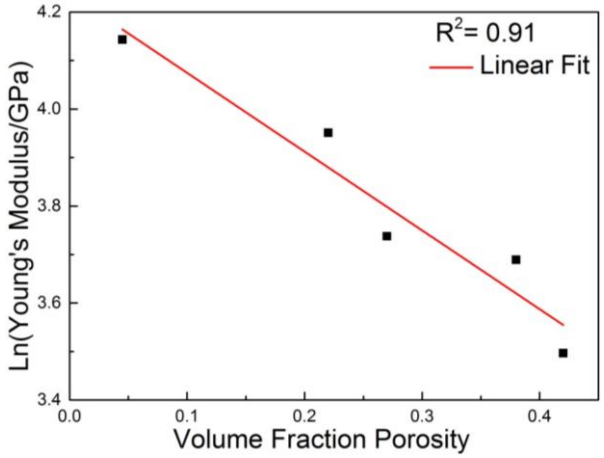

Figure 2.11 Young's modulus of BSCF as a function of porosity determined by ring-on-ring bending tests. The data points were obtained from the references [19, 112].

2.6.1.3 Effect of temperature on the Young's modulus of BSCF

Normally, the Young's modulus of ceramics tends to reduce with increasing temperature because of lattice softening[136]. According to Watchman *et al.*[136], the Young's modulus of polycrystalline ceramics exhibit a reduction of about 1% per 100 ℃ temperature rise. However, some perovskite-structured materials show anomalous behaviour of Young's modulus as a function of temperature. In the case of $BaTiO_3$, the value of the Young's modulus obtained at 450 ℃ was reported to be much higher than that value at RT, because there was a phase transition from rhombohedral to cubic structure in the temperature range from RT to 450 ℃[137]. Huang *et al.*[19] have reported that the Young's modulus of BSCF with a porosity of 4.5% also showed an anomalous tendency as a function of temperature. The reason for this anomalous behaviour of BSCF is different from that of $LaCoO_3$. In terms of BSCF, the Young's modulus showed a local minimum value at 200 ℃, and then increased with temperature up to 400 ℃, followed by a slight decrease up to 800 ℃. It has been demonstrated that this anomaly in Young's modulus can be ascribed to spin transition effect of Co^{3+} [19]. To be more specific, the transition from low to high spin state is accompanied by an anomalous expansion of Co ions, which affects the mechanical behaviour of BSCF[138]. In addition, a similar tendency of Young's modulus as a function of temperature from RT to 800 ℃ was observed for both dense[19] and porous BSCF[111, 112] in Figure 2.12.

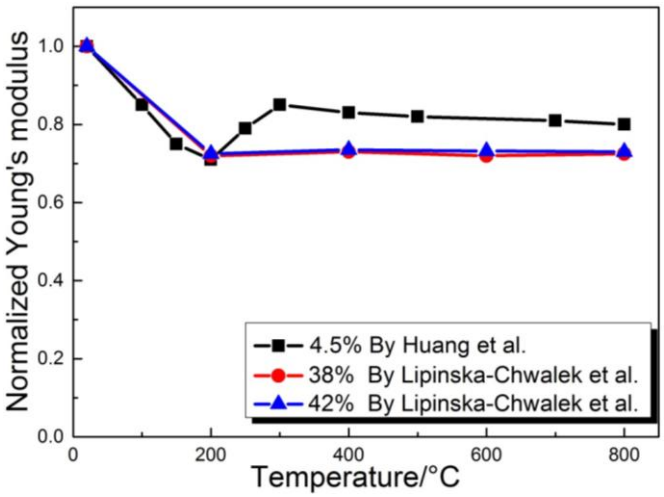

Figure 2.12 Normalised Young's modulus of dense and porous BSCF materials as a function of temperature. All data sets are normalised with respect to the RT values. The data points were obtained from the references [19, 111, 112].

2.6.2 Hardness

Hardness, another important parameter for a brittle material, is an assessment of its resistance to plastic deformation [139]. Indentation hardness test is a convenient method conducted within a small volume of material. The detailed process of the hardness test consists of applying a certain load with an indenter and measuring under a microscope, the resultant indentation imprint on the surface after removing the load. There are different conventional indenters, including Vickers, Berkovich and Knoop. In this study, the Vickers test only is discussed in detail. The hardness, H_v, is calculated by the ratio of the applied load via a pyramidal contact area, A[128]:

$$H_v = \frac{P}{A} = \alpha \frac{P}{d^2} \tag{2.20}$$

where P is the applied load, d is a measure of the impression size, and α is indenter geometry (1.8544). As illustrated the Table 2.5, the hardness of dense perovskite-structured materials normally is in the range from 4 to 10 GPa. It also shows that the hardness is highly dependent on composition, porosity, load and temperature. According to the research by Rice[140], grain size also can influence the hardness in

ceramic materials. However, there are no publications related to the effect of grain size on the hardness of BSCF. Therefore, the effects of load, porosity, and temperature on hardness of BSCF are discussed in detail below.

Table 2.5 Hardness of perovskite-structured materials with different porosities and various temperatures

Composition	Porosity	Grain size (μm)	Hardness (GPa)	Temperature (℃)	Load (N)	References
$Ba_{0.5}Sr_{0.5}Co_{0.8}Fe_{0.2}O_{3-\delta}$	4.5%	10	9.1	RT	0.01	[109]
			7.5		0.1	
			6.1		1	
			5.8		10	
			4.2	100	10	
			4.0	150		
			3.9	200		
			3.8	250		
			3.7	350		
	4.5%	10.1	5.7	RT	0.1	[141]
			5.8		0.2	
			5.6		0.4	
			5.5		0.6	
			5.2		0.8	
			5.3		1	
	38%	5	0.95	RT	3	[112]
			0.93		5	
			0.89		10	
			0.87		15	
			0.90	100	3	
			0.85		5	
			0.82		10	
			0.80		15	
			0.73	200	3	
			0.74		5	
			0.70		10	
			0.68		15	
			0.67	300	3	
			0.66		5	
			0.66		10	
			0.60	400	3	
			0.60		5	
			0.60		10	
$La_{0.8}Sr_{0.2}Co_{0.2}Fe_{0.8}O_{3-\delta}$	5%	1.9	6.8	RT	20	[142]
$La_{0.2}Sr_{0.8}Co_{0.2}Fe_{0.8}O_{3-\delta}$		21.9	6.0			

$La_{0.8}Sr_{0.2}Co\ O_{3-\delta}$	10%	2~3	7~9	RT	3	[115]
$La_{0.8}Ca_{0.2}Co\ O_{3-\delta}$	1.5%	1~2	9~11			
$La_{0.9}Sr_{0.1}Ga_{0.2}Mg_{0.8}O_{3-\delta}$	5%	17	7~8	RT	50	[143]
$La_{0.8}Sr_{0.2}Cr_{0.2}Fe_{0.8}\ O_{3-\delta}$	7%	2.1	7.3	RT	20	[144]
$La_{0.6}Sr_{0.4}Cr_{0.2}Fe_{0.8}O_{3-\delta}$	3%	0.5	6.8			
$La_{0.4}Sr_{0.6}Cr_{0.2}Fe_{0.8}O_{3-\delta}$	3%	1.4	5.4			
$La_{0.2}Sr_{0.8}Cr_{0.2}Fe_{0.8}O_{3-\delta}$	4%	3.6	4.6			
$La_{0.9}Sr_{0.1}Ga_{0.2}Mg_{0.8}O_{3-\delta}$	5%		7	RT	50	[145]
$La_{0.9}Ba_{0.1}Ga_{0.8}Mg_{0.2}O_{3-\delta}$			8.4			
$La_{0.9}Ca_{0.1}Ga_{0.8}Mg_{0.2}\ O_{3-\delta}$		23.5	8.6			
$La_{0.8}Sr_{0.2}Ga_{0.9}Mg_{0.1}O_{3-\delta}$	2%		8.2			
$La_{0.9}Sr_{0.1}Ga_{0.85}Mg_{0.15}\ O_{3-\delta}$	3%		7.8			
$Y_{0.8}Ca_{0.2}CrO_{3-\delta}$	3%		9.9	RT	50	[146]
$Y_{0.75}Ca_{0.25}Cr\ O_{3-\delta}$	4%		10.8			
$La_{0.75}Ca_{0.25}Cr\ O_{3-\delta}$	4%		7.1			

2.6.2.1 Effect of applied load on the hardness of BSCF

When a low load is applied in the Vickers test, the value of hardness obtained is normally high. With an enhancement of applied load, the values show a reduction. This fluctuation between hardness and applied load is often regarded as the indentation size effect (ISE)[147]. This phenomenon is typically observed in single crystals with diverse types of bonding, including ionic, metallic and covalent[147, 148]. The indentation size effect has been attributed to surface effects[149], strain gradient effects[150-152], structural non-uniformity of the deformed volume[153], changes in the contributions of elastic and plastic deformation at the indentation[147], and friction between the indenter and the sample[154].

According to the references [139, 155, 156], the curves of hardness against the applied load have a tendency to flatten out and the values of hardness becomes stable. A good empirical equation of the Meyer law can be written as:

$$P = Cd^n \tag{2.21}$$

where P is the applied load, d is the indentation size, C is a constant, and n is the Meyer

coefficient[139, 155, 156]. With comparison of Equations (2.20) and (2.21), it can be found that hardness remains a constant independent of the applied load and the graph of hardness against the applied load is flat when *n* equals to 2. However, for most ceramics, *n* is normally greater than 2 and hardness decreases with increasing the applied load.

It has also been reported that the ISE was observed at elevated temperatures by micro-indentation tests as for BSCF with the porosities of 4.5%[109] and 38%[112] as shown below in Figure 2.15.

2.6.2.2 Effect of porosity on the hardness of BSCF

The hardness of BSCF with a porosity of 4.5% at RT is 5.8 GPa[109], while the hardness of the sample with a porosity of 38% is 0.89 GPa at the same applied loading[112]. Therefore, the hardness of BSCF is strongly dependent on porosity. The indentation hardness of the sintered BSCF samples prepared in literature is a strong function of the volume fraction porosity as illustrated in Figure 2.13 [109, 112].

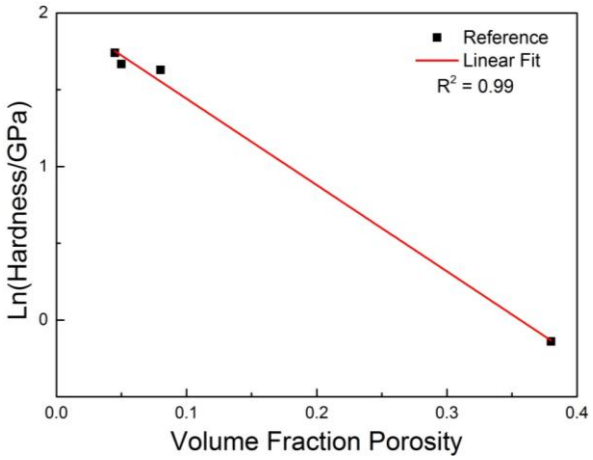

Figure 2.13 Hardness of BSCF as a function of porosity. The data points were obtained from the references[109, 112].

The porosity dependence of hardness is consistent with the Minimum Solid Area (MSA) model proposed by Rice[157, 158]. The MSA model has been employed to describe the porosity dependence of mechanical properties, such as hardness[159, 160], fracture

strength[161], and elastic modulus[159, 162] of a variety of ceramic materials. For hardness, the MSA model can be represented by[158]

$$H_{IT} = H_0 exp(-bp) \tag{2.22}$$

where H_{IT} is the measured indentation hardness, H_0 is the indentation hardness value corresponding to a specimen with zero porosity, b is a material dependent constant and p is the volume fraction porosity of the specimen. The hardness-porosity relationship [Equation (2.22)] can also be written in a linearised form such that

$$ln(H_{IT}) = -bp + ln(H_0) \tag{2.23}$$

The linear fit to Equation (2.23) yields values of 8 GPa for H_0 and 3.4 for the constant b, with a R^2 value of 0.99.

2.6.2.3 Effect of temperature on the hardness of BSCF

Both Chanda *et al.*[109] and Lipinska-Chwalek *et al.*[112] have found that the hardness decreased with increasing temperature as shown in Figure 2.14. A similar indentation size effect was also found at elevated temperature. The hardness decreased by around 35% from RT to 400 ℃ for dense (4.5%) and porous (38%) samples. Because hardness is dependent on the elastic and inelastic deformation, the decrease in hardness with increasing temperature can be partially caused by the reduction in Young's modulus[109]. However, no recovery effect was observed for the hardness of BSCF at 400 ℃, which differed from the trend in Young's modulus.

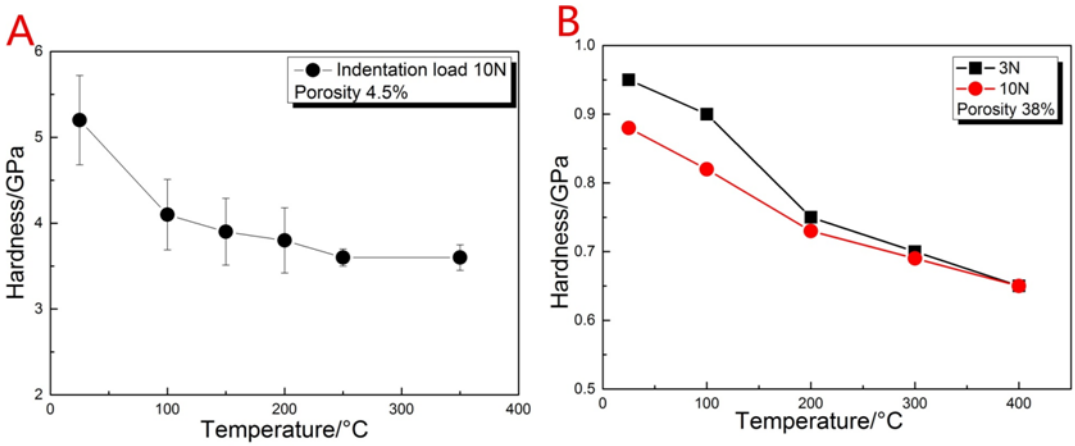

Figure 2.14 Hardness of BSCF as a function of temperature with different porosities: (A) 4.5%; (B) 38%. The data points were obtained from references [109, 112].

2.6.3 Fracture stress

Fracture stress is another important parameter to define the mechanical properties of brittle materials. The fundamental cause of fracture is that the chemical bonds are broken between atoms and fracture always happens originating from a critical defect[163]. The cohesive stress in theory is calculated by the following equation:

$$\sigma_c = \sqrt{\frac{E\gamma_s}{x_0}} \tag{2.24}$$

where E is Young's modulus, γ_s is the surface energy and x_0 is the distance between atoms in equilibrium.

According to the study of fractography for brittle materials by Quinn[164], the fracture stress of brittle materials is mainly influenced by the location of critical flaws and their sizes. They can be located on the surface or close to the surface, also at the edge of bar-shaped samples due to machining effect. It has been reported by Green[165] that surface cracks are the most severe flaws, while voids in the bulk are the next severe population.

With respect to uniaxial and biaxial bending tests, the highest probability of failure due

to the flaws will be close to the location where the maximum tensile stress occurs. The fracture stress scatter data related to the effect of the defect size distribution can be evaluated statistically by a Weibull approach[166]. Weibull statistics are regarded as an acceptable approach in engineering to evaluate the reliability of a material or component[165]. It provides a way of accessing the dependability of the material, disclosing the probability of failure at any selected level of stress[167]. The simplest treatment of the size dependence of strength is through the application of Weibull statistical fracture theory. According to this theory, the probability of failure of a component, *F* is given by[168, 169]

$$F = 1 - exp[-(\frac{\sigma_{max}}{\sigma_c})^m V_{eff}] \quad (2.25)$$

where σ_{max} is reference maximum stress in the stressed solid, m Weibull modulus, σ_c characteristic strength, and V_{eff} effective stress volume defined by

$$V_{eff} = \int (\frac{\sigma}{\sigma_{max}})^m d_V \quad (2.26)$$

where σ = local stress in an elemental stressed volume d_V.

The fracture stresses of perovskite-structured materials with different porosities at various temperatures are shown in Table 2.6. According to the literature, the fracture stress depends on the measurement method, porosity and temperature. For BSCF, the effect of the measurement method on fracture stress of BSCF will be discussed in Chapter 4.2 below. The following discussion focuses on the effects of porosity and temperature on fracture stress of BSCF.

Table 2.6 Fracture stress of perovskite-structured materials with different porosities at various temperatures

Composition	porosity	Grain size (μm)	Fracture stress(MPa)	Temperature (℃)	Test methods	References
$Ba_{0.5}Sr_{0.5}Co_{0.8}Fe_{0.2}O_{3-\delta}$	5%	10.1	99	RT	Ring-on-ring	[141]
			58	200		
			52	300		
			50	400		
			68	500		
			74	700		
			76	800		
	8%		86	RT	Ring-on-ring	[110]
	9%	7	86±4	RT	Ring-on-ring	[83]
	34%		31±1	RT	Ring-on-ring	
	38%	5	34	RT	Ring-on-ring	[112]
			32	200		
			30	400		
			36	600		
			50	800		
			22	RT		
			16	200		

	42%		30	800	Ring-on-ring	[111]
$La_{0.8}Sr_{0.2}Co_{0.2}Fe_{0.8}O_{3-\delta}$	4%	1.8	155	RT	Biaxial	[142]
$La_{0.6}Sr_{0.4}Co_{0.2}Fe_{0.8}O_{3-\delta}$	5%	2.9	165	RT		
$La_{0.4}Sr_{0.6}Co_{0.2}Fe_{0.8}O_{3-\delta}$	3.5%	6.3	52	RT		
$La_{0.2}Sr_{0.8}Co_{0.2}Fe_{0.8}O_{3-\delta}$	5%	21.9	40	RT		
$La_{0.8}Sr_{0.2}Cr_{0.2}Fe_{0.8}O_{3-\delta}$	7%	2.1	243	RT		[144]
$La_{0.6}Sr_{0.4}Cr_{0.2}Fe_{0.8}O_{3-\delta}$	3.2%	0.5	138	RT		
$La_{0.9}Sr_{0.1}Ga_{0.8}Mg_{0.2}O_{3-\delta}$	5.1%	3~5	164	RT		[170]
			55	900		
$La_{0.5}Sr_{0.5}Co_{0.5}Fe_{0.5}O_{3-\delta}$	3%	1.1	128	RT	Four-point bending	[171]
			166	800		
			181	1000		
$La_{0.5}Sr_{0.5}Co_{0.75}Fe_{0.25}O_{3-\delta}$	3%	1.4	71	RT		
			61	400		
			121	600		
			120	800		
$La_{0.5}Sr_{0.5}CoO_{3-\delta}$	1%	1.7	138	RT		
			181	800		
$La_{0.8}Sr_{0.2}CoO_{3-\delta}$	9.5%	2~3	76	RT		[115]
			57	850		
$La_{0.8}Ca_{0.2}CoO_{3-\delta}$	0.15%	1~2	150	RT		
			63	800		
	3.6%	9	123	RT		[172]

$La_{0.75}Ca_{0.25}CrO_{3-\delta}$			64	600		
			62	800		
			59	1000		
$La_{0.7}Ca_{0.3}CrO_{3-\delta}$	2.8%	6.6	107	RT		
			105	200		
			84	400		
			42	600		
			35	800		
			23	1000		
$La_{0.7}Sr_{0.3}CrO_{3-\delta}$	4%		145	600		[173]
			130	700		
			110	800		
			102	900		
			91	1000		
$La_{0.5}Sr_{0.5}Cr_{0.8}Co_{0.2}O_{3-\delta}$	4%		210	600		
			190	700		
			157	800		
			143	900		
			126	1000		
	1%		79	RT		[174]
			58	200		
			108	400		
			172	600		

$La_{0.5}Sr_{0.5}MnO_{3-\delta}$			189	700		
			202	800		
$La_{0.5}Sr_{0.5}Mn_{0.96}Co_{0.04}O_{3-\delta}$	20%		38	RT		
			59	300		
			142	450		
			115	600		
			115	750		
$LaCr_{0.9}Mg_{0.1}\ O_{3-\delta}$	5%		140	RT		[175]
			247	125		
			170	400		
			87	1000		
$La_{0.7}Sr_{0.3}O_{3-\delta}$	6%		234	RT	Three-point bending	[176]
$La_{0.7}Ca_{0.3}O_{3-\delta}$			256	RT		
$La_{0.875}Sr_{0.125}MnO_{3-\delta}$	4%	4.4	164	RT		[177]
			109	400		
			150	800		
			222	1000		
$La_{0.8}Sr_{0.2}Ga_{0.85}Mg_{0.15}O_{3-\delta}$	<5%	10~15	139	RT		[178]
$La_{0.9}Sr_{0.1}Ga_{0.8}Mg_{0.2}O_{3-\delta}$			162	RT		
$La_{0.8}Sr_{0.2}Ga_{0.8}Mg_{0.2}O_{3-\delta}$			115	RT		

2.6.3.1 Effect of porosity on the fracture stress of BSCF

The dependence of fracture stress on porosity is consistent with the Minimum Solid Area (MSA) model that has been proposed by Rice[157, 158]. In the case of fracture stress, the MSA model can be represented by[158]

$$\sigma_f = \sigma_0 exp(-bp) \tag{2.27}$$

where σ_f is the measured fracture stress, σ_0 is the fracture stress value corresponding to a specimen with zero porosity, *b* is a material dependent constant and *p* is the volume fraction porosity of the specimen.

Figure 2.15 shows the fracture stress of the sintered BSCF samples as a function of the volume fraction porosity. It is clearly shown that fracture stress decreases with increasing porosity. The fracture stress-porosity relationship [Equation (2.27)] can also be written in a linearised form such that

$$ln(\sigma_f) = -bp + ln(\sigma_0) \tag{2.28}$$

The linear fit to Equation (2.28) yielded values of 118 MPa for σ_0 and 3.7 for the constant *b*, with a R^2 value of 0.97, as shown in Figure 2.15

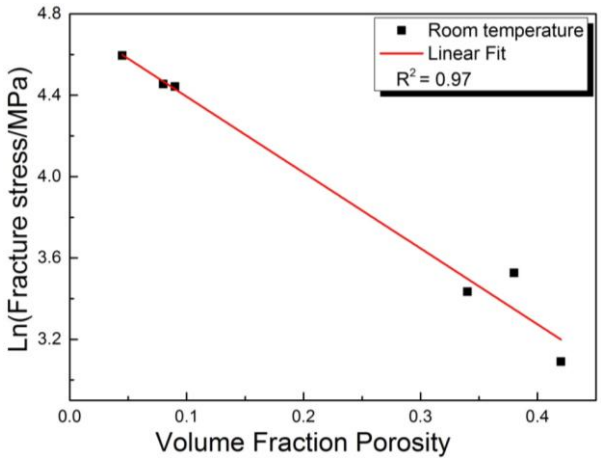

Figure 2.15 Fracture stress of BSCF determined by ring-on-ring bending test as a function of porosity. The data points were obtained from the references [19, 111, 112].

2.6.3.2 Effect of temperature on the fracture stress of BSCF

For ceramic materials, the fracture stress normally decreases with increasing temperature. This phenomenon of perovskite-structured materials can be clearly observed in Table 2.6[115, 170, 172, 173]. However, some peroskite-structured materials show an anomaly in fracture stress behaviour. In the case of $La_{0.5}Sr_{0.5}Fe_{1-x}Co_xO_{3-\delta}$[171], the fracture stress increases with increasing temperature. This anomalous behaviour can be ascribed to relaxation of the frozen-in stress gradients at the surface of the materials during cooling[171]. For $LaCr_{0.9}Mg_{0.1}O_{3-\delta}$[175] and $La_{0.875}Sr_{0.125}MnO_{3-\delta}$[177], it has been demonstrated that a phase transition from rhombohedral to orthorhombic structure results in the anomalous behaviour of fracture stress.

With regard to BSCF, the reason for its anomalous behaviour of fracture stress is different from those of other perovskite-structured materials mentioned above. According to the research by Huang *et al.*[19], the fundamental reason for this anomalous behaviour can be related to spin transitions of Co^{3+}. For either dense or porous BSCF, the fracture stress decreased with increasing the temperature up to 400 ℃, and then it increased with the temperature increasing up to 800 ℃. For dense BSCF, the fracture stress at 800 ℃ only recovered to 70% of its value at room temperature. However, the fracture stress at 800 ℃ was much greater than the value obtained at room temperature for porous BSCF. According to the investigation of fracture surfaces of porous BSCF by Lipinska-Chwalek[111], there were precipitates at the grain boundaries of porous BSCF after the test at 800 ℃. This additional phase possibly inhibited crack propagation. With respect to the mechanical reliability of porous BSCF, the material seems to be more resistant to failure at higher temperature. Different groups [19, 111,

112] have investigated the fracture stress as a function of temperature for dense (4.5%) and porous(38% and 42%) BSCF membranes as shown in Figure 2.16. Although the fracture stress of BSCF strongly depends on the porosity, they showed the similar tendency with a function of temperature.

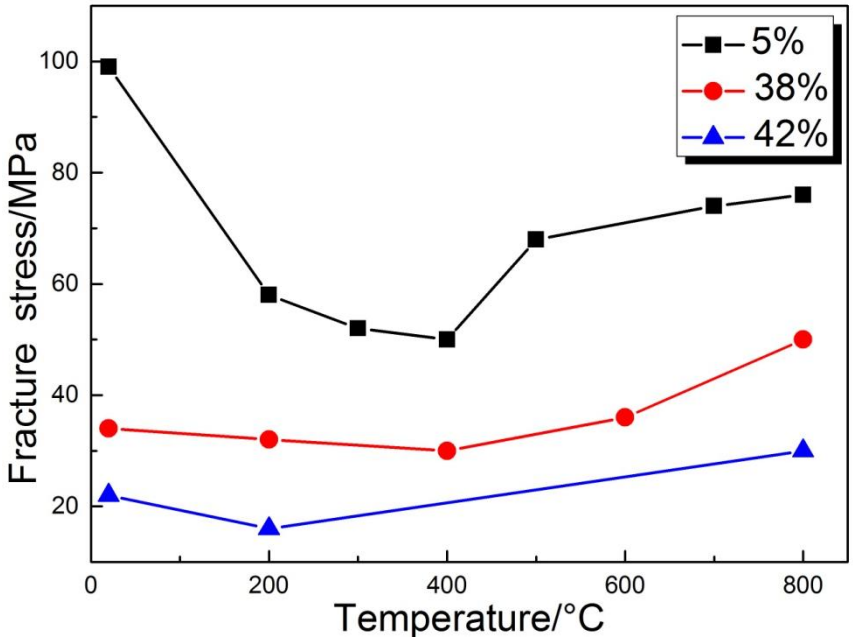

Figure 2.16 Fracture stress of BSCF with different porosities as a function of temperature. The data points were obtained from the references [139, 149, 150].

2.6.4 Fracture toughness

Fracture toughness is a property that describes the ability of a material to resist crack growth and fracture, and is one of the most important properties of ceramics considered for design application[165]. There are different popular methods to determine the fracture toughness, such as indentation crack measurement method, indentation strength method, single edge notched beam, single edge V-notch beam and double torsion[165]. According to the summarised fracture toughness of perovskite-structured materials in Table 2.7, it is dependent on the composition, measurement method, temperature, porosity, and grain size.

It has been reported by Huang *et al.*[179] that annealing has an influence on the fracture toughness of BSCF determined by indentation strength method, and the value of BSCF without annealing is approximately 33% lower than that of annealed ones. However, for the similar perovskite material $La_{0.58}Sr_{0.4}Co_{0.2}Fe_{0.8}O_{3-\delta}$, the results revealed that annealing almost had no influence on the fracture toughness. According to the literature [180-183], the grain size can influence the fracture toughness. But in the case of BSCF, there is no reference related with the effect of grain size on the fracture toughness. The following discussion will focus on the influence of measurement method, porosity and temperature on the fracture toughness of BSCF.

Table 2.7 Fracture toughness of perovskite materials determined by different techniques at various temperatures

Composition	porosity	Grain Size (μm)	Fracture toughness (MPa $m^{0.5}$)	Temperature(℃)	Test method	references
$Ba_{0.5}Sr_{0.5}Co_{0.8}Fe_{0.2}O_{3-\delta}$	4.5%	10.1	0.85	RT	Micro-indentation	[141]
			0.54	100		
			0.45	150		
			0.44	200		
			0.44	250		
			0.43	350		
	4.5%	10	0.9	RT	Micro-indentation	[109]
			1.2			
			1.3			
			1.4			
			1.44			
			1.22	RT	Indentation strength(Ring-on-ring)	
			0.75	200		
			0.58	400		
			0.78	600		
			0.92	800		
	4.5%	10	0.69	RT		[179]
			1.03		Indentation strength(Ring-on-ring)	
			0.96		Micro-indentation	

			1.01			
			1.37		Indentation strength(Ring-on-ring)	
	38%	5	0.70	RT	Micro-indentation	[112]
			0.66	100		
			0.52	200		
			0.50	300		
			0.46	400		
			0.60	RT	Indentation strength(Ring-on-ring)	
			0.52	200		
			0.45	400		
			0.60	600		
			0.92	800		
			2.08	RT	Indentation strength(three-point bending)	[184]
			2.00	200		
			1.49	400		
			1.37	600		
			1.66	800		
			1.45	RT		
			1.07	200		
			1.14	400		
			0.98	600		
			1.35	800		
$La_{0.8}Sr_{0.2}Co_{0.2}Fe_{0.8}O_{3-\delta}$	4%	1.8	1.5	RT	Indentation crack measurement	[142]
$La_{0.6}Sr_{0.4}Co_{0.2}Fe_{0.8}O_{3-\delta}$	5%	2.9	1.1			

$La_{0.4}Sr_{0.6}Co_{0.2}Fe_{0.8}O_{3-\delta}$	3.6%	6.3	0.95			
$La_{0.2}Sr_{0.8}Co_{0.2}Fe_{0.8}O_{3-\delta}$	5%	21.9	1.1			
$La_{0.9}Sr_{0.1}Ga_{0.8}Mg_{0.2}O_{3-\delta}$	5%	23.5	1.12	RT		[145]
$La_{0.9}Ba_{0.1}Ga_{0.8}Mg_{0.2}O_{3-\delta}$			0.76			
$La_{0.9}Ca_{0.1}Ga_{0.8}Mg_{0.2}O_{3-\delta}$			0.68			
$La_{0.8}Sr_{0.2}Ga_{0.9}Mg_{0.1}O_{3-\delta}$			1.00			
$La_{0.9}Sr_{0.1}Ga_{0.85}Mg_{0.15}O_{3-\delta}$			1.11			
$La_{0.8}Sr_{0.2}Co\ O_{3-\delta}$	9.5%	2~3	0.73	RT		[115]
$La_{0.8}Ca_{0.2}Co\ O_{3-\delta}$	0.15%	1~2	0.98			
$BaTiO_3$	1.5%		1	RT		[185]
$La_{0.76}Sr_{0.24}Cr\ O_{3-\delta}$	8%	4.1	1.1	RT		[172]
$LaFeO_3$	4%	3.3	2.5	RT	Single edge notched beam	[114]
			2.3	400		
			2.2	600		
			3.1	800		
$La_{0.5}Sr_{0.5}CoO_{3-\delta}$	1%	1.7	1.47	RT		[171]
			2.88	800		
$La_{0.9}Sr_{0.1}Ga_{0.8}Mg_{0.2}O_{3-\delta}$	5%	23.5	2.06	RT		[145]
			1.95	200		
			1.05	400		
			0.76	600		
			0.81	800		
			0.97	1000		
$LaCr_{0.9}Mg_{0.1}O_{3-\delta}$	<5%		2.77	RT		[175]

			3.93	125		
			2	1000		
$La_{0.5}Sr_{0.5}Fe_{0.8}Co_{0.2}O_{3-\delta}$	5%	1.1	1.16	RT	Single edge V-notch beam	[171]
			1.48	800		
			2.26	1000		
$LaCoO_3$	<7%	<5	1.23	RT		[186]
			1.19	150		
			0.93	260		
			0.95	400		
			1.05	700		
			1.06	800		
$La_{0.8}Ca_{0.2}CoO_{3-\delta}$	<7%	<5	1.92	RT		
			1.53	150		
			1.21	200		
			0.76	400		
			0.78	550		
			1.03	700		
			1.14	800		

2.6.4.1 Effect of measurement method on the fracture toughness of BSCF

The indentation crack measurement method shows a unique simplicity and economy in test procedure[187]. The value of fracture toughness can be easily determined from indentation crack measurement[128]:

$$K_{ind} = \chi \frac{F}{{C_0}^{1.5}} \tag{2.29}$$

where C_0 is the crack length and $\chi=0.016(\frac{E}{H})^{0.5}$ represents the elastic plastic behaviour. Furthermore, Young's modulus E and hardness H are also directly accessible from the depth sensitive indentation test. However, this method is limited to a relatively low temperature environment. As shown in Table 2.7, indentation strength method has been also used to determine the fracture toughness of BSCF. The calculation of fracture toughness can be expressed as [165]

$$K_{IC} = 0.59(\frac{E}{H})^{\frac{1}{8}}[\sigma_f p^{\frac{1}{3}}]^{\frac{3}{4}} \tag{2.30}$$

where E is Young's modulus; H hardness; σ_f fracture stress; P indentation load

The value of fracture toughness obtained from the indentation strength method at room temperature was reported to be slightly higher than those determined by the other two techniques, with an uncertainty of 10%. Both Huang *et al.* [179] and Chanda *et al.* [109] determined the fracture toughness of BSCF as being in the range from 1 to 1.4 MPa $m^{0.5}$. According the results obtained from Chanda *et al*.[109], both the indentation crack measurement and indentation strength method showed a very similar temperature-dependence of the fracture toughness in a low temperature range. Beside the similar values of fracture toughness obtained at room temperature, even at elevated

temperatures, roughly the same proportion of reduction in the toughness was observed in both methods. However, compared with the indentation crack measurement method, the indentation strength method can be used at much higher temperatures.

Because of the limitations of the testing device, the fracture toughness evaluated by the indentation crack measurement method at high temperatures (up to 800 ℃) is difficult to achieve. Therefore, the indentation strength method is a more practical option particularly for membrane materials that are designed for high temperature in applications. In this way, it requires no special sample preparation techniques. In the case of highly porous membrane materials, the indentation crack measurement method is difficult to determine the fracture toughness due to the difficulty of crack measurement, while indentation strength method is considered to be a useful tool for fracture toughness determination due to the lack of requirement for crack measurement[188].

2.6.4.2 Effect of porosity on the fracture toughness of BSCF

Figure 2.17 shows the changes in fracture toughness of dense and porous BSCF as a function of temperature. Below 800 ℃, the fracture toughness of dense BSCF is higher than that of the porous materials while both values become similar at 800 ℃. Considering the absolute values of fracture toughness of BSCF in Table 2.7, the values obtained from dense BSCF (4.5%) were twice as large as those determined from porous materials (38%) at RT. Therefore, the fracture toughness of BSCF is strongly dependent on porosity. Rice *et al*. [159, 180] have demonstrated that the intrinsic fracture toughness can be associated with the measured toughness according to the following equation:

$$K_{IC} = {K_{IC}}^{0} exp(-bp) \quad (2.31)$$

where K_{IC} is the measured toughness; $K_{IC}{}^{0}$ is the intrinsic toughness (when porosity of the material is zero); *b* is a characteristic parameter; *p* is the porosity of the material. Many researchers[162, 189] have summarised and reported that the *b* values for fracture toughness are between 2 and 5.

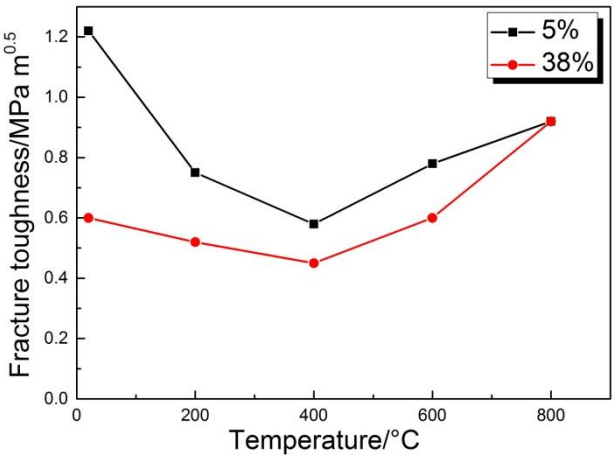

Figure 2.17 Fracture toughness of dense and porous BSCF as a function of temperature. The data points were obtained from the references [109, 112].

Because there are not enough data points of fracture toughness from the references, the intrinsic toughness cannot be obtained from the Equation (2.31).

2.6.4.3 Effect of temperature on the fracture toughness of BSCF

Huang *et al.* [19] first reported the fracture toughness for dense BSCF materials between RT and 350 ℃ by indentation crack measurement method. The fracture toughness was found to be strongly dependent on temperature and decreased sharply from 0.85 to 0.43 MPa $m^{0.5}$ with temperature increasing from room temperature to 100 ℃. Then it reduced slightly up to 350 ℃. Further investigation of the fracture toughness of dense BSCF has been performed using the indentation strength method between RT and 800 ℃ by Chanda *et al.*[109]. It has been demonstrated that the dependence of the fracture toughness of dense and porous BSCF on temperature shows

a similar tendency as shown in Figure 2.18. The fracture toughness of BSCF reduced from RT to 400 ℃, and then increased up to 800 ℃. For dense BSCF, the value obtained at 800 ℃ was nearly 80% of that measured at RT while for porous BSCF, the value at 800 ℃ was approximately 50% higher than that at RT.

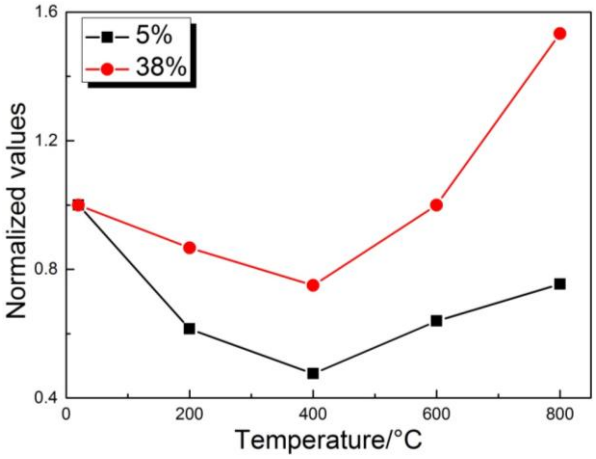

Figure 2.18 Comparison of normalised values of fracture toughness of BSCF with different porosities determined by the indentation strength method in the temperature range from RT to 800 ℃. The data points were obtained from the references [109, 112]. Both data sets are normalised with respect to the RT values.

It has been shown that the fracture toughness of some perovskite-structured materials increases with increasing temperature (Table 2.7). There are several possible reasons to explain this behaviour, including phase transformation[176] and domain switching[186]. In the case of $LaCr_{0.9}Mg_{0.1}O_{3-\delta}$[175], the fracture toughness obtained at 125 ℃ was higher than that determined at RT due to the existence of a phase transition from rhombohedral to orthorhombic structure. The phase transition was also observed in $La_{0.58}Sr_{0.4}Co_{0.2}Fe_{0.8}O_{3-\delta}$[179]. To be more specific, the transformation from rhombohedral to cubic of $La_{0.58}Sr_{0.4}Co_{0.2}Fe_{0.8}O_{3-\delta}$ occurs between 700 ℃ and 850 ℃ in air, and correspondingly, a steep rise of the fracture toughness from 700 ℃ and 850 ℃ is observed along with transition process[130, 179]. Phase transformation toughing is a typical mechanism for increasing fracture toughness[165]. Orlovskaya *et al.*[186] have

reported that domain switching also can cause an increase in fracture toughness of $LaCoO_3$ due to the absorption of mechanical energy in the stress field near to a crack tip. However, for BSCF, there is neither phase transition nor domain switching. The cause of this behaviour is different from other perovskite-structured materials discussed above. It has been found that the temperature–dependence of fracture toughness data showed a similar tendency with the fracture strength obtained by Huang *et al.*[109]. It appears that a strong decrease in fracture toughness was coupled to the decrease in elastic modulus and both are related to the inherent bond strength. Since the fracture toughness is as a function of the Young's modulus and fracture strength according to the Equation (2.30), the decrease in fracture toughness is partially due to the reduction in Young's modulus. According to Huang *et al.*[19], this can be attributed to the spin transition of Co^{3+}.

2.7 Mechanisms of failure

2.7.1 Subcritical crack growth

2.7.1.1 General background

Subcritical crack growth (SCG) is often regarded as 'static fatigue', 'delayed fracture', 'environmentally-assisted cracking' or 'slow crack growth', which is quite common in ceramics subject to externally applied stresses[165]. During SCG, the inter-atomic bonding at the crack tip is weakened by the chemical reaction with the environment, which facilitates crack propagation at low stress levels and eventually leads to fracture after a certain period of time[190]. SCG is not only related with stress conditions but also associated with environments, such as temperature, humidity as well as the chemistry of the atmosphere. Ceramic materials are normally sensitive to SCG when the stress intensity factor is below fracture toughness[191]. It has been reported that SCG

behaviour can be expressed by

$$v = AK^n exp(\frac{-Q}{RT}) \quad (2.32)$$

where v is crack growth rate; A and n are constants that depend on the materials, environment, and temperature; K is the stress intensity factor; Q is the apparent activation energy; R is the gas constant; and T is absolute temperature.

It is well-known that under a certain threshold value of the stress intensity factor, there is no crack propagation[192]. The higher value of the threshold, the higher the reliability and consequently the lifetime are obtained. This threshold indicates an inherent property for a given material, different to the widely used toughness which is only applicable to fast crack growth. However, for ceramics which are sensitive to SCG, their strengths increase with decreasing lifetime in real application conditions. Studying SCG can predict the materials' lifetime and consider the structural design of brittle materials. The lowest crack growth rates are the most important for lifetime predictions. With regard to lifetime predictions in particular, it is of considerable interest to acquire information about very slow crack growth rates down to 10^{-12} m/s[193]. For the ceramics under conditions of SCG, a finite lifetime has to be expected. When the crack growth relation [Equation (2.32)] can be applied, the lifetime will be predicted analytically. A variety of methods of plotting the *K*-*v* curves are available in the literature[194, 195].

2.7.1.2 Measurement methods

In order to obtain the parameters of SCG, two different methods have been employed as follows, referred to as constant load test and constant stress rate test.

2.7.1.2.1 Constant load test

The SCG is often characterised by the dependence of the crack velocity, v, on the mode *I* stress intensity factor K_I, and is often expressed by the empirical power relationship[196]

$$v = A(\frac{K_I}{K_{IC}})^n \tag{2.33}$$

where *A* and *n* are constant for a given material and environment system, and K_{IC} is the critical stress intensity factor or the fracture toughness of the material. The parameter *n* is a characteristic of the resistance of a material to SCG. A low value of *n* indicates a high sensitivity to SCG. The K_I is determined by the following equation [196]:

$$K_I = Y\sigma\sqrt{c} \tag{2.34}$$

where σ is the applied stress, *Y* is crack shape factor, and *c* is the crack length.

The specimens are subjected to different static loads under a prescribed duration Δt. The crack length is measured by SEM or optical microscope, and *v* is defined as the ratio of the crack increment Δc to the duration Δt:

$$v = \frac{\Delta c}{\Delta t} \tag{2.35}$$

Combining Equations (2.34) and (2.35), a *K*-*v* curve can be plotted. According to the *K*-*v* curve, the SCG parameters can be calculated from the slope. Regarding BSCF, no results of SCG parameters determined from this method were found in the literature.

2.7.1.2.2 Constant stress rate test

The SCG effect can be also assessed in a test with a constant stress rate $\dot{\sigma}$, where the fracture stress σ_f is correlated with the stress rate using the equation[197]:

$$log\sigma_f = \frac{1}{n+1} log\dot{\sigma} + logD \tag{2.36}$$

where *n* and *D* (Pa/s) are the SCG parameters. It can be seen from this equation that fracture stress depends on the stress rate. Bending tests normally are performed with different stress rates to evaluate the sensitivity to SCG.

Table 2.8 SCG parameters of dense and porous materials at RT

Materials	Porosity	Parameters		References
		n	D	
Dense BSCF	4.6%	30	94	[125]
Porous BSCF	34%	83	29	[125]
Dense LSCF	4.1%	49	73	[125]
Porous LSCF	46%	∞	20	[125]

Figure 2.19 shows the fracture stress of several perovskite materials as a function of stress rate at RT. The results of SCG parameters are listed in Table 2.8. The parameter n for dense BSCF and LSCF is lower than that of their porous counterparts, which suggests that dense materials are more sensitive to the SCG effect. This can be ascribed to the fact that in porous materials the crack tip is blunted by pores during crack propagation. In addition, the parameter n of BSCF is lower than that of LSCF, which implies that BSCF is more sensitive to the SCG effect at room temperature. For comparison, much higher values of $n \sim 50\text{-}70$ have been reported for Al_2O_3[198, 199].

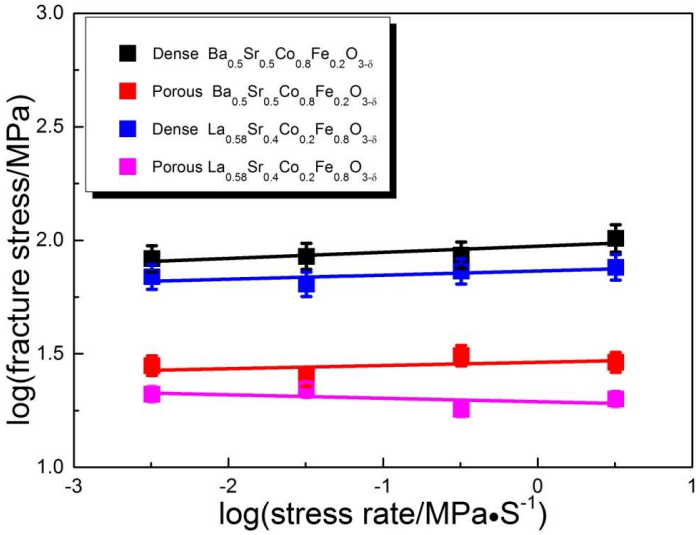

Figure 2.19 Fracture stress as a function of stress rate at room temperature. The data points were obtained from the references[106, 125].

2.7.1.3 The effect of temperature on SCG parameters

For ceramic materials, the SCG parameter n normally decreases with increasing temperature[200]. It indicates that these ceramic materials are more susceptible to SCG at higher temperature. There are several mechanisms responsible for the slow crack growth process, i.e. stress corrosion, grain boundary sliding, thermally activated bond rupture[201]. For example, no SCG was observed for silicon carbide at room temperature[202]. However, SCG parameters (*n*) of silicon carbide are 110 and 16 at 800 ℃ and 1400 ℃, respectively[202]. Stress corrosion induced by oxidation was suggested to be the mechanism operating at 800 ℃ while crack propagation by plastic deformation at grain boundaries caused a lower parameter *n* at 1400 ℃ [202]. It is also reported that no SCG for silicon nitride at room temperature. However, the SCG parameter (*n*) was 10 at 1400 ℃[203]. This indicates that silicon nitride was much more susceptible to slow crack growth at 1400 ℃ due to grain boundary sliding induced by the viscosity of grain-boundary phase[203]. The slow crack growth parameter *n* of single-crystal alumina was reported to decrease with increasing temperature between 800 and 1500 ℃ due to thermally activated bond rupture[201].

In terms of perovskite-structured materials, the value of *n*=30 for BSCF has been determined by biaxial bending tests under different loading rates at RT[204]; while the value of *n*=24 for $La_{0.2}Sr_{0.8}Co_{0.8}Fe_{0.2}O_{3-\delta}$ was determined by four-point bending tests under different loading rates at RT. However, a value of *n*=12 for $La_{0.2}Sr_{0.8}Co_{0.8}Fe_{0.2}O_{3-\delta}$ determined at 1000 ℃ has been reported[205]. This indicates that $La_{0.2}Sr_{0.8}Co_{0.8}Fe_{0.2}O_{3-\delta}$ perovskite membranes show little susceptibility to SCG at RT in air. However, these membranes are more susceptible to SCG at 1000 ℃ due to the decomposition and partial phase transitions from cubic to orthorhombic[205]. There is

no literature as the SCG parameters of BSCF at high temperature.

2.7.2 Creep rupture

2.7.2.1 General background

Creep refers to a plastic deformation process that is the tendency of a solid material to move slowly or deform perpetually under a fixed load at elevated temperature. It occurs because materials are exposed chronically to high levels of stress that are below the yield strength or ultimate strength of materials[206]. It commonly occurs when the temperature is above $0.4T_m$ (absolute melting temperature), but the stress is below the yield strength of the material. Normally, the strain rate enhances with increasing the temperature [54, 207, 208]. Generally, creep can be reported by three different stages: primary, secondary and tertiary creep as shown in Figure 2.20[16]:

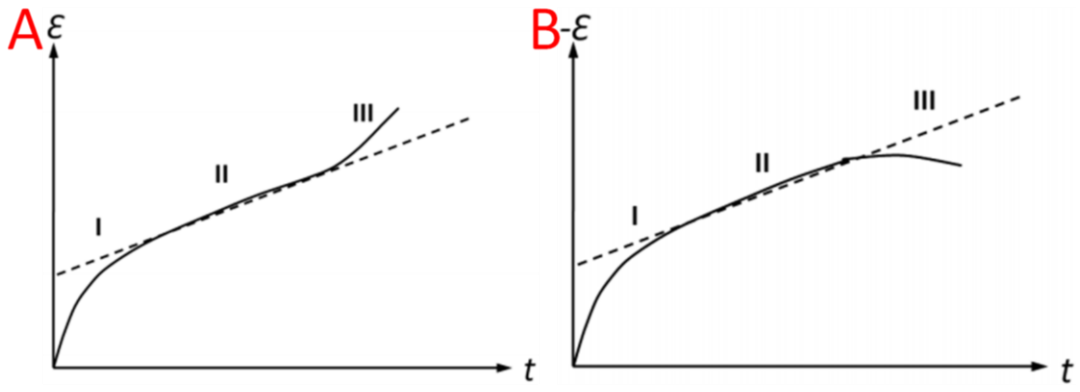

Figure 2.20 (A) Three stages of creep in tension: I) primary II) secondary III) tertiary; (B) Three stages of creep in compression: I) primary II) secondary III) tertiary

In the initial stage (primary creep), as the strain increases, the strain rate slows down but remains relatively high. This is because of work hardening. In the secondary stage (steady-state creep), the strain rate arrives at a minimum and becomes a stable value, because work hardening and annealing (thermal softening) have reached a dynamic balance. Generally, the strain rate of creep refers to the rate in the secondary stage. In

the tertiary stage (accelerating creep), this is mostly a period when deformation rate exponentially increases due to impending fracture, which finally results in the failure of the materials[209, 210].

For many ceramics, the creep rate in the secondary stage is mathematically described by the following equation[211]:

$$\frac{d\varepsilon}{dt} = A(\frac{1}{d})^p (P_{O_2})^m \sigma^n exp(-\frac{E_a}{RT}) \quad (2.37)$$

where $\frac{d\varepsilon}{dt}$ is the steady-state creep rate, A is a constant, d is the grain size, p is the inverse grain size exponent, P_{O_2} is the partial pressure of oxygen, m is the oxygen partial pressure exponent, σ is the applied stress, n is the stress exponent, E_a is the activation energy, R is the universal gas constant and T is the absolute temperature. P_{O_2}, T and σ can be controlled during the experiment. Note that the parameters n, m and p are determined by the linear regression of $ln\frac{d\varepsilon}{dt} = f(ln\sigma)$, $ln\frac{d\varepsilon}{dt} = f(lnP_{O_2})$ and $ln\frac{d\varepsilon}{dt} = f(ln\frac{1}{d})$, respectively[212]. Therefore, their average values of the fitting parameters are used in Equation (2.37).

2.7.2.2 Creep mechanisms

It is apparent that the creep mechanisms are dependent on grain size, loading stress and temperature as well as atmosphere according to the equation (2.37). Although there are several mechanisms proposed, generally three main mechanisms are the controlling factors in creep behaviour, e.g. diffusion, dislocation movement and grain boundary sliding[165].

Diffusion-controlled creep includes vacancy movements along the grain boundary or through the lattice. With regard to the inverse grain size exponent, p=2 indicates that the

creep is primarily dominated by the lattice diffusion (Nabarro-Herring creep) whereas p=3 demonstrates that the creep is controlled by the grain boundary diffusion (Coble creep)[54, 207]. Dislocation creep is controlled by the movement of dislocations, including glide and climb[16]. This creep process allows the dislocation to move to an adjacent slip plane in a short range[16]. It has been reported that dislocation creep is independent of grain size and normally exists in metals under high applied stress and relatively low temperature[213]. Grain boundary sliding normally happens in ceramic materials due to the formation of glassy phase in their grain boundaries at high temperature[165].

Figure 2.21 shows how creep parameters are related to the creep mechanisms. Diffusional creep is promoted by low stress while dislocation creep is dominant of high stress[165]. Additionally, Coble creep dominates over Nabarro-Herring creep at lower temperature and with finer grain size[165].

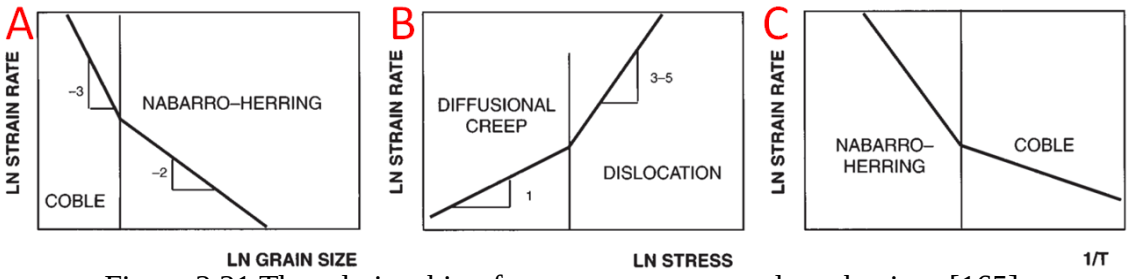

Figure 2.21 The relationship of creep parameters and mechanisms[165]

2.7.2.3 Creep behaviour of BSCF

In the case of the industrial application of BSCF membranes, the stress is generated from the oxygen chemical potential gradient through the membrane and the completely different pressures between feed and permeate sides at high temperature[214, 215]. In order to maintain the structural stability over a long period of operation, creep behaviour is one of the key parameters to estimate the lifetime limits[106]. Creep rates of BSCF are shown in Table 2.9 with various applied stresses, grain sizes as well as temperatures.

To be more specific, creep rate increases with increasing applied stress at the same temperature; it increases with the decrease in grain size under the same applied stress at the same temperature; and it increases with increasing temperature under the same applied stress.

Table 2.9 Creep rates in air for perovskite-structured BSCF materials under different conditions

Materials	Stress (MPa)	Temperature (℃)	Creep rate (s^{-1})	Grain size (μm)	Reference
$Ba_{0.5}Sr_{0.5}Co_{0.8}Fe_{0.2}O_{3-\delta}$	5	800	3×10^{-9}	6.9	[216]
		850	8×10^{-9}		
		900	1×10^{-7}		
		950	4×10^{-7}		
	10	800	5×10^{-9}		
		850	1×10^{-8}		
		900	3×10^{-7}		
		950	5×10^{-7}		
	15	850	2×10^{-8}		
		900	6×10^{-7}		
		950	8×10^{-7}		
	20	800	7×10^{-9}		
		850	4×10^{-8}		
		900	7×10^{-7}		
		900	3×10^{-8}	29	[212]
		950	1.5×10^{-7}		
	30	700	1.3×10^{-9}		
		800	1.5×10^{-9}		
		850	2.3×10^{-9}		
		900	5×10^{-8}		
		950	2.6×10^{-7}		
		900	1×10^{-8}	88	
		950	6×10^{-8}		
		875	4×10^{-8}	140	
		900	7×10^{-8}		
		925	1.1×10^{-7}		
		950	5×10^{-7}		
	63	900	1.7×10^{-7}	29	
		925	4.5×10^{-7}		
		950	1.3×10^{-6}		

2.7.2.3.1 Activation energy (Q)

Figure 2.22 shows the Arrhenius plots of the creep rates of BSCF measured in air. With respect to the activation energy (*Q*) in the Equation (2.37), it can be determined from the linear regression of a plot of ln(creep rate) versus inverse temperature at a constant load. The activation energy for creep of BSCF is determined to lie in the range from 287 to 338 kJ/mol. As the activation energy for oxygen diffusion in BSCF varies from 50 to 92 kJ/mol [212, 216], which is much smaller than the activation energy for creep of BSCF, it is suggested that the creep rate of BSCF is controlled by the diffusion of cations.

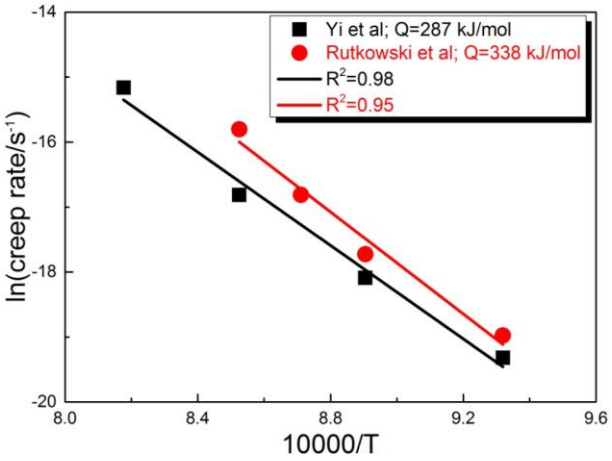

Figure 2.22 Arrhenius plots of the creep rate of BSCF measured in air. The data points were obtained from the references [212, 216].

2.7.2.3.2 Stress exponent (n)

Figure 2.23 shows applied stress as a function of the creep rate measured for two BSCF samples. The stress exponent (*n*) of the two samples is determined to be 0.76 and 1.7, respectively, depending on their grains size, service temperature and the range of the applied stress. These values of the stress exponent n suggest that the creep of BSCF is dominantly governed by diffusion between 5 and 60 MPa around 900 ℃.

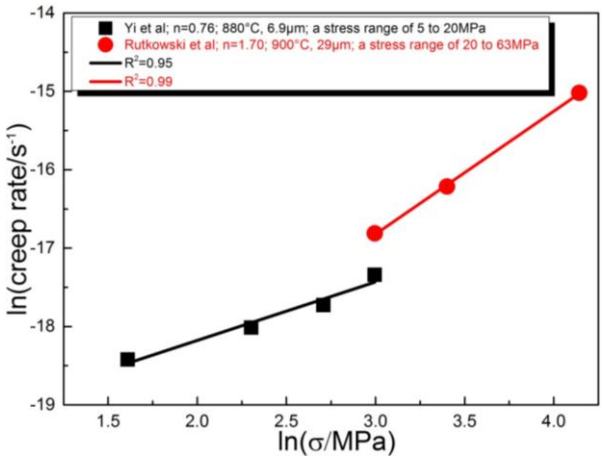

Figure 2.23 Applied stress dependence of the creep rates measured for BSCF. The grain sizes were 6.9 and 29 μm, respectively. The data points were obtained from the references [212, 216].

2.7.2.3.3 Inverse grain size exponent (p)

Figure 2.24 shows the dependence of the grain size on the creep rate measured for four BSCF samples under different experimental conditions. The inverse grain size exponent is determined to be around 2.5 in a grain size range from 2.5 to 17.4 μm, suggesting that the creep is governed by both lattice and grain boundary diffusion[212, 216]. However, the inverse grain size exponent is around 2 in a grain size range from 29 to 140 μm, which implies that the creep is dominantly controlled by the lattice diffusion.

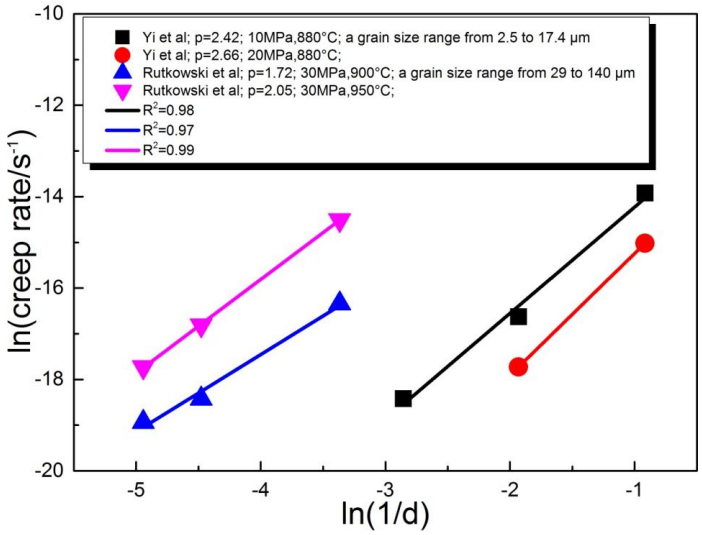

Figure 2.24 Grain size dependence of the creep rate measured for BSCF ceramics under different conditions. The data points were obtained from the references [212, 216].

Chapter 3 Experimental procedures

In order to obtain comprehensive information regarding sintering behaviours and mechanical properties of BSCF oxygen transport membranes, the experiments in this study were carried out to establish microstructure and mechanical property relationships of BSCF. In addition, the effect of Ni doping on the sintering behaviours and mechanical properties of BSCF was also evaluated. The fracture stress was determined by uniaxial and biaxial bending tests in the temperature range from RT to 800 ℃. The hardness was measured by micro-indentation test at RT. The Young's modulus was determined by uniaxial and biaxial bending tests between RT and 800 ℃ as well as micro-indentation test at RT. The fracture toughness was measured by indentation strength method between RT and 800 ℃ and indentation crack measurement method at RT. The subcritical crack growth (SCG) behaviour of BSCF was assessed by constant load method at RT and by constant stress rate method at 800 ℃. On the basis of SCG parameters, the strength-probability-time (SPT) diagram can be also constructed for design proposes. Microstructures of the samples were characterised by scanning electron microscopy (SEM) and electron backscatter diffraction (EBSD). Phase analysis was carried out by X-ray diffraction (XRD).

3.1 Sample preparation

3.1.1 $Ba_{0.5}Sr_{0.5}Co_{0.8}Fe_{0.2}O_{3-\delta}$

$Ba_{0.5}Sr_{0.5}Co_{0.8}Fe_{0.2}O_{3-\delta}$ powders used in this study were supplied by Treibacher Industrie AG, Austria[100]. The powder was uniaxially pressed at a pressure of 100 MPa in a cylindrical stainless steel die. Cold isostatic pressing was used prior to

sintering. In order to investigate the effect of sintering temperature on sintering behaviours and mechanical properties, a first group of BSCF samples was sintered at a number of temperatures ranging from 900 to 1150 ℃ for 10 hours in air and nine different sample types were obtained with various relative densities and different grain sizes. To evaluate the influence of dwell time on sintering behaviours and mechanical properties, a second group of BSCF samples was sintered at 1100 ℃ for different periods of time ranging from 1 to 100 hours and six different sample types were obtained with similar relative densities and different grain sizes. A third group of BSCF samples was sintered according to the following 3×3 temperature-time matrix. The sintering temperatures were 1075 ℃, 1100 ℃ and 1125 ℃ and the dwell times were 5, 10, and 24 hours.

All the heating and cooling rates during the process of sintering of the samples above were set to be 180 ℃/hour. The samples were cut into disc-shaped and bar–shaped samples using a diamond cutting blade in a precision cut-off machine (Accutom 5, Struers). The samples were ground with SiC paper with different grit sizes from P400 to P1200, and then polished with diamond paste descending from 6 μm to a final stage of 0.25 μm. The BSCF materials sintered under different conditions are listed in Table 3.1

Table 3.1 BSCF sintered under different conditions and corresponding abbreviations

Number	Temperature(℃)	Time(hour)	Abbreviation
#1	900	10	900-10
#2	950	10	950-10
#3	1000	10	1000-10
#4	1025	10	1025-10
#5	1050	10	1050-10
#6	1075	5	1075-5
#7	1075	10	1075-10
#8	1075	24	1075-24
#9	1100	1	1100-1
#10	1100	5	1100-5
#11	1100	10	1100-10
#12	1100	24	1100-24
#13	1100	50	1100-50
#14	1100	100	1100-100
#15	1125	5	1125-5
#16	1125	10	1125-10
#17	1125	24	1125-24
#18	1150	10	1150-10

3.1.2 $Ba_{0.5}Sr_{0.5}(Co_{0.8}Fe_{0.2})_{1-X}Ni_XO_{3-\delta}$

$Ba_{0.5}Sr_{0.5}(Co_{0.8}Fe_{0.2})_{1-X}Ni_XO_{3-\delta}$ (BSCF-Ni) powders with X=0, 0.02, 0.04, 0.06, 0.08, 0.15, 0.20, and 0.25 were supplied from Huanghai Lu who is a colleague of my research group in this study. The detail of powder preparation and other properties can be found in the reference[217]. Disc-shaped samples were obtained by uniaxial pressing at a pressure of 100 MPa and were then sintered at 1100 ℃ for 10 hours in air. They were used to investigate the effect of the Ni doping on microstructural evolution and mechanical properties. The compositions of Ni-doped BSCF samples sintered at 1100 ℃ for 10 hours are listed in Table 3.2

Table 3.2 The BSCF doped with different Ni content sintered at 1100 ℃ for 10 hours and corresponding abbreviations

Number	Composition	Temperature (℃)	Time (hour)	Abbreviation
#19	$Ba_{0.5}Sr_{0.5}(Co_{0.8}Fe_{0.2})_{0.98}Ni_{0.02}O_{3-\delta}$	1100	10	BSCF-Ni2
#20	$Ba_{0.5}Sr_{0.5}(Co_{0.8}Fe_{0.2})_{0.96}Ni_{0.04}O_{3-\delta}$	1100	10	BSCF-Ni4
#21	$Ba_{0.5}Sr_{0.5}(Co_{0.8}Fe_{0.2})_{0.94}Ni_{0.06}O_{3-\delta}$	1100	10	BSCF-Ni6
#22	$Ba_{0.5}Sr_{0.5}(Co_{0.8}Fe_{0.2})_{0.92}Ni_{0.08}O_{3-\delta}$	1100	10	BSCF-Ni8
#23	$Ba_{0.5}Sr_{0.5}(Co_{0.8}Fe_{0.2})_{0.85}Ni_{0.15}O_{3-\delta}$	1100	10	BSCF-Ni15
#24	$Ba_{0.5}Sr_{0.5}(Co_{0.8}Fe_{0.2})_{0.80}Ni_{0.20}O_{3-\delta}$	1100	10	BSCF-Ni20
#25	$Ba_{0.5}Sr_{0.5}(Co_{0.8}Fe_{0.2})_{0.75}Ni_{0.25}O_{3-\delta}$	1100	10	BSCF-Ni25

To study the effect of Ni doping on sintering mechanism of BSCF, the sample with a Ni-doping content of 8 mol%, $Ba_{0.5}Sr_{0.5}(Co_{0.8}Fe_{0.2})_{0.92}Ni_{0.08}O_{3-\delta}$ powder was studied by using different sintering conditions. In one case, the sintering time was fixed at 10 hours and temperatures ranging from 1000 ℃ to1200 ℃ were used. In the other case, the sintering temperature was fixed at 1100 ℃, and the sintering time varied from 1 to 50 hours. After sintering, the Ni-doped BSCF samples were ground and polished using the same procedure as that used for the pure BSCF. The BSCF-Ni8 samples sintered under different conditions are listed in Table 3.3

Table 3.3 The BSCF-Ni8 sintered under different conditions and corresponding abbreviations

Number	Temperature (℃)	Time (hour)	Abbreviation
#26	1000	10	Ni8-1000-10
#27	1025	10	Ni8-1025-10
#28	1050	10	Ni8-1050-10
#29	1075	10	Ni8-1075-10
#30	1100	1	Ni8-1100-1
#31	1100	5	Ni8-1100-5
#32	1100	24	Ni8-1100-24
#33	1100	50	Ni8-1100-50
#34	1125	10	Ni8-1125-10
#35	1150	10	Ni8-1150-10
#36	1175	10	Ni8-1175-10
#37	1200	10	Ni8-1200-10

3.2 Uniaxial bending tests

The BSCF sintered at 1100 ℃ for 10 hours were cut into bar-shaped samples and they were without introducing machine damage. The dimension was about 2.1×2.3×14 mm^3. The three-point bending test was conducted as a uniaxial stress test to measure the fracture stress and Young's modulus of BSCF. The mechanical test machine (Instron 5569) is shown in Figure 3.1. Before testing the samples, the machine compliance was characterised at a given temperature (RT, 200, 400, 600, 800 ℃). The displacement in the loading system (machine compliance, d_C) was recorded by the sensor. To measure the fracture stress and Young's modulus, each test sample was put in the fixture, as shown in Figure 3.1. The test piece was in good contact with the supporting and loading rods as shown in Figure 3.2. The test force was applied at a specified rate of 100 N/min by a computer-driven load cell and a sensor was used to record the applied load versus the displacement of the samples. After testing the samples, the displacement (d_R) recorded by the sensor was taken as the sum of the displacements in the samples (d_S) and the loading system ($d_R=d_S+d_C$). The maximum load at fracture was used for the calculation of fracture stress [Equation (3.1)] and the linear part of the load-displacement curve and the sample displacement (d_S) were used to determine the Young's modulus [Equation (3.2)]. The load was applied within an accuracy of 0.01 N and the displacement measurement was recorded within an accuracy of 0.001 mm. Thermocouples were used to monitor the temperatures of the test specimens.

Figure 3.1 Image of mechanical machine (Instron 5569)

A schematic diagram of the three-point bending test is shown in Figure 3.2. The calculations were performed using the procedure based on ASTM Standard C 1161[218].

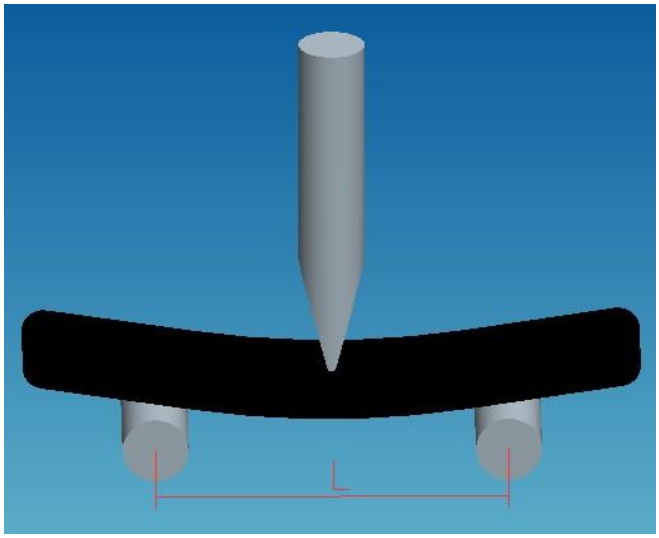

Figure 3.2 The schematic diagram of three-point bending test

The fracture stress is calculated using the following equation:

$$\sigma_f = \frac{3FL}{2bh^2} \tag{3.1}$$

The Young's modulus E is calculated using the following equation:

$$E = \frac{L^3 \Delta F}{4bh^3 \Delta d} \tag{3.2}$$

where F is the load, L is the distance between the two support points, b is the width of the cross section under the applied load, and h is the thickness of the specimen. The mean values of b, h, L were 2.1, 2.3, and 8 mm, respectively. d is the central deflection of the specimen.

At RT and 800 ℃, 10 specimens were tested to obtain fracture stress and Young's modulus. Between 200 ℃ and 600 ℃, 5 specimens were tested for each temperature. For the tests at elevated temperatures, a heating rate and a cooling rate of 180 ℃/hour were used, and a dwell time of 1 hour was chosen to reach a uniform temperature all over the sample before testing in air.

3.3 Biaxial bending tests

In order to compare with the uniaxial bending tests, the ring-on-ring bending test was also employed as a biaxial bending test to measure fracture stress and Young's modulus. The disc-shaped samples sintered at 1100 ℃ for 10 hours were applied in these tests, and they were without introducing machine damage. The thickness was approximately 1 mm, and the diameter was around 21.8 mm. The variation of the thickness of the test specimens was less than 0.02 mm. Before testing the samples, the machine compliance was characterised at a given temperature (RT, 200, 400, 600, 800 ℃). The displacement in the loading system (machine compliance, d_C) was recorded by the sensor. To measure the fracture stress and Young's modulus, each test sample was put in the fixture, as shown in Figure 3.1. The test piece was in good contact with the supporting and loading rods as shown in Figure 3.3. After testing, the displacement (d_R) recorded by the sensor was taken as the sum of the displacements in the samples (d_S) and the loading system ($d_R=d_S+d_C$). The test force was applied at a specified rate of 100 N/min by a

computer-driven load cell and a sensor was used to record the applied load versus the displacement of the specimen. The maximum load at fracture was used for the calculation of fracture stress [Equation (3.3)] and the linear part of the load-displacement curve and the sample displacement (d_S) were used to determine the Young's modulus [Equation (3.4)]. The load was applied within an accuracy of 0.01 N and the displacement measurement was recorded within an accuracy of 0.001 mm. Thermocouples were used to monitor the temperatures of the test specimens. The schematic picture of the test is displayed in Figure 3.3:

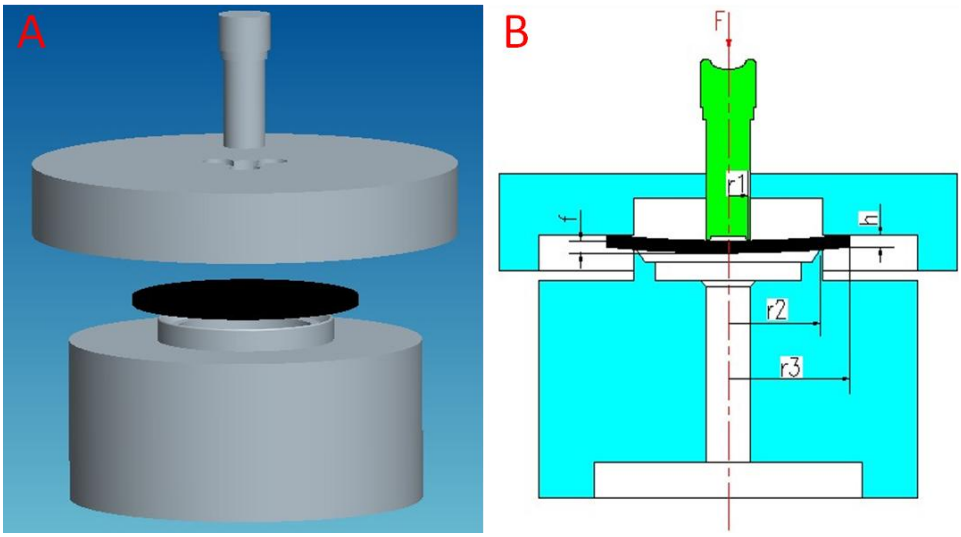

Figure 3.3 Schematic representation of the ring-on-ring test: (A) overview; (B) cross-section

The test conditions are in accordance with the ASTM standard C1499-05[123]. The fracture stress was calculated using the following equation:

$$\sigma_f = \frac{3P}{2\pi {t_h}^2}\left[(1+\nu)\, ln\left(\frac{r_2}{r_1}\right) + \frac{1-\nu}{2}\left(\frac{{r_2}^2-{r_1}^2}{{r_3}^2}\right)\right] \tag{3.3}$$

The Young's modulus E is calculated using the following equation:

$$E = \frac{3(1-\nu^2){r_1}^2 \Delta P}{2\pi {t_h}^3 \Delta d}\left[\left(\frac{r_2}{r_1}\right)^2 - 1 - ln\left(\frac{r_2}{r_1}\right) + \frac{1}{2}\left(\frac{1-\nu}{1+\nu}\right)\frac{({r_2}^2-{r_1}^2)^2}{{r_2}^2{r_3}^2}\right] \tag{3.4}$$

where P is the loading force, t_h is the specimen thickness, ν is the Poisson ratio, r_1,r_2,r_3 are the radii of the loading ring, the supporting ring and samples, respectively.

The values of t_h , r_1, r_2, and r_3 were 1.0, 1.9, 8.4, 21.8 mm, respectively. Likewise, the mean values of the tests were also obtained. *d* is the central deflection of the specimen.

At RT and 800 ℃, 10 specimens were tested to obtain fracture stress and Young's modulus. Between 200 ℃ and 600 ℃, 5 specimens were tested for each temperature. For the tests at elevated temperatures, a heating rate and a cooling rate of 180 ℃/hour were used, and a dwell time of 1 hour was chosen to reach a uniform temperature all over the sample before testing.

3.4 Micro-indentation test

The micro-indentation test is widely used to measure the mechanical properties of brittle ceramics[128]. Depth-sensitive indentation is widely used to determine the hardness[128]. In order to be comparable with the hardness values reported in the literature, a Vickers indenter was used in the present study. The tip is pyramid-shaped and has 4 sides with an angle of 136 °between opposite sides[127].

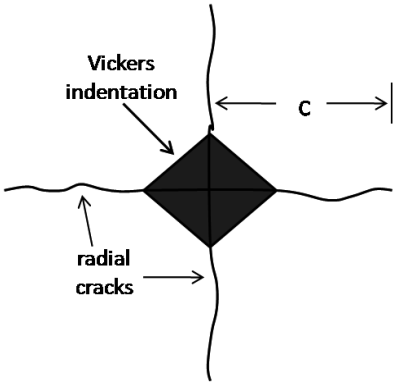

Figure 3.4 Schematic indentation impression[141]

Figure 3.4 shows the typical Vickers indentation. The hardness H_{IT} can be derived as[141, 219];

$$H_{IT} = \frac{F_m}{A_p} \tag{3.5}$$

where F_m is the maximum load, A_p is the projection area of the impression. The

calculation of indentation Young's modulus E_{IT} is based on[128]:

$$E_{IT} = \frac{(1-\nu_s{}^2)}{\frac{1}{E_r}-\frac{(1-\nu_i{}^2)}{E_i}} \tag{3.6}$$

where E_i is the Young's modulus of the indenter(1141 GPa for diamond); ν_s, ν_i are the Poisson's ratio of the tested samples and indenter(0.07 for diamond), respectively. The reduced modulus E_r, which is calculated from the indentation data is defined as[128]:

$$E_r = \frac{\sqrt{\pi}}{2\beta}\frac{S}{\sqrt{A_p}} \tag{3.7}$$

where β is indenter constant; S is the maximum slope of the load-displacement curve; A_p is the projected contact area at applied load.

The indentations were made on the polished faces of the BSCF samples using a diamond indenter (CSM Instruments, Peseux, Switzerland). The tip geometry and machine compliance were calibrated prior to testing in order to make the data more reliable and reproducible. The procedures of making indentations were followed by a sequence of loading (30 seconds), dwelling at the maximum load (10 seconds) and unloading (30 seconds). Two 10×10 indentation matrices per sample were made, and the distance between adjacent points was more than 5 times the indentation size. Indentations with surface chipping were not included in the analysis. All the values of hardness were calculated by software (Wilson Tukon 2100, Instron, Germany), as described in Appendix A.

3.5 In situ observation of crack growth with annealing

BSCF samples sintered at 1100 ℃ for 10 hours were used for in-situ observation of crack growth at high temperature. Before the observation, a Vickers indentation at a load of 10 N was made on each sample. The samples were heated from RT to target

temperatures (100, 200, 300, 400, 500, 600, 700, 800 ℃), using a hot stage (TS1200, Linkam Scientific Instruments as shown in Figure 3.5) fitted to an optical microscope (Olympus BH-2-UMA). The heating rate and cooling rates were both 10 ℃/min. The samples were held at each target temperature for 10 mins in order to reach a uniform state. Then the crack length measurement was made at target temperature.

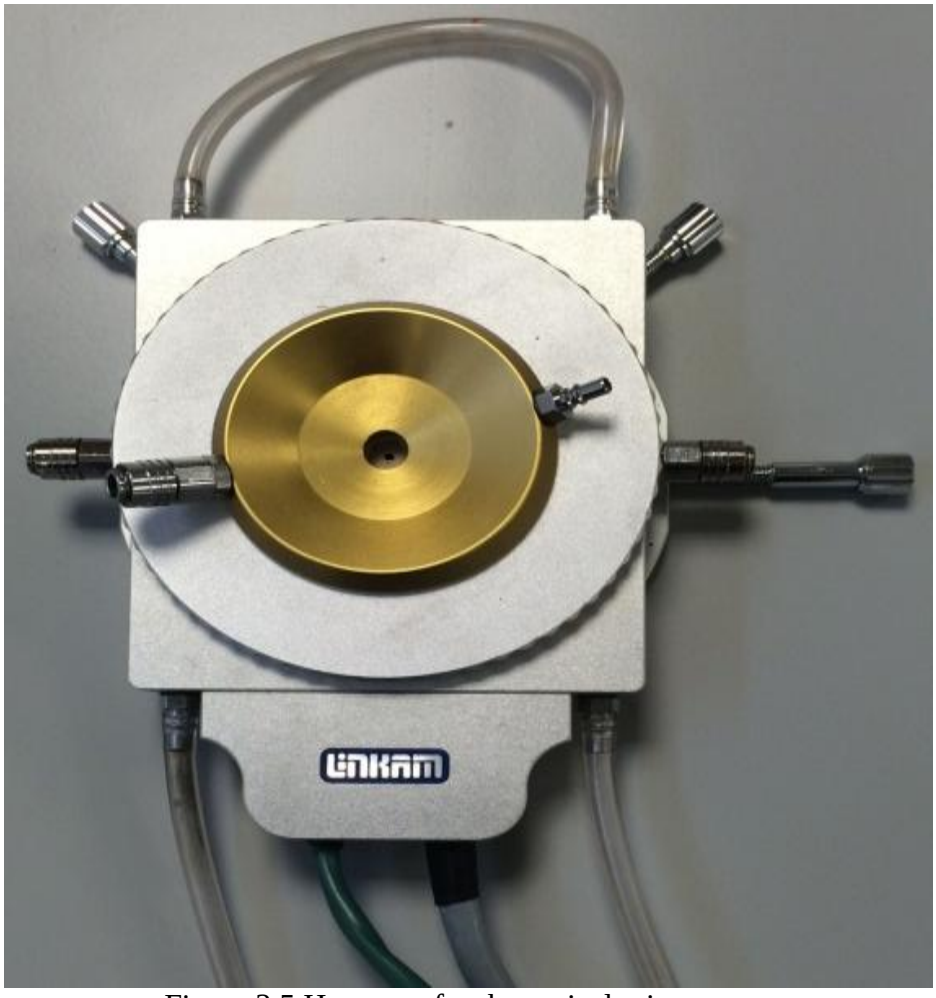

Figure 3.5 Hot stage for the optical microscope

3.6 Subcritical crack growth tests

The samples sintered at 1100 ℃ for 10 hours were used to investigate subcritical crack growth (SCG) at RT and 800 ℃ in air using the constant load method and constant stress rate method, respectively. SCG parameters can be determined from this study. On the basis of these parameters, the strength-probability-time diagram will be constructed

for design proposes.

3.6.1 Constant load method at room temperature

The ring-on-ring bending configuration was carried out using the constant load method. The SCG rate is characterised by the dependence of the crack velocity, v, on the mode I stress intensity factor K, and is expressed by the empirical power relationship[220]:

$$v = A_0(\frac{K}{Kc})^n \tag{3.8}$$

where A_0 and n are constant for a given material, and K_c is the critical stress intensity factor or the fracture toughness of the material. The average crack growth rate was measured by the increase in crack length (Δc) before and after the experiment during the elapsed time (Δt) as follows:

$$v = \frac{\Delta c}{\Delta t} \tag{3.9}$$

The stress intensity factor K is determined by the following equation [220]:

$$K = Y\sigma\sqrt{c} \tag{3.10}$$

The stress can be obtained from Equation (3.11).

$$\sigma = \frac{3P}{2\pi {t_h}^2}[(1+v)\, ln\left(\frac{r_2}{r_1}\right) + \frac{1-v}{2}\left(\frac{{r_2}^2-{r_1}^2}{{r_3}^2}\right)] \tag{3.11}$$

The parameters of the ring-on-ring bending test were the same as described above. BSCF samples were indented in air at a load of 10 N. In order to eliminate residual stress around the indented areas, the samples were annealed at 800 ℃ for 30 mins.

The samples were subjected to different static loads under a prescribed duration Δt. The prescribed durations were 10 s, 100 s, 1000 s, 1 hour, 10 hours, 100 hours and 14 days. The stress intensity factor was in the range from 0.54 to 0.75 MPa $m^{0.5}$. When the stress intensity factor was over 0.75 MPa $m^{0.5}$, it is difficult to control the crack growth

because the sample fractured so fast. The crack length was measured via SEM after unloading, with a precision of ±0.1 μm, and v is defined as the ratio of the crack increment Δc (the crack length from c_1 to c_2) to the duration Δt (the time from t_1 to t_2):

$$v = \frac{c_2 - c_1}{t_2 - t_1} \tag{3.12}$$

The corresponding average intensity factor can be determined as follows:

$$K = \frac{\int_{t_1}^{t_2} Y\sigma\sqrt{c}\, dt}{t_2 - t_1} \tag{3.13}$$

3.6.2 Constant stress rate at 800 ℃

Ring-on-ring bending tests were used to investigate the slow crack growth at 800 ℃ in air. The preparation of disc-shaped BSCF samples sintered at 1100 ℃ for 10 hours was the same as before (chapter 3.3). Four different loading rates, 0.1 N/min, 1 N/min, 10 N/min, and 100 N/min, were used, corresponding to the stress rates of 0.1012 MPa/min, 1.012 MPa/min, 10.12 MPa/min and 101.2 MPa/min. Five samples were tested at each loading rate at 800 ℃ in air. Each sample was held at 800 ℃ for 1 hour before testing. The heating rate was 180 ℃/hour. The SCG effect can be assessed in a test with constant stress rate $\dot{\sigma}$, where the fracture stress σ_f is correlated with the stress rate using the equation[197]:

$$log\sigma_f = \frac{1}{n+1} log\dot{\sigma} + logD \tag{3.14}$$

where n and D (Pa/s) are the SCG parameters. The stress rate is calculated from[123]

$$\dot{\sigma} = \frac{3\dot{P}}{2\pi {t_h}^2}\left[(1+\nu)\, ln\left(\frac{r_2}{r_1}\right) + \frac{1-\nu}{2}\left(\frac{{r_2}^2 - {r_1}^2}{{r_3}^2}\right)\right] \tag{3.15}$$

where $\dot{P}$ is the load rate (N/min), other parameters have the same meaning as in Equation (3.3).

The SCG parameters n and D are then determined by a linear regression analysis using

log fracture stress as a function of log stress rate. The slope of the linear regression line, α, can be calculated as[197]:

$$\alpha = \frac{K\sum_{j=1}^{K}\left(log\,\dot{\sigma_j}\,log\,\sigma_j\right)-\left(\sum_{j=1}^{K}log\,\dot{\sigma_j}\,\sum_{j=1}^{K}log\,\sigma_j\right)}{K\sum_{j=1}^{K}(log\,\dot{\sigma_j})^2-\left(\sum_{j=1}^{K}log\,\dot{\sigma_j}\right)^2} \quad (3.16)$$

where K is the sample size, σ_j and $\dot{\sigma_j}$ are the fracture stress and stress rate of individual test samples, respectively. The SCG parameter n is calculated as $n = (1/\alpha) - 1$.

The intercept of the linear regression line is calculated as[197]:

$$\beta = \frac{\left(\sum_{j=1}^{K}log\,\sigma_j\right)\sum_{j=1}^{K}(log\,\dot{\sigma_j})^2-\left(\sum_{j=1}^{K}\left(log\,\dot{\sigma_j}\,log\,\sigma_j\right)\right)\left(\sum_{j=1}^{K}log\,\sigma_j\right)}{K\sum_{j=1}^{K}(log\,\dot{\sigma_j})^2-\left(\sum_{j=1}^{K}log\,\dot{\sigma_j}\right)^2} \quad (3.17)$$

The SCG parameter D is calculated as $D = 10^{\beta}$.

3.7 Microstructural and chemical analysis

As introduced previously, the cubic structure of BSCF exhibits high permeation. Therefore, phase identification is very important. The phases present in all of the BSCF samples were determined by X-ray diffraction (XRD; PW1830, Philip, Eindhoven, the Netherlands) with CuK_α radiation (λ=1.54060 Å) operating at 40 kV/40 mA. Each sample was step-scanned from 20 to 85 ° with a step size of 0.05 ° and a dwell time of 8 seconds. The phase identification was established using High-Score Plus software (Philip). The patterns were refined by TOPAS software (Bruker 4.2). The Lorentz Polarisation factor was fixed to 17. The parameter of the instrument was fixed to the following values: Primary radius 173 mm, Secondary radius 173 mm, Receiving slit width 0.2, FDS angle 1, Full Axial Convolution and Filament length 12mm, Sample length 15mm, Receiving Slit length 12 mm, Primary Sollers 2.3 and Secondary Sollers 2.3. The background was fit by Chebychev polynomials of 3rd order. The peaks were fit

using PV_TCHZ function. The refined parameters were zero error, the lattice parameter and crystal size. The cubic phase was refined using Tomkiewicz, A.C structure model[221] based on a cubic cell (*Pm-3m*). The Debye-Waller factor *B* of oxygen atom was fixed at 1.0 due to the insensitivity of laboratory XRD used in this study. This relatively simple model gives very reproducible results. The error bars in the figures refer to error of the fitting during the refinement.

Microstructural investigations of the samples were carried out by scanning electron microscope (SEM, Quanta 650) and electron backscatter diffraction (EBSD). As reported, grain orientation has an influence on the mechanical properties of ceramic materials. To identify the orientation of the grains, EBSD measurements were used on the surface of the samples. To ensure a good pattern quality, in this case one more polishing step was performed dowm to a 0.04 μm finish using an OPS colloidal silica suspension. These EBSD measurements were taken using EBSD detector with HKL CHANNEL 5 Oxford Instruments software attached to a SEM(FEI, Quanta 650). The results were obtained with an accelerating voltage of 20 kV and a probe current of 20 nA. The sample tilt was 70 degrees and the working distance was 15 cm. The chemical composition was determined by energy-dispersive X-ray spectroscopy(EDX) equipped on a SEM (FEI, Quanta 650). In order to observe crack path below the surface, the focused ion beam (FIB, Quanta 3D, FEI) was used to cut the grain with an accelerating voltage of 30 kV and a tilt angle of 52 degrees.

The density was determined by Archimedes method[222]. The grain size was analysed by EBSD method using the area counting technique. To be more specific, the diameter was calculated by the equivalent area ($D = \sqrt{\frac{4S}{\pi}}$). The large number of grains was analysed to ensure that a representative average value could be measured for the

samples. The pore size was measured by the Image-Pro Plus 6.0 software.

3.8 Thermal property characterisation

For the evaluation of mass loss during sintering, thermogravimetry (TG, SETARAM, K/SETEVO15-1A) of BSCF was carried out between RT and 1150 ℃ in air. The heating and cooling rates were 180 ℃/hour. When the temperature reached 1000 ℃, every interval of 25 ℃ was held at target temperature for 10 hours. The change in mass was recorded as a TG curve. The measurement of temperature was recorded within an accuracy of 0.01 ℃, while mass was recorded within an accuracy of 0.02 μg.

Chapter 4 Results and discussion

4.1 Sintering behaviours of perovskite-structured BSCF membranes

In this section, the sintering behaviours of BSCF ceramics are presented and discussed. The results described include powder characterisation, phase identification, relative density, quantitative analysis of the grain growth behaviour and sintering mechanisms.

4.1.1 Powder characterisation

The XRD pattern of the starting BSCF powder is shown in Figure 4.1. The powder is identified as a single phase cubic perovskite structure and the diffraction peaks correspond to the reflections (100), (110), (111), (200), (210), (211), (220), (300), (310), (311), and (321). The XRD analysis is in agreement with the results of previous work[13], which has revealed no other phases in the starting powder. Thus, it can be inferred that the starting powder is highly crystalline and composed of pure cubic BSCF particles.

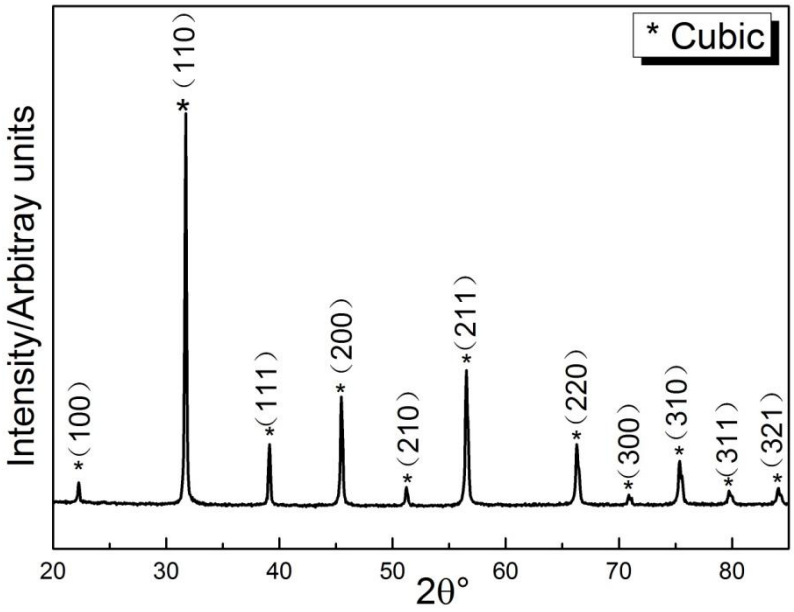

Figure 4.1 XRD pattern of commercial BSCF powder at room temperature

The particle size distribution of the powder is shown in Figure 4.2, which shows a broad range of particle sizes with a bimodal distribution. The average particle size is determined to be around 3 μm.

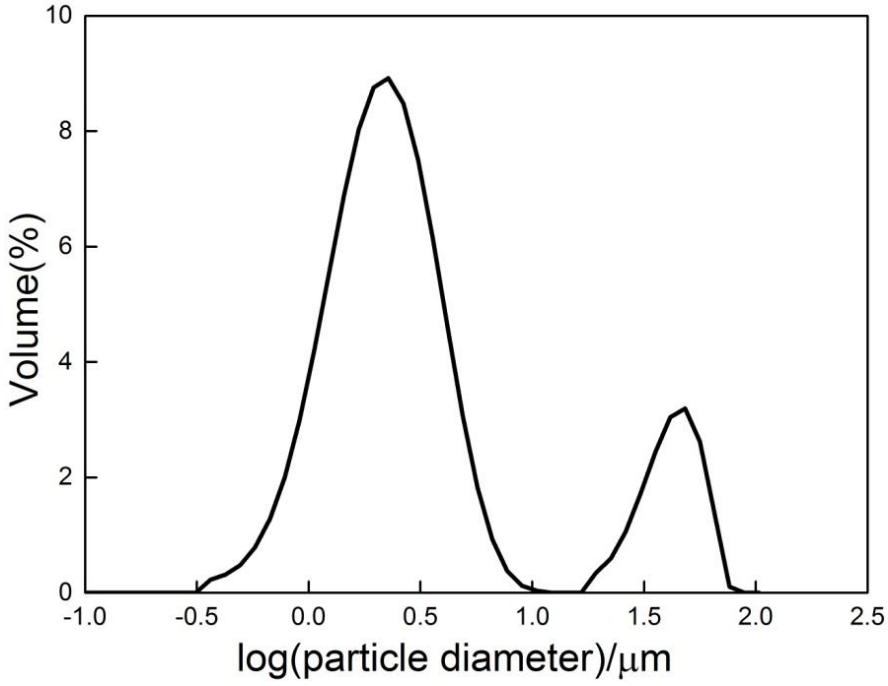

Figure 4.2 Particle size distribution of the starting commercial BSCF powder

SEM micrographs of the powder (see Figure 4.3) confirmed the presence of soft agglomerates and a wide primary particle size distribution.

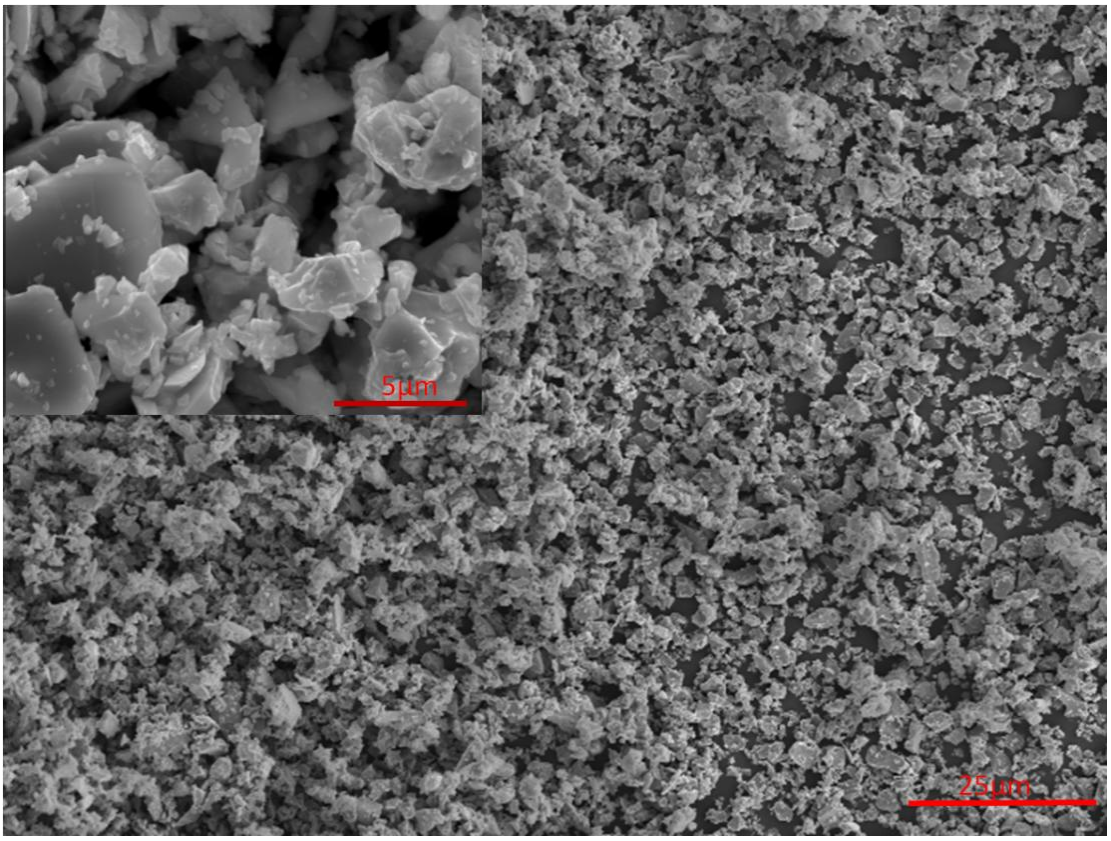

Figure 4.3 SEM of the commercial BSCF powder exhibiting the presence of soft agglomerates.

4.1.2 X-ray diffraction

Figure 4.4 shows the room temperature XRD patterns of the BSCF samples sintered under different conditions in this study with all peaks corresponding to the ICSD card NO.109462[223]. All peaks are well indexed as a cubic perovskite structure in line with previous reports [224-226]. Even at high temperatures, up to 1150 ℃, the BSCF samples do not decompose and no other phase can be found by XRD. This means that BSCF exhibits good phase and structure stability at high temperature in air.

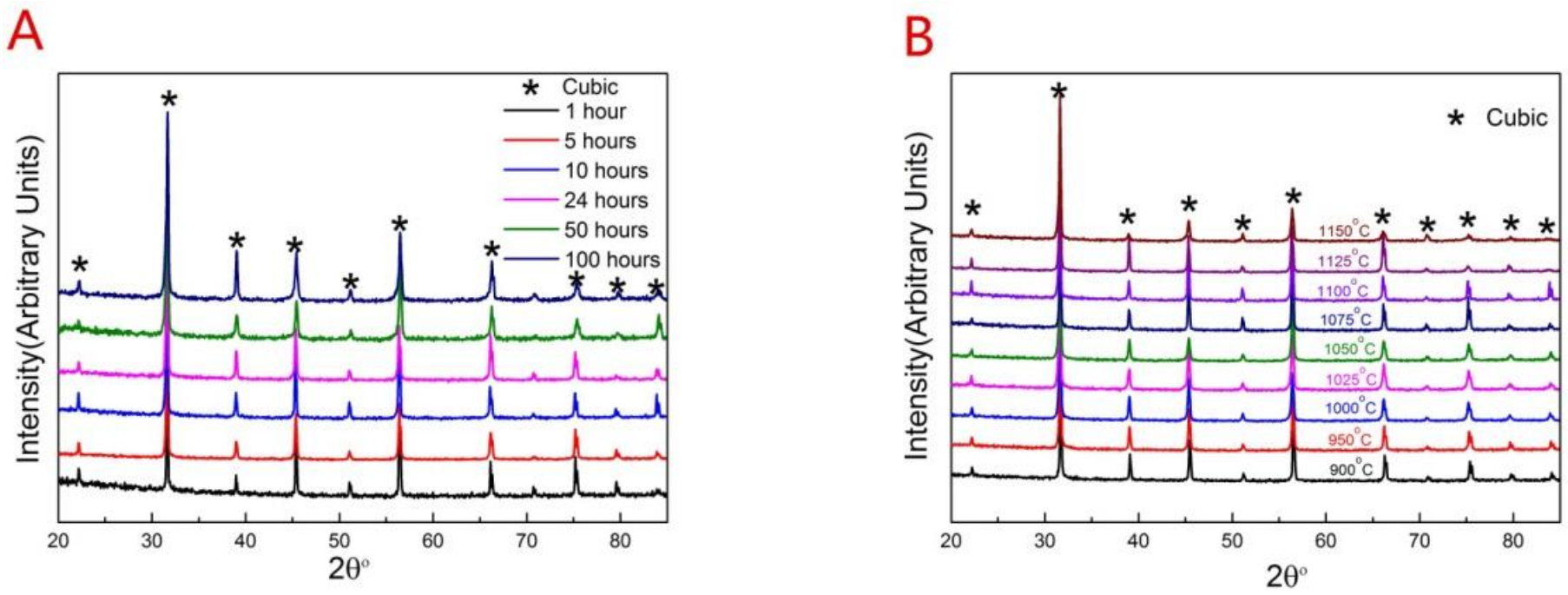

Figure 4.4 XRD patterns of BSCF samples sintered under different conditions: (A) sintered at 1100 ℃ for different time; (B) sintered at various temperatures for 10 hours

Figure 4.5 shows the lattice parameters of BSCF sintered under different conditions determined using Rietveld refinement on the basis of the XRD data. The lattice parameter of the starting powder at room temperature is determined as 3.9790 Å in this work, which is similar to the diffraction data of BSCF reported by Koster *et al.* (3.9830 Å)[227]. As shown in Figure 4.5(A), the lattice parameter of BSCF increases from 3.9862 to 3.9905 Å as the dwell time increases from 1 to 10 hour at 1100 ℃. Subsequently, the lattice parameter shows little change from 10 to 100 hours. For a given sintering time (10 hours) in Figure 4.5(B), it can be observed that the lattice parameter increases linearly with increasing sintering temperature, which is consistent with the results obtained by Wang *et al.*[45]. Within the temperature range studied, the maximum variation of the lattice parameters of BSCF is 0.32%.

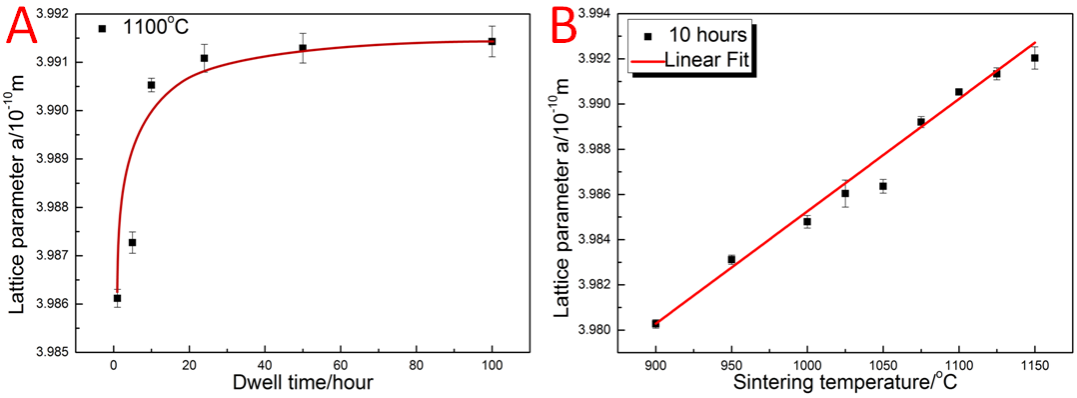

Figure 4.5 Lattice parameters as a function of (A) dwell time and (B) sintering temperature

Figure 4.6 shows the weight change of BSCF sintered between 1000 ℃ and 1150 ℃. In the whole temperature range covered (between 1000 ℃ and 1150 ℃), the weight of BSCF keeps decreasing. Between 1000 ℃ and 1100 ℃, the weight loss predominantly occurs during the heating up stage, and when the samples are held at a certain temperature, there is little weight loss. Between 1125 ℃ and 1150 ℃, the weight loss is higher than that between 1000 ℃ and 1100 ℃. Also, when the samples are held at

1125 ℃ and 1150 ℃, the weight loss can also be observed and the weight loss at 1125 ℃ is similar to that at 1150 ℃. According to the research from other groups [24, 36, 228, 229], the weight loss is mainly associated with the loss of lattice oxygen. This causes the formation of oxygen vacancies and the valence change of transition metal ions. The associated reaction can be written in the Kroger-Vink notation as[16]

$$O_O^X + 2M_M^{\cdot} \overset{\text{Heating}}{\longleftrightarrow} \frac{1}{2}O_2 \uparrow + V_O^{\cdot\cdot} + 2M_M^X \tag{4.1}$$

where M refers to Fe or Co. The weight losses at 1125 ℃ and 1150 ℃ are heavier, which suggests that the loss mechanism of lattice oxygen in this range becomes more active. It has been reported [24, 228, 229] that these changes are closely linked with the decrease from high valence state Fe^{4+} and Co^{3+} to low valence state Fe^{2+} and Co^{2+}, with the loss of lattice oxygen, which also can be expressed by

$$2Co_{Co}^{\cdot} + O_O^X \leftrightarrow 2Co_{Co}^X + V_O^{\cdot\cdot} + \frac{1}{2}O_2 \uparrow \tag{4.2}$$

$$2Fe_{Fe}^{\cdot} + O_O^X \leftrightarrow 2Fe_{Fe}^X + V_O^{\cdot\cdot} + \frac{1}{2}O_2 \uparrow \tag{4.3}$$

The loss of oxygen results in oxygen vacancies. In order to maintain the charge neutrality, high valence state Fe^{4+} and Co^{3+} can be changed into Fe^{2+} and Co^{2+} and the effective ionic radii are enlarged[230]. According to McIntosh *et al.*[36], the increase in concentration of oxygen vacancies can result in an increase of lattice parameter. Therefore, the loss of lattice oxygen and the formation of oxygen vacancies can be the reason for the observed increase in lattice parameters with increasing sintering temperature.

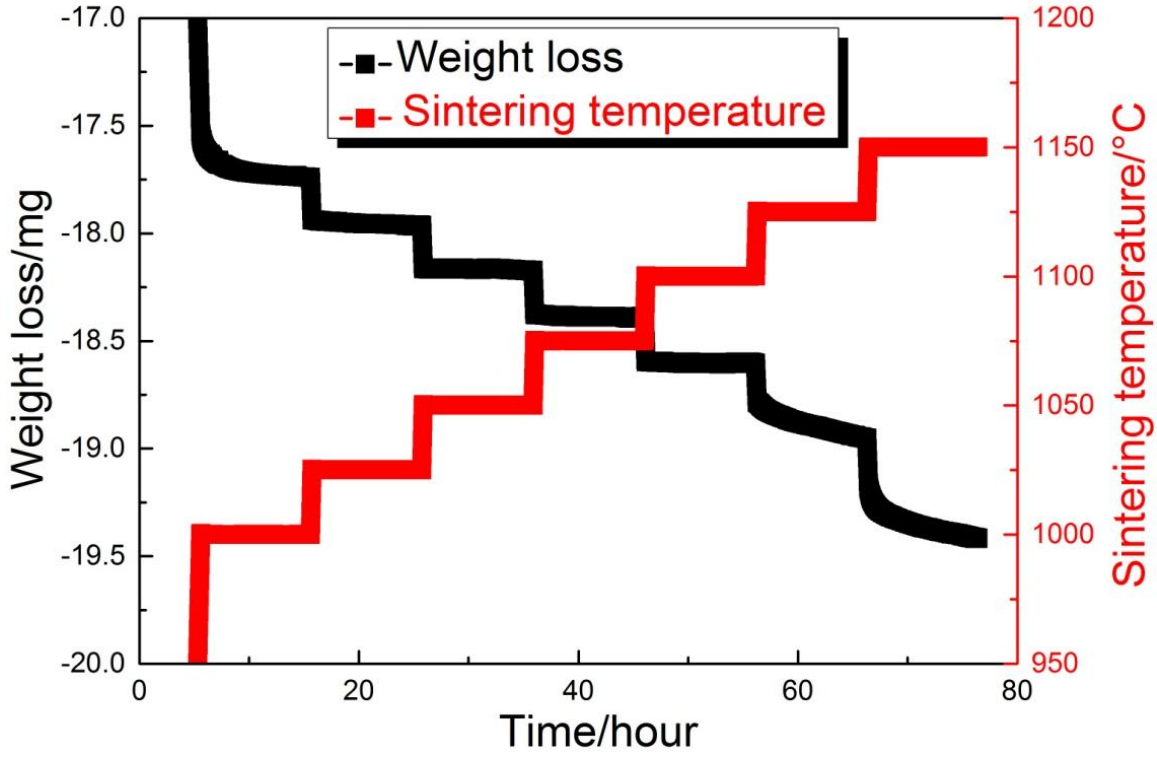

Figure 4.6 TG results for BSCF sintered at different temperatures for 10 hours

4.1.3 Relative density

Figure 4.7(A) shows the effect of dwell time on relative density. For a given sintering temperature (1100 ℃), the relative density of BSCF increases gradually during sintering from 1 to 10 hours, and then stays almost constant with further increase in the dwell time up to 100 hours. Figure 4.7(B) shows that for a given dwell time of 10 hours the relative density increases from 76% to 95.5% as the sintering temperature increases from 900 ℃ to 1100 ℃. Between 1100 ℃ and 1150 ℃, the density shows little change with temperature. The relative density obtained in this study is slightly lower than the values obtained by other groups[100] due to differences in the starting powders, processing routes and sintering histories.

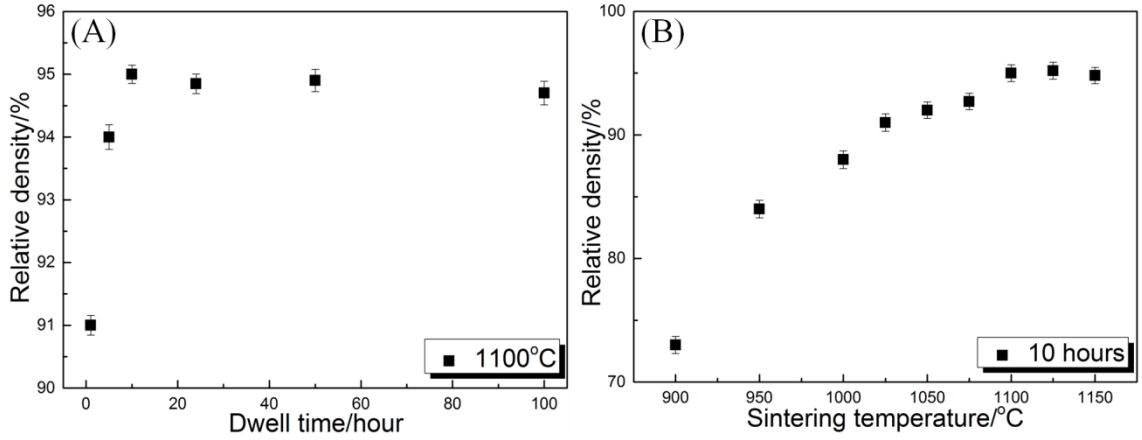

Figure 4.7 The effect of sintering temperatures and dwell time on relative density: (A) at constant temperature (1100 ℃); (B) at constant time (10 hours).

4.1.4 Grain growth evaluation

4.1.4.1 Effect of dwell time on grain growth

For a given sintering temperature of 1100 ℃, the average grain size grows rapidly as the dwell time increases from 1 to 10 hours, followed by a gradual decrease in the growth rate as the thermal exposure time further increases from 10 to 100 hours, as shown in Figure 4.8.

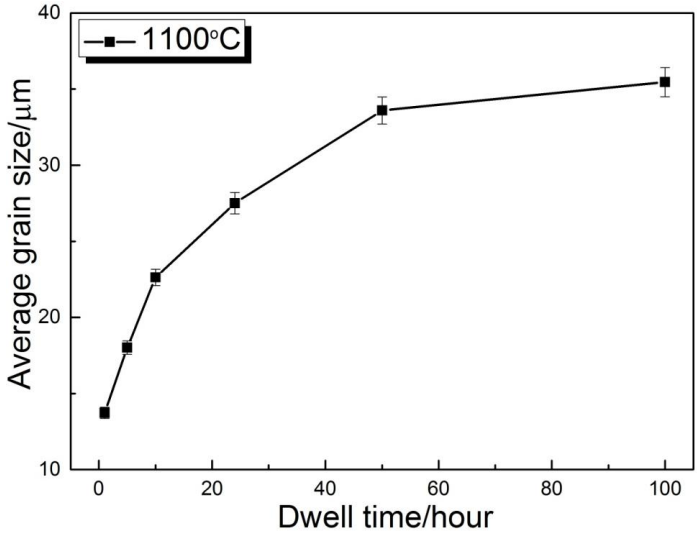

Figure 4.8 Average grain sizes of BSCF sintered at 1100 ℃ as a function of dwell time.

Figure 4.9 shows the microstructure of BSCF sintered at 1100 ℃ for various dwell

times. It is noted that the average grain size increases with increasing dwell time. The average grain sizes of the samples sintered at 1100 ℃ from 1 to 100 hours are found to be in the range from 14 μm to 35 μm.

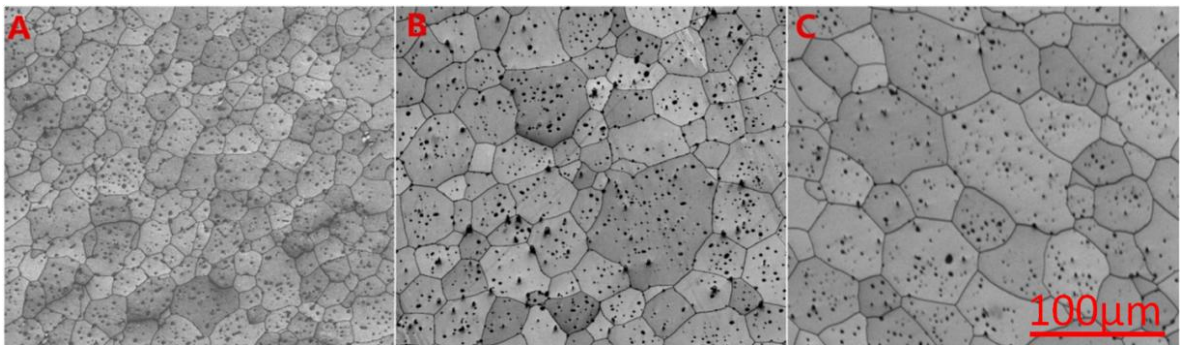

Figure 4.9 EBSD band contrast micrographs of BSCF sintered at 1100 ℃ for (A) 5 hours; (B) 24 hours; (C) 100 hours

According to Hillert [231] and Mendelson [232] concerning analysis of grain growth kinetics, investigators[68, 89, 95, 233, 234] have obtained the following time dependence of the grain growth kinetics at a constant temperature:

$$D^n - {D_0}^n = tK_0 exp(-\frac{Q}{RT}) \quad (4.4)$$

where D (μm) is average grain size at the time t; D_0 is the initial average grain size; the n value is the kinetic grain growth exponent, K_0 is a constant, Q is the apparent activation energy (kJ/mol); R is the gas constant, 8.314 J/mol K; T is the absolute temperature (K).

Because the average grain size of the samples sintered at 900 ℃ is 1.52 μm, the original grain size D_0 should be no more than 1.52 μm. Normally, the value of n is in the range from 1 to 4. The grain sizes of BSCF sintered at 1100 ℃ are in the range from 14 μm to 35 μm. Therefore, $\frac{D^n - {D_0}^n}{D^n}$ is approximately 1, and the equation is simplified as follows:

$$D^n = tK_0 exp(-\frac{Q}{RT}) \quad (4.5)$$

Equation (4.5) can be expressed in the form:

$$\ln(D) = \frac{1}{n} ln(t) + \frac{1}{n} [lnK_0 - (\frac{Q}{RT})] \quad (4.6)$$

From the slope (*1/n*) of the *ln* (grain size) versus *ln* (time) line, the value n of the grain growth kinetic exponent can be determined. Figure 4.10 demonstrates the isothermal grain growth data for the BSCF ceramics from 1 to 100 hours at 1100 ℃ in the form of Equation (4.6). At a sintering temperature of 1100 ℃, the slope *1/n* is determined to be 0.33. This means that the value n of the grain growth exponent equals 3.0. It is implied that the grain growth of BSCF during sintering can be expressed by

$$D^3 = K_0 \, t \, exp(\frac{-Q}{RT}) \quad (4.7)$$

The value of the grain growth exponent of BSCF (n=3) is consistent with that obtained by other groups (n=3.1) [226] and other related perovskite-structured materials such as $PrBaCo_2O_{5+\delta}$ (n=3) sintered at 1150 ℃ from 6 to 48 hours[95].

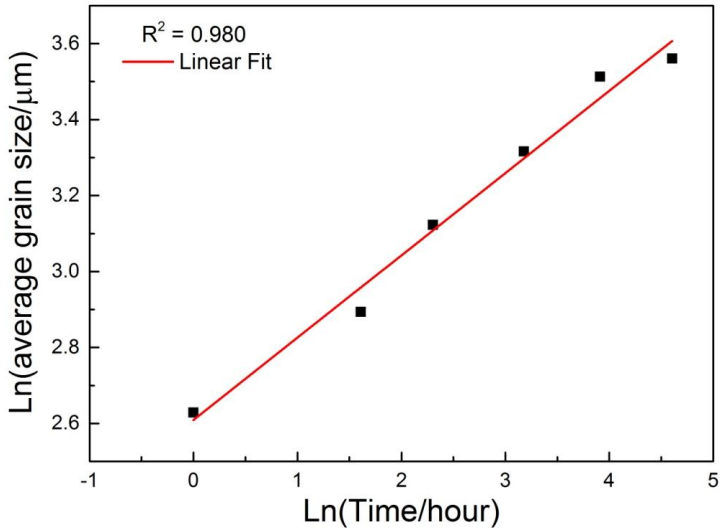

Figure 4.10 Dwell time dependence of grain size at a sintering temperature of 1100 ℃

4.1.4.2 Effect of sintering temperature on grain growth

As shown in Figure 4.11, the average grain size grows with an increase in sintering temperature for a given sintering time (10 hours). The grain size increases slowly with

the sintering temperature up to 1000 ℃, followed by a faster growth rate in the range from 1000 to 1100 ℃. Between 1100 ℃ and 1150 ℃, the grain size enters a period of rapid growth.

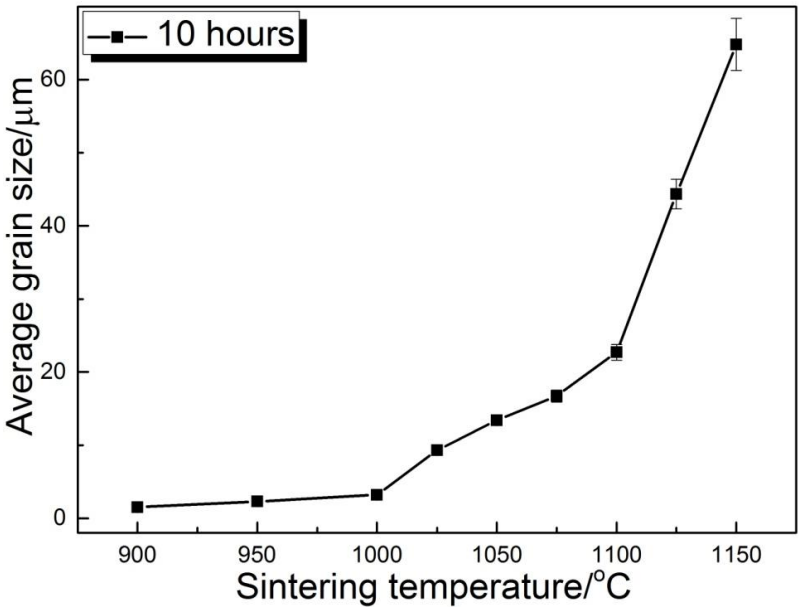

Figure 4.11 The average grain sizes of BSCF sintered for 10 hours as a function of sintering temperature. The line is a guide to the eye.

For instance, the average grain sizes of BSCF samples sintered at 1000, 1100, and 1150 ℃ are determined to be 3.2, 22.7 and 64.8 μm, respectively. Microstructures of the BSCF ceramics sintered under different conditions are shown in Figure 4.12.

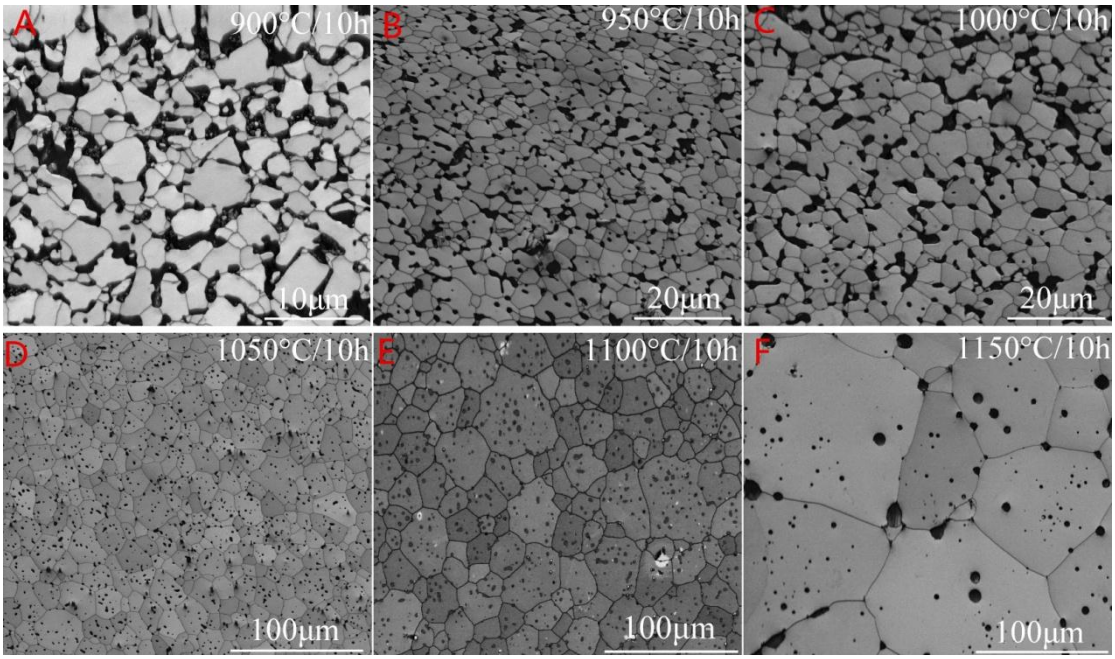

Figure 4.12 EBSD band contrast micrographs of BSCF sintered at various temperatures

for 10 hours: (A) 900 ℃ ; (B) 950 ℃ ; (C) 1000 ℃ ; (D) 1050 ℃ ; (E)1100 ℃ ; (F) 1150 ℃.

Figure 4.13 shows an Arrhenius plot obtained by constructing the data of average grain sizes from a constant dwell time, in which $ln(D^3/t)$ is plotted versus the reciprocal of the absolute temperature ($1/T$). Assuming that the grain growth exponent (n=3) is independent of temperature, it is used to determine the activation energy for BSCF grain growth. The logarithm of Equation (4.7) obtains the slope which can be used for calculation of the apparent activation energy for the grain growth.

$$ln\left(\frac{D^3}{t}\right) = -\frac{Q}{R}\left(\frac{1}{T}\right) + lnK_0 \tag{4.8}$$

There exists a reasonably good linear relationship between $\ln(D^3/t)$ and 1/T from 900 to 1150 ℃ at a constant dwell time (10 hours) in this study (R^2=0.950). The grain growth activation energy determined from the slope of Figure 4.13(A) is 650.7±30 kJ/mol. Although Salehi *et al.*[100], Baumann *et al.*[235] and Yoon *et al.*[101] have not reported an activation energy for grain growth of BSCF, analysing their average grain size data yields activation energies in the range from 372 to 741 kJ/mol as plotted in Figure 4.13(B), which agree fairly well with the result in this study.

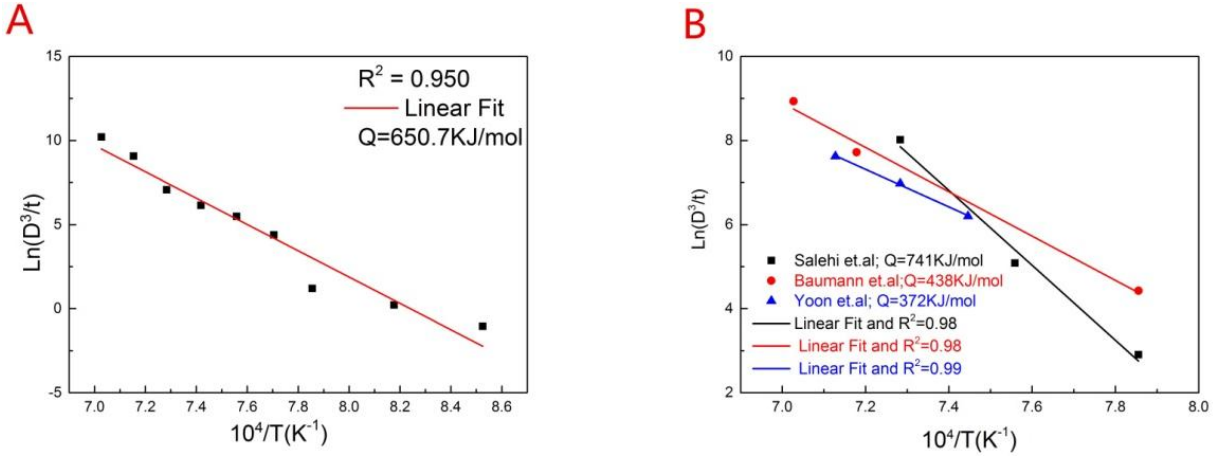

Figure 4.13 Arrhenius plot of ln(average grain size) against reciprocal of sintering temperatures for BSCF: (A) this study; (B) references

4.1.5 Grain aspect ratio distributions

Figure 4.14 presents the grain aspect ratio distributions obtained by image analysis for the BSCF samples sintered under different conditions. It can be clearly observed that the sintering temperature and dwell time have little effect on the grain aspect ratio and its distribution. The average grain aspect ratios of all the samples under the different sintering conditions are approximately 1.8.

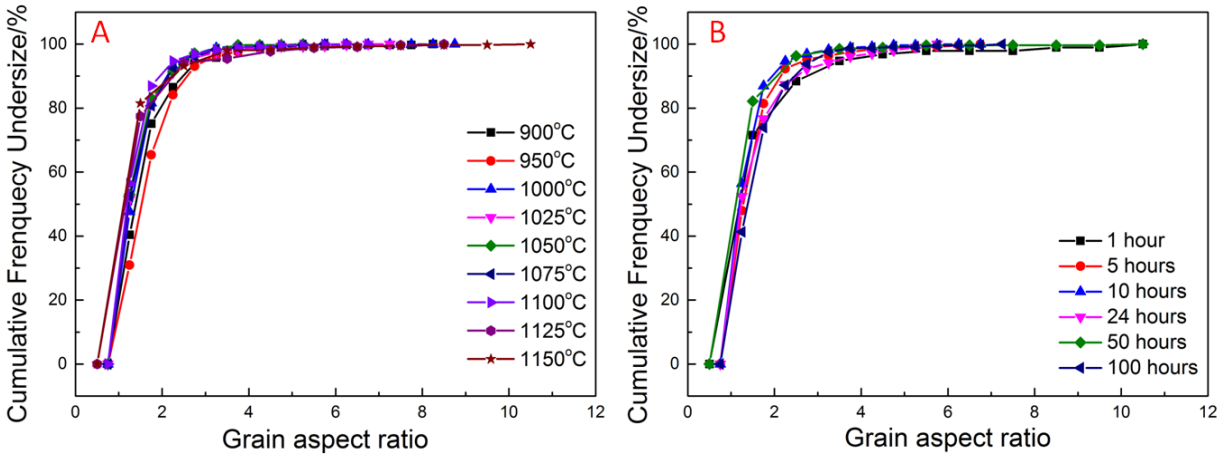

Figure 4.14 Grain aspect ratio distributions of BSCF sintered (A) from 900 ℃ to 1150 ℃ for 10 hours and (B) between 1 and 100 hours at 1100 ℃.

4.1.6 Mechanisms of densification and grain growth

It is a very difficult undertaking to unambiguously identify the controlling mechanisms taking account of the simultaneous occurrence of densification and coarsening processes. Coble *et al.*[16] have proposed a model to determine the controlling mechanism of densification for the final stage of sintering. This model predicts the densification rate $\frac{d\rho}{dt}$ as the following equation:

$$\frac{d\rho}{dt} = \frac{CN\xi\gamma_s\Omega}{D^m} \tag{4.9}$$

where ρ represents the density, C denotes a constant, N is the number of pores inside a grain, γ_s refers to the surface energy, Ω denotes volume per cation, D is average grain

size to the power m, where m depends on the rate-controlling mechanism for densification, ξ is the relevant diffusion coefficient. For m=3 densification is controlled by lattice diffusion or interface reaction, while for m=4 grain boundary diffusion controls the densification. Accordingly, the m value can be determined by plotting a log-log of Equation (4.8) to determine the slope. Combining Equations (4.5) and (4.9) leads to the following equation:

$$\frac{d\rho}{dt} = \frac{CN\xi\gamma_s\Omega}{tK_0 exp\,(-\frac{Q}{RT})} \tag{4.10}$$

Equation (4.10) can be integrated to obtain the following equation:

$$\rho = \frac{CN\xi\gamma_s\Omega}{K_0 exp\,(-\frac{Q}{RT})}\ln(t) + \Theta \tag{4.11}$$

Taking the logarithm of both sides of Equation (4.9) leads to the following equation:

$$log\left(\frac{d\rho}{dt}\right) = -mlog(D) + \Phi \tag{4.12}$$

where all the alphabetic symbols denote the same meaning as before; Θ and Φ are constants.

The experimental data obtained from the samples sintered at 1100 ℃ from 5 to 100 hours are plotted in this way for the density range from 93.7% to 95.5% in Figure 4.15(A). At 1100 ℃, the calculated value of m from the plot is 3.98±0.29 for BSCF in Figure 4.15(B). Considering the values of m, it suggests that the grain boundary diffusion is the dominant controlling mechanism for BSCF at 1100 ℃.

In the case of grain growth kinetics, the grain growth exponent n of BSCF is determined to be 3. In other words, the grain growth kinetics of BSCF materials does not follow the classical parabolic law (n=2). A higher grain growth exponent indicates slowly coarsening grains. It has been reported that the driving force for grain growth is the local curvature of the grain boundary[16]. When the pores are dragged along the grain

boundary, it will lower the driving force for grain boundary mobility thereby slowing grain growth[165]. A grain growth exponent greater than 2 can be related to pores and impurity contents of the oxide materials [27, 28]. Therefore, the pores can be the dominant factor for the higher grain growth exponent, as shown in Figure 4.12.

With regard to the activation energy for grain growth of BSCF, it is calculated to be 650.7±30 kJ/mol. Because the activation energy for oxygen ion diffusion (45-105 kJ/mol[103, 104]) is much lower than that for grain growth, it is suggested that cations are the rate-controlling species of grain growth rather than oxygen ions. According to the studies performed by Lein *et al*. [104, 105], the diffusion of Sr/La has been observed to be slower than that of Co/Fe in $La_{0.5}Sr_{0.5}Co_{0.8}Fe_{0.2}O_{3-\delta}$ and the activation energy for Sr/La diffusion is 619 kJ/mol. Therefore, in terms of BSCF, it can be speculated that the Ba/Sr diffusion can be the rate-controlling species during the sintering process.

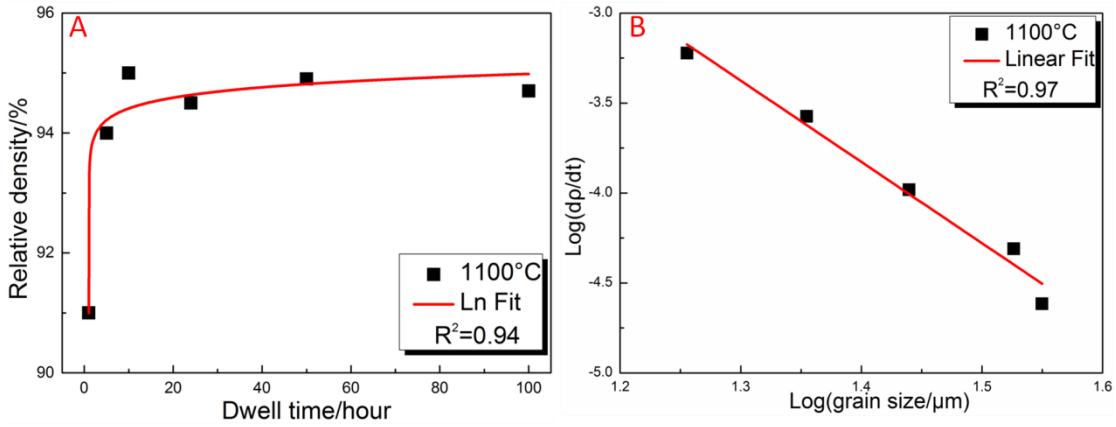

Figure 4.15 (A) relative density of BSCF sintered at 1100 ℃ for various dwell times; (B) Plot of log(dρ/dt) versus log(grain size) for 1100 ℃

4.1.7 Predicting the grain size distributions in BSCF membranes

The BSCF samples were sintered according to the following 3×3 temperature-time matrix. The sintering temperatures were 1075, 1100 and 1125 ℃ and the dwell time was 5, 10, and 24 hours.

4.1.7.1 Comparing the grain size distributions in the sintered BSCF ceramics

Figure 4.16 shows the EBSD band contrast micrographs of the same sintered samples at two different fields. It can be clearly inferred that microstructural features in these two fields are very similar in appearance. Figure 4.17 shows the relationship between the cumulative frequencies of the grain undersize against the grain size for the two SEM micrographs of Figure 4.16. It is clearly observed that the microstructures exhibit a close quantitative match. The overlap of grain size distributions in Figure 4.17 proves that the grain size analysis by EBSD method is repeatable and reproducible. This indicates that EBSD method is suitable for making further analysis in this study.

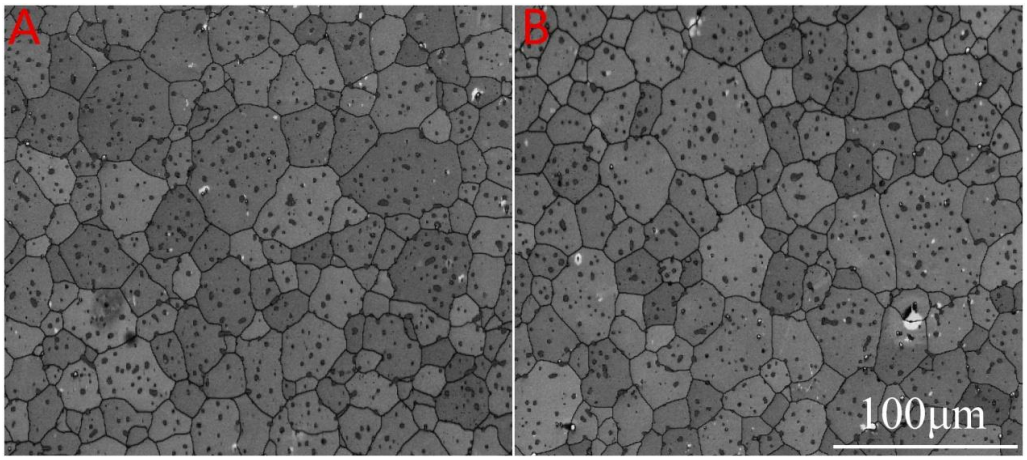

Figure 4.16 EBSD band contrast micrographs of the BSCF samples sintered at 1100 ℃ for 10 hours with two different fields show similar morphology.

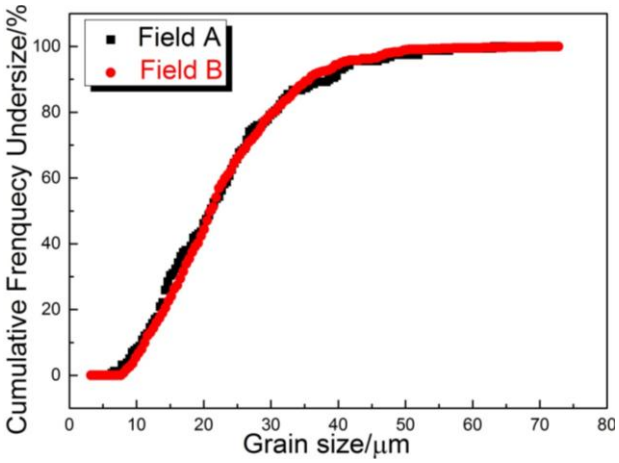

Figure 4.17 Grain size distributions for Figure 4.16 show the results with reproducibility

Figure 4.18 shows the grain size distributions of the sintered samples obtained under various sintering conditions. These four profiles were selected because they were reasonably far apart from each other, making it possible to clearly distinguish the data points. It is apparent from the plots presented in Figure 4.18 and Figure 4.19 that, whereas the shape of each grain size distribution profile keeps essentially similar, the grain size distribution curve shifts toward the coarser size profile as a function of prolonging dwell time and/or increasing temperature. After that, it is possible to give basically the same grain size distribution under appropriate conditions for different combinations of time and temperature. It can be inferred from Equation (4.5) that the combination of a high sintering temperature and short dwell time would give the same average grain size and grain size distribution as that of a relatively lower temperature and longer time.

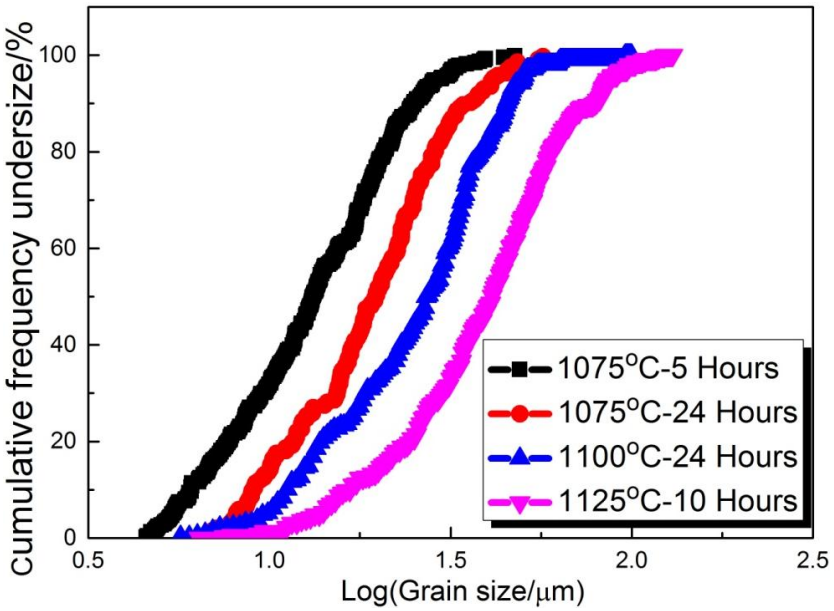

Figure 4.18 Grain size distributions of BSCF having various sintering conditions expose similarity of the profile shapes.

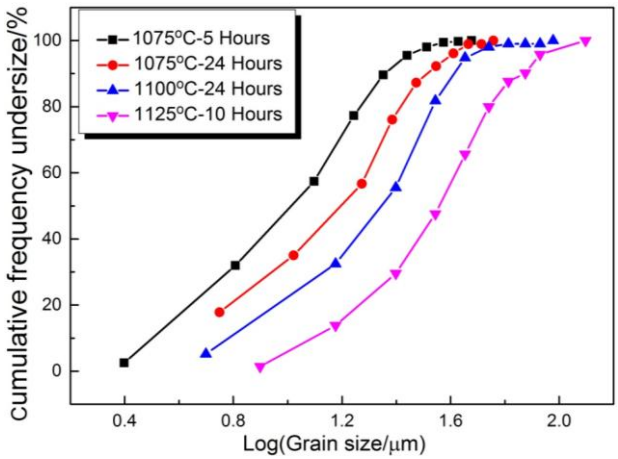

Figure 4.19 Taking every tenth point of the data in Figure 4.18 was replotted in the distribution

Unexpectedly, even within the inadequate number of sintering studies conducted this provisional projection was demonstrated experimentally. Figure 4.20 shows that the EBSD band contrast micrographs of microstructures of the sintered bodies under different conditions look visually similar. It has been demonstrated that the grain size distributions of these two samples in Figure 4.20 are plotted similarly, as shown in Figure 4.21.

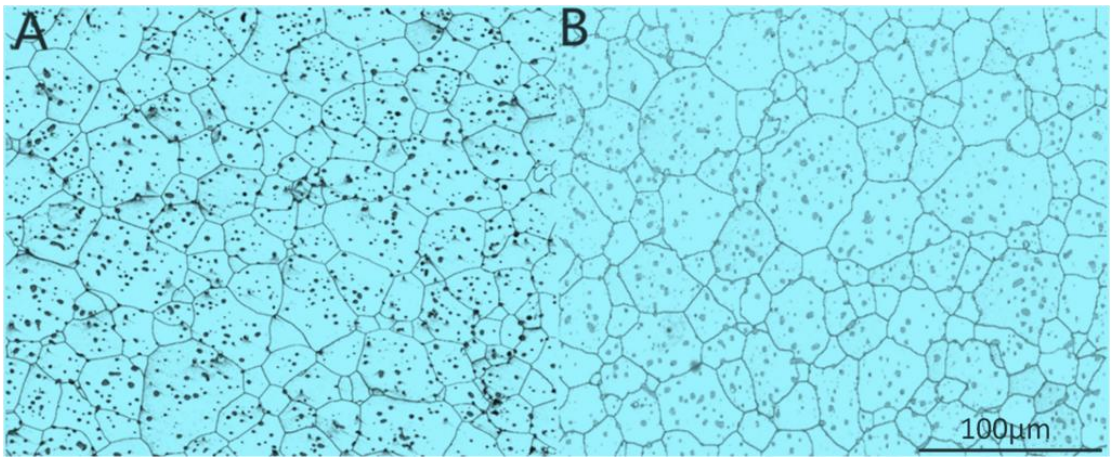

Figure 4.20 Scanning Electron micrographs of two BSCF samples sintered at different time-temperature conditions showing similar micro-structural features (A)1075 ℃-24 hours; (B)1100 ℃-10 hours

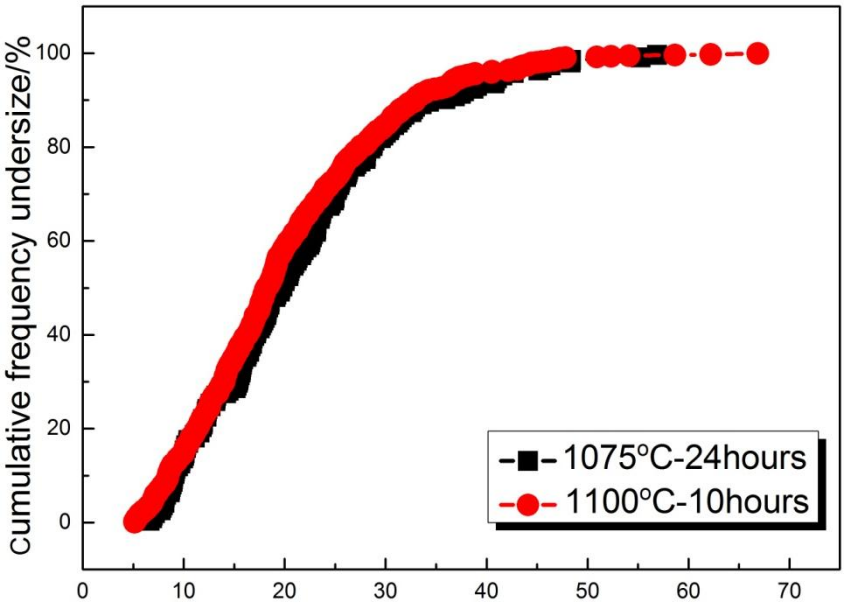

Figure 4.21 Measured grain size distributions for the two SEM micrographs of Figure 4.20 are similar.

4.1.7.2 Self-similar grain size distributions in sintered BSCF

It was noted above that while the plot profile tends towards a coarse grain size range during grain growth, the shape of the grain size distribution profiles remain similar in Figure 4.18 and Figure 4.19. When the grain size distributions of these samples are replotted based on a nondimensionalised size, defined as the median size of the individual distribution, several plots are obtained as shown in Figure 4.22. Grain size distributions with this characteristic are defined as self-similar size spectra. Self-similarity characteristics suggests that the same dominant mechanism governs grain growth kinetics [233].

For the grain size distribution curves in Figure 4.22, the nondimensional grain size is defined as[233]

$$X = \frac{x}{x_{0.5}} \tag{4.13}$$

where X is the defined dimensionless grain size corresponding to the grain with a size x (μm), and $x_{0.5}$ is the number-based median size (μm) of the distribution.

Figure 4.22 shows the dimensionless grain size distributions for the data obtained under different sintering conditions. As replotted in this way, the different grain size distribution curves shown in Figure 4.22(A) and 4.22(B) overlap into a single curve in Figure 4.22(C) and 4.22(D), respectively. Thus, the standard of self-similarity can be used in sintered bodies as well, which are consisting of numerous connected grains arranged in this system [233].

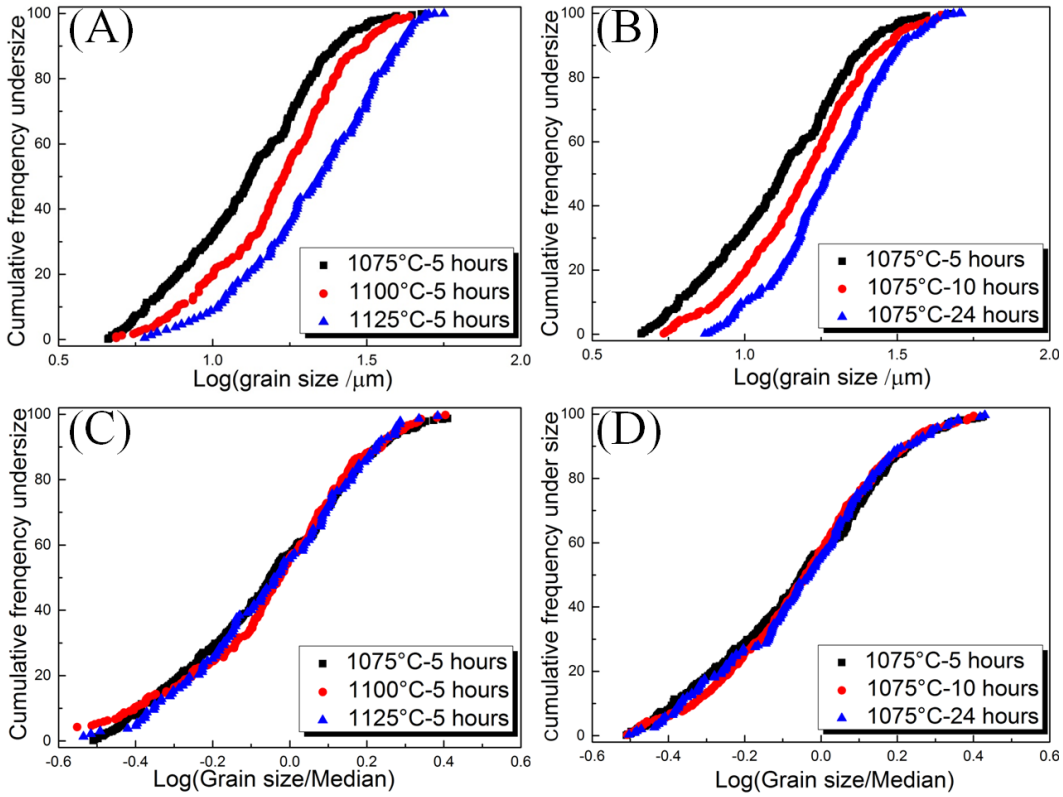

Figure 4.22 Comparison of normalised grain size distributions for different sintering conditions

As aforementioned, concerning the dominant grain growth mechanism in systems with self-similarity, this implies that the appropriate time-temperature region for normal grain growth can be predicted. Self-similarity for ceramics during grain growth has been reported. For example, Burke *et al*. [67] have reported that the shape of the grain size distribution curve is independent of the grain size. Self-similar grain size distributions suggest that the nondimensional grain size distributions in sintered bodies for the BSCF ceramics are independent of the sintering histories. It can be inferred that with respect to

the width of the distribution, the ratio of the largest grain to the smallest grain can be independent of the sintering history. Although a limited range of experimental conditions have been used in this study, self-similarity has important implications. First, when the sintering temperature-time programmes are changed, it is accompanied by translation of the whole grain size distribution plot horizontally along the temperature axis rather than shifting any point in the plot. Second, the single measurement of any distribution, specifically its median size, can predict the entire grain size distribution if the characteristic self-similarity and grain size distributions plots have been already obtained. This phenomena is also observed in alumina[233].

4.2 Mechanical characteristics and fractography of perovskite-structured BSCF membranes

In this section, fracture stress, hardness, Young's modulus, fracture toughness, and slow crack growth behaviour are measured and discussed sequentially. Macro-mechanical behaviour determined from biaxial and uniaxial bending tests as well as micro-mechanical properties measured from indentation tests are presented. The various characterisation results are discussed to explain the mechanical behaviours of perovskite-structured BSCF membranes. To be more specific, fracture stress is determined from biaxial and uniaxial bending tests between RT and 800 ℃; hardness is evaluated by micro-indentation test at RT; Young's modulus is measured by biaxial and uniaxial bending tests between RT and 800 ℃ as well as using micro-indentation tests at RT; fracture toughness is determined by the initial crack measurement method at RT and by an indentation strength method between RT and 800 ℃; slow crack growth tests are determined by the direct measurement method at RT and by the constant stress rate method at 800 ℃.

4.2.1 Fracture stress

The fracture stress of BSCF sintered at 1100 ℃ for 10 hours was determined by both ring-on-ring and three-point bending tests. Weibull analysis was conducted to evaluate these two methods and fractography principles were used to characterise the fracture surfaces [236].

4.2.1.1 Uniaxial and biaxial bending tests

The fracture stress of BSCF was measured by three-point and ring-on-ring bending tests between RT and 800 ℃ as shown in Figure 4.23. In the case of three-point bending tests, a value of 127±15 MPa was obtained at RT. With increasing the temperature, there was a sharp reduction in fracture stress at 200 ℃, and then it slightly decreased and showed a minimum at 400 ℃. At higher temperature, the fracture stress increased considerably at 600 ℃ and recovered 70% of the RT value and increased slightly up to 800 ℃. Although the values of fracture stress obtained from ring-on-ring bending tests were lower than those determined by three-point bending tests, it is clearly observed that two curves of fracture stress as a function of temperature showed a similar trend with a stress minimum at an intermediate temperature. Therefore, this unexpected behaviour is independent of mechanical testing methods. Huang *et al*.[19] have reported that this anomalous behaviour was attributed to the spin transition of Co^{3+}. The discrepancy of fracture stress between these two methods will be discussed in the following section.

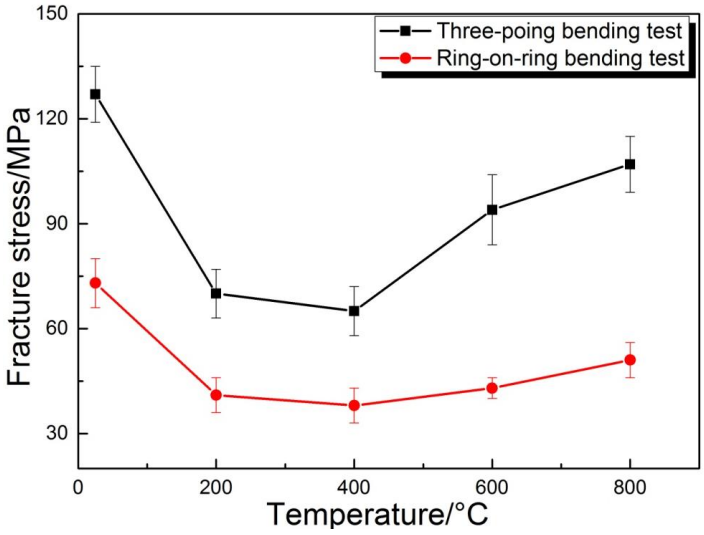

Figure 4.23 Fracture stress determined by three-point bending and ring-on-ring tests as a function of temperature. Each data point is the mean of tests and the error bar shows the standard deviation; 10 specimens for RT and 800 ℃ and 5 specimens for other temperatures.

4.2.1.2 Comparison of uniaxial and biaxial bending tests

As mentioned previously, the values of fracture stress obtained from the ring-on-ring bending tests were lower than those determined by the three-point bending tests. However, in both tests there is a similar trend in behaviour with a minimum in the failure stress found between RT and 800 ℃. These data will be analysed in more detail in this part.

Because these two methods represent different stress states and different test volumes or surface areas, Weibull analysis was used to study this difference and determine whether it is simply an effect of loading geometry. The simplest treatment of the size dependence of strength is through the application of Weibull statistics based fracture theory. According to this theory, the probability of failure of a component, F is given by[168, 169]

$$F = 1 - exp[-(\frac{\sigma_{max}}{\sigma_c})^m V_{eff}] \quad (4.14)$$

where σ_{max} is reference maximum stress in the stressed solid, m Weibull modulus, σ_c

characteristic strength, and V_{eff} effective stress volume defined by

$$V_{eff} = \int (\frac{\sigma}{\sigma_{max}})^m d_V \quad (4.15)$$

where σ = local stress in an elemental stressed volume d_V. In many situations, a two-parameter Weibull distribution can be assumed. And it can be simplified as follows:

$$\ln\left(\frac{1}{1-\mathrm{F}}\right) = (\frac{\sigma_{\max}}{\sigma_c^*})^{\mathrm{m}} \quad (4.16)$$

where the parameter σ^*_c [$\sigma^*_c = \sigma_c(V_{eff})^{\frac{1}{m}}$] represents the specific characteristic strength of the specimen at F=0.632; and *F*, the failure probability, is defined by the relation[165]:

$$F = (i - 0.5)/N \quad (4.17)$$

where *i* is ranking number of a specimen in sample *N* in increasing order of fracture stress σ. To analyse fracture stress data, it can be obtained from the Equation (4.16) as follows[165]:

$$\ln\ln\left(\frac{1}{1-\mathrm{F}}\right) = \mathrm{m}\ln\sigma_{\max} - \mathrm{m}\ln\sigma_c^* \quad (4.18)$$

Hence, a plot of the left side of Equation (4.18) as a function of the natural logarithm of fracture stress should obtain a straight line.

Average strengths in two tests are related to the effective volumes by the relation[166]:

$$\frac{\sigma_{3P}}{\sigma_{ROR}} = (\frac{V_{ROR}}{V_{3P}})^{\frac{1}{m}} \quad (4.19)$$

The effective volume for ring-on-ring test have been given by Batdort[237] and Breder[238]:

$$V_{ROR} = 2t\pi {r_i}^2 m^{0.45} \quad (4.20)$$

where r_i is the radius of the loading ring. The effective volume for the three-point bending test is given by [239]:

$$V_{3P} = \frac{Lhb}{2(m+1)^2} \quad (4.21)$$

L is the distance between the two support points, *b* is the width of the cross section at the applied load, and *h* is the thickness of the specimen. The effective volume is regarded as an assumed volume where the tensile stress is applied. The equations were substituted with the measured mean strength to calculate the predicted values.

Biaxial and uniaxial fracture stress was measured at both RT and 800 ℃ using the ring-on-ring configuration and three-point bending test. The results are summarised in Table 4.1 which gives the sample number (N), the mean fracture stresses and standard deviations, coefficients of variation, the characteristic strength (σ_c), the Weibull modulus (m) and standard errors, coefficients of correlation (R^2).

For all the specimens evaluated in the present experiment in Table 4.1, it is reasonable that the coefficient of variation obtained at 800 ℃ is twice as high as that at RT for both tests, which may be caused by the change of defect size during heating due to the thermal expansion and the randomness of mechanical property measurement at high temperature. The coefficients of variation determined by the biaxial bending tests at RT and 800 ℃ were less than those determined with the use of uniaxial bending tests (Table 4.1). However, the standard deviations determined in the biaxial method at RT and 800 ℃ are still slightly higher, which may be attributed to the complex stress state developed and the frictional force between the contact surface[240].

Table 4.1 The results of uniaxial and biaxial bending tests at RT and 800 ℃

Method	Temperature	Sample number (N)	Mean fracture stress σ_f (MPa)	Standard deviation (MPa)	Coefficient of variation (%)	Weibull modulus (m)	Standard error	Characteristic strength (σ_c)	Coefficients of correlation (R^2)
Uniaxial test	RT	10	127	15	11.8	9.6	0.7	133	0.95
	800 ℃	10	107	24	22.4	5.4	0.3	116	0.96
Biaxial test	RT	10	73	7	9.6	10.2	1.1	77	0.91
	800 ℃	10	45	9	20	5.5	0.4	48	0.95

Figure 4.24 and Figure 4.25 show Weibull plots of fracture stress evaluated by both methods at RT and 800 ℃, *lnln(1/1-F)* as a function of *lnσ*. The Weibull modulus *m* and characteristic strength σ_c are determined from the slope and the intercept, respectively. The fitting of straight line was done using linear regression. The values are summarised in Table 4.1.

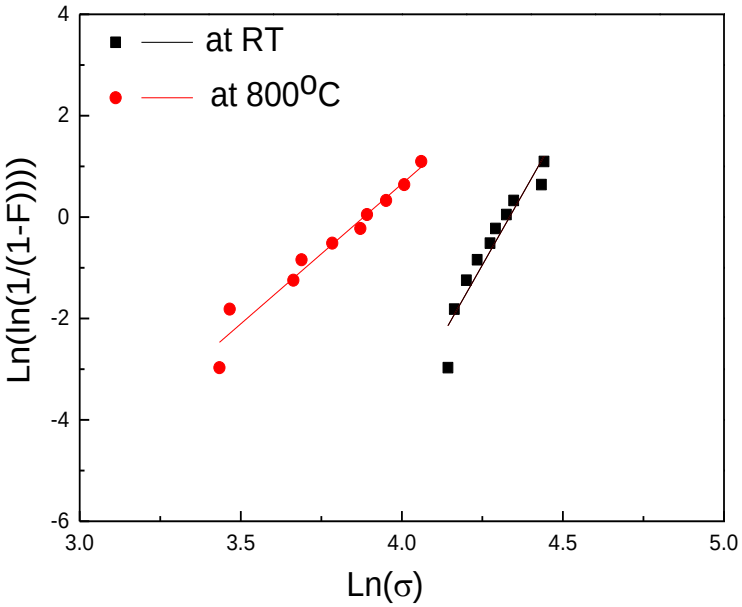

Figure 4.24 Linearised Weibull plots of fracture stresses for BSCF evaluated in the ring-on-ring bending tests at RT and 800 ℃

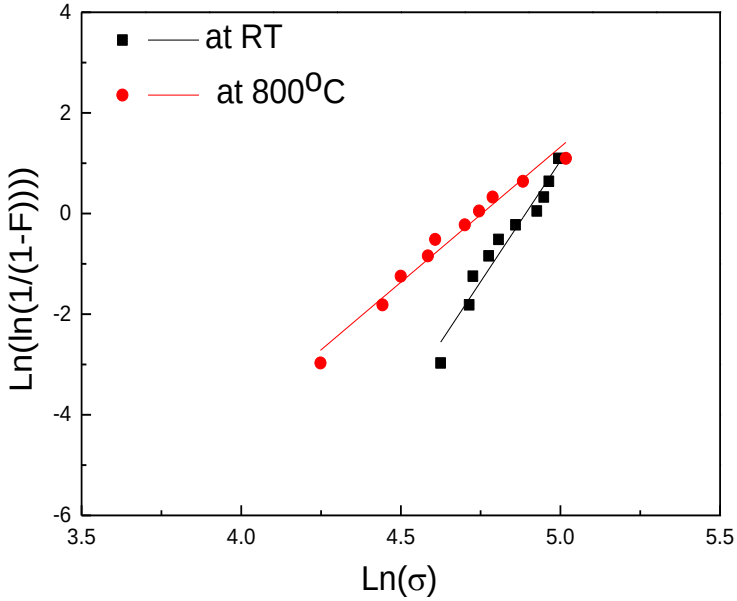

Figure 4.25 Linearised Weibull plots of fracture stresses for BSCF evaluated in the three-point bending tests at RT and 800 ℃

Comparison with the strengths of BSCF between RT and 800 ℃ obtained from Huang *et al.*[225] using the ring-on-ring bending tests, it is noted that the value of those determined from the present biaxial experiments are relatively lower. Because of the similar porosity and different grain size, there are two possible reasons for explaining the difference. One possible explanation of the difference is that the defect size can be related to the grain size. Another possible reason is a larger effective volume for this present experiment although the same method is used to determine the fracture stress.

For all the samples evaluated in the present experiment between RT and 800 ℃, as shown in Figure 4.23, the values of fracture stress provided in uniaxial tests are significantly higher than those determined by the biaxial tests. This finding was consistent with a study conducted on alumina by Shetty *et al.*[166]. The discrepancy is attributed to the difference in the effective area or volume of the material subjected to maximum stress between the two tests[238]. To be more specific, by accounting for the effective volume of the materials under stress [Equations (4.20) and (4.21)] it was found that biaxial specimens (V_{eff}=20.5 mm^3) were subjected to a larger effective volume than that of the three-point bending specimens (V_{eff}=0.17 mm^3). Therefore, using the theory of Weibull [18] it was established that the three-point bending strength will be larger than the biaxial strength due to smaller effective volume.

As displayed in Table 4.1, the biaxial strength data gives the values of m=10.2 ($R^2 = 0.91$) at RT and m=5.5 ($R^2 = 0.95$) at 800 ℃, while the corresponding values for the uniaxial strength at RT and 800 ℃ were 9.6 ($R^2 = 0.95$) and 5.4 ($R^2 = 0.91$), respectively. The Weibull modulus obtained from the biaxial tests are similar to those obtained from the uniaxial tests at RT and 800 ℃, respectively. This indicates there is little difference in the flaw population between these two experiments and the effective

volume calculations are valid for the both room and high temperature data.

Table 4.2 The results of measured values of two methods and the predicted values of three-point bending tests

Temperature	Measured		Predicted	Ratio	
	σ_{3p} (MPa)	σ_{bia} (MPa)	σ_{3p} (MPa)	σ_{3p}/σ_{bia}	σ_{3p}(predicted)/σ_{bia}
RT	127	73	119	1.74	1.63
800 ℃	107	45	96	2.38	2.18

Using Batforf's approach[237], the predicted curves are displayed in Figure 4.26 and Figure 4.27. It is acceptable that the predicted strengths of three-point bending tests based on ring-on-ring bending tests are 6.3% and 10.3% lower than the measured values of strength from three- point bending tests at RT and 800 ℃ (in Table 4.2), respectively. This comparison suggests that the predicted approach is adequate for the present case.

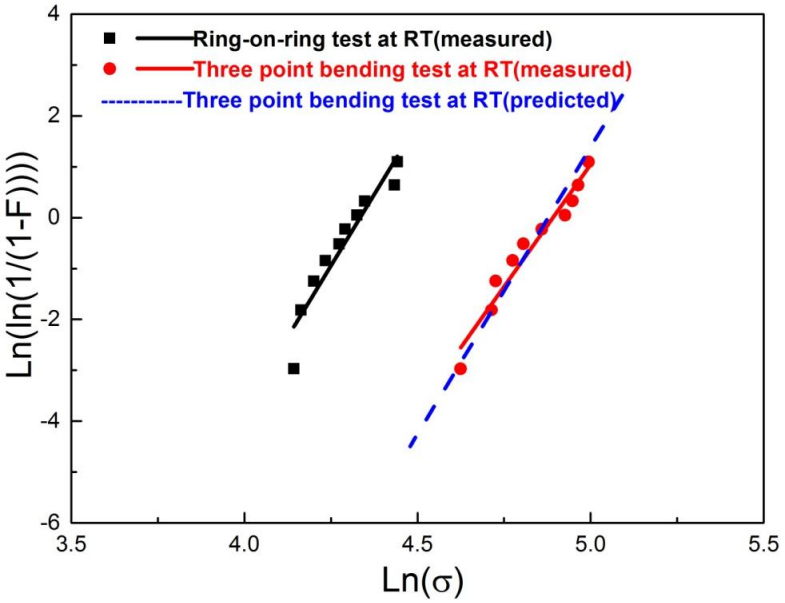

Figure 4.26 Strength distributions of both methods at RT and three- point bending strengths predicted from the biaxial tests.

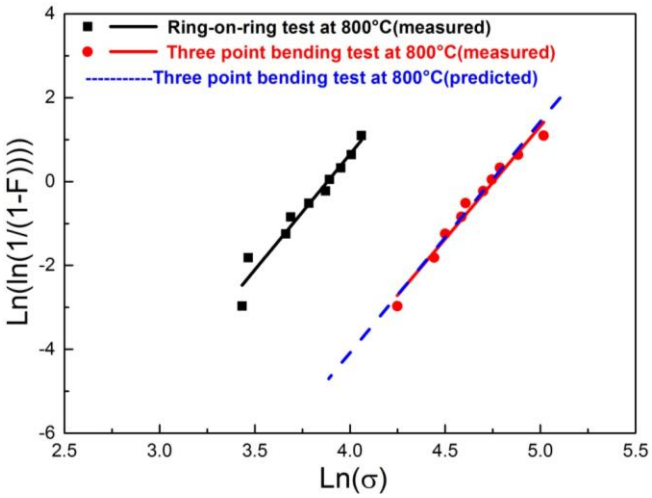

Figure 4.27 Strength distributions of both methods at 800 ℃ and three-point bending strengths predicted from the biaxial tests.

Figure 4.28 shows the load-displacement curves of different testing methods at both RT and 800 ℃. In the case of the same method, the moving deflection/area of specimen at 800 ℃ is larger than that at RT. On the other hand, the load-deflection curves obtained from these two methods at RT are linear while the curves obtained at 800 ℃ are nonlinear. This indicates that the plastic deformation of BSCF specimens (e.g creep) occurs at 800 ℃. The nonlinear load-deflection curve was also observed in $LaCrO_{3-\delta}$ and was attributed to the formation of oxygen vacancies at high temperature[241]. According to the studies of thermal properties [229, 242], BSCF materials release oxygen and form oxygen vacancies at high temperature. However, according to the load-deflection curves at 800 ℃, the creep resistance increases with increasing the deflection. Therefore, the vacancies cannot be the dominant factor in the nonlinear curves. A more plausible explanation is pore closure induced by compressive stress at 800 ℃. Compared with the three point bending tests, the deflections in ring-on-ring bending tests are larger at both RT and 800 ℃ due to their larger effective volume.

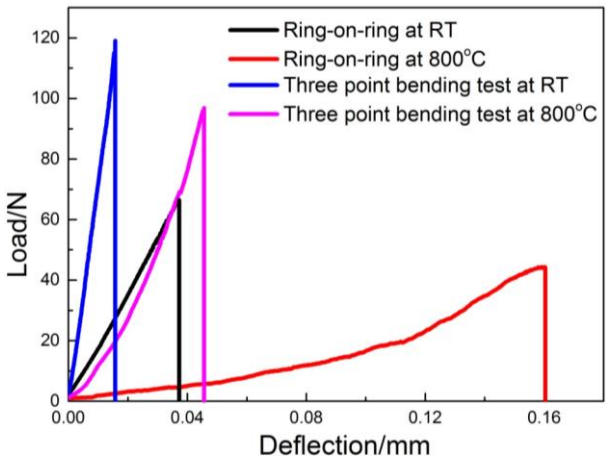

Figure 4.28 The typical load-displacement curves of different methods at RT and 800 ℃

4.2.1.3 Fractography

It is very important to study the fracture surfaces, fractography, which can recognise not only the process of fracture but also failure origins[243]. Fracture surfaces are often described as transgranular or intergranular. After ring-on-ring and three-point bending tests, the fracture surfaces of BSCF at different temperatures were investigated by SEM to determine the fracture mode in Figure 4.29 and 4.30. The transgranular mode was observed at all the temperatures. In addition, no intergranular mode was observed at high temperatures which is consistent with the results reported by others [225]. However, as for $La_{0.58}Sr_{0.4}Co_{0.2}Fe_{0.8}O_{3-\delta}$, the fracture mode is very different from BSCF. At room temperature, transgranular mode is only observed whilst at 200 ℃ a mixture of about 80% transgranular and the rest of intergranular mode are observed. At 700 ℃ the proportion of transgranular mode decreases to 15% and the ratio of intergranular increases to 85%. At 800 ℃, intergranular mode is only observed and no transgranular mode exists. The transition of fracture mode of $La_{0.58}Sr_{0.4}Co_{0.2}Fe_{0.8}O_{3-\delta}$ demonstrates that the grain boundaries become weaker and weaker with the enhancement of temperature compared with the cohesion in the lattice[225]. This phenomenon was also observed in $La_{0.8}Ca_{0.2}CoO_3$ materials[115], of which fracture surface showed a transgranular mode at RT while mixed modes were observed at high temperature.

As shown in Figure 4.29(B), additional phases exist along the grain boundary and small particles are observed in the inner part of the grain after high temperature testing. However, the XRD investigation does not give any indication with respect to the presence of other phases, probably due to the fact that the amount of these particles is less than 5%. The only detectable phase on the fracture surface from all the samples of BSCF was cubic. Similarly, in conjunction with EDX, these small particles also cannot be determined. Additional work is required to unequivocally determine these small particles by TEM in future. Although a secondary phase can lead to lower strengths with increasing the temperature and the strength degradation is aided by the decomposition of the grains, a small amount of secondary phase caused no interfacial weakening and no deterioration of the mechanical properties according to the research of Huang *et al*. [225].

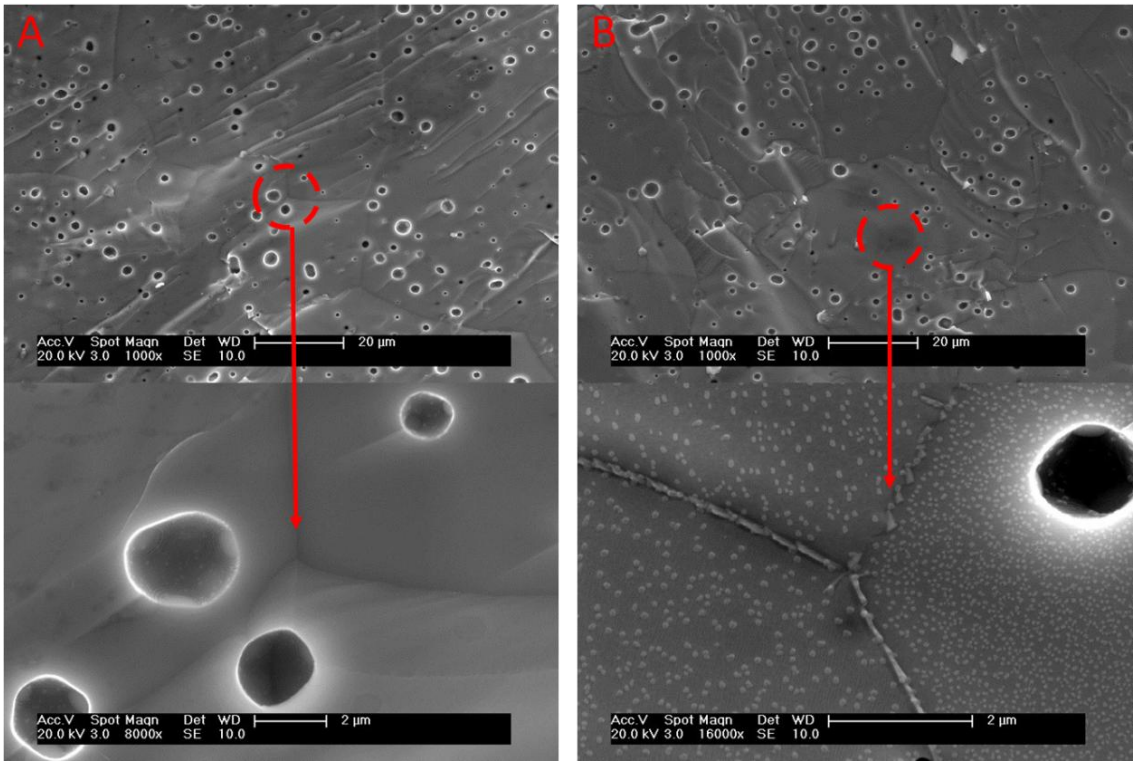

Figure 4.29 Typical fracture sufaces of BSCF at different temperatures: (A) RT; (B)800 ℃

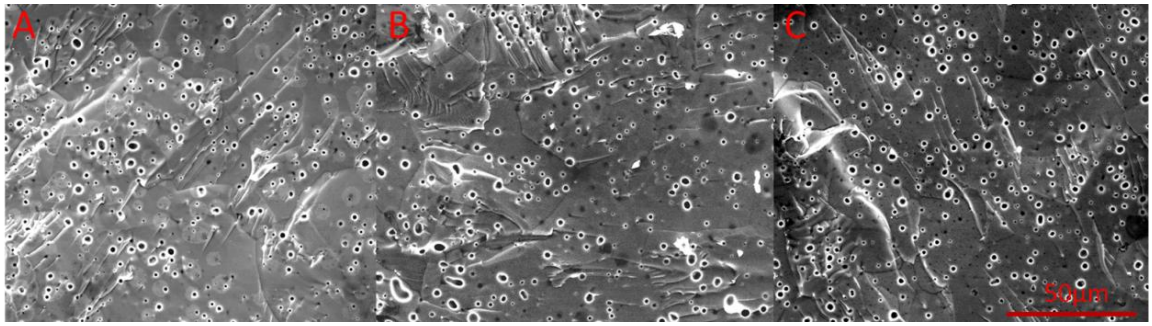

Figure 4.30 Typical fracture sufaces of BSCF at different temperatures: (A)200 ℃; (B)400 ℃; (C)600 ℃

4.2.1.4 Discussion

As mentioned above, there is little difference in flaw distributions between these two methods. In addition, compared with the examination of fracture surfaces obtained from ring-on-ring bending tests, the failure origins of the specimens broken by three-point bending tests were much more convenient to be examined.

Figure 4.31 shows the character of a failure origin of each sample carried out by three-point bending tests at RT and 800 ℃. Fractography analysis is performed on the fracture surface of BSCF indicated by an arrow in Figure 4.31. A capital letter with an arrow refers to the character of a fracture origin; *P*, *E* and *C* correspond to a pore, edge fracture and surface crack. The origins of failure were also observed in Figures 4.32 and 4.33. Fracture surfaces of all the specimens were carefully investigated by SEM. For each case, fracture positions always initiated on or near the tensile side of specimens. In the three-point bending tests, the specimens were transversely divided into two pieces at the point of loading. This large pore, near the tensile face, acted as a stress concentrator and led to a failure of the specimen, because the region surrounding the fracture origin was smoother than the remainder of the surface and fracture lines emanated from the large pore as shown in Figure 4.32

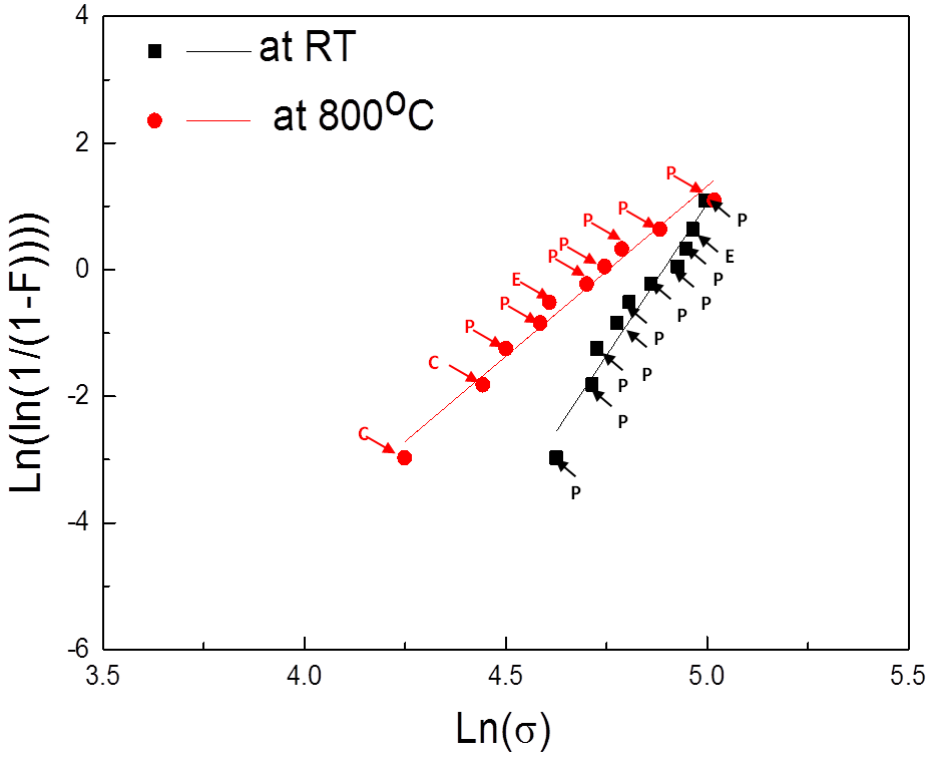

Figure 4.31 Point out the character of a failure origin of each sample carried out by three-point bending tests at RT and 800 ℃

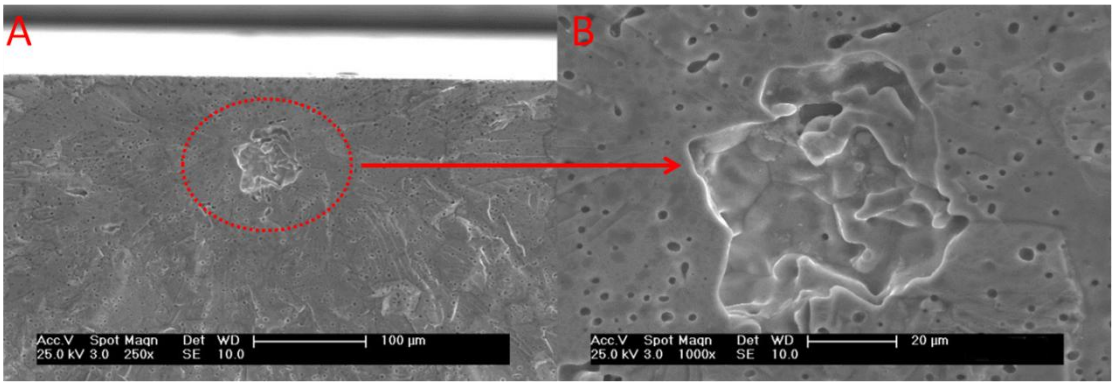

Figure 4.32 Fracture origin of BSCF carried out by three-point bending tests at RT.

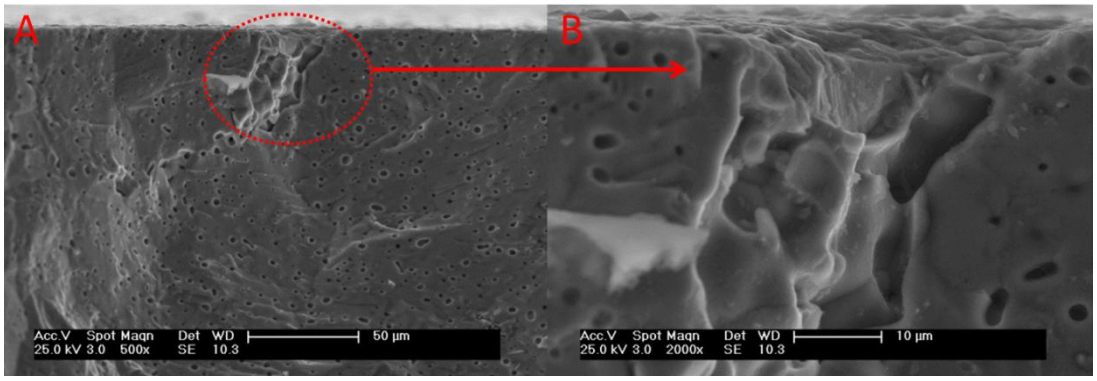

Figure 4.33 Fracture origin of BSCF carried out by three-point bending tests at 800 ℃.

The sizes of fracture origins at both temperatures were porous regions with extension 40–80 μm, as shown from selected fractography in Figure 4.32 and 4.33. This is different from the maximum defect size (56 μm) measured on the sintered body surface in Figure 4.34. In addition, the pore size distributions between the maximum and minimum fracture strengths of the specimens are similar in Figure 4.34(B). The maximum defect size (56 μm) measured is lower than the maximum fracture origins observed from fracture surface (～80 μm). This disagreement might be ascribed to a relatively small area (1 mm^2) used for counting defects on the sintered body surface. According to the model proposed by Quinn[239], the effective area of a flexural BSCF sample by the three-point bending test at RT can be determined to be 3.62 mm^2 with Weibull modules of 9.6 in this study. It is necessary to enlarge the examination area for counting defects to discover those contributions to the fracture of flexural samples of the employed specimen size. It is useful to extrapolate the defect frequency data to the larger defect size region to estimate the maximum defect size possibly existing in the flexural sample. The number of defects at a given size was recalculated per 1 mm^2. Note that the number of defect sizes also depends on the range for counting and is normalised by dividing it by the employed counting range, 1μm. The result is shown in Figure 4.35. The defect frequency corresponding to the flexural sample is determined to be 0.31, statistically (One defect for the effective surface areas 3.62 mm^2; 1/3.62=0.28). And the resultant defect size is 80 μm. This gives a relatively acceptable defect size, although more detailed observations are needed for this defect frequency.

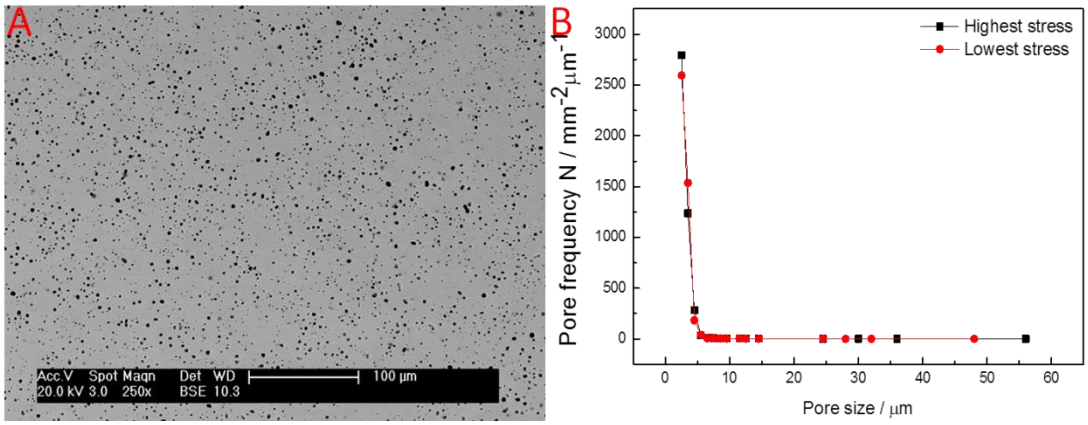

Figure 4.34 (A) Typical low magnification SEM micrograph of BSCF sintered at 1100 ℃ for 10 hours; (B) Histogram of the pore size distributions of BSCF samples with highest stress and lowest stress.

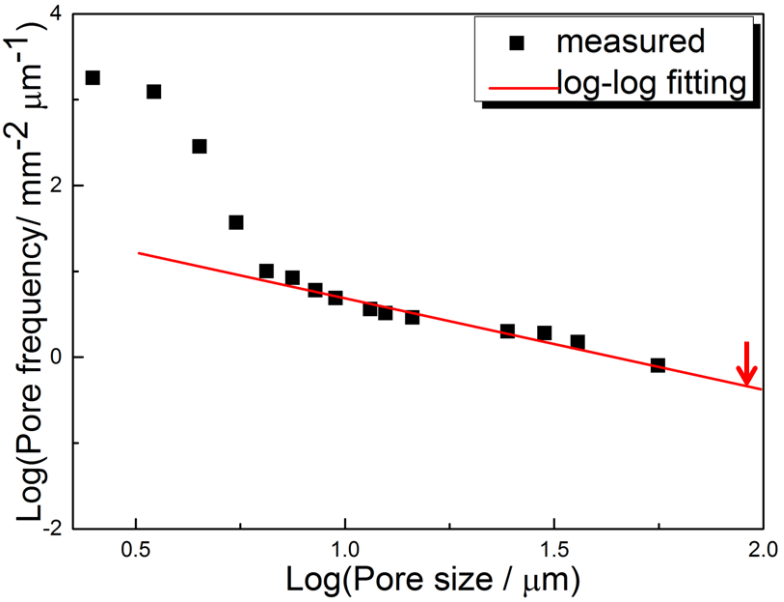

Figure 4.35 Defect size estimation for a large area measured from BSCF sintered at 1100 ℃ for 10 hours. Arrow indicates the estimated largest defect size corresponds to the effective surface area of BSCF.

4.2.2 Hardness

4.2.2.1 Indentation size effect

The micro-indentation test by a Vickers tip is affected by the pore of the BSCF, but it mainly shows well defined indentation with cracks from the four corners. The samples sintered at 1100 ℃ for 10 hours were used in this part. Figure 4.36 shows SEM micrograph of BSCF with indentation under different loads. The size of indentation

increases with increasing the applied load. Figure 4.37 shows the typical indentation of BSCF under the applied load 10 N.

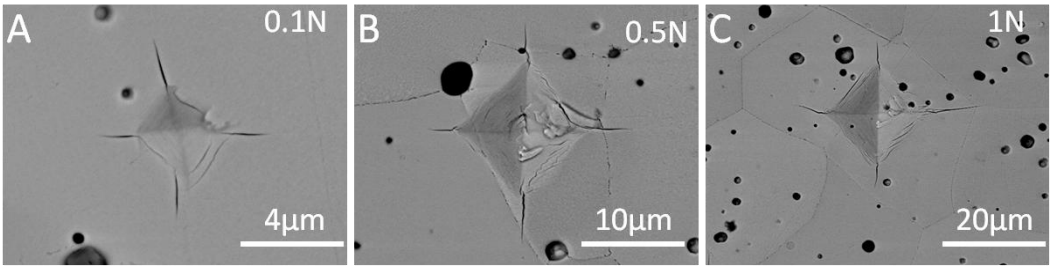

Figure 4.36 SEM micrograph of BSCF with indentation under different loads: (A) 0.1 N; (B) 0.5 N; (C) 1 N.

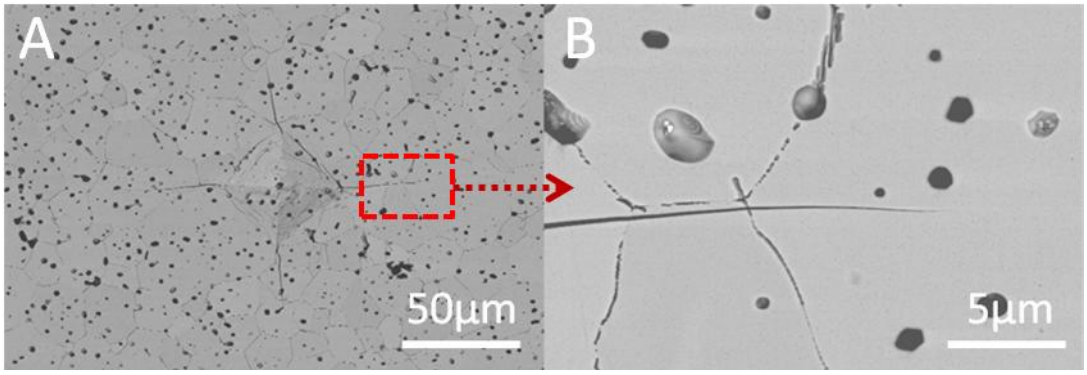

Figure 4.37 SEM micrographs of BSCF with indentation under 10 N (A) and high magnification bottom corner of the indentation (B).

The hardness of BSCF is determined from the load-displacement curves as shown in Figure 4.38. The hardness decreases with increasing the applied load. As previously introduced, this is well-known as the indentation size effect (ISE)[148]. This phenomenon is typically observed in single crystals with various types of bonding, including ionic, metallic and covalent[147, 148]. The indentation size was related to surface effects[149], the strain gradient effects[150-152], the structural non-uniformity of the deformed volume[153], the change in the contribution of the elastic and plastic deformation at the indentation[147], the friction between the indenter and the sample[154]. Although the dependence of hardness and toughness on grain size have been reported for nanocrystalline ceramic, the volume fraction of grain boundary for normal material (grain size>1 μm) is very small[244]. Therefore, both the surface effect

and the strain gradient effect are recognised to contribute the indentation size effect[149, 150].

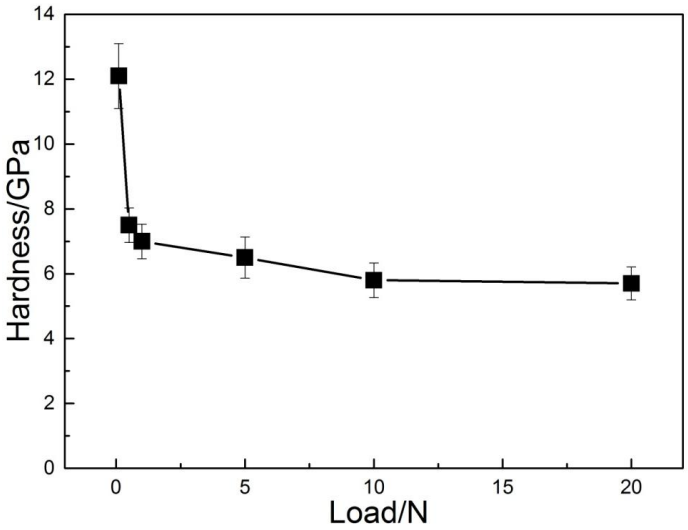

Figure 4.38 Hardness of BSCF determined by Vickers indentation as a function of applied load. For each load 10×10 indentations were used.

4.2.2.2 Effect of grain size on hardness

The porosities of BSCF samples sintered at 1100 ℃ for different periods of time (from 5 to 100 hours) were very similar (5%) while the average grain size of these samples showed a range from 18.0 to 35.2 μm [Figure 4.39(A)]. As shown in Figure 4.39(B), there appears to be a small linear dependency of the indentation hardness of sintered BSCF samples on the inverse square root of the grain diameter, $1/\sqrt{D}(\mu m^{-\frac{1}{2}})$, [$R^2$ (coefficient of determination) =0.35]. In view of this poor correlation coefficient and the very small implied linear coefficient [Figure 4.39(B)], it is apparent that the hardness values of the sintered BSCF samples in this study are probably independent of grain size.

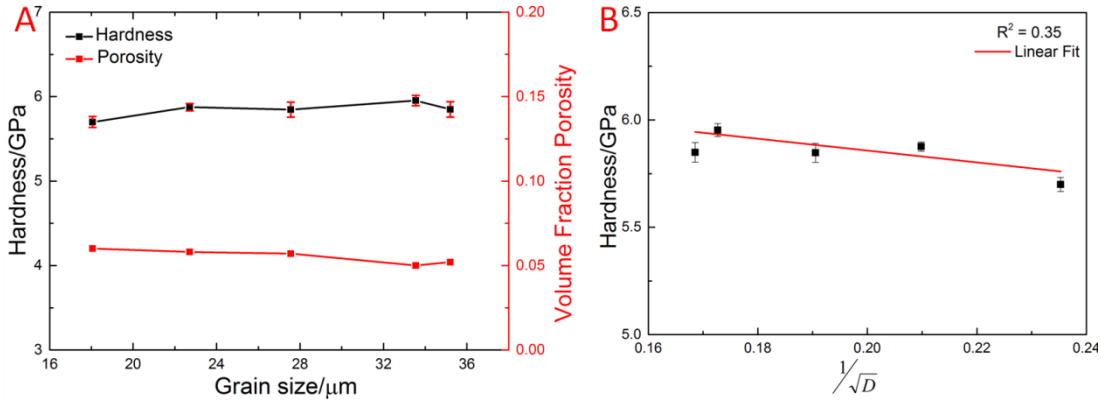

Figure 4.39 (A) The indentation hardness under 10 N and volume fraction porosity as a function of the average grain sizes of BSCF samples sintered at 1100 ℃ from 5 to 100 hours; (B) The indentation hardness as a function of the inverse square root of the grain size. Note that there is no clear trend of hardness as a function of grain size

4.2.2.3 Effect of grain orientation on hardness

Figure 4.40(A) shows the EBSD map of the area on the sample sintered at 1100 ℃ for 10 hours where indentations were made. The orientation of the individual grains is plotted, with the colour coding representing their crystallographic orientation with respect to surface normal in the inverse pole figure displayed in the inset. The black areas in the image, which are not indexed in the EBSD orientation maps, correspond to pores and indentations. One matrix of the indentation impressions has been framed with white dotted lines.

As seen in Figure 4.40(B), there is no substantial difference in depths of penetration into the surface and the nearly 80 load-displacement curves are overlapped. This indicates that the hardness shows no clear correlation with the crystallographic orientation.

For the BSCF samples, the values of indentation hardness were chosen from the indentation on pore-free surface area and away from grain boundaries as shown in Figure 4.40(A). In this way, the effect of the pores on the indentation hardness is less critical. The average indentation hardness under the 100 mN loading is 12.1±0.48 GPa, which is much larger than the average indentation hardness under a 10 N load, this

increase is believed to be due to indentation size effect[225, 245]. The deviation among the measured values is very small (less than 4%). Therefore, there is no significant influence of grain orientation on indentation hardness

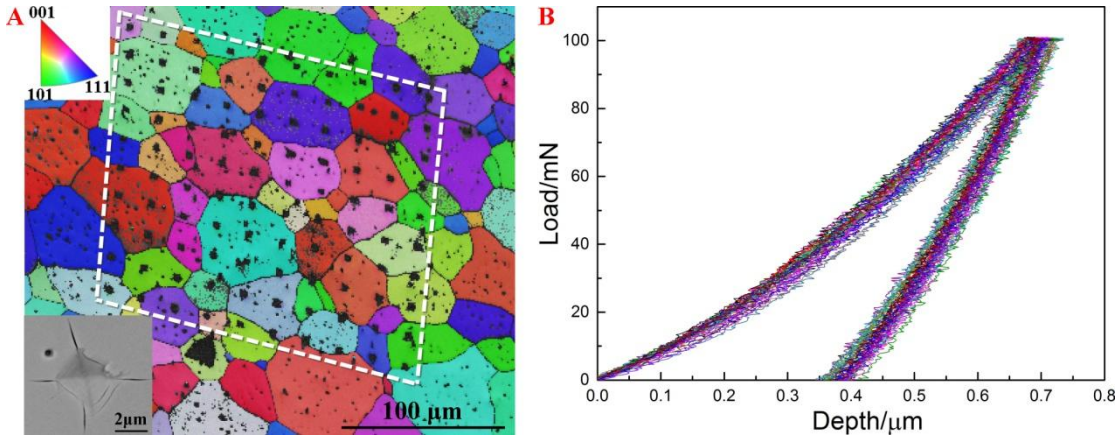

Figure 4.40 (A) Micro-indentation test under the loading 100 mN with EBSD mapping; typical SEM image of selected indentation impression without surface pores and not near grain boundary shown on the bottom left. (B) Comparison of load-displacement curves of different indentations selected above

4.2.2.4 Effect of porosity on hardness

Samples of BSCF sintered from 900 to 1150 ℃ for 10 hours were used to investigate the effect of porosity on hardness. The volume fraction of porosity ranged from about 0.05 to 0.27, with the average grain size ranging from approximately 1.52 to 64.8 μm.

The indentation hardness of the sintered BSCF samples prepared in this study is a strong function of the volume fraction porosity, as displayed in Figure 4.41(A). The dependence of hardness on porosity is consistent with the Minimum Solid Area (MSA) model that has been proposed by Rice[157, 158]. For hardness, the MSA model can be represented by[158]

$$H_{IT} = H_0 exp(-bp) \tag{4.22}$$

where H_{IT} is the measured indentation hardness, H_0 is the indentation hardness value corresponding to a specimen with zero porosity, b is a material constant and p is the volume fraction porosity of the specimen.

The hardness-porosity relationship [Equation (4.22)] can also be written in a linearised form such that

$$ln(H_{IT}) = -bp + ln(H_0) \quad (4.23)$$

where H_0 is the indentation hardness of the sample with zero porosity. The linear fit to Equation (4.23) yielded values of 7.05±0.94 GPa for H_0 and 3.40±0.42 for the constant b, with a R^2 value of 0.954. The zero-porosity value of indentation hardness H_0, 7.85±0.87 GPa was obtained from the literature values [109, 111] by the linear regression analysis exceeded indentation hardness (H_0=*7.05 GPa*) measurements on the BSCF samples in this study, this is believed to be caused by indentation size effect [225, 245], because literature values used 1 N loading for hardness measurements and this work used 10 N loads in this study.

Figure 4.42(A) shows the indentation hardness of BSCF as a function of porosity. As shown in Figure 4.41(B), the indentation hardness increases rapidly with increasing the sintering temperature from 900 ℃ to 1000 ℃, but above this temperature there is little further change and maybe a small decrease at the highest temperature. This correlates with the porosity decreasing from 0.27 to 0.05. As the sintering temperature increases further the total porosity of the BSCF samples remains practically unchanged and the average grain size increases from 22 to 64.8 μm. However, the indentation hardness shows little change. As previously discussed, the grain size and grain orientation show no clear trend with the values of indentation hardness of BSCF samples. In other words, the total porosity is the dominant factor to determine the values of indentation hardness of BSCF samples.

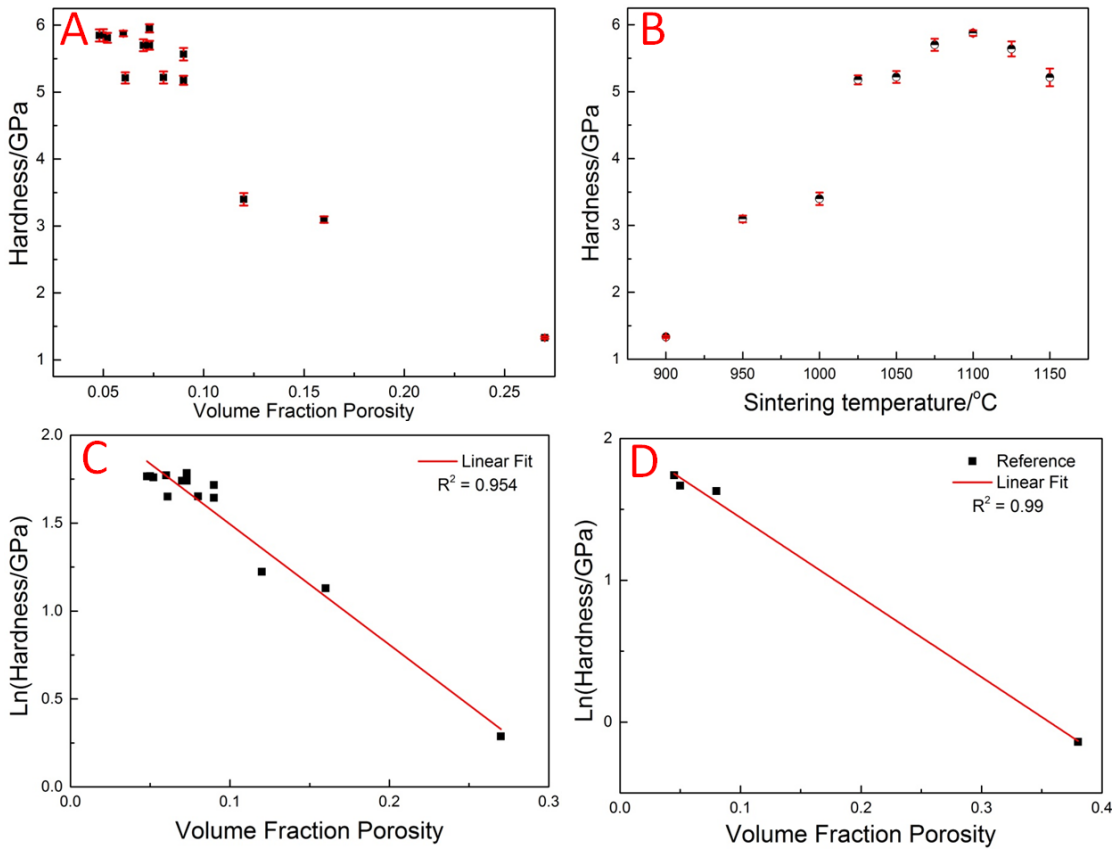

Figure 4.41 (A) Hardness as a function of volume fraction porosity of samples sintered under different conditions; (B) Hardness as a function of various sintering temperature; (C) The lines represent the fit of the individual data sets to Equation(4.23) in this study; (D) The indentation hardness, H_{IT}, as a function of volume fraction porosity, P in the references.

The microstructures of the BSCF samples sintered at 1100 ℃, 1125 ℃, and 1150 ℃ for 10 hours were shown in Figure 4.42. The average pore size is 1.56, 1.62 and 2.51 μm for the BSCF samples sintered at 1100, 1125, and 1150 ℃ for 10 hours, respectively, determined by the Image-pro Plus 6.0 software. The average pore size increases with increasing the temperature from 1100 to 1150 ℃, which is attributed to the "Ostwald Ripening" mechanism[246]: vacancies diffuse away from regions of high curvature (small pores) and sink at the relatively large pores which have low surface curvature, causing them to grow. It has been reported that increasing pore size negatively influences mechanical properties[247]. Therefore, it is possible that the small reduction in hardness is associated with the increase in average pore size; however, further work is needed to confirm this.

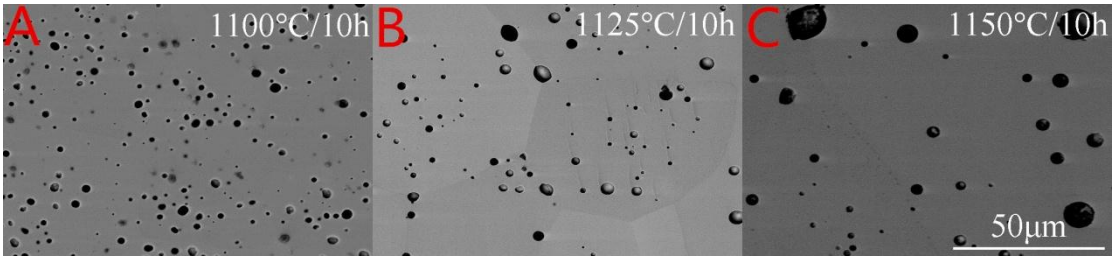

Figure 4.42 The SEM micrographs of BSCF sintered at different temperatures for 10 hours: (A) 1100 ℃; (B) 1125 ℃; (C) 1150 ℃

4.2.3 Young's modulus

4.2.3.1 Uniaxial and biaxial bending tests

The Young's modulus of BSCF was measured between RT and 800 ℃ by three-point and ring-on-ring bending tests in Figure 4.43. Both testing configurations produced broadly similar results with a Young's modulus obtained in the range from 63 to 65 GPa at RT. With increasing temperature, a sharp reduction in Young's modulus occurs with a minimum at 200 ℃. This is followed by an increase in the value up to 400 ℃, followed by a gradual decrease to 800 ℃ with the Young's modulus at 800 ℃ around 0.71 of the RT value. This behaviour is observed with both testing configurations. For most ceramics, the Young's modulus decreases with increasing the temperature. This anomalous behaviour of BSCF with an intermediate minimum value has been attributed to the spin transition of Co^{3+}[138]. The temperature dependence of Young's modulus obtained from these two different configurations are similar with those obtained from Huang *et al*.[19] as shown in Figure 4.44.

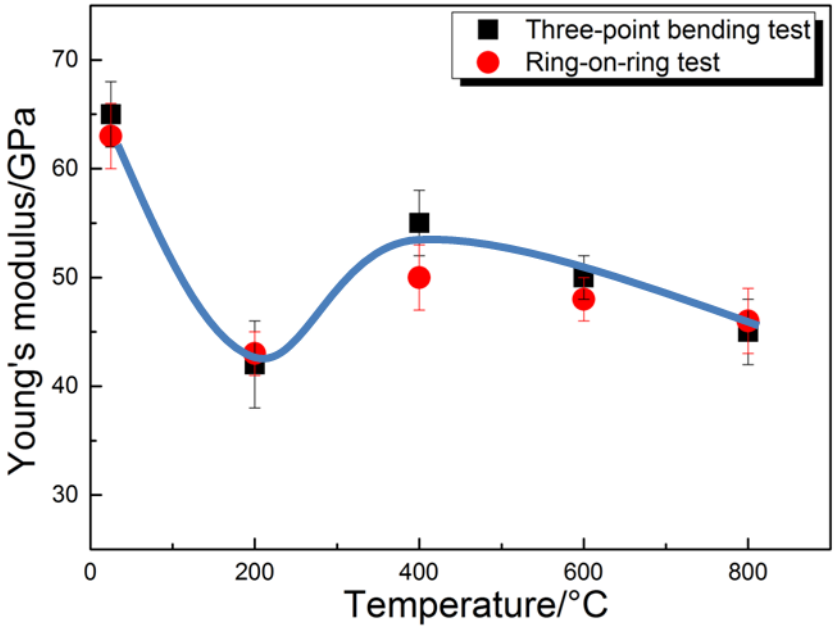

Figure 4.43 Young's modulus of BSCF determined by three-point ring-on-ring bending tests as a function of temperature between RT and 800 ℃. The line is a guide to the eye.

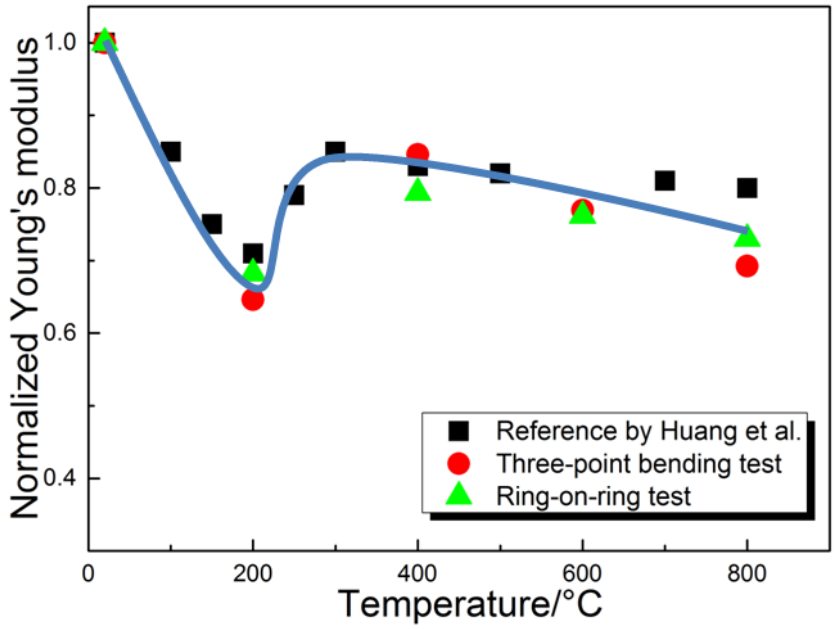

Figure 4.44 Young's modulus normalised regarding the value measured at RT as a function of temperature between RT and 800 ℃ determined by different methods and compared to the values determined by Huang *et al.*[19]. The line is a guide to the eye.

4.2.3.2 Micro-indentation

Figure 4.45 shows Young's modulus of BSCF as a function of sintering temperature (A) and porosity (B). The variation of the Young's modulus as a function of the sintering temperature is due to the influence of porosity. The measured Young's modulus

decreases with the increase in the relative porosity. The Young's modulus of the porous sample is expressed by[248]:

$$E_{IT} = E_0 \cdot exp(-bp) \quad (4.24)$$

where E_0 is the Young's modulus of the fully dense material, p is volume fraction of the porosity and b is an empirical constant ranging between 2 to 5. The Young's modulus-porosity relationship can also be written in a linearised form such that

$$ln(E_{IT}) = -bP + ln(E_0) \quad (4.25)$$

According to Figure 4.45(B), the linear fit to Equation (4.25) yielded values of 105.6±2.05 GPa for E_o and 4.18±0.29 for the constant b, with a R^2 value of 0.950. However, the values of E_0 and b are much higher than those obtained from other groups possibly due to indentation size effect and differences in the processing of the samples. The indentation Young's modulus measured in this study (80 GPa) is consistent with that value obtained from Malzbender *et al*. (78 GPa)[113]. The Young's modulus value as a function of temperature [Figure 4.45(A)] follows a similar trend to the microhardness data [Figure 4.41(B)] and these are probably related.

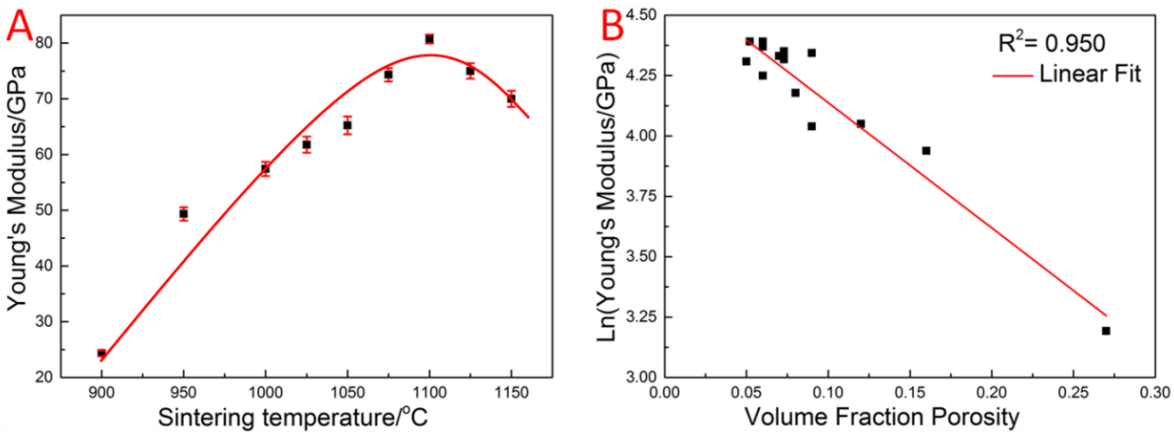

Figure 4.45 (A) Young's modulus of BSCF as a function of sintering temperature; (B) Young's modulus as a function of porosity

4.2.4 Fracture toughness

4.2.4.1 In-situ observation of crack growth in BSCF with annealing

The BSCF samples sintered at 1100 ℃ for 10 hours were used to investigate in-situ observation of crack growth with annealing. Before annealing, each sample was indented with a 10 N load at RT in air to nucleate cracks from the corner of each indentation.

The samples were subsequently tested between RT and 800 ℃, with a heating rate and cooling rate of 10 ℃/min, and the crack length measured. Up to a temperature of 100 ℃, there was no crack growth, as the temperature increased to 200 ℃ the crack grew approximately 12 μm as observed in Figure 4.46. After that, no further crack growth was observed up to 800 ℃. This crack growth occurred during the heating stage with no crack growth observed during cooling. After five further cycles of heating up and cooling down process, there was no crack growth in Figure 4.47.

Because there is no external load, there are several other driving forces for crack growth. The first possible driving force is the residual stress induced by phase transformation when the temperature increases. This phenomenon can be observed in other ceramic materials[249]. But according to the high temperature XRD patterns [242, 250], no other phase can be observed. Therefore, the residual stress induced by phase transformation cannot be the driving force for crack growth.

The second possible driving force is the stress induced by thermal processing. If thermal stress can be the driving force for crack growth, the crack will propagate during the heating or cooling process. However, after five cycles of heating up and cooling down,

no crack growth was observed. Therefore, thermal stress cannot be the driving force for crack propagation.

The third possible driving force for crack growth is the residual stress induced by the indentation. When the samples are annealed at high temperature, the residual stress relaxation drives the crack growth. But when the residual stress is fully relaxed, there is no further driving force for the crack growth up to 800 ℃ or after thermal cycling.

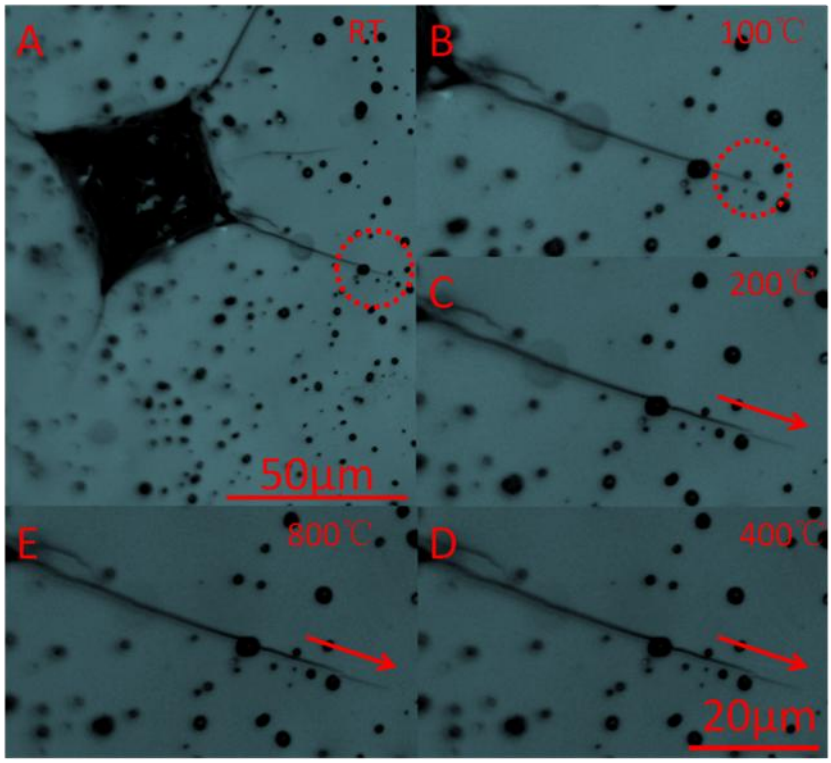

Figure 4.46 In-situ observation of crack growth at different temperatures: (A) RT; (B) 100 ℃; (C) 200 ℃; (D) 400 ℃; (E) 800 ℃

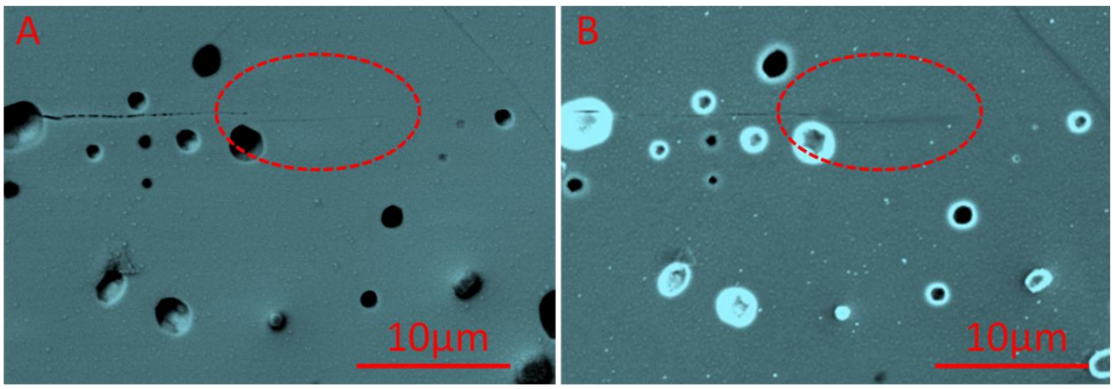

Figure 4.47 No crack growth was observed with comparison of before (A) and after 5 cycles (B) heating procedure.

4.2.4.2 Crack shape determination

The BSCF samples sintered at 1100 ℃ for 10 hours were used to determinate crack shape. The calculation of Vickers indentation fracture toughness must be determined from the crack profile under the indenter, whether the cracks are of the Palmqvist mode or median-radial mode, which are illustrated in Figure 4.48. The median-radial cracks are formed by the joining of radial cracks, as shown in Figure 4.48(A), while the Palmqvist crack system is always shallow and the two correspondent radial cracks are separated from each other as displayed in Figure 4.48(B).

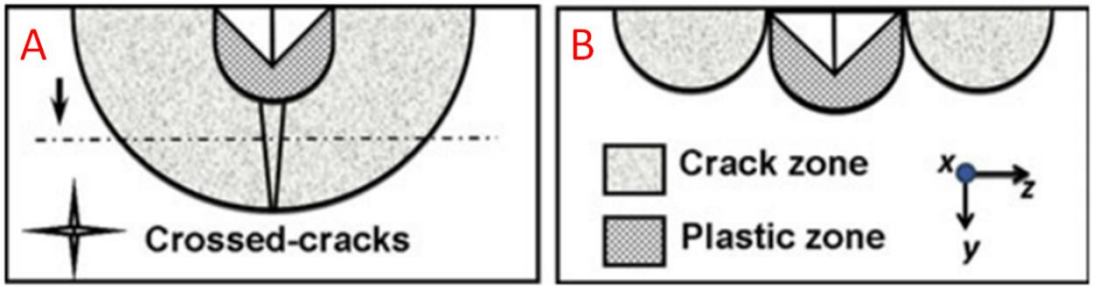

Figure 4.48 Cross-section view of Vickers indentation: (A)median-radial crack shape; (B) Palmqvist crack shape[251]

Figure 4.49 show the cross-section of the indentation of BSCF under a load 10 N. In order to observe the crack impression under the indenter on the polished external surface, an indentation as in Figure 4.50(A) with a final indentation depth of 9.7 μm was sequentially polished with 6 μm diamond plate and was fined with 1 μm as well as 0.25 μm diamond plate. At first, the surface was polished off the indentation. Then the plastic deformation zone was exposed together with the radial cracks after polishing off 15 μm as shown in Figure 4.50(B). Afterward polishing off 20 μm until the plastic deformation zone was completely removed as shown in Figure 4.50(C). If the crack shape is Palmqvsit mode, no crack can be observed after removing the plastic zone of indentation. Therefore, the surface showed that radial cracks crossed over each other as illustrated in Figure 4.50(C), which confirms the presence of median-radial mode cracks

under 10 N loading with the Vickers indenter.

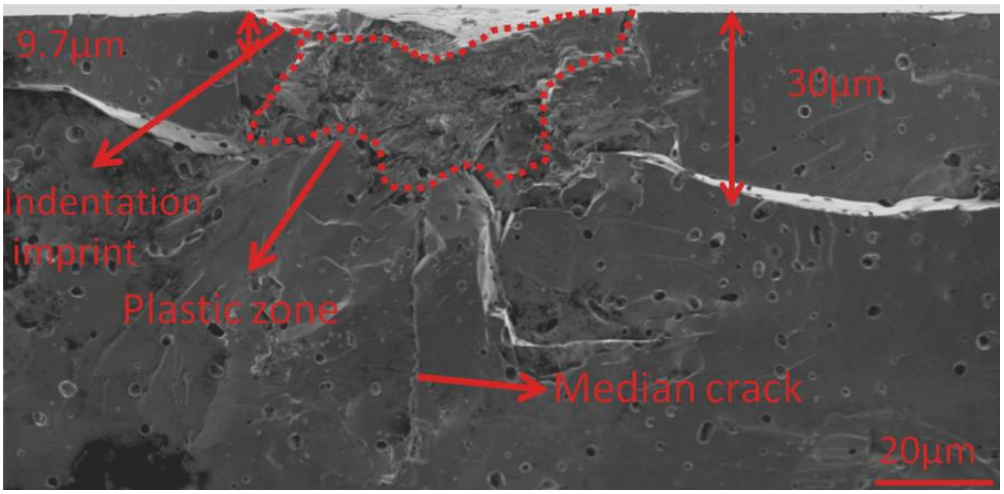

Figure 4.49 The cross-section of indentation under 10 N

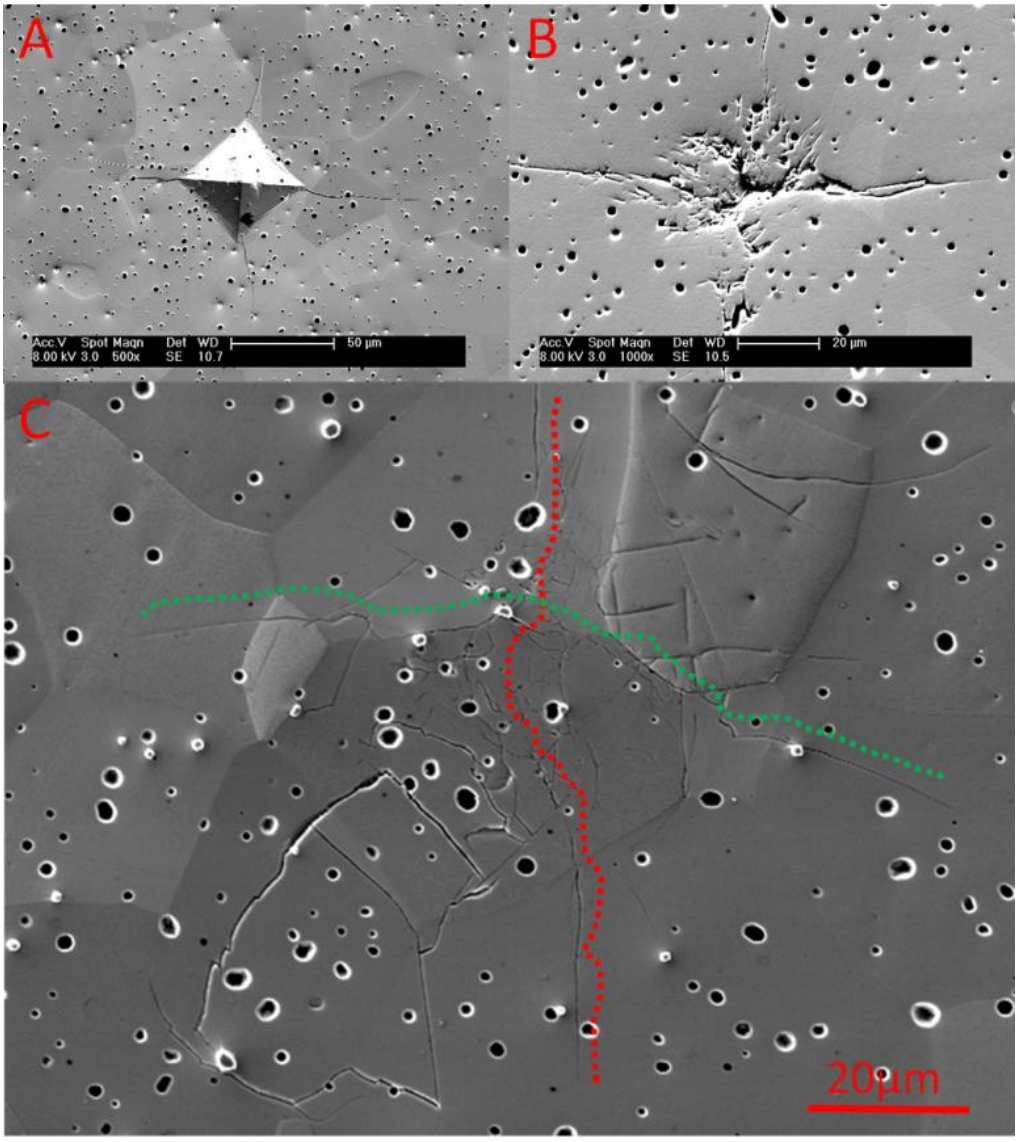

Figure 4.50 (A) The original indentation under 10 N; (B) image after removal of indentation impression; (C) image after removal of the plastic deformation zone.

The five polished samples showed the same crack propagation mode, and this is consistent with previous reports where a median-radial crack system has been observed in BSCF under 10 N loading[109].

4.2.4.3 Effect of annealing on fracture toughness

The BSCF samples sintered at 1100 ℃ for 10 hours were used to measure the fracture toughness determined by the indentation strength method. The fracture toughness can be calculated by [165]

$$K_{IC} = 0.59(\frac{E}{H})^{\frac{1}{8}}[\sigma_f p^{\frac{1}{3}}]^{\frac{3}{4}} \quad (4.26)$$

where *E* Young's modulus; *H* hardness; σ_f fracture stress; *P* indentation load

According to the research of Chantikul *et.al*[188], uncertainties in the values of *E/H* are relatively unimportant. Indeed, since this ratio varies only between 10 and 50 for most ceramics, replacement of $0.59(\frac{E}{H})^{0.125}$ by an averaged quantity would add no more than 10% to the error in the K_{IC} evaluation for a material whose elastic/plastic parameters are totally unknown[188]. Additionally, the value of fracture toughness from indentation strength method was less than 5% different from that measured using the standard indentation technique at room temperature[109]. In other words, these two methods are in good agreement with each other for BSCF.

Figure 4.51 shows fracture toughness of BSCF as a function of temperature and comparison of them with and without annealing. The fracture toughness of BSCF with or without annealing as a function of temperature shows a similar trend to fracture stress [Figure (4.23)]. There is a small decrease in fracture toughness with annealing at all test temperatures. From the literature, there are several proposed mechanisms for the effect of annealing on fracture toughness, including phase transformation[181], twinning[252]

and domain switching[253]. However, in the case of BSCF, none of these three phenomena can be observed. It has been reported by Paulik *et al.*[172] that the fracture toughness of $La_{0.8}Ca_{0.2}CrO_{3-\delta}$ depends on the distribution of oxygen vacancies in the lattice. According to the TG curves in the Figure 4.52, the weight loss can be observed. As previously mentioned, the weight loss suggests the oxygen release from the lattice and more oxygen vacancies formation. Therefore, this may be a possible reason for the reduction in fracture toughness of BSCF with annealing. Additionally, cracks may grow during annealing as discussed earlier. In this way, the fracture stress reduces as the crack becomes longer. However, this cannot explain the reduction in fracture toughness. In addition, when all the samples are tested at high temperatures, they will become homogenous. With the temperature increasing, the effect of annealing on fracture toughness gradually reduces. According to the Equation (4.26), fracture toughness increases with increasing fracture stress. Therefore, annealing causes the release of residual stress, thereby forcing the crack growth and reducing the fracture stress.

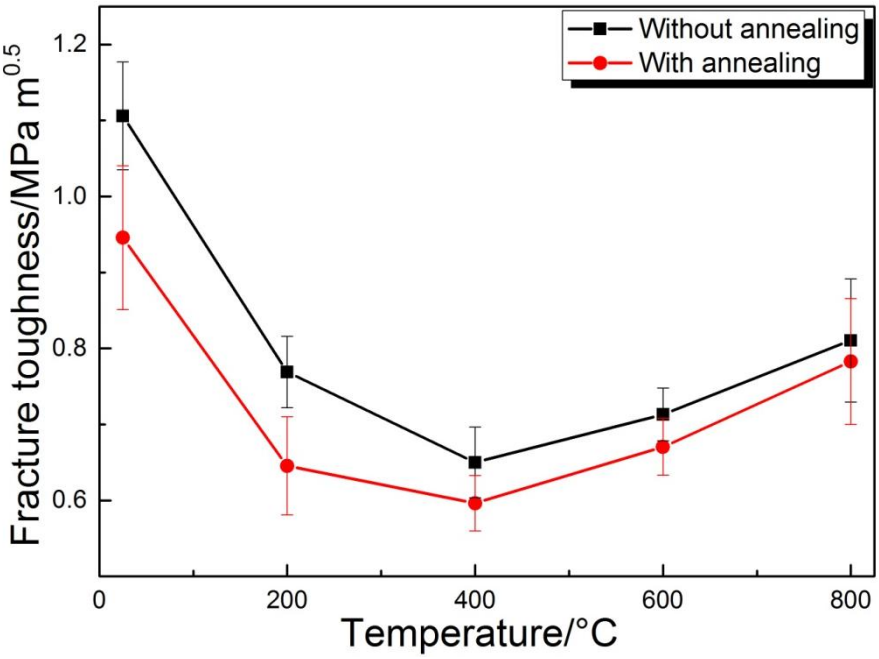

Figure 4.51 Fracture toughness of BSCF sintered at 1100 ℃ for 10 hours as a function of temperature. Comparison of fracture toughness of BSCF between with and without annealing.

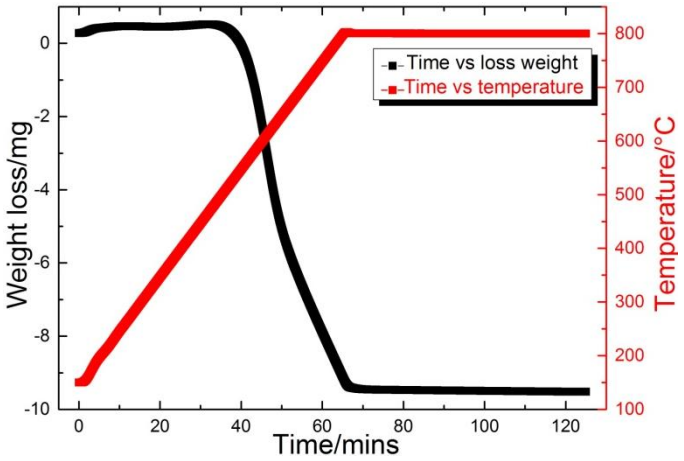

Figure 4.52 TG data of BSCF

4.2.4.4 Effect of grain size on fracture toughness

The samples of BSCF sintered at 1100 ℃ from 5 to 100 hours were used to investigate the effect of grain size on the fracture toughness determined by indentation crack measurement method. Figure 4.53 shows fracture toughness of BSCF as a function of grain size. It is clearly observed that fracture toughness seems to be constant. According to the Figure 4.37, no significant crack deflection or grain bridging was observed, and the crack propagation was mainly transgranular, which was consistent with observations of the fracture surface in Figure 4.30. This suggests that the fracture is controlled by bond strength rather than grain boundaries for BSCF. In other words, fracture toughness of BSCF is independent of grain size.

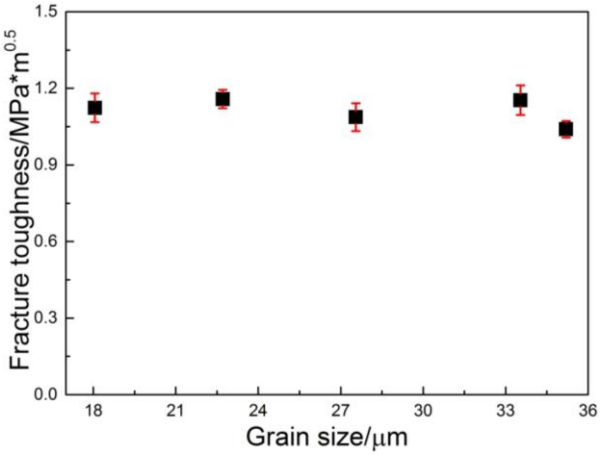

Figure 4.53 Fracture toughness of BSCF sintered at 1100 ℃ from 5 to 100 hours as a function of grain size.

4.2.4.5 Effect of porosity on fracture toughness

The indentation crack measurement method was used to investigate the effect of porosity on the fracture toughness of BSCF, with samples sintered from 900 ℃ to 1150 ℃ for 10 hours. The value of fracture toughness can be easily determined from indentation-induced crack length [128]:

$$K_{ind} = \chi \frac{F}{C_0^{1.5}} \tag{4.27}$$

where C_0 is the crack length and $\chi=0.016(\frac{E}{H})^{0.5}$ represents the elastic-plastic behaviour. Furthermore, Young's modulus E and hardness H are also directly accessible from the depth sensitive indentation test.

Porosity is well-known to reduce fracture toughness. According to Rice's model, it has been shown that the intrinsic toughness can be associated with the measured toughness:

$$K_{IC} = {K_{IC}}^0 exp(-bp) \tag{4.28}$$

where K_{IC} and ${K_{IC}}^0$ are the measured and intrinsic toughness (zero-porosity), respectively; p is the porosity and b is a constant. It has been reported that the value of b for fracture toughness are between 2 and 5 for many ceramics that have been fabricated by different methods.

Figure 4.54(A) shows fracture toughness of BSCF as a function of sintering temperature. It is clearly observed that fracture toughness increases with increasing sintering temperature due to the decrease in porosity between 900 ℃ and 1100 ℃. Then fracture toughness deceases with increasing the temperature up to 1150 ℃. This is similar to the changes in all the mechanical properties measured earlier and the only observed change in microstructure is an increase in pore size as mentioned previously. The intrinsic fracture toughness can be estimated from the linear fit of the data in Figure 4.54(B) to

obtain the value of 1.49±0.11 MPa $m^{0.5}$, and 2.49±0.34 for the constant b, with a R^2 value of 0.959.

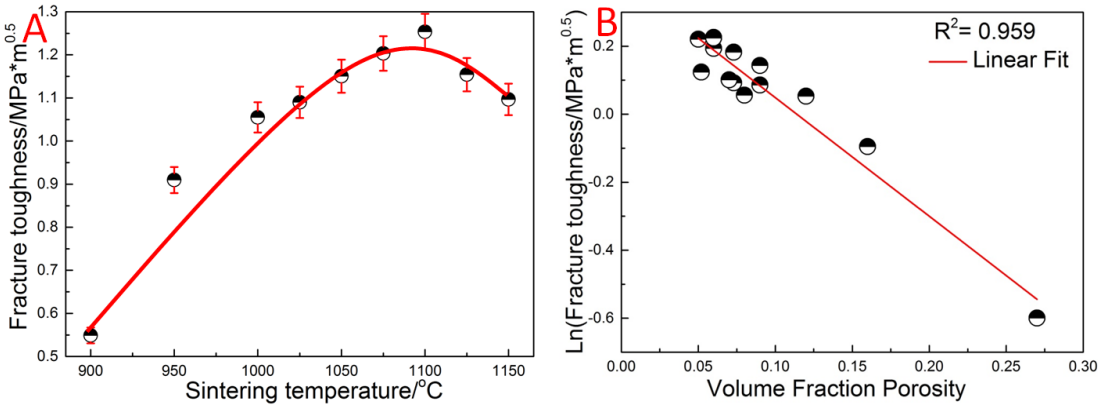

Figure 4.54 (A) Fracture toughness of BSCF as a function of sintering temperature; (B) Fracture toughness as a function of porosity

Figure 4.55 shows relative Young's modulus (E/E_0) and relative fracture toughness (K_{IC}/K_{IC}^0) as a function of porosity. Although *E* and K_{IC} have the same dependence on porosity following an exponential relationship as proposed by others[158, 162], the fracture toughness decreases with porosity more moderately than Young's modulus. This is possibly caused by the fact that pores result in crack blunting and microcracks can be regarded as obstacles during fracture.

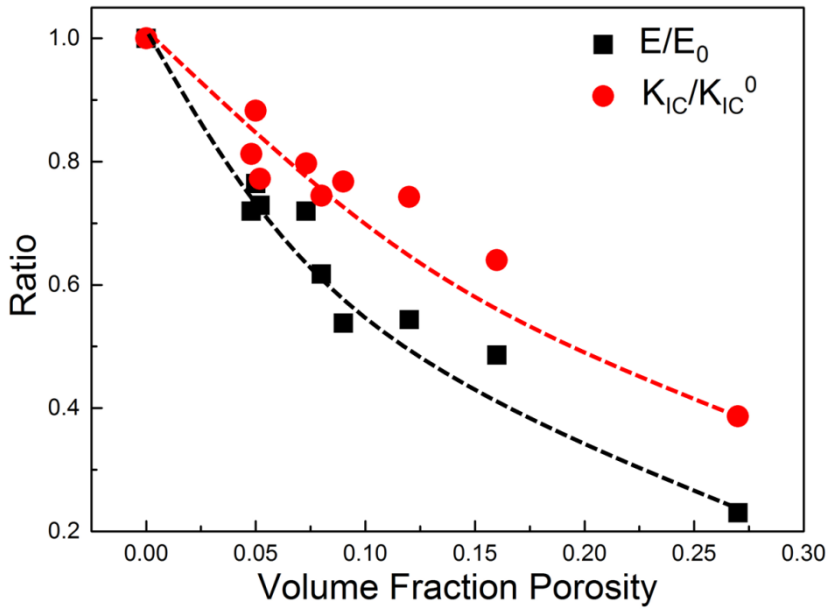

Figure 4.55 Relative Young's modulus E/E_0, relative fracture toughness K_{IC}/K_{IC}^0 as a function of porosity. The lines are a guide to the eye.

4.2.5 Subcritical crack growth

BSCF samples sintered at 1100 ℃ for 10 hours are used to investigate subcritical crack growth behaviour at room temperature and 800 ℃. A constant load method (ring-on-ring bending tests) was used to investigate different crack growth rates at room temperature. A constant stress rate method (ring-on-ring bending tests) was used to study the subcritical crack growth at 800 ℃. The results are discussed and correlated to a SCG model. The parameters of the model are determined. The strength-probability-time diagrams at RT and 800 ℃ are also plotted for design purposes.

4.2.5.1 Determination of subcritical crack growth parameters at room temperature

The subcritical crack growth (SCG) behaviour is often characterised by the dependence of the crack velocity(v), on the mode I stress intensity factor K_I, as expressed by the empirical power relationship[220]:

$$v = \frac{\Delta c}{\Delta t} = A_0 (\frac{K_I}{K_{IC}})^n \tag{4.29}$$

where A_0 and n are constant for a given material, and K_{IC} is the critical stress intensity factor or the fracture toughness of the material. K_I is determined as follows [220]:

$$K_I = Y\sigma\sqrt{c} \tag{4.30}$$

where $$\sigma = \frac{3P}{2\pi {t_h}^2}[(1+\nu)\, ln\left(\frac{r_2}{r_1}\right) + \frac{1-\nu}{2}\left(\frac{{r_2}^2 - {r_1}^2}{{r_3}^2}\right)] \tag{4.31}$$

Figure 4.56 shows a schematic indentation impression (A) and a SEM image (B) of an indentation impression made on a BSCF sample under a maximum load of 10 N. Figure 4.57 shows that a crack tip propagated 6.0 μm at the stress intensity factor 0.681

MPa $m^{0.5}$ during 1 hour, and the crack rate was 1.67×10^{-9} m/s.

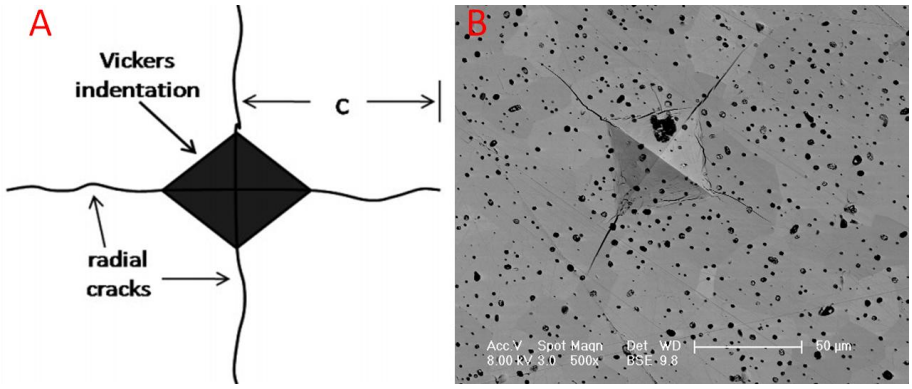

Figure 4.56 (A)Schematic indentation impression[225]; (B)SEM image of indentation impression

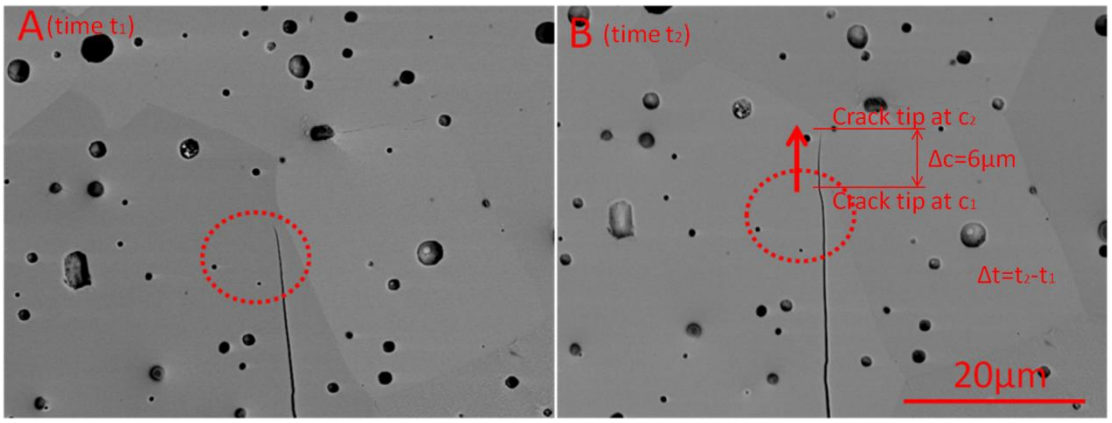

Figure 4.57 (A) The image of crack tip at time t_1; (B) The image of crack growth under constant loading at time t_2

The results obtained by ring-on-ring tests are represented in Figure 4.58. Above the stress intensity factor 0.76 MPa $m^{0.5}$, the crack growth rate is too fast to capture, and finally the samples are fractured. When the applied stress intensity factors of K_I is between 0.55 and 0.75 MPa $m^{0.5}$, a detailed measurement over a wide range of crack velocities has been conducted. Further reduction of the applied stress intensity factor down to 0.54 MPa $m^{0.5}$, led to no crack propagation even after two weeks. As mentioned previously, the maximum length of time is 14 days for the test procedure, so the threshold values are proposed based on the assumption that crack velocities higher

than 10^{-13}~10^{-14} m/s are detectable with the experimental procedure used. Nevertheless, further crack propagation might take place after sufficiently long time but this lies below the detection limit of the method used. For most oxide ceramics, it is believed that[195, 254] stress corrosion by water at the crack tip is the mechanism that is responsible for slow crack propagation at room temperature. The value of the exponent n [Equation (4.29)] is known as the fatigue susceptibility parameter. The data in Figure 4.58 yields n=24.3±3.1 with a R^2=0.908, which reasonably agrees with that determined by the constant stress rate method at RT by Pećanac *et al.*[125].

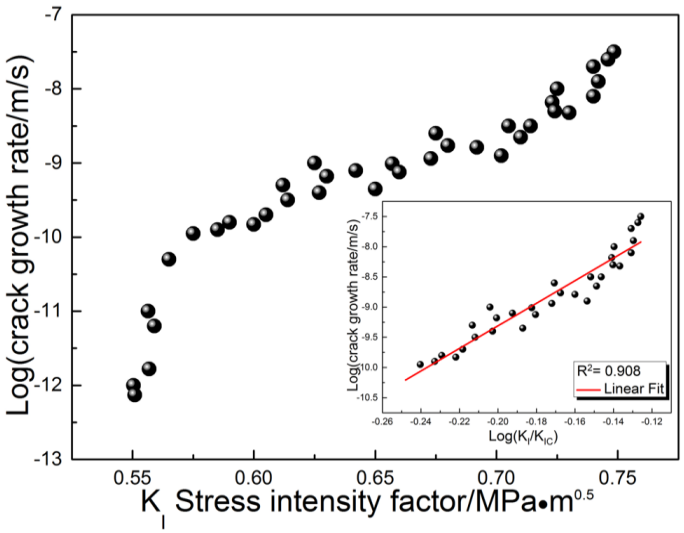

Figure 4.58 Crack growth rate of BSCF as a function of stress intensity factor determined by ring-on-ring bending method.

The scatter of the data of crack growth rate is due to crack blunting and crack branching caused by microstructural defects (e.g. pores), which can induce an increase in crack tip stress intensity factor[255, 256] as illustrated in Figure 4.59.

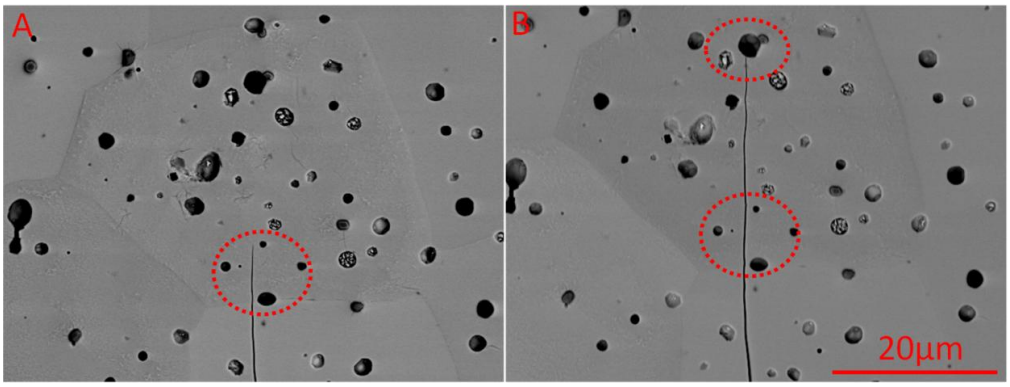

Figure 4.59 Crack blunting was observed when crack propagated at (A) time t_1 and (B) time t_2

When a crack meets a pore in a ceramic material, the crack tip blunts[255]. This decreases the stress intensity at the crack tip and requires an increasing external load to propagate the crack. Therefore, the pores are regarded as barriers for crack growth.

As shown in Figure 4.60, crack branching was observed on the surface when a main crack propagates. It has been reported that crack branching can be the result of many interacting microcracks or microbranches[256]. To be more specific, when a crack propagates in a material containing a great many pores, the crack passes through these pores and some pores can change the crack growth plane[257]. In addition, crack branching also can be caused by the microcracks that are enteirely embedded in the interior of the bulk[256]. Figure 4.61 shows a cross-section of a crack cut through the BSCF sample surface using a FIB. It is clearly shown that crack branching occured in the interior of the bulk.

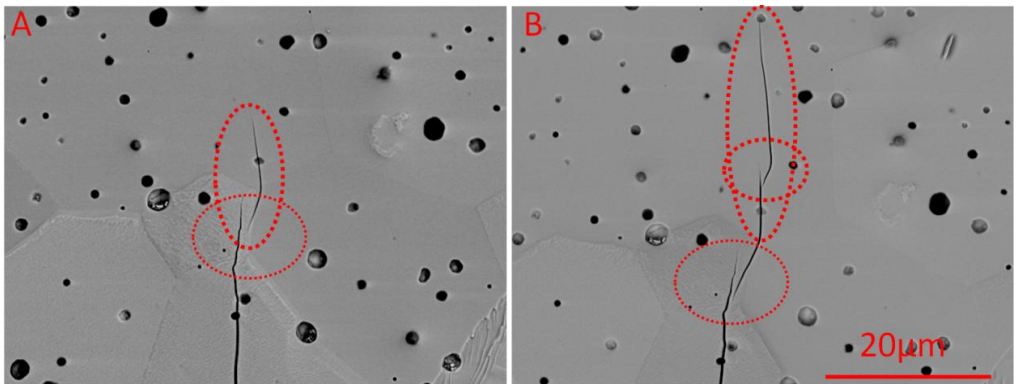

Figure 4.60 Crack cracking was observed when crack propagated at (A) time t_1 and (B)

time t_2

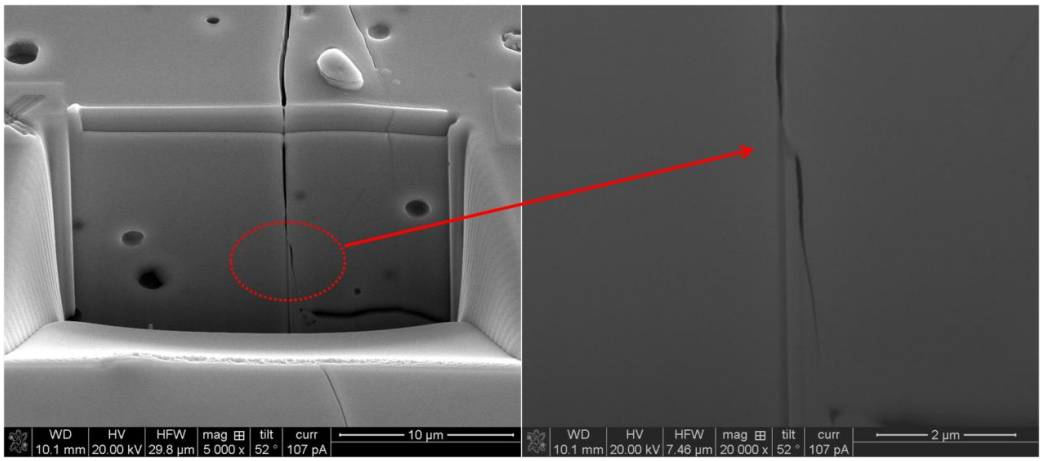

Figure 4 61 Crack branching observed in the interior of the bulk

4.2.5.2 Determination of subcritical crack growth parameters at 800 ℃

The SCG effect can be assessed in a test with a constant stress rate $\dot{\sigma}$, where the fracture stress σ_f is correlated with the stress rate using the equation[197]:

$$log\sigma_f = \frac{1}{n+1} log\dot{\sigma} + logD \tag{4.32}$$

where n and D (Pa/s) are the SCG parameters. The stress rate is calculated from the load-time curve of the specimen tested

$$\dot{\sigma} = \frac{3\dot{P}}{2\pi {t_h}^2}[(1+\nu)\, ln\left(\frac{r_2}{r_1}\right) + \frac{1-\nu}{2}\left(\frac{{r_2}^2-{r_1}^2}{{r_3}^2}\right)] \tag{4.33}$$

where $\dot{P}$ is the load rate (N/s), other parameters have the same meaning as those in Equation (4.3).

The SCG parameters n and D can be obtained by fitting log (fracture stress) against log (stress rates) using a linear regression analysis. The slope of the linear regression line, α, is determined by the following equation [197]:

$$\alpha = \frac{K\sum_{j=1}^{K}(\log\dot{\sigma_j}\log\sigma_j) - (\sum_{j=1}^{K}\log\dot{\sigma_j}\sum_{j=1}^{K}\log\sigma_j)}{K\sum_{j=1}^{K}(\log\dot{\sigma_j})^2 - (\sum_{j=1}^{K}\log\dot{\sigma_j})^2} \tag{4.34}$$

where *K* is the sample size, $\dot{\sigma_j}$ *is* stress rate and σ_j is the fracture stress. The SCG parameter *n* is determined as $n = (1/\alpha) - 1$.

The intercept of the linear regression line is determined by the following equation [197]:

$$\beta = \frac{(\sum_{j=1}^{K} \log \sigma_j) \sum_{j=1}^{K} (\log \dot{\sigma}_j)^2 - \left(\sum_{j=1}^{K} (\log \dot{\sigma}_j \log \sigma_j)\right)(\sum_{j=1}^{K} \log \sigma_j)}{K \sum_{j=1}^{K} (\log \dot{\sigma}_j)^2 - (\sum_{j=1}^{K} \log \dot{\sigma}_j)^2} \quad (4.35)$$

The SCG parameter *D* is determined by $D = 10^{\beta}$

The plot of Equation (4.32), log (fracture stress) vs log (stress rate), is shown in Figure 4.62. The SCG parameters n and D are determined as 13.8 ±0.4 and 30.3 ±1.1 at 800 ℃, respectively.

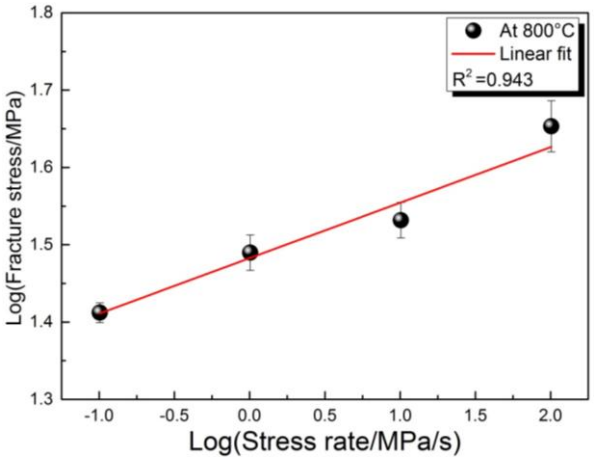

Figure 4.62 Fracture stress of BSCF determined by ring-on-ring bending tests as a function of stress rate (log-log plot) at 800 ℃

4.2.5.3 Stress-probability-time (SPT) diagrams

Considering the design in applications, it is essential to predict the life time of the ceramic membranes. Therefore, it is desirable to construct a SPT diagram of BSCF which describes the failure probability as a function of stress and time. To set up SPT diagrams, the stress is changed to an equivalent stress, σ_{1s}, which denotes that the stress transforms the failure stress σ_f tested at a stress rate $\dot{\sigma}$ into an equivalent stress that would result in the failure of the sample in 1 second[258] using the following equation:

$$\sigma_{1s} = \sigma_f \left(\frac{\sigma_f}{\dot{\sigma}(n+1)}\right)^{1/n} \quad (4.36)$$

where n is the SCG parameter.

4.2.5.3.1 SPT at room temperature

As previously mentioned, the characteristic strength of the ring-on-ring bending samples at RT, σ_c is 77 MPa and the Weibull modulus m is 10.2. The corresponding stress rate is 101.2 MPa/min. The basic processes of constructing SPT diagrams for the samples are as follows:

(i) Using the SCG parameter n=24.3 and σ_c =77 MPa in Equation (4.36), the equivalent stress that would result in the failure of the sample at 1 second is 78 MPa.

(ii) Combination of this stress and 1-F=1/e (corresponding to the characteristic strength σ_c; e is Euler's constant), where F is failure probability, shows the first data point on the 1 second line on the SPT diagram.

(iii) Plot the 1 second line with a slope of Weibull modulus 10.2.

(iv) A series of lines parallel to the 1 second line, with a spacing between the lines equal to (ln10)/n or 2.3/n. The spacing 2.3/n represents a change in life-time by a factor of 10 [205]. Each line represents a decade increase in life time.

Some selected prediction lines are shown in Figure 4.63

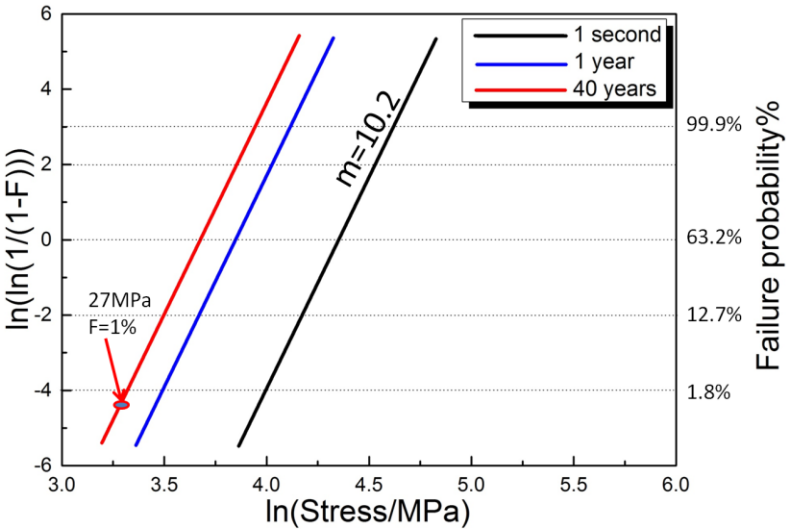

Figure 4.63 Strength-probability-time diagrams for the BSCF tested at RT

On the basis of the SPT diagram in Figure 4.63, the stress of design for a tolerable failure probability can be predicted; for example the stress for a lifetime of 40 years should not exceed 27 MPa to assure a failure probability of 1% at RT. This implies that the applied stress which imposes on the membranes should not be beyond this value at RT.

4.2.5.3.2 SPT at 800 ℃

As previously mentioned, the characteristic strength of the ring-on-ring bending samples at 800 ℃, σ_c is 48 MPa and the Weibull modulus m is 5.5. The corresponding stress rate is 101.2 MPa/min. The basic processes of constructing SPT diagrams for the samples are as follows:

(i) Using the SCG parameter n=13.8 and σ_c=48 MPa in Equation (4.36), the equivalent stress that would result in the failure of the sample at 1 second is 51 MPa.

(ii) Combination of this stress and 1-F=1/e (corresponding to the characteristic strength σ_c), where F is failure probability, gives the first data point on the 1

second line on the SPT diagram.

(iii) Plot the 1 second line with a slope of Weibull parameter 5.5.

(iv) A series of lines parallel to this line, with a spacing between the lines equal to (ln10)/n or 2.3/n. Each line represents a decade increase in life time.

Some selected prediction lines are shown in Figure 4.64

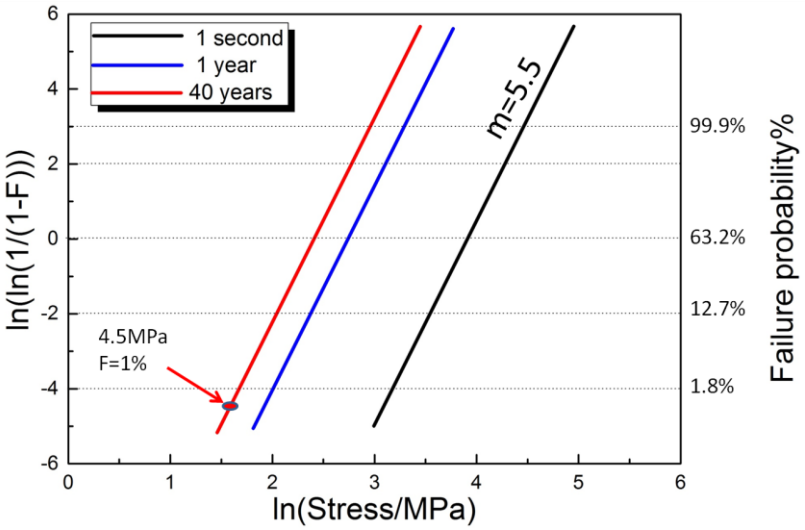

Figure 4.64 Strength-probability-time diagrams for the BSCF tested at 800 ℃

On the basis of the SPT diagram in Figure 4.64, the stress of design for a tolerable failure probability can be predictable; for example the stress for a lifetime of 40 years should not exceed 4.5 MPa to assure a failure probability of 1% at 800 ℃. This implies that the applied stress which imposes on the membranes should not be beyond this value at 800 ℃.

4.2.5.4 Discussion

As discussed previously, the SCG parameter n characterises the resistance of a material to SCG. A high value of n is usually interpreted as a low susceptibility to SCG. The high value of n=24.3 at room temperature indicates that BSCF is not very susceptible to slow crack growth, which is a good agreement with other groups[259]. However, the value of

n of BSCF decreases dramatically to 13.8 as the temperature rises to 800 ℃, which is approximately 43% of the value at room temperature. A similar trend has been also found in other perovskite-structured materials[205]. It indicates that BSCF is much more sensitive to SCG at 800 ℃ than that at room temperature. There can be several possible contributions to this phenomenon. The main possible reason is the thermally activated bond rupture due to the reduction in chemical bonding energy at high temperature. The other possible reasons are related to the secondary phase along grain boundary and the formation of oxygen vacancies in the grain bulk.

As shown in Figure 4.65(A), only cubic phase has been detected by XRD. However, the main peak (110) of BSCF samples shifted to large 2 theta angles after testing at 800 ℃ [Figure 4.65(B)], which indicated that the lattice parameter had decreased.

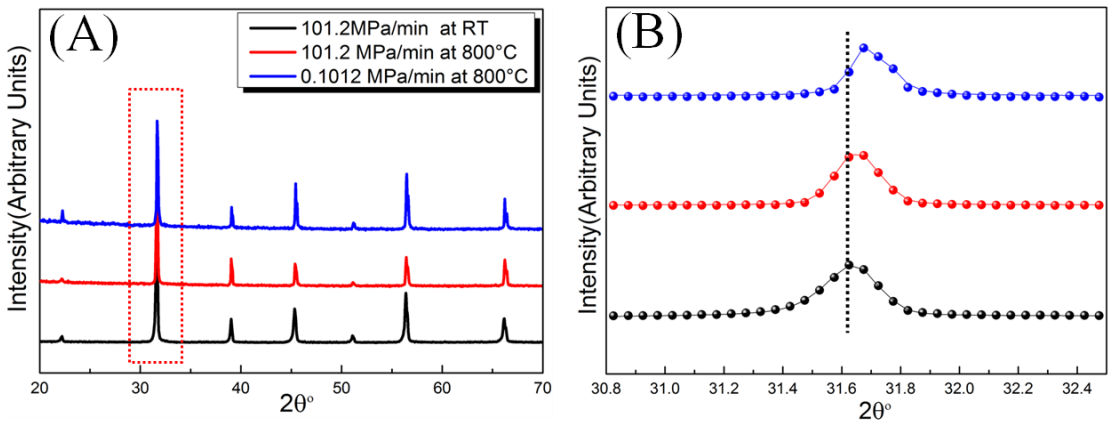

Figure 4.65 (A) XRD patterns of fractured BSCF samples under different conditions; (B) Refined XRD patterns of the main peak (110) of fractured BSCF samples

EDX linescans analysis across the grain boundary indicated that the bulk of the grain exhibited the same elemental composition at 800 ℃ as that at room temperature in Figure 4.66. However, it is clearly observed in Figure 4.66(B) there were an increase in oxygen and a decrease in cations at grain boundaries at 800 ℃. In combination with XRD analysis, it suggests that oxygen vacancies were formed in the grain bulk possibly due to the diffusion of oxygen ions from grain bulk to grain boundary. In addition, EDX

linescans were recorded to quantitatively analyse the composition of the grain boundary phase and the grain bulk. The compositions are given in at.%. The ratio of Ba-, Sr-, Co-, Fe-, and O- concentrations along a line scan across the grain boundary is around 12.6:12.4:20:5:50 at RT while the ratio of these compositions is approximate 10:10:16:4:60 at 800 ℃. According to the previous investigation, Švarcová *et al*.[260] have demonstrated that the ratio of Ba-, Sr-, Co-, Fe-, and O- concentrations 10:10:16:4:60 exhibits the hexagonal structure. Other groups[261] have reported that in terms of BSCF annealed at 800 ℃, cubic-to-hexagonal phase transition can be found at grain boundary by TEM. It suggests that the grain boundary phase possibly exhibits hexagonal structure.

It has been reported by Evans *et al*.[262]that grain boundary phases can be in response to the strength degradation and the decrease in the value of slow crack growth parameter n. Additionally, oxygen vacancies also can result in the strength degradation at high temperature due to the decrease in bond strength[263]. As seen in Figure 4.67, it shows the existence of secondary phases at the grain boundaries in the interior of the bulk. Therefore, thermally activated bond rupture, grain boundary phase and oxygen vacancies can be the reasons for the reduction in the value of n at 800 ℃.

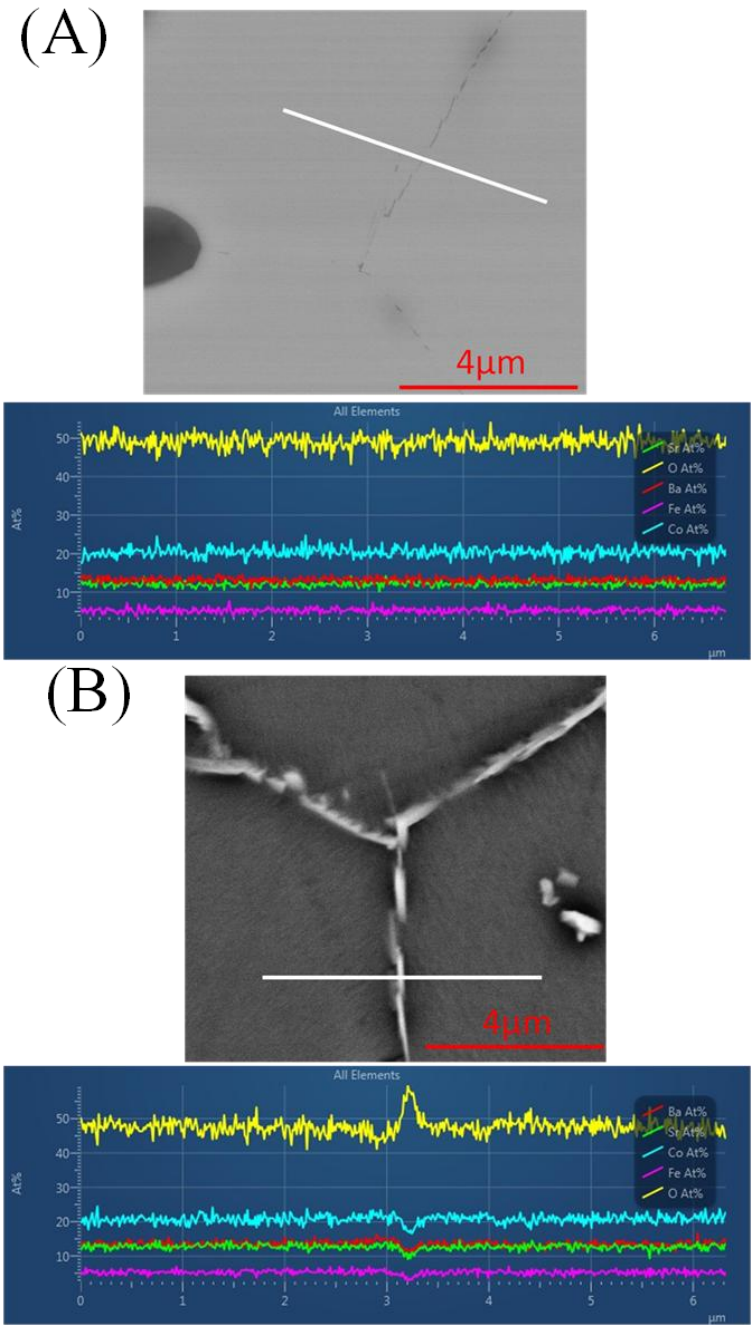

Figure 4.66 EDX linescans across the grain boundary of fractured BSCF samples: (A) 101.2 MPa/min at RT; (B) 0.1012 MPa/min at 800 ℃

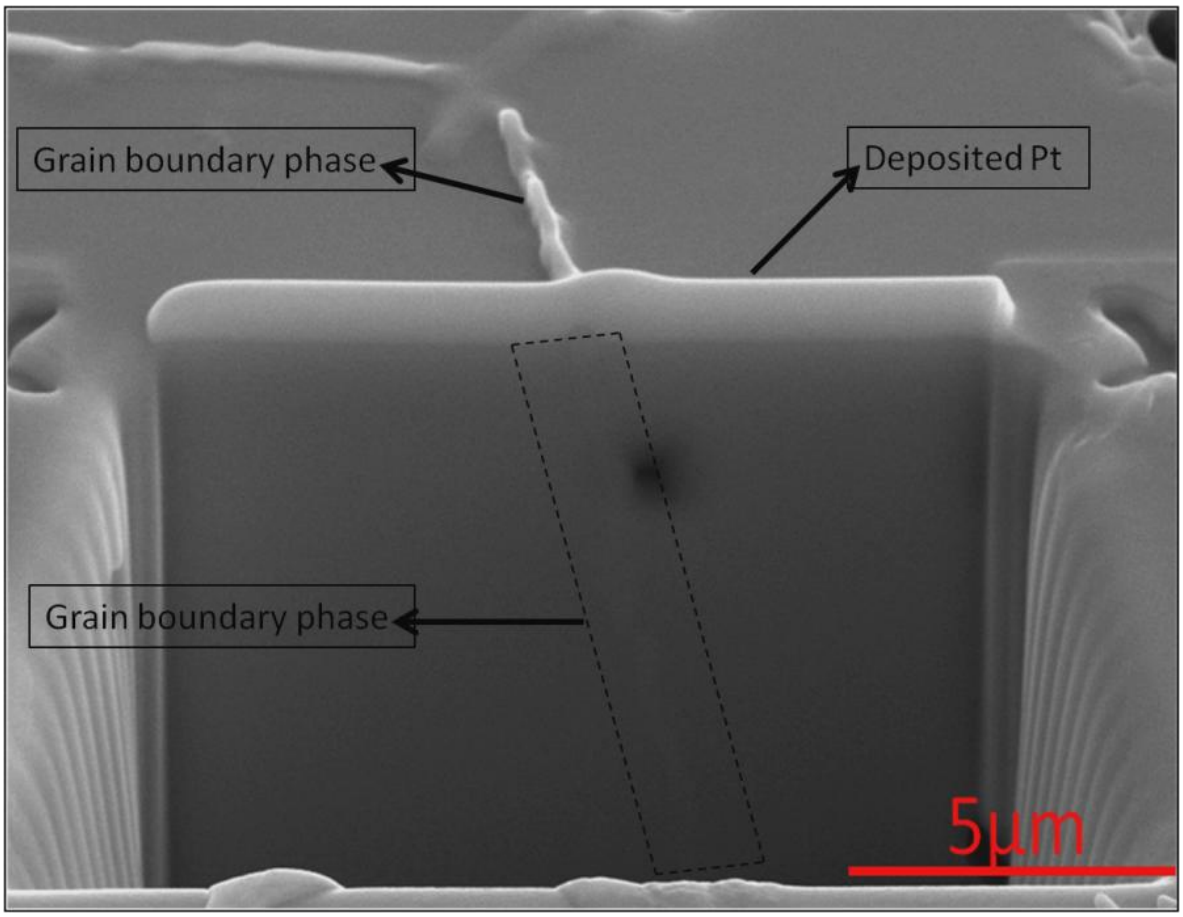

Figure 4.67 Grain boundary phase was observed in the interior of the BSCF bulk at 800 ℃ by FIB.

4.3 Sintering of Ni-doped BSCF membranes

How to improve the properties of BSCF including thermal stability, mechanical property and permeability at operating conditions remains to be dealt with. For instance, a phase transition from cubic to hexagonal structure occurs at elevated temperature and reduces the permeation rate of BSCF[216]; additionally, spin transition of Co^{3+} decreases the Young's modulus of the membrane at elevated temperature thereby becoming mechanical instability[138]. Recently, studies have been tried to substitute rare earth metal ions (e.g. Zr, Bi, La and Gd) to modify the microstructure of BSCF-based materials, thereby improving their performances [83, 102, 264-267]. A promising solution seems to be the partial substitution of B-site cations (Fe and Co) to

eliminate the effect of spin transition of Co^{3+}. It has been reported that Ni doping has been demonstrated to improve different properties of perovskite-structured materials (e.g. $LaFeO_{3-\delta}$[268] and $GdBaCo_2O_{5+\delta}$[269]). However, there are few investigations on Ni-doped BSCF. This motivated the author to conduct the present study to attain a comprehensive understanding of the effect of Ni substitution on the properties of BSCF.

4.3.1 Variation of Ni content doped in BSCF

In this section, all the $Ba_{0.5}Sr_{0.5}Co_{0.8}Fe_{0.2}O_{3-\delta}$ with different Ni contents doped in the B-site (BSCF-NiX; X=0, 2, 4, 6, 8, 15, 20, 25 mol %) were sintered at 1100 ℃ for 10 hours. The sintering behaviours of Ni-doped BSCF are presented and discussed. These include phase identification, grain evolution, and porosity.

4.3.1.1 X-ray diffraction analysis

Figure 4.68 shows the X-ray diffraction patterns (A) of all the sintered samples and the lattice parameter as a function of the Ni doping content (B). As shown in Figure 4.68(A), when the content of Ni doping is below 25 mol%, diffraction patterns of different contents of Ni-doped BSCF are indexed by a single cubic phase. For the patterns of BSCF-Ni25, a secondary phase of NiO [PDF 47-1049] was identified. For BSCF samples with a low Ni doping level (＜4%), the lattice parameter increases with increasing Ni doping content. When the Ni doping content is above 4 mol%, the lattice parameter shows little change in Figure 4.68(B). These results suggest that the solid solubility limit lies in around 4 mol% Ni.

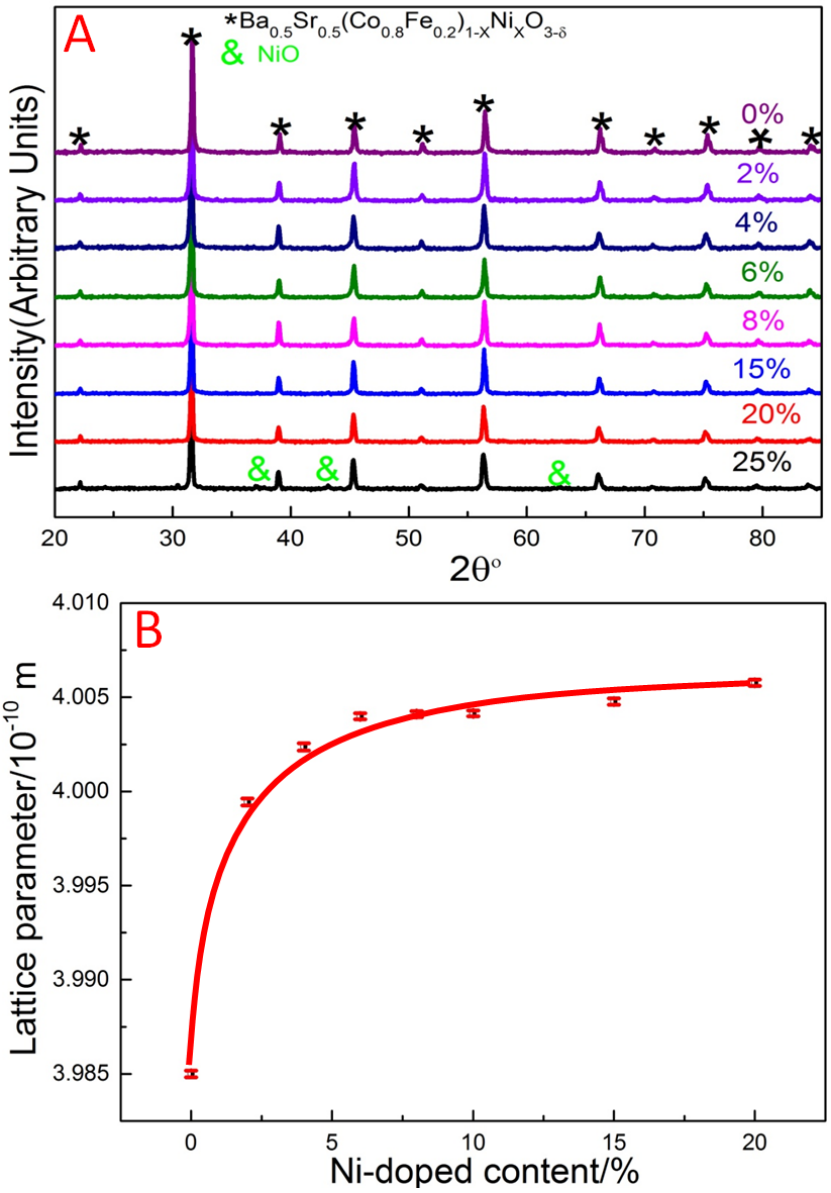

Figure 4.68 (A) XRD patterns of different contents of Ni-doped BSCF; (B) Lattice parameter as a function of Ni doping content. The line is a guide to the eye.

Previous studies have shown that the lattice parameters of Bi-doped[270], Y-doped[87] and Zr-doped BSCF [102, 271] increase with increasing doping content to a certain due to the replacement of the host ions by dopant ions having a larger ionic radius. It has been also found in $LaCoO_3$ [272] that the lattice parameters increase with increasing Ni substitution of Co in a certain content range, because the ionic radius of Ni^{2+} is larger than that of Co^{3+}. On the other hand, for La doping in BSCF[273], the lattice parameter decreases with increasing La doping level because of the substitution of smaller La^{3+}

cation. Therefore, the lattice parameter significantly depends on the radii of substitution ions. In the case of Ni-doped BSCF, the lattice parameter increases with increasing the Ni doping content due to the substitution of larger Ni^{2+}(0.74 Å) cations on B-site for Fe^{4+} (0.59 Å) and Co^{3+} (0.61 Å) cations.

4.3.1.2 Grain evolution

4.3.1.2.1 Grain growth

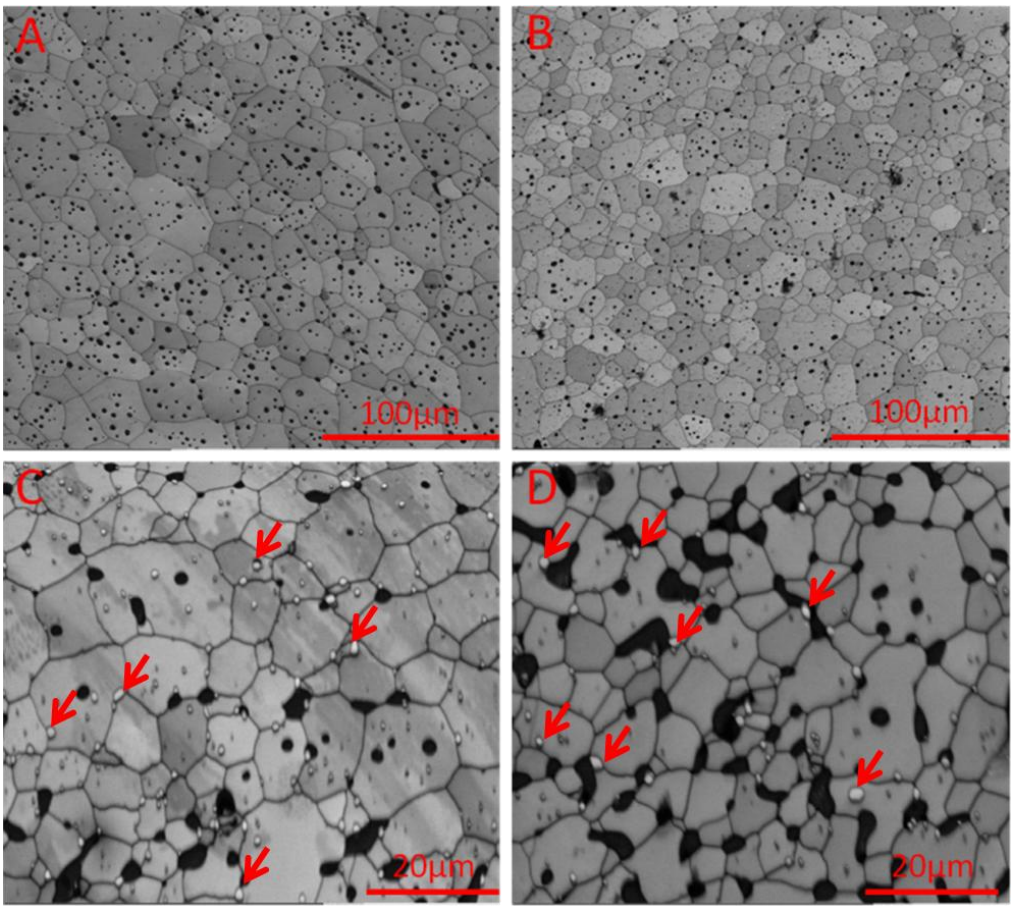

Figure 4.69 EBSD band contrast micrographs of sintered BSCF with different Ni contents: (A) 2 mol%; (B) 4 mol%; (C) 15 mol%; (D) 20 mol%. Red arrows point at secondary-phase particles

Figure 4.69 shows EBSD band contrast micrographs of BSCF with different Ni contents (2, 4, 15, 20 mol%) sintered at 1100 ℃ for 10 hours. It is clearly observed that a secondary phase exists in BSCF doped with 15 and 25 mol% Ni. According to the EDX

spectrum of the secondary phase in Figure 4.70, the atom ratio between Ni and O is calculated to be approximately 1, which suggests that secondary phase is NiO. This observation is consistent with the XRD spectra presented in Figure 4.68 above.

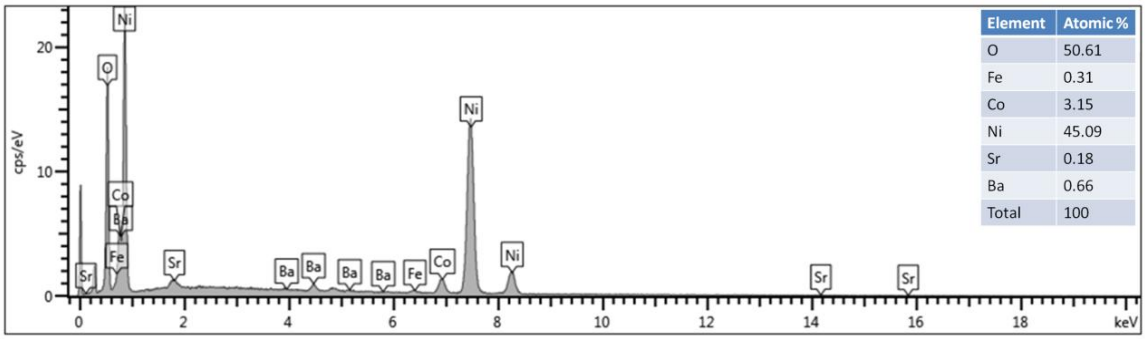

Figure 4.70 EDX spectrum of secondary phase of Ni-doped BSCF

Figure 4.71 shows the average grain size in BSCF (BSCF-NiX, X=0, 2, 4, 6, 8, 15, 20, 25 mol %) ceramics as a function of Ni doping content. It is clearly observed that the average grain size of Ni-doped BSCF decreases with increasing the Ni doping content. The grain size reduces gradually with increasing Ni doping content up to 4 mol%; and then the reduction rate slows down with the further increase in Ni doping content. This indicates that the Ni doping affects the grain growth of BSCF through two mechanisms. As reported by Garcia *et al.*[274], the decrease in grain size can be related to the impurity content. In the case of Ni doping in BSCF, the Ni ions can be incorporated into the lattice as a solid solution or precipitated as a secondary phase (NiO).

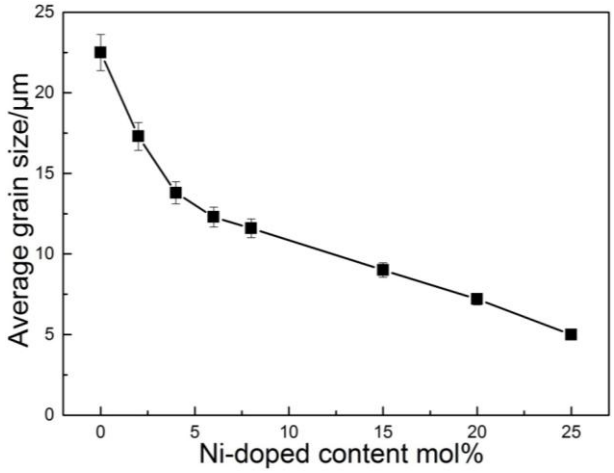

Figure 4.71 Average grain sizes of Ni-doped BSCF as a function of the Ni doping content.

In the range of Ni doping from 0 to 4 mol%, it can be concluded that the grain size decreases with increasing the doping content due to Ni ions being dissolved into the lattice, because Ni doping restricts the diffusion of other ions thereby constraining grain growth. This phenomenon has also been found in Ni-doped $BaTiO_3$[275].

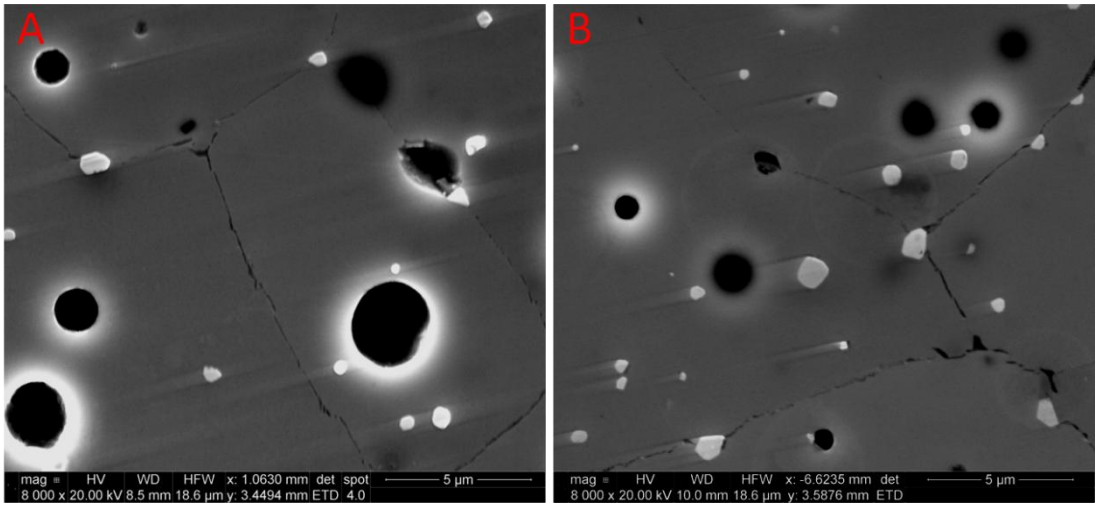

Figure 4.72 Microstructure of BSCF doped with 6 mol% (A) and 8 mol% (B) Ni sintered at 1100 ℃ for 10 hours

In the range from 4 to 25 mol% Ni, apart from the constraint from Ni^{2+} solute in the BSCF lattice, the decrease in the grain size with increasing the doping content can be also due to precipitation of the secondary phase which constrains grain growth. It can be clearly observed in Figure 4.72 that particles are distributed both inside the grain and along the grain boundaries. Furthermore, with increasing the Ni doping content, the number of particles increases. Under the same sintering conditions (1100 ℃, 10 h), the grain size for BSCFNi-25 is a factor 4.5 smaller in comparison with that of the pure BSCF as shown in Figure 4.71. A similar phenomenon was observed in BSCF with Zr-doping[271]. According to the explanation of Stournari *et al.*[271], the suppressed grain growth in Zr-doping BSCF can be ascribed to a secondary phase pinning or dragging mechanism, because small Zr-rich crystallites can be found along the grain boundaries. Therefore, by analogy it can be suggested that both Ni solute and the secondary-phase NiO particles can constrain the grain growth of BSCF.

It can be also clearly observed that the number of secondary phase particles (NiO) located on the grain boundaries increases with increasing the Ni content, especially above 15 mol%, as shown in Figure 4.69(C-D). As mentioned above, secondary phase particles can inhibit grain growth by pinning or dragging the migration of grain boundaries, which is often called the Zener pinning or drag effect [276, 277]. The total pinning force F_{TP} is given by

$$F_{TP} = \frac{3f\gamma_b sin\theta cos\theta}{r} \quad (4.37)$$

where f is the volume fraction of particles at the grain boundaries, γ_b is the grain boundary energy per unit area, θ the angle between the grain boundary surface and the point of intersection with particle, and r is the particle radius. These parameters f and r were determined by Image analysis based on SEM micrographs (Image-Pro Plus 6.0 software). With increasing in the Ni doping level, the volume fraction of the secondary phase particles increased, and since the particle radius changed only slightly, the total pinning force of the secondary phase particles increases according to Equation (4.37). Therefore, the grain size gradually decreases.

The first quantitative model to describe the effect of inclusion particles on the grain growth in polycrystalline materials was developed by Zener *et al*.[278, 279]. In this model, the limiting grain size *G* of the main phase is given by:

$$G = \frac{2d}{3f} \quad (4.38)$$

where *d* is the average size of the particles. Zener's model involves two major assumptions: one is the existence of a stabilised microstructure, in which grain growth stops or a constant grain/particle size ratio prevails during extended heating; the other is that isolated spherical inclusion are randomly dispersed in the matrix. Since many experimental results showed that the observed limiting grain sizes were not in

agreement with those predicted by Zener's equation, modified models have been suggested. The general form of the modified equation is [280-282]

$$G = C\frac{d}{f^m} \tag{4.39}$$

$$log\left(\frac{G}{d}\right) = -mlog(f) + log(C) \tag{4.40}$$

where *C* and *m* are constants.

To evaluate Zener's effect, the value of C and m can be determined from the experimental data by plotting log (G/d) versus log (f) and comparing with the ones predicted by the models. Since these models are based on a preferential location of the secondary phase particles at the grain boundaries, samples with a doping level above 15 mol% Ni were used. The data for these three different doping levels are shown in Figure 4.73. From this plot, the values of C and m obtained are 0.94 and 0.55, respectively. These values do not agree well with the original Zener's model(C=0.67, and m=1), but they are in close agreement with the ones in the modified models of Haroun and Budworth (C=1.03 and m=0.5)[280] and Gladman *et al*. (C=0.88 and m=0.5)[281].

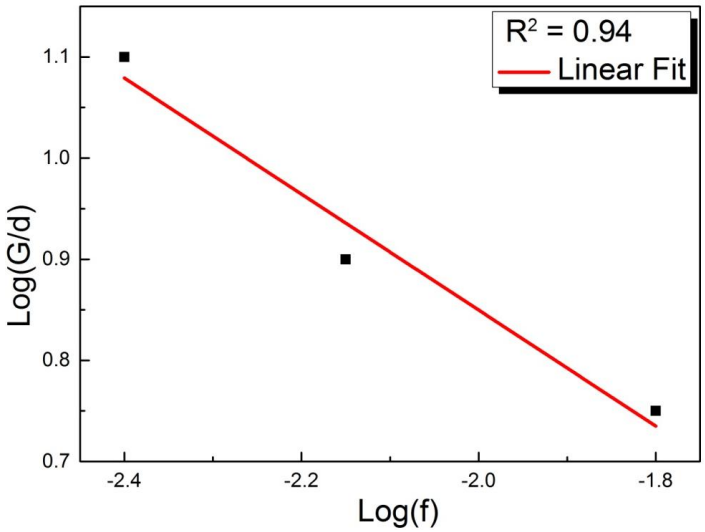

Figure 4.73 log (G/d) as a function of log(f) for the sample of BSCF doped with 15, 20, 25 mol% Ni sintered at 1100 ℃ for 10 hours.

4.3.1.2.2 Grain size distributions and grain aspect ratio distributions

Figure 4.74 shows grain size distributions and grain aspect ratio distributions of sintered BSCF with various Ni doping contents sintered at 1100 ℃ for 10 hours. It has been reported that dopants can induce abnormal grain growth in some ceramics systems [283-286]. As shown in Figure 4.69, all the samples of Ni-doped BSCF show regular equiaxed grains and no abnormal grain growth can be found. As shown in Figure 4.74(A), the shape of the grain size distribution profile of each curve remains essentially similar while the grain size distribution curves shift toward the finer end of the size profile as a function of Ni doping content. This phenomenon is also found in other doped ceramic systems [79, 80, 287].

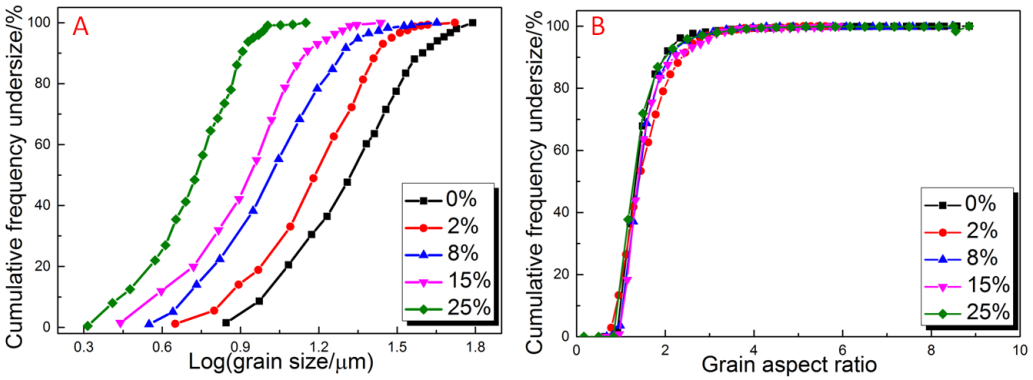

Figure 4.74 Grain size distributions (A) and grain aspect ratio distributions (B) of sintered BSCF with various Ni doping contents

From the literature [288, 289], it has been proved that doping can influence the grain aspect ratio of ceramics materials as well. However, the grain aspect ratios of BSCF doped with different content Ni are approximately 1.8 and are almost the same as those of pure BSCF.

4.3.1.3 Porosity

Figure 4.75 shows the dependence of porosity of BSCF on the Ni doping content. It is clearly observed that the porosity increases with increasing the Ni doping content. In

other words, Ni doping clearly inhibits densification of BSCF at 1100 ℃. With increasing Ni doping concentration from 2 to 8 mol%, the porosity increases gradually. However, upon further increasing the dopant concentration, the porosity increases sharply up to 25 mol% to a level around 16%, which is more than twice that at 15 mol%. The porosity increases with the increase in Ni doping level. In sum, the densification rate of BSCF is reduced by the Ni doping, and the reduction rate increases with the increase in Ni doping level. This phenomenon indicates that the diffusion rate and/or the sintering stress were reduced by Ni doping.

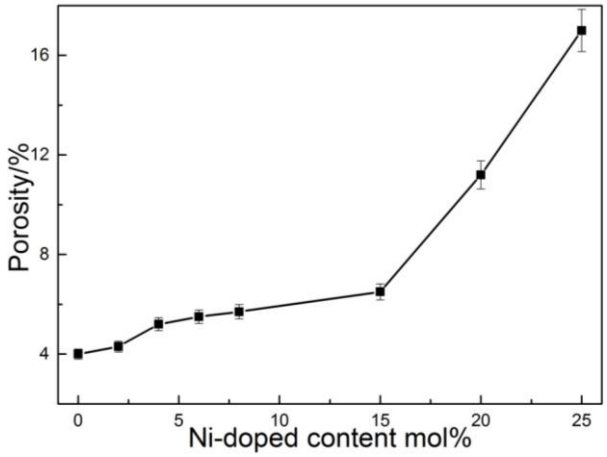

Figure 4.75 Porosity as a function of Ni doping content for BSCF sintered at 1100 ℃ for 10 hours.

The dissolution of Ni into BSCF leads to a decrease of diffusion coefficient of the cations by depressing the concentration of this species. Studies on Ni doping in $BaTiO_3$[275] have shown that Ni constrains the diffusion rate of Ti. Additionally, Ti is the rate controlling species due to its the highest activation energy of diffusion in $BaTiO_3$[275]. Therefore, Ni doping retards the densification of $BaTiO_3$[275]. Similarly, in the case of Ni doping in BSCF, it suggests that one reason for the increase in the porosity with increasing Ni doping content can be attributed to the diffusion of cations constrained by Ni.

With respect to the process of sintering, the densification occurs by means of the pore

surface moving to the pore centre. Very small inclusions will be possibly dragged and gathered together with the aid of the movement of pore surfaces during the sintering[79]. The force of these particles obstructing the movement of the surface is equivalent to the influence of inclusions on the grain boundary mobility[79]. In this way, the drag effect of the particles on the pore-surface motion consequently decreases the sintering stress. Therefore, besides restraining the diffusion rate, Ni doping can retard the densification of BSCF by means of the restraint of the diffusion rate and the reduction in the sintering stress.

4.3.1.4 Pore evolution

Figure 4.76 shows the pore size distributions and pore aspect ratio distributions of BSCF with 0, 15 and 25 mol% Ni doping sintered at 1100 ℃ for 10 hours. The average pore size with standard deviation of these three different samples are 1.80±0.47 μm (0 mol%), 2.37±0.68 μm (15 mol%), and 3.13±1.01 μm (25 mol%) while the average pore aspect ratio with standard deviation are 1.27±0.36 μm (0 mol%), 1.65±0.59 μm (15 mol%), and 1.90±0.72 μm (25 mol%). It is clearly observed that both pore size distributions and pore aspect ratio distributions are unimodal and become broader with increasing Ni doping content.

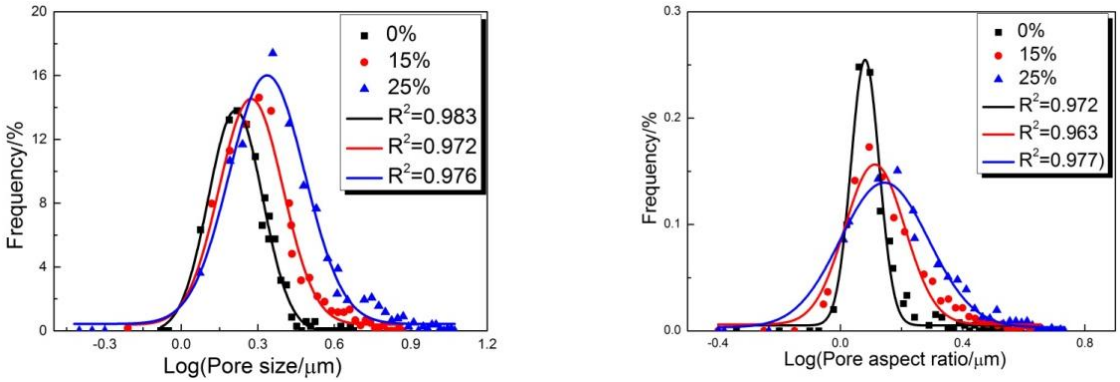

Figure 4.76 (A) Pore size distributions and (B) pore aspect ratio distributions of Ni doping in BSCF sintered at 1100 ℃ for 10 hours

4.3.2 BSCF doped with 8 mol% Ni (BSCF-Ni8)

In this part, the structure and sintering behaviours of BSCF-Ni8 are presented and discussed. The samples were sintered from 1000 ℃ to 1200 ℃ for 10 hours. The characterisation techniques used include structural analysis by XRD, relative density, and microstructural analysis.

4.3.2.1 X-ray diffraction analysis

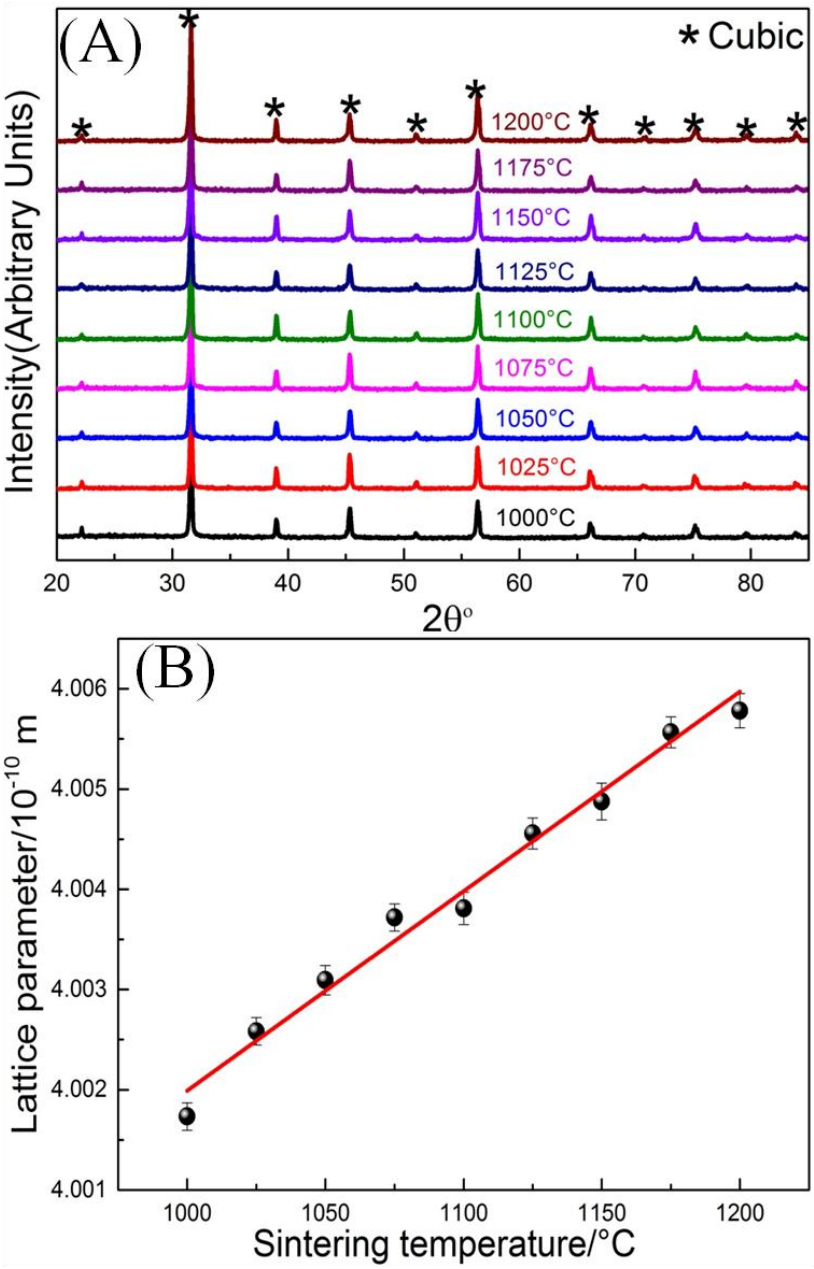

Figure 4.77 (A) XRD patterns of sintered BSCF-Ni8 at different temperatures for 10 hours; (B) Lattice parameter of BSCF-Ni8 as a function of sintering temperature.

The XRD patterns obtained for BSCF-Ni8 sintered between 1000 ℃ and 1200 ℃ for 10 hours indicates that it is well indexed as a cubic perovskite structure, as illustrated in Figure 4.77 (A). Even up to 1200 ℃, the BSCF samples do not shown any decomposition and no other phase can be identified by XRD. As shown in Figure 4.77(B), it can be observed that the lattice parameters of BSCF doped with 8 mol% Ni increase approximately linearly with the sintering temperature, which is also observed in undoped BSCF. As mentioned in Chapter 4.1, it is caused by the release of oxygen, and hence an increase in the oxygen vacancy concentration with increasing temperature. Within the temperature range studied, the variation of the lattice parameters of BSCF is 0.12%, which is much lower than that of BSCF. This suggests that the sintering temperature has less influence on the lattice parameter of BSCF-Ni than that of BSCF.

4.3.2.2 Relative density

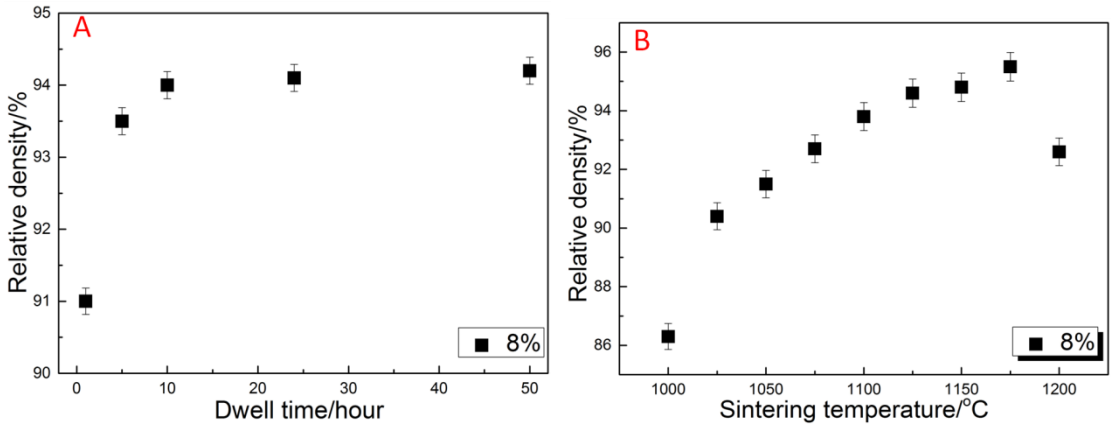

Figure 4.78 Relative density of BSCF-Ni8 as a function of dwell time (A) and sintering temperature (B). The lines are a guide to the eye.

Figure 4.78 shows the relative density as a function of the dwell time and sintering temperature for BSCF doped with 8 mol% Ni. For a given temperature of 1100 ℃, the relative density reaches the maximum after 10 hours. Subsequently, the density remains approximately constant with further increase of the sintering time up to 50 hours. For a given dwell time of 10 hours, the relative density gradually increased as the sintering

temperature increased in the range from 1000 ℃ to 1175 ℃. When the sintering temperature reached 1200 ℃, the relative density decreased from 95.5% to 92.6%. By comparison with the BSCF-Ni8 samples sintered at temperatures between 1175 ℃ and 1200 ℃, the value of linear shrinkage at 1175 ℃ (9.03%) is higher than the value at 1200 ℃ (8.87%). In other words, the densification rate decreased at 1200 ℃.

4.3.2.3 Microstructural evolution

4.3.2.3.1 Grain growth

The changes in microstructure as a function of dwell time and sintering temperature are presented in Figures 4.79 and 4.80, while the results of the microstructural analysis are summarised in Figure 4.81. It is evident that the average grain size grows gradually as the sintering time increased from 1 to 50 hours, as displayed in Figure 4.81(A). The average grain sizes of the BSCF-Ni8 ceramics sintered at 1100 ℃ from 1 to 50 hours were in a range from 7.8 to 16.1 μm as shown in Figure 4.79. As displayed in Figure 4.81(B), for a given time 10 hours, the average grain size grows with increasing sintering temperature. The grain size increases slowly with the sintering temperature up to 1050 ℃ and then grows gradually with the sintering temperature in the range from 1050 to 1175 ℃. Between 1175 ℃ and 1200 ℃, the grain size enters a period of rapid growth. For instance, the average grain sizes of BSCF samples sintered at 1025, 1075 and 1200 ℃ are determined as 3.6, 9.2, and 34.1 μm, respectively as shown in Figure 4.80.

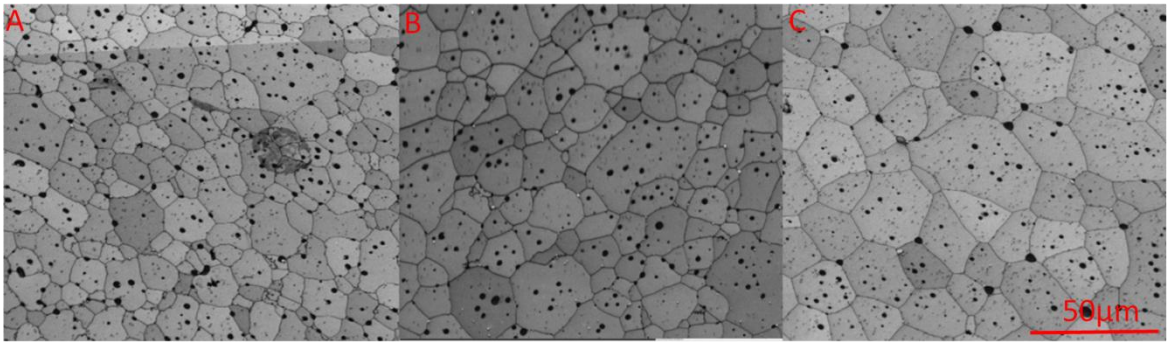

Figure 4.79 EBSD band contrast micrographs of BSCF-Ni8 sintered at 1100 ℃ for various time: (A) 1 hour; (B) 10 hours; (C) 50 hours

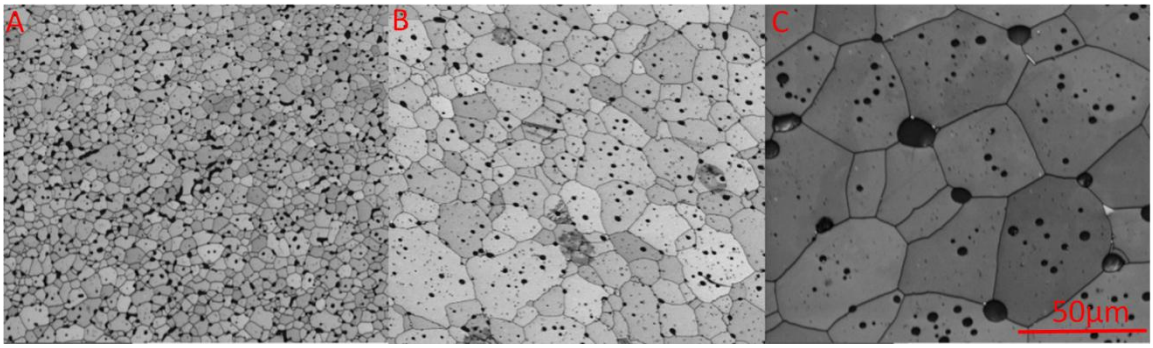

Figure 4.80 EBSD band contrast micrographs of BSCF-Ni8 sintered at different temperatures for 10 hours (A) 1025 ℃; (B) 1075 ℃; (C) 1200 ℃

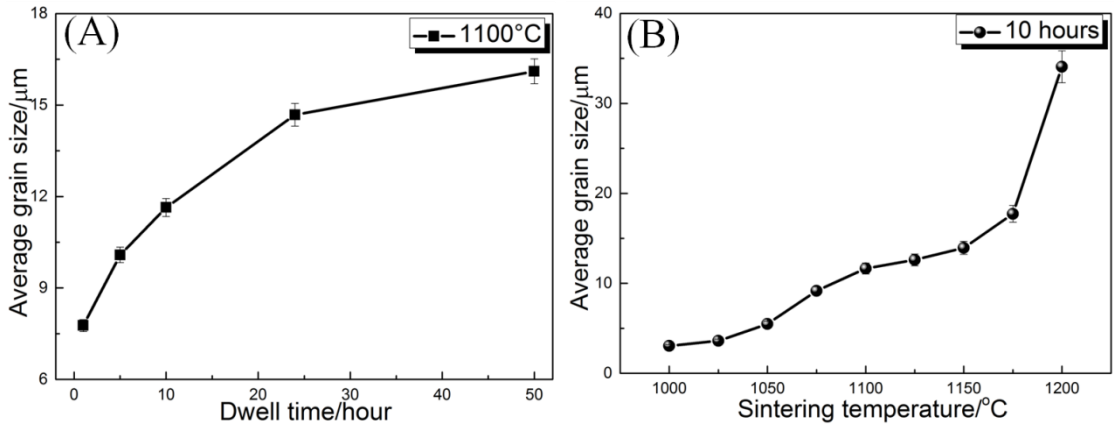

Figure 4.81 Average grain size as a function of (A) dwell time at 1100 ℃ and (B) sintering temperature for 10 hours.

It is noted that the average grain size increases with increasing dwell time. The phenomenological kinetic grain growth equation can be expressed in the following equation:

$$\ln(D) = \frac{1}{n} ln(t) + \frac{1}{n}[lnK_0 - (\frac{Q}{RT})] \quad (4.41)$$

From the slope (*1/n*) of the *ln* (grain size) versus *ln* (time) line, the value n of the grain

growth kinetic exponent can be calculated.

Figure 4.82 shows the grain growth kinetics for BSCF-Ni8 sintered at 1100 ℃, with a ln-ln plot of grain size against time. It demonstrates the isothermal grain growth data for the BSCF ceramics over a time period from 1 to 50 hours at a temperature of 1100 ℃ in the form of Equation (4.41). The slope *1/n* is determined to be 0.212. This means that the value n of the grain growth exponent is approximately 4.7. The temperature-dependence of grain growth during sintering for BSCF-Ni8 can be expressed as

$$D^{4.7} = K_0\, t\, exp(\frac{-Q}{RT}) \tag{4.42}$$

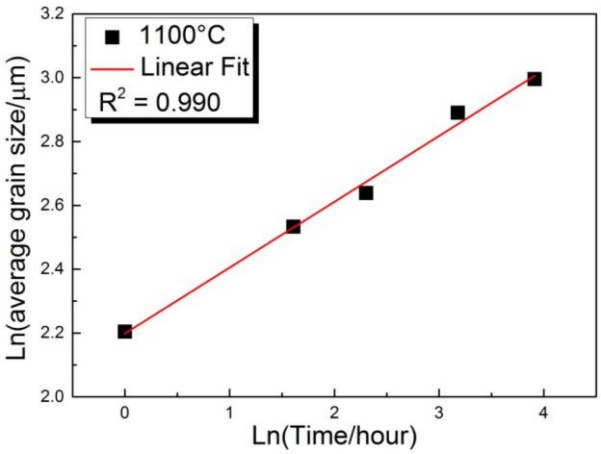

Figure 4.82 Graph of ln(grain size) versus ln(time) for BSCF-Ni8 sintered at 1100 ℃

Figure 4.83 shows an Arrhenius plot by constructing the data of average grain size from a constant dwell time, in which $ln(D^n/t)$ is plotted versus the reciprocal of the absolute temperature (*1/T*). Rearranging the Equation (4.42) yields,

$$ln\left(\frac{D^n}{t}\right) = -\frac{Q}{R}\left(\frac{1}{T}\right) + lnK_0 \tag{4.43}$$

the slope of which can be used for calculation of the apparent activation energy for the grain growth procedure. For BSCF-Ni8 (n=4.7), there exists a reasonably good linear relationship between ln ($D^{4.7}$/t) and 1/T from 1000 to 1200 ℃ at the constant sintering time(10 hours) in this study. The grain growth activation energy determined from the

slope of Figure 4.83 is 803.4±30 kJ/mol.

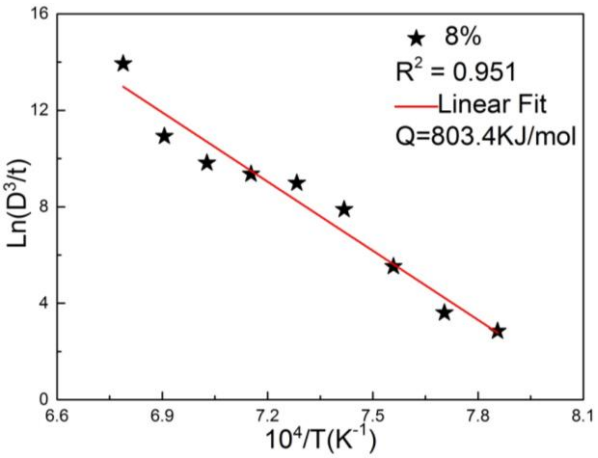

Figure 4.83 Graph of grain growth rate versus inverse temperature for the determining activation energy for grain growth, all the results are shown for the BSCF-Ni8

4.3.2.3.2 Grain size distributions and grain aspect ratio distributions

Figure 4.84 and Figure 4.85 present the grain size distributions and grain aspect ratio distributions for the BSCF-Ni8 samples sintered under different conditions. It is clearly evident from the plots presented in Figure 4.84(A) and Figure 4.85(A) that, the shape of the grain size distribution profile of each curve remains essentially similar, whereas the grain size distribution curves shift toward the coarser end of the size profile as a function of prolonging sintering time and/or increasing temperature. Additionally, the average grain aspect ratios of BSCF-Ni8 sintered under different conditions are approximately 1.8 and are similar to those of undoped BSCF as shown in Figure 4.84(B) and Figure 4.85(B).

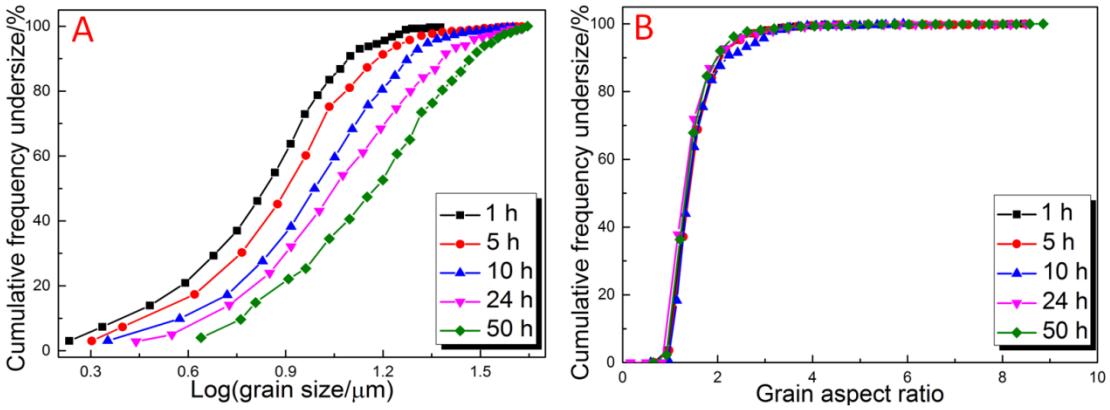

Figure 4.84 Grain size distributions (A) and grain aspect ratio distributions (B) of BSCF-Ni8 sintered at 1100 ℃ for different dwell time

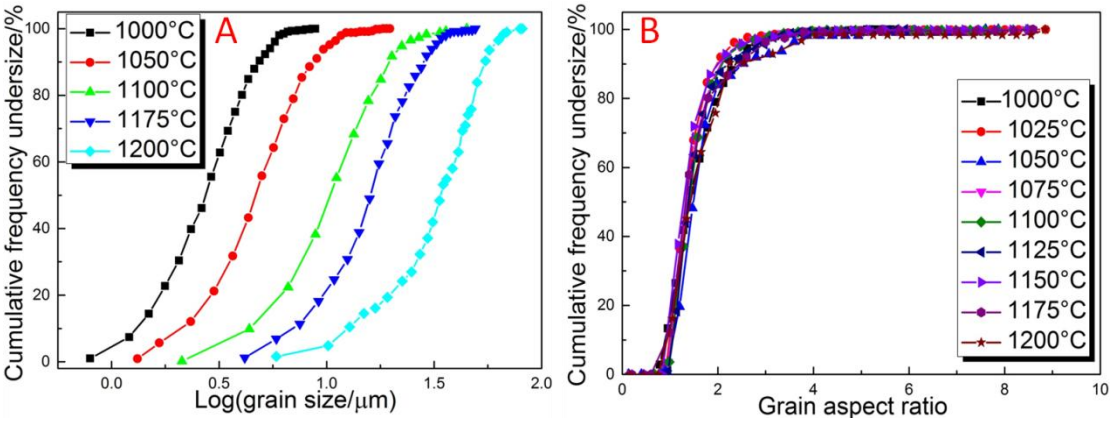

Figure 4.85 Grain size distributions (A) and grain aspect ratio distributions (B) of BSCF-Ni8 sintered at different temperatures for 10 hours

4.3.2.4 Mechanisms of densification and grain growth of BSCF-Ni8

As mentioned previously in Chapter 4.1, the model proposed by Coble *et al.*[54] predicts the densification rate $\frac{d\rho}{dt}$ as the following equation:

$$\frac{d\rho}{dt} = \frac{CN\xi\gamma_s\Omega}{D^m} \tag{4.44}$$

Combining the Equations (4.5) and (4.8), yields the following equation:

$$\frac{d\rho}{dt} = \frac{CN\xi\gamma_s\Omega}{tK_0 exp\,(-\frac{Q}{RT})} \tag{4.45}$$

Equation (4.45) can be integrated to transform to the following equation:

$$\rho = \frac{CN\xi\gamma_s\Omega}{K_0 exp\,(-\frac{Q}{RT})}\ln(t) + \Theta \tag{4.46}$$

Taking logarithm of both sides of Equation (4.44) yields the following equation:

$$log\left(\frac{d\rho}{dt}\right) = -mlog(D) + \Phi \quad (4.47)$$

where all the alphabetic symbols denotes the same meaning as before; Θ and Φ are constants.

The experimental data obtained from the samples sintered at 1100 ℃ from 5 to 50 hours are plotted in this way for the densities ranging from 93.7% to 95% in Figure 4.86. It shows relative density of BSCF-Ni8 sintered at 1100 ℃ from 1 to 50 hours(A) and plot of log(densification rate) versus log(grain size)(B). At 1100 ℃, the calculated value of m from the plot is 3.57±0.14 for BSCF-Ni8 in Figure 4.86(B). Considering the value of m, the predominant mechanism for controlling densification is not clear. It seems that both grain boundary and lattice diffusions are the equally dominant controlling mechanisms for BSCF-Ni8 at 1100 ℃.

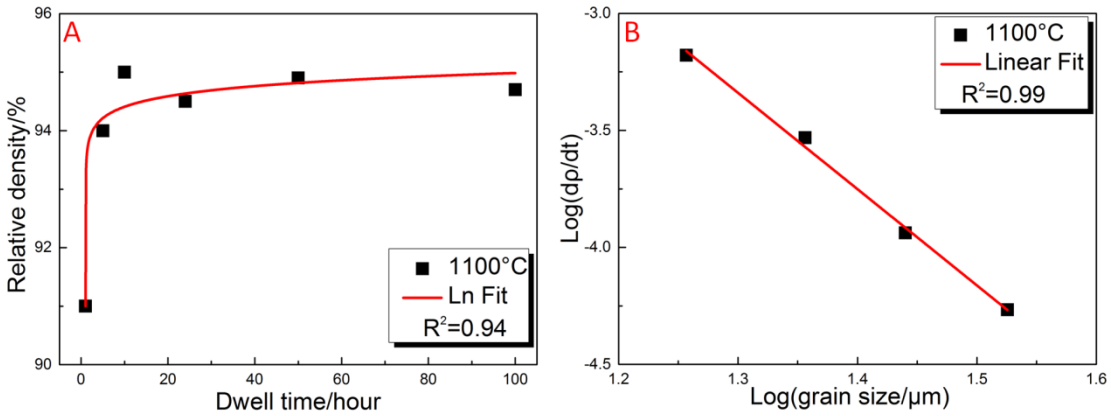

Figure 4.86 (A) relative density of BSCF-Ni8 sintered at 1100 ℃ for various dwell times; (B) Plot of log(dρ/dt) versus log(grain size) for 1100 ℃

In the case of grain growth kinetics, the grain growth exponent n of BSCF-Ni8 is determined to be 4.7. In other words, the grain growth kinetics of BSCF-Ni8 do not follow the classical law of parabolic growth (n=2). A higher grain growth exponent indicates that grains slowly coarsen. As mentioned before, the driving force for grain growth is the local curvature of the grain boundary[16]. When the pores are dragged along the grain boundary, it will lower the driving force for grain boundary mobility thereby slowing grain growth[165]. It has been reported [290, 291]that grain growth

exponent higher than 2 can be related to porosity and the impurity content of the oxide material. Therefore, it can be observed in Figure 4.72 that both pores and secondary phase particles lead to the higher grain growth exponent.

With regard to the activation energy for grain growth of BSCF-Ni8, it is calculated to be 803.4±30 kJ/mol. As mentioned before, the activation energy for oxygen ion diffusion (45-105 kJ/mol[103, 104]) is much lower than that for grain growth of BSCF-Ni8. Accordingly, cations diffusions are the rate-controlling species of grain growth rather than oxygen ions. Although there is no literature about the activation energy for Ni diffusion in BSCF, it has been reported that the activation energy for Ni diffusion in nickel oxide is 285 kJ/mol [292] which is much lower than that for grain growth of BSCF-Ni8. Therefore, it suggests that Ni diffusion cannot be the rate-controlling specie of grain growth of BSCF-Ni8. On the other hand, Lein *et al*. [104, 105] have reported that the diffusion of Sr/La in $La_{0.5}Sr_{0.5}Co_{0.8}Fe_{0.2}O_{3-\delta}$ is slower than that of Co/Fe. Therefore, in terms of BSCF-Ni8, it can be speculated that the Ba/Sr cations can be the rate-controlling species during the sintering process.

4.3.2.5 Comparison of density and grain growth between undoped BSCF and 8 mol% Ni-doped BSCF

Grain growth processes in sintered undoped BSCF and BSCF-Ni8 ceramics have been systematically investigated in the preceding sections. It is shown that Ni doping has a negative influence on the density and grain size of BSCF. First, as mentioned previously, the grain growth kinetics of both undoped and Ni-doped BSCF do not follow the typical correlation of parabolic growth (n=2). Furthermore, the grain growth exponent of 4.7 for BSCF-Ni8 is higher than that value of undoped BSCF (n=3). The increased n value is most likely due to the presence of secondary phase (NiO) particles which inhibits the

grain boundary mobility as mentioned before. Second, the apparent activation energy for grain growth of BSCF-Ni8 (Q=803.4±37 kJ/mol) is also greater than that value of undoped BSCF (Q=650.7±30 kJ/mol). According to Jud *et al*. [293], lattice diffusion usually exhibits a higher activation energy than grain boundary diffusion. Additionally, the mechanism of grain growth in undoped BSCF is grain boundary diffusion while grain growth of BSCF-Ni8 is equally controlled by grain boundary diffusion and lattice diffusion as discussed before. Therefore, the change in mechanism of grain growth results in the higher activation energy for grain growth of BSCF-Ni8.

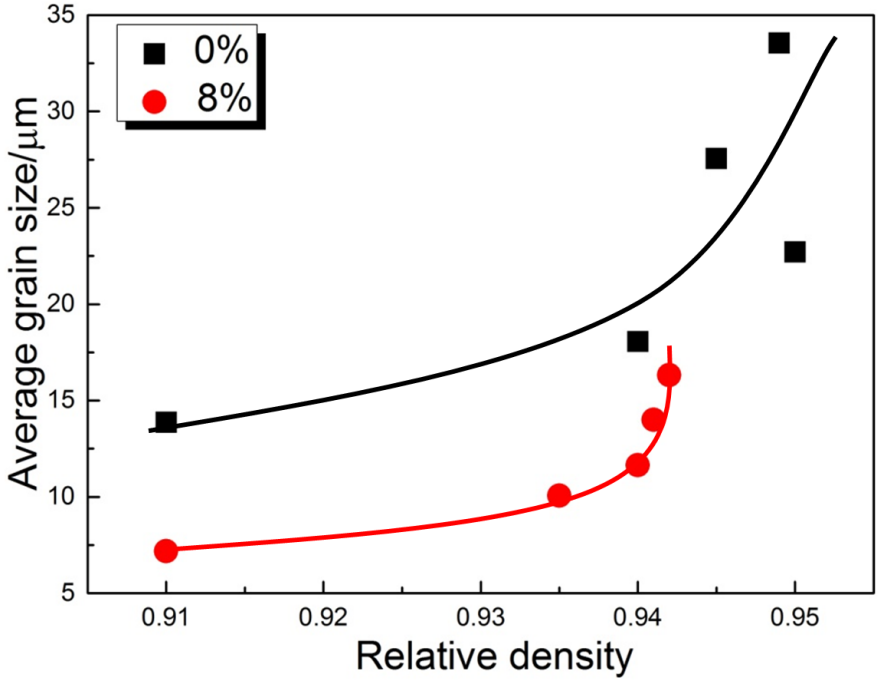

Figure 4.87 Average grain size as a function of relative density curves for undoped and 8 mol% Ni-doped BSCF sintered at 1100 ℃. The lines are a guide to the eye.

Figure 4.87 shows grain size-density curves for undoped and Ni-doped BSCF sintered at 1100 ℃. The grain size-density curve shows the ratio of the grain growth rate to the densification rate. The curve for undoped BSCF lies higher than that for the doped BSCF-Ni8, with the Ni effect being stronger in retarding grain growth than on the densification. It suggests that grain coarsening in undoped BSCF seems faster than in Ni-doped materials at this stage. This observation is consistent with the idea that Ni

doping inhibits grain boundary mobility at 1100 ℃. Additionally, it can be observed that some secondary phase particles exist along grain boundaries, although most are located within the grains. It has been reported that precipitates on grain boundaries have been shown in two-dimensional theoretical simulations to have a significant effect in retarding grain growth even at very low volume concentrations in this range[294].

Figure 4.88 shows average grain size and the ratio of average grain sizes between undoped and Ni-doped BSCF as a function of sintering temperature. It can be clearly observed that grain growth rate decreases fast as the sintering temperature increases. The ratio of grain size between undoped and Ni-doped BSCF is 1.04 at 1000 ℃, increasing to 4.64 at 1150 ℃. This observation indicates that Ni doping inhibits grain boundary mobility more significantly with increasing the sintering temperature between 1000 ℃ and 1150 ℃.

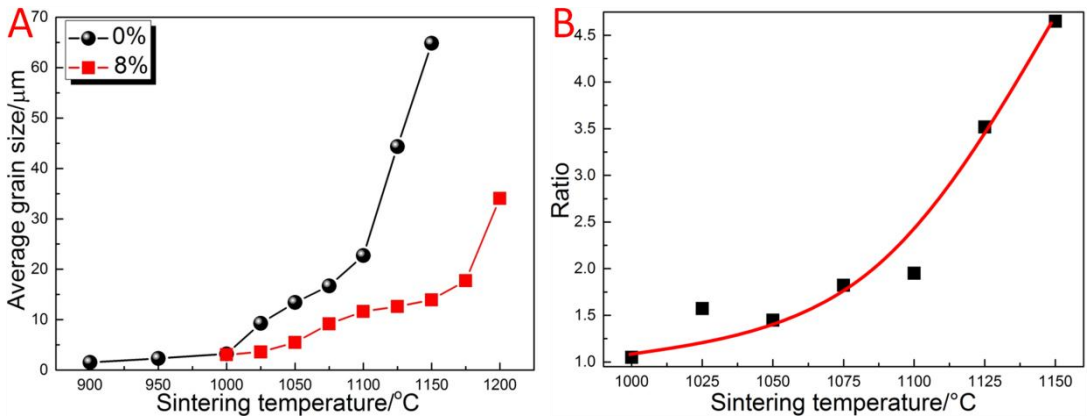

Figure 4.88 Average grain size (A) and the ratio of average grain sizes between undoped and Ni-doped BSCF (B) as a function of sintering temperature. The lines are a guide to the eye.

4.4 Mechanical properties of Ni-doped BSCF

4.4.1 Variation of Ni doping level in BSCF

In this section, all the Ni-doped BSCF samples (BSCF-NiX; X=0, 2, 4, 8, 15, 20, 25 mol%) were sintered at 1100 ℃ for 10 hours. Mechanical properties of Ni-doped BSCF

are evaluated and discussed. Hardness and Young's modulus are determined by the micro-indentation method. Fracture toughness is measured by indentation crack measurement method. Two 10×10 indentations matrices are measured for each sample.

4.4.1.1 Hardness and Young's modulus

Figure 4.89 shows the hardness and Young's modulus as a function of various Ni doping contents in BSCF sintered at 1100 ℃ for 10 hours. It is clearly observed that both hardness and Young's modulus show a non-monotonic trend with Ni doping content. In a lower doping level (from 0 to 8 mol%), they increase with Ni doping content, while at a higher doping level (from 8 to 25 mol%), they decrease with increasing Ni doping content.

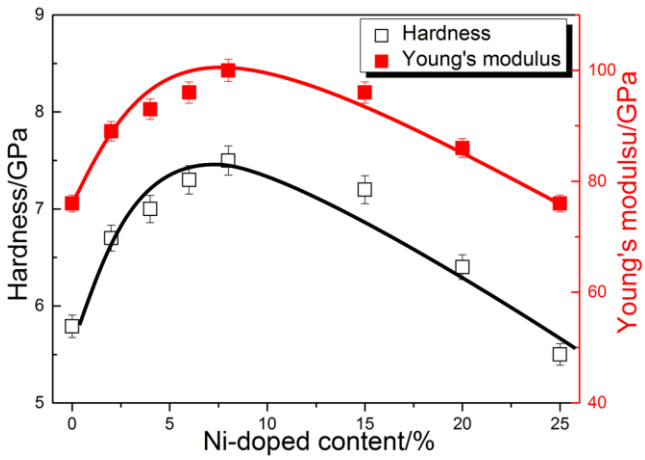

Figure 4.89 Hardness and Young's modulus as a function of different Ni doping contents. Solid lines are an eye-guidance.

As mentioned in Chapter 4.3, Ni doping causes an increase in the lattice parameter, an increase in porosity, and an increase in the amount of secondary phase but a decrease in grain size. In the case of hardness of Ni-doped BSCF, the increase from 0 to 4 mol% is probably caused by the strain induced by lattice distortion, because the ionic radius of Ni^{2+} is larger than those of both Fe^{4+} and Co^{3+}[275]. Ling *et al.*[295] have also found this phenomenon in other perovskite-structured materials and have attributed it to a solute solution strengthening mechanism. From 4 to 8 mol%, the increase in hardness of

Ni-doped BSCF is due to formation of secondary phase, because the hardness of a secondary phase (NiO) is much higher that of pure BSCF and the amount of secondary phase increases. Between 8 and 25 mol%, the reduction in hardness may be due to the sharp increase in the porosity. Although the amount of secondary phase increases with increasing the Ni doping level, the porosity of Ni-doped BSCF shows even more dramatic increase at this range. As a result, the hardness of secondary phases cannot compensate the loss caused by the increase in porosity.

With respect to the Young's modulus of Ni-doped BSCF, the curve shows a similar trend to that of hardness. As reported in the literature [296-298], doping can result in the change in bond length thereby changing bond energy. The Young's modulus significantly depends on the bond length and bond energy [297, 298]. It has been reported that Ni-O bond energy (392 kJ/mol) is higher than that of Co-O bond (368 kJ/mol) [299]. Therefore, the change in bond length and bond energy could be the reason for the increase in Young's modulus. From 4 to 8 mol% the increase in Young's modulus can be attributed to secondary phase particles, because the Young's modulus of secondary phase particle NiO (263 GPa) is much higher than that value of BSCF[300] and the amount of secondary phase increases. Between 8 and 25 mol%, the reduction in Young's modulus is due to the sharp increase in porosity, since Young's modulus is sensitive to the porosity as discussed previously.

4.4.1.2 Fracture toughness

Figure 4.90 shows the indentation fracture toughness for BSCF doped with different contents of Ni. It is clearly observed that Ni doping increases the fracture toughness compared with pure BSCF. There are three possible factors to explain this phenomenon. Firstly, Ni doping increases the Young's modulus when the content is below 8 mol%.

Secondly, the fracture toughness of NiO (1.65MPa $m^{0.5}$) [301] is larger than that of pure BSCF. Thirdly, crack deflection by secondary phase causes the increase in the fracture toughness.

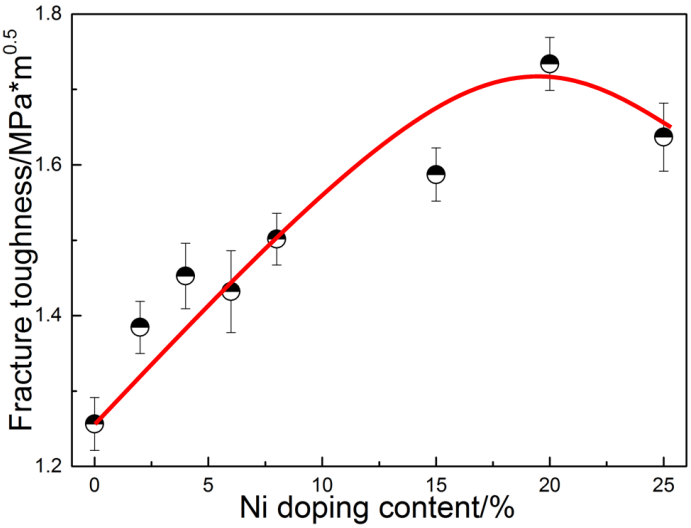

Figure 4.90 The indentation fracture toughness as a function of different Ni doping contents. Solid line is an eye-guidance. The line is a guide to the eye.

From 0 to 4 mol%, the increase in fracture toughness of Ni-doped BSCF can be ascribed to the increase in Young's modulus. From 4 to 8 mol%, the increase is attributed to the larger fracture toughness of secondary-phase NiO particles. In addition, the amount of secondary phases increases with increasing the content of Ni doping. As shown in Figure 4.91, no substantial crack deflection was found and crack propagation was primarily transgranular as for BSCF-Ni8.

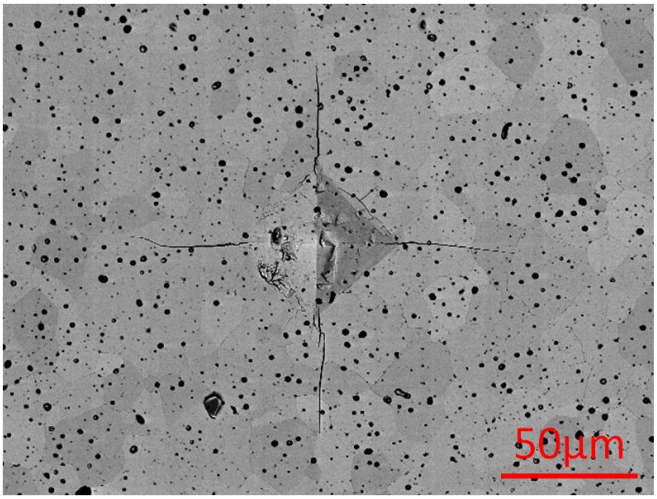

Figure 4.91 Typical indentation impression of BSCF-Ni8

As shown in Figure 4.92, secondary phase in Ni-doped BSCF samples can serve to deflect cracks for BSCF-Ni20 and results in a modest enhancement in fracture toughness, while straight cracks pass though the grains for less than 8 mol% Ni doping in BSCF. This phenomenon also can be observed in other perovskite-structured materials [145, 302, 303]. Between 20 and 25 mol%, the reduction in fracture toughness is probably due to the increase in porosity.

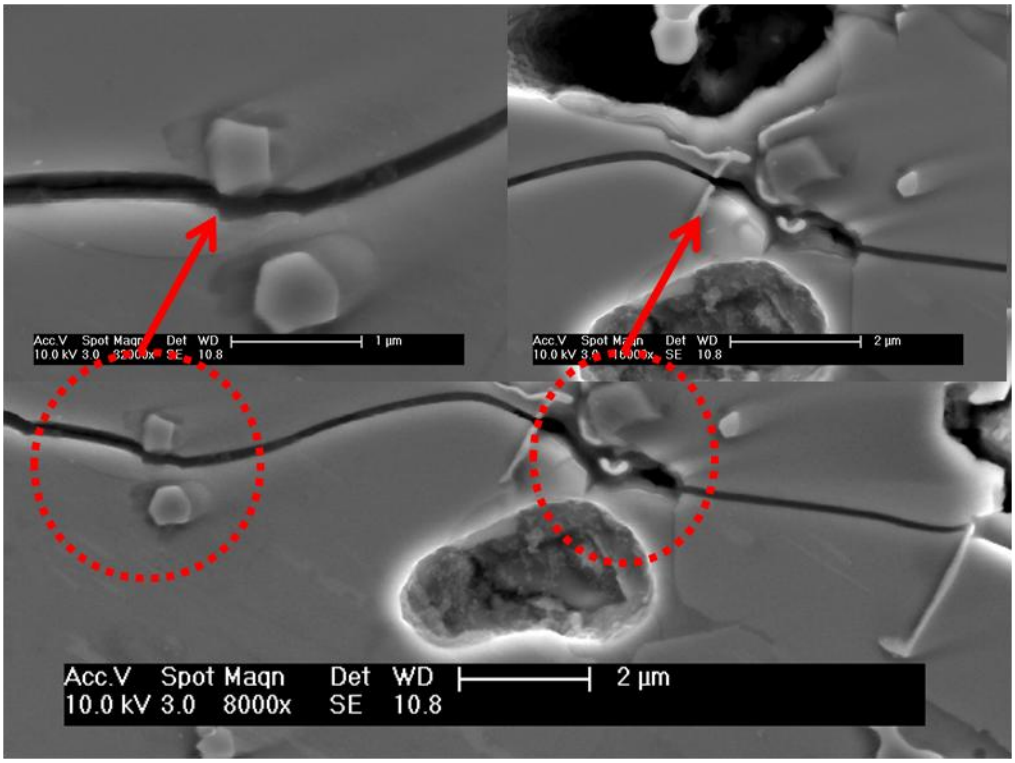

Figure 4.92 SEM micrographs of crack induced by Vickers indentation for BSCF-Ni20 (The inserted micrographs show the high magnification of cracks).

Figure 4.93 shows EDX mapping of secondary phase adjacent the crack in BSCF-Ni20 and NiO can be identified. Crack propagation has been changed as shown in Figure 4.93, which is believed to be affected by the thermal internal stress due to the thermal expansion mismatch between the matrix and the NiO particles. Because of the different thermal expansion coefficients (TEC) of the BSCF matrix and NiO, the thermal residual stress is produced between matrix grains and the NiO particles when the samples were cooling from the sintering temperature (1100 ℃) to room temperature. Assuming all

particle inclusions are spherical, the residual stress can be determined by the equation derived by Selsing[304]:

$$\sigma = \frac{(\alpha_m - \alpha_p)\Delta T}{\frac{1+\nu_m}{2E_m} + \frac{1-2\nu_p}{E_P}} \quad (4.48)$$

where α_m and α_p are the thermal expansion coefficient (TEC) of the matrix and the particle, respectively. ΔT is the temperature change; E and ν are the Young's modulus and Poisson's ratio respectively. In this study, the TEC of matrix and NiO particles are 19.7×10^{-6} and 17.1×10^{-6} $℃^{-1}$, respectively[305]. The Young's modulus and Poisson's ratio for NiO particles are 263 GPa and 0.37, respectively[305]. The thermal residual stress can be calculated from the Equation (4.48). The value of thermal residual stress yields 233 MPa in tension in the radial direction and 117 MPa in compression in the tangential direction at the interface of the matrix/NiO particles. Crack propagation can bypass the NiO particles induced by the thermal residual stress.

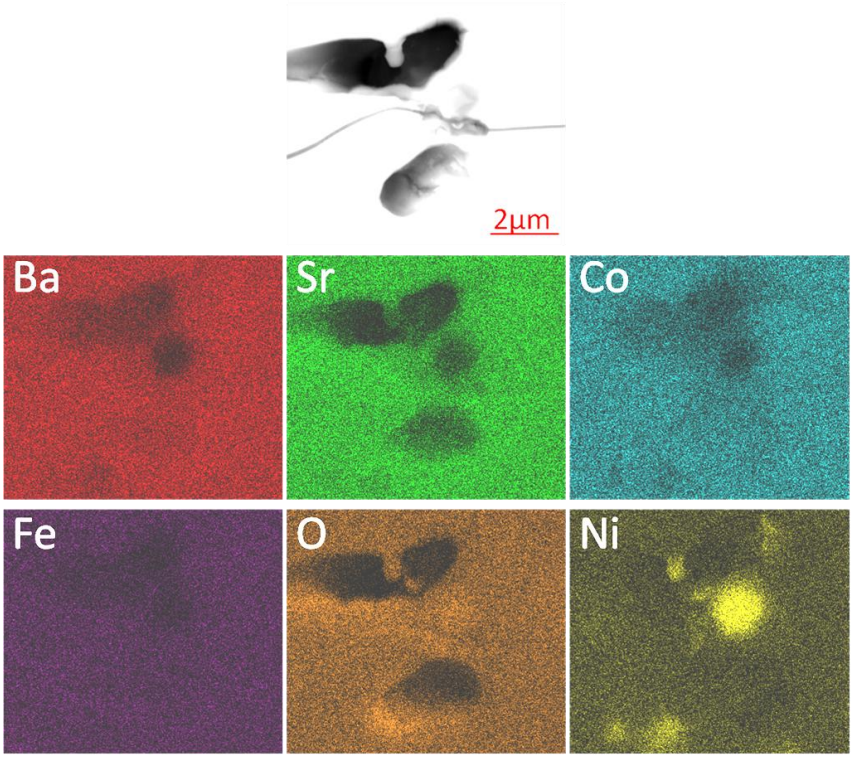

Figure 4.93 EDX mapping of secondary phase adjacent to the crack in BSCF-Ni20

As shown in the Figure 4.94, it can be observed that crack deflection induced by

secondary phase occurs under the surface. Therefore, the increase in fracture toughness can be attributed to crack deflection[303]. This phenomenon was also found in Ni doping in other ceramic materials[300].

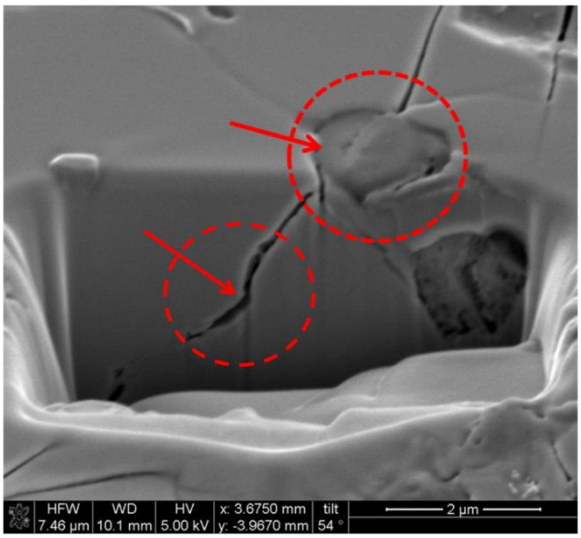

Figure 4.94 SEM image of the FIB-milled region BSCF-Ni20, where crack path below the surface has been exposed.

4.4.2 BSCF doped with 8 mol% Ni (BSCF-Ni8)

The BSCF-Ni8 samples were sintered between 1000 ℃ and 1200 ℃ and obtained different porosities. Hardness and Young's modulus are determined by micro-indentation method. Fracture toughness is measured by the indentation crack measurement method.

4.4.2.1 Hardness and Young's modulus

Figure 4.95 shows hardness and Young's modulus of BSCF-Ni8 as a function of sintering temperature. It can be clearly observed that hardness and Young's modulus show a similar trend. Both hardness and Young's modulus increase with increasing the sintering temperature between 1000 ℃ and 1175 ℃, then they decrease as the furthering increasing temperature up to 1200 ℃. Compared with the density as a function of this range of sintering temperatures, they show a similar trend. This

indicates that the porosity is the dominant factor for Young's modulus and hardness.

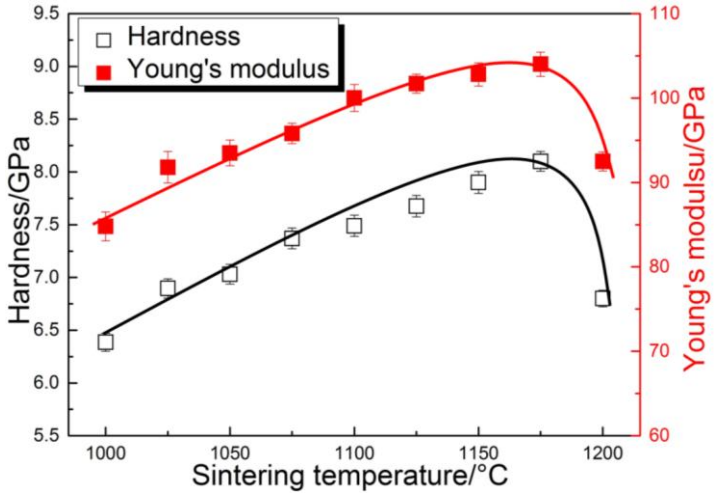

Figure 4.95 Hardness and Young's modulus of BSCF-Ni8 as a function of sintering temperature for 10 hours. Solid lines are an eye-guidance.

The hardness-porosity relationship can also be written in a linearised form such that

$$ln(H_{IT}) = -bp + ln(H_0) \tag{4.49}$$

where H_0 is the indentation hardness H normalised by the zero porosity hardness H_0. The normalisation that was used allowed a direct comparison among the data from this study in terms of the indentation hardness, H_{IT} (GPa). The linear fit to Equation (4.49) yields values of 9.02±0.64 GPa for H_0 and 3.10±0.42 for the constant b, with a R^2 value of 0.947 as shown in Figure 4.96.

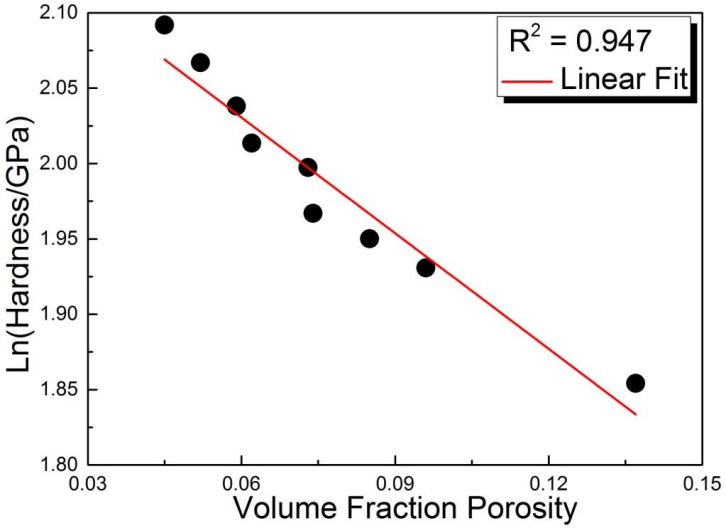

Figure 4.96 Hardness of BSCF-Ni8 as a function of porosity

The intrinsic hardness of BSCF-Ni8 is higher than that value of undoped BSCF, which

is indicative of the increased resistance to penetration of a polycrystalline assemblage. This can be attributed to solute solution strengthening mechanism.

The variation of the Young's modulus as a function of the sintering temperature is due to the different porosity. The Young's modulus of the porous sample is expressed by[248]:

$$E_{IT} = E_0 \cdot exp(-bp) \tag{4.50}$$

where E_0 is the Young's modulus of the fully dense material, p is volume fraction of the porosity and b is an empirical constant ranging between 2 to 5. The Young's modulus-porosity relationship can also be written in a linearised form such that

$$ln(E_{IT}) = -bp + ln(E_0) \tag{4.51}$$

As shown in Figure 4.97, the linear fit to Equation (4.51) yields values of 121.5±2.45 GPa for E_o and 4.18±0.29 for the constant b, with a R^2 value of 0.958. The intrinsic Young's modulus of BSCF-Ni8 is higher than that value of non-doped BSCF, suggesting that bond strengths of BSCF-Ni8 are higher than those of pure BSCF.

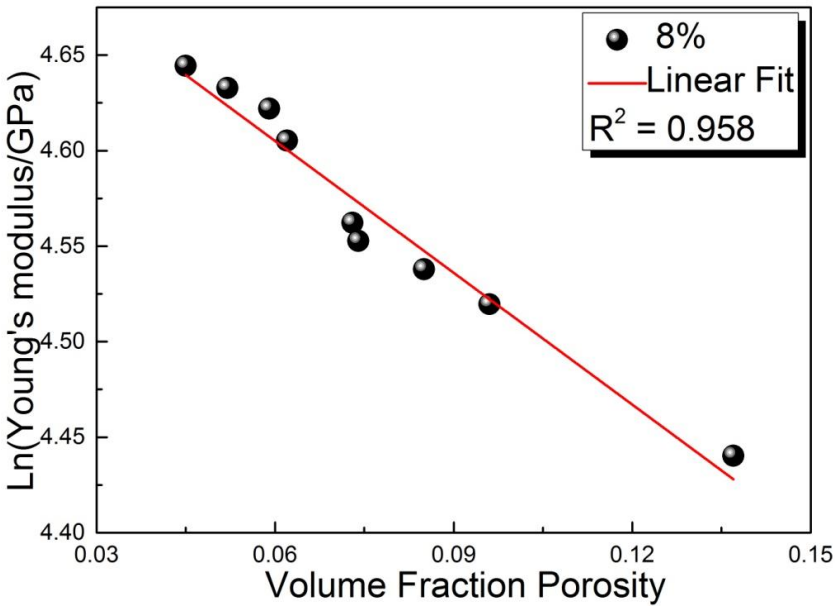

Figure 4.97 Young's modulus of BSCF-Ni8 as a function of porosity

4.4.2.2 Fracture toughness

The value of fracture toughness can be easily determined from indentation-induced crack[128]:

$$K_{ind} = \chi \frac{F}{C_0^{1.5}} \quad (4.52)$$

where C_0 is the crack length and $\chi=0.016(\frac{E}{H})^{0.5}$, representing the elastic plastic behavior. Furthermore, Young's modulus E and hardness H are also directly accessible from the depth sensitive indentation test.

Porosity is well-known to reduce fracture toughness. According to Rice's model[180], it has been shown that the intrinsic toughness can be associated with the measured toughness:

$$K_{IC} = K_{IC}^{0} exp(-bp) \quad (4.53)$$

where K_{IC} and K_{IC}^{0} are the measured and intrinsic toughness (zero-porosity), respectively; *p* is the porosity and b is a constant. It has been reported that the value of b for fracture toughness is between 2 and 5 for many ceramics.

As shown in Figure 4.98, the intrinsic fracture toughness of BSCF-Ni8 can be obtained from the linear fit of the Equation (4.53) and get the value of 1.63 MPa $m^{0.5}$, and 2.43±0.31 for the constant b, with a R^2 value of 0.939. Excluding the influence of porosity on the fracture toughness, the intrinsic toughness of BSCF-Ni8 is significantly better than undoped BSCF due to the increase in Young's modulus. In other words, it suggests that Ni doping can offer an advantage at least in terms of mechanical integrity at room temperature. However, it is still significantly lower than yttria-stabilised zirconia, a typical ceramic material.

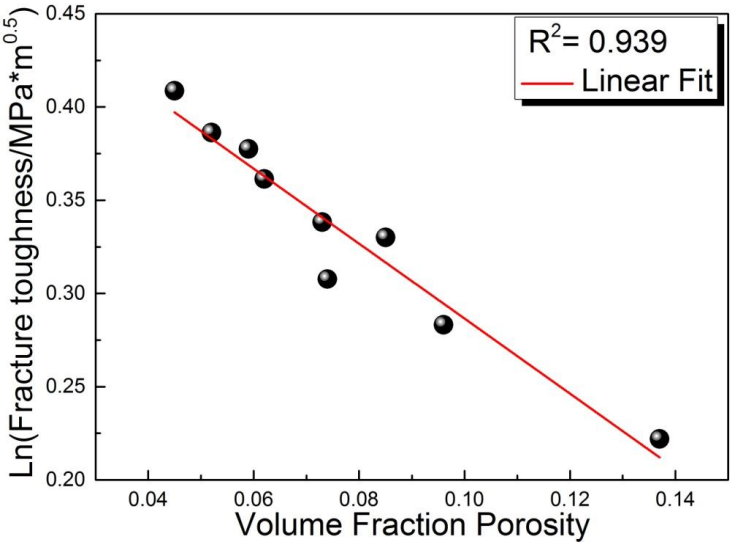

Figure 4.98 Fracture toughness of BSCF-Ni8 as a function of porosity

As shown in Figure 4.99, Hardness, Young's modulus and fracture toughness have the similar dependency of porosity. All of them decrease with increasing the porosity. Compared with these three curves, the relative Young's modulus is the smallest one while the fracture toughness is the largest one at the same porosity. In other words, the reduction in fracture toughness is relatively small compared with the change in Young's modulus with porosity. This phenomenon may originate from the deteriorated microstructure of BSCF-Ni8 with extra pores and microcracks as obstacles during fracture.

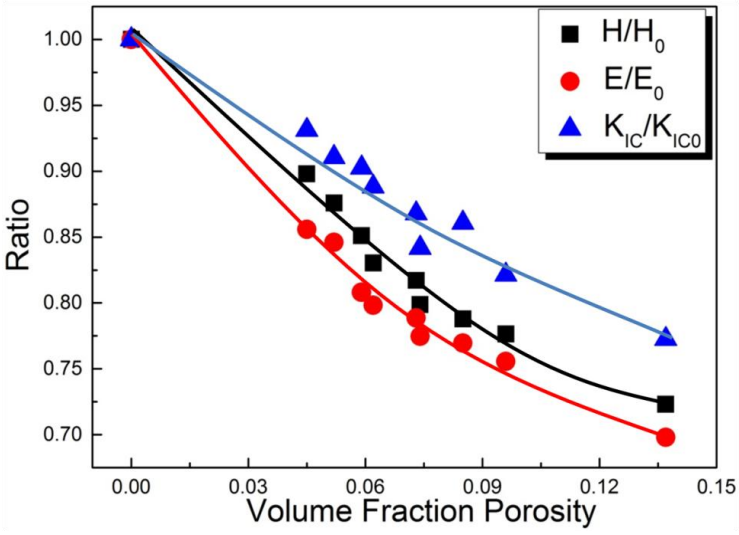

Figure 4.99 Relative hardness H/H_0, relative Young's modulus E/E_0, relative fracture toughness K_{IC}/K_{IC}^0 as a function of porosity; H_0, E_0, and K_{IC}^0 correspond to the data of BSCF-Ni8 with the porosity of zero. The lines are a guide to the eye.

Chapter 5 Study of grain orientation in BSCF ceramics by EBSD

5.1 Introduction

Based on $SrCoO_{3-\delta}$ materials with oxygen permeability, improvements have been realised by the substitution of foreign ions on the A and/or B sites [34, 35, 38, 49]. The aims of these dopants are to either keep better chemical stability and/or increase oxygen permeability.

In the case of copper doped systems in perovskite materials, it has been reported that $La_{0.6}Sr_{0.4}Co_{0.8}Cu_{0.2}O_{3-\delta}$ exhibits the best oxygen permeability among $La_{1-x}Sr_xCo_{1-y}M_yO_{3-\delta}$(M=Cu, Fe, Ca) perovskite materials[306]. Additionally, Zhao *et al*. [307]have found that $Ba_{0.5}Sr_{0.5}Fe_{0.8}Cu_{0.2}O_{3-\delta}$ shows high conductivity at relatively low temperature, which enable it to be used as a cathode material in solid oxide fuel cell.

With respect to Nb doped systems in perovskite materials, it has been found that $SrCo_{0.9}Nb_{0.1}O_{3-\delta}$ exhibits higher electrical conductivity, higher oxygen permeability and better phase stability as well compared with pure $SrCoO_3$[308]. In addition, Fang *et al*.[309] have reported that partial substitution of Nb in BSCF maintains better phase stability at high temperature and leads to lower thermal expansion coefficiency compared with pure BSCF.

In terms of Ni doped systems in perovskite materials, Ni doped into the B site of $LaFeO_3$ causes higher ionic conductivity and higher oxygen permeability compared with pure $LaFeO_3$[268]. Additionally, it has been found that partial substitution of Ni in $LaMO_3$(M=Co,Ga) shows higher electrical conductivity and higher oxygen permeability

compared with $LaMO_3$(M=Co,Ga)[50, 310-312].

As discussed above, Cu, Nb, and Ni dopants have improved the phase stability, conductivity, and /or permeability of different systems in perovskite materials. It has been found that the oxygen permeability of perovskite membranes significantly depends on microstructure features, such as grain size, grain orientation and grain boundary structure. Grain orientation is one of the most important properties of microstructure. Additionally, it has been reported that dopants can influence the grain orientation of ceramics materials[313, 314]. In this study, the effect of dopants(Ni, Nb and Cu) on grain orientation will be assessed.

5.2 Experimental procedure

5.2.1 Sample preparation

Powders of $Ba_{0.5}Sr_{0.5}(Co_{0.8}Fe_{0.2})_{0.92}Nb_{0.08}O_{3-\delta}$(abbreviated as BSCF-Nb) were prepared by solid state reaction. Stoichiometric amounts of $BaCO_3$, $SrCO_3$, Co_3O_4, Fe_2O_3, and Nb_2O_5 (Sigma-Aldrich, > 99%) were ball-milled for 24 h. The powder mixtures were dried, and calcined at 900 ℃ for 10 hours in air and then cooled (180 ℃/hour) to RT. Powders of $Ba_{0.5}Sr_{0.5}(Co_{0.8}Fe_{0.2})_{0.92}Cu_{0.08}O_{3-\delta}$ (abbreviated as BSCF-Cu) were synthesised by solid state reactions. $BaCO_3$, $SrCO_3$, Co_3O_4, Fe_2O_3, and CuO (Sigma-Aldrich, > 99%) were weighted according to their stoichiometry and ball-mixed. The mixtures were calcined at 900 ℃ for 10 h. The detailed preparation procedure of these doped BSCF powders are described by Lu[217]. Preparation methods of powders of $Ba_{0.5}Sr_{0.5}Co_{0.8}Fe_{0.2}O_{3-\delta}$ and $Ba_{0.5}Sr_{0.5}(Co_{0.8}Fe_{0.2})_{0.92}Ni_{0.08}O_{3-\delta}$ (abbreviated as BSCF-Ni) have been described in Chapter 3.

All the powders were sintered at 1100 ℃ for 10 hours, and the heating/cooling rates were set to be 180 ℃/hour. The samples were ground with several different sizes of grinding paper from P400 to P1200, and then polished with diamond paste descending from 6 μm to 0.25 μm. Then, colloidal silica liquid (OPS) was used at the final stage of polishing.

5.2.2 Electron Backscattered Diffraction (EBSD)

Electron backscattered diffraction (EBSD) technique is broadly applied in quantitative metallography, especially for subgrain imaging and texture determination [315-317]. Backscatter Kikuchi patterns generated from an EBSD system are collected for each point of analysis. The crystallographic orientation is determined after indexing of the corresponding diffraction pattern. For the EBSD sample preparation, the sintered samples were ground and polished to achieve a smooth strain-free surface. All the EBSD data were collected in a Quanta 650 SEM equipped with a NordlysNano EBSD detector (Oxford Instruments). The results were obtained under an accelerating voltage of 20 kV and a probe current of 20 nA, a sample tilt 70 degrees and the working distance 15 mm. The data was processed and analysed by HKL Channel 5 software.

5.3 Results and discussion

Figure 5.1 shows EBSD images of undoped BSCF and doped BSCF (Ni, Nb and Cu) sintered at 1100 ℃ for 10 hours. The colours in the images represent the crystallographic orientation of each grain relative to the sample surface normal. The black spots in Figure 5.1 are areas that have not been indexed, corresponding to pores. The pores of BSCF, BSCF-Ni, and BSCF-Cu are located both inside the grains and at

the grain boundaries. However, in the case of BSCF-Nb, most pores are located at the triple junctions. The overall porosity (determined by image analysis) was about 4.4%, 5.6%, 12.2% and 9.1% for BSCF, BSCF-Ni BSCF-Cu and BSCF-Nb, respectively.

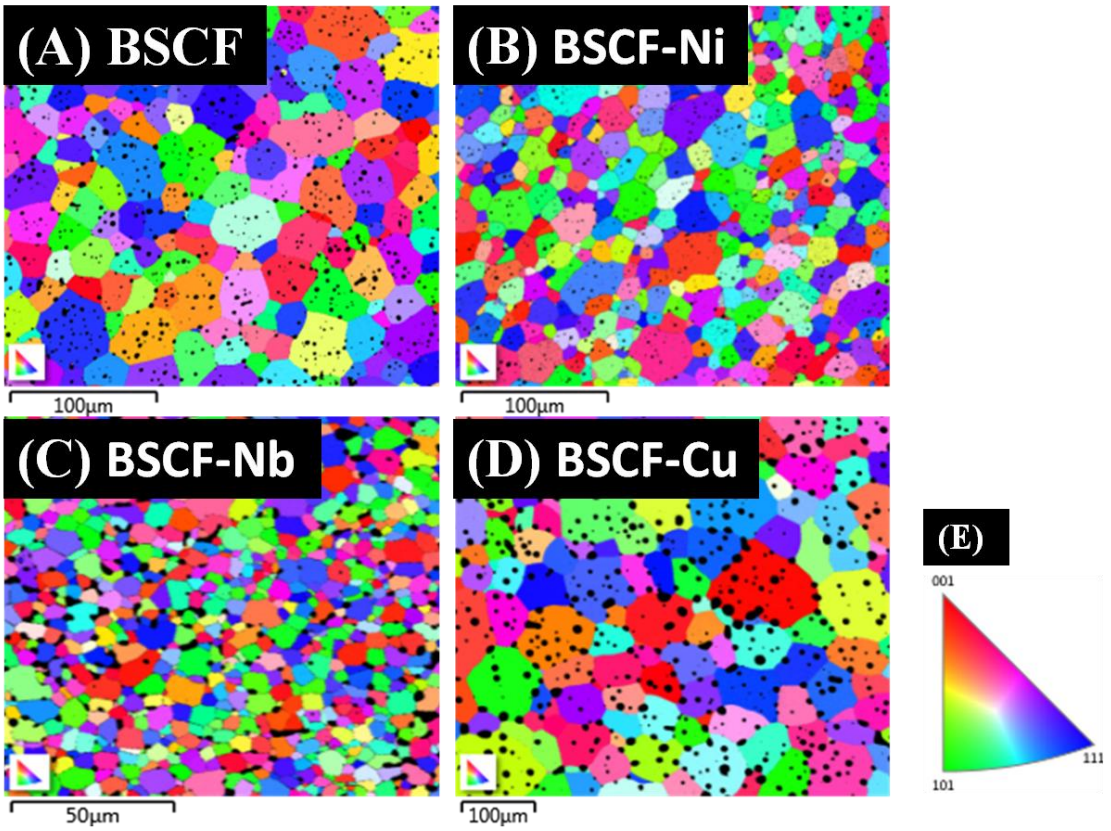

Figure 5.1 EBSD images of undoped BSCF and doped BSCF with different dopants sintered at 1100 ℃ for 10 hours:(A)BSCF; (B)BSCF-Ni; (C)BSCF-Nb; (D)BSCF-Cu; (E) the crystallographic orientations are shown in the stereographic triangle

The grain size distributions and grain aspect ratio distributions of undoped BSCF and doped BSCF sintered at 1100 ℃ for 10 hours are presented in Figure 5.2. It has been reported that dopant can induce abnormal grain growth in some ceramics systems [283-286]. As shown in Figure 5.1, all the samples of undoped and doped BSCF show regular equiaxed grains and no abnormal grain growth can be found. Specifically, Cu doping positively affects grain growth of BSCF while Nb doping negatively affects grain growth. It is clearly observed in Figure 5.2(A) that dopants have little influence on the shape of the grain size distributions but the profile shifts with different dopants. This phenomenon has also been reported in other doped ceramic systems [79, 80, 287].

From the literature [288, 289], it has been observed that doping can influence the grain aspect ratio of ceramic materials as well. However, grain aspect ratios of doped BSCF are approximately 1.8 and are almost the same as those of undoped BSCF as shown in Figure 5.2(B).

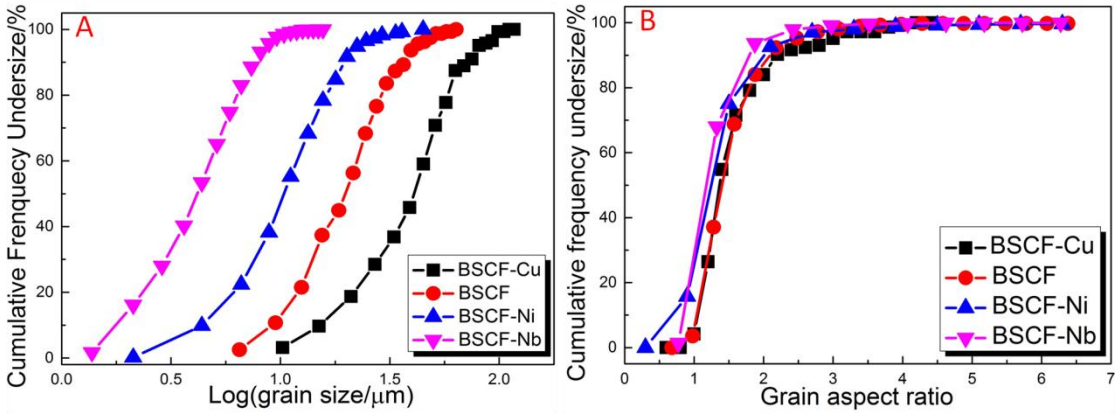

Figure 5.2 Grain size distributions (A) and grain aspect ratio distributions (B) of undoped BSCF and BSCF with different dopants (Ni, Nb and Cu) sintered at 1100 ℃ for 10 hours

In order to further explore texture information, the distributions of the transverse direction (TD), rolling direction (RD) and normal direction (ND) with respect to crystallographic axes of the cubic BSCF phase are plotted in inverse pole figures (IPFs), as shown in Figure 5.3. The poles are distributed evenly over the inverse pole figures, suggesting that the undoped and doped BSCF grains are almost randomly oriented. In other words, it is apparent from the IPFs that none of the specimens exhibits a significant texture (i.e. preferred orientation). The orientation image maps from undoped and Ni-doped BSCF were obtained at the same magnification. Due to the smaller grain size of the Nb-doped BSCF and larger grain size of the Cu-doped BSCF, an enlarged and reduced magnification has been applied, respectively. Table 5.1 summarises the EBSD acquisition parameters and the specimen grain size.

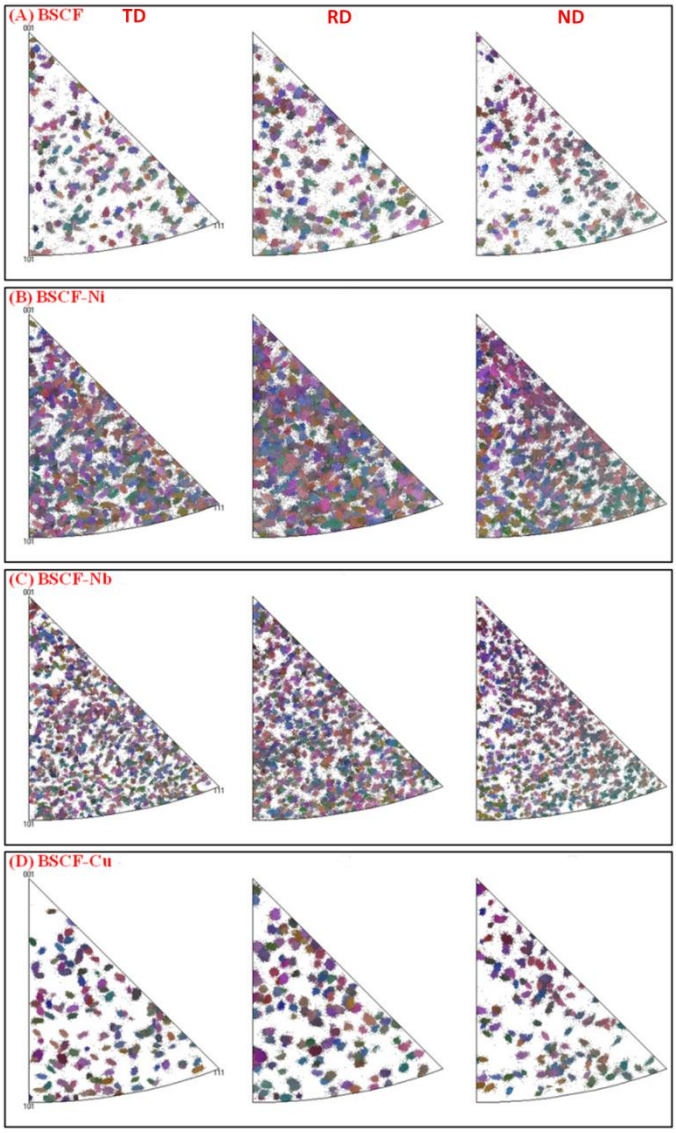

Figure 5.3 Inverse pole figure of undoped BSCF and doped BSCF sintered at 1100 ℃ for 10 hours:(A)BSCF; (B)BSCF-Ni; (C)BSCF-Nb; (D)BSCF-Cu.

Table 5.1 EBSD acquisition parameters and grain size data

Materials	Data points	Scan area(μm^2)	Step size(μm)	Total number of grains	Average grain size(μm)*
BSCF	929418	305×267	0.2828	161	22.70
BSCF-Ni	1391545	305×267	0.2309	519	11.64
BSCF-Nb	267074	134×117	0.2542	703	4.86
BSCF-Cu	1059862	585×511	0.5163	144	44.86

*Average grain size (Diameter $= \sqrt{4S/\pi}$), S is grain area

It is found that the distributions of grain boundary misorientation angles for both undoped and doped BSCF agree well with the theoretical distribution of a randomly oriented sample, as illustrated in Figure 5.4. Over 97% of high angle grain boundaries

(>15 °) exist in both undoped and doped BSCF. Additionally, for each misorientation interval, the number fraction for the three different doped specimens were averaged and compared with those of undoped BSCF as shown in Figure 5.5. Overall, the dopants were found to exert little influence on the overall misorientation angle distribution.

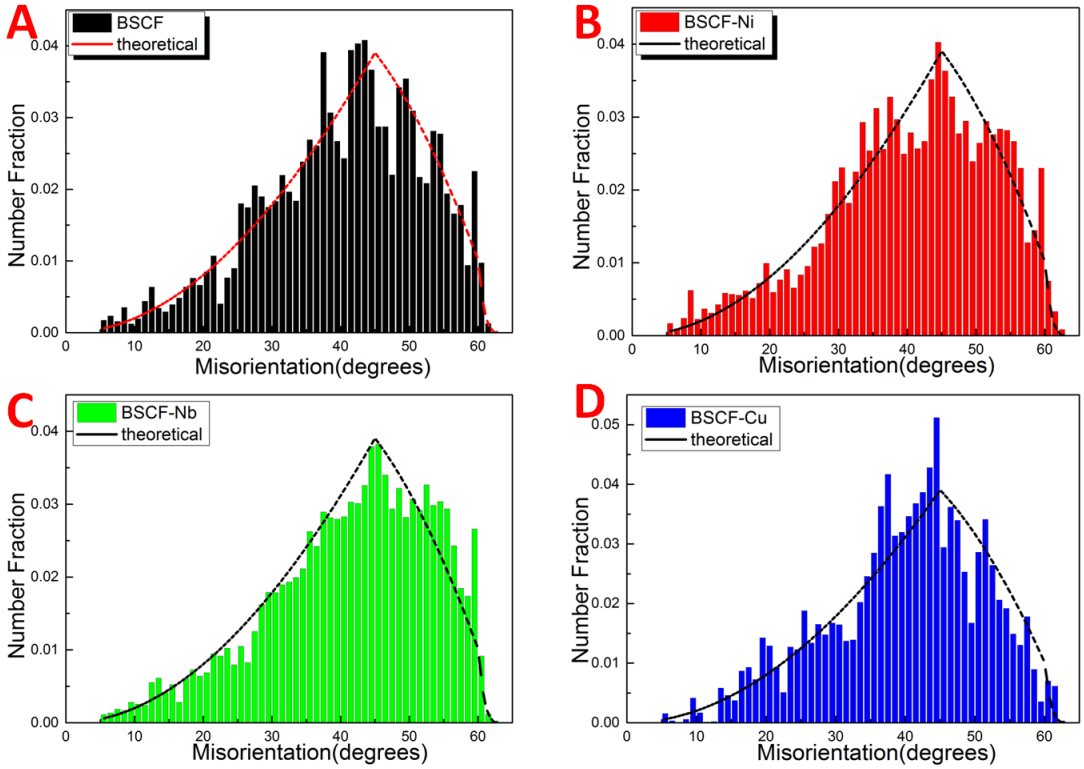

Figure 5.4 Misorientation angle histograms for undoped and various doped BSCF: (A)BSCF; (B)BSCF-Ni; (C)BSCF-Nb; (D)BSCF-Cu;

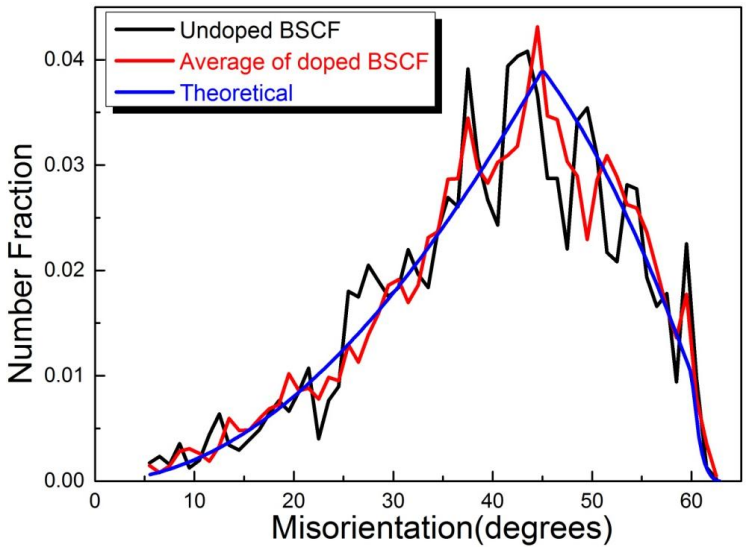

Figure 5.5 Comparison of misorientation angle distributions between doped and undoped BSCF. The curve from doped BSCF represents the average misorientation distribution of the three different doped BSCF

Therefore, it has been demonstrated that dopants have little influence on the lattice preferred orientation and the distributions of grain boundary misorientation angles of BSCF ceramics.

5.4 Summary

EBSD mapping on BSCF with different dopants (Ni, Nb and Cu) was successfully conducted. The undoped and doped BSCF samples did not show any significant texture. It has also been demonstrated that dopants have little influence on grain orientation and the distribution of grain boundary misorientation angles of BSCF.

Chapter 6 Conclusions and suggestions for future work

In this chapter, the main conclusions are extracted from the experimental results and the analyses of underlying mechanisms. The conclusions for undoped and Ni-doped BSCF are presented separately.

6.1 BSCF

In terms of sintering behaviours, the grain growth kinetics was studied using the simplified phenomenological grain growth kinetic equation $D^n=K_0texp(-Q/RT)$ together with microstructure and densification of the sintered samples. The grain growth exponent values (n) and the apparent activation energy were found to be 3 and 651 kJ/mol, respectively. Grain boundary diffusion was the dominant controlling mechanism and the Ba/Sr diffusion can be the rate-controlling species during the sintering process of BSCF at 1100 ℃. When the grain size of the individual distribution was nondimensionalised by their median size, the dimensionless grain size distribution curves became a single self-similar grain size distribution plot. The dimensionless grain size distribution was invariable independent of the sintering temperature-time conditions employed. This strongly indicated that a lower sintering temperature and/or a shorter dwell time did not make the grain size distribution narrower, although it showed a finer microstructure. In the light of these observations, an algorithm was proposed for predicting the grain size distributions as a function of the sintering temperature-time profiles. In addition, the average grain aspect ratio and grain size aspect ratio distribution were constant irrespective of the sintering temperature-time profiles.

With respect to mechanical properties, the fracture stress of BSCF was measured by three-point and ring-on-ring bending tests. Although the fracture stress determined by three-point bending tests was higher than that measured by ring-on-ring test, by utilising Weibull statistics a close prediction can be made of the three-point values from the ring-on-ring values. The fracture surfaces showed only a transgranular fracture mode between RT and 800 ℃. Annealing reduced the fracture toughness of BSCF determined by indentation strength method. The intrinsic hardness, intrinsic Young's modulus and intrinsic fracture toughness of BSCF determined by micro-indentation method were 7.05 GPa, 105.6 GPa and 1.49 MPa $\cdot m^{0.5}$, respectively. The crack shape was determined as median-radial crack mode. The subcritical crack growth (SCG) of BSCF was also studied using constant load method at room temperature and using constant stress rate method at 800 ℃. The high value of SCG parameter, n=24.3, at room temperature indicated that BSCF was not very susceptible to SCG while the value of n 13.8 showed that it was much more sensitive at 800 ℃. The results were subsequently used as the basis for a strength–probability–time (SPT) lifetime prediction. On the basis of the SPT diagram, the stress for a lifetime of 40 years should not exceed 27 and 4.5 MPa to assure a failure probability of 1% at RT and 800 ℃, respectively.

6.2 Ni-doped BSCF

In terms of sintering behaviours, the porosity and grain size decreased with increasing the Ni doping contents. Ni doping retarded the densification of BSCF by means of the restraint of the diffusion rate and the reduction in the sintering stress. In addition, Ni doping constrained the grain growth due to both Ni solute and secondary phase particles.

Ni doping had little influence on grain size distributions and grain aspect ratio distributions. The grain growth exponent values (*n*) and the apparent activation energy were found to be 4.7 and 803 kJ/mol for 8 mol% Ni-doped BSCF, respectively. Both grain boundary and lattice diffusions were the equally dominant controlling mechanisms for BSCF-Ni8 at 1100 ℃.

With respect to mechanical properties, both hardness and Young's modulus showed a non-monotonic trend with Ni doping content. In a lower doping level (0 to 8 mol%), they increased with Ni doping content, while at a higher doping level (8 to 25mol%), they decreased with increasing Ni doping content. The porosity and secondary phase were the dominant factors for this phenomenon. The intrinsic hardness, intrinsic Young's modulus and intrinsic fracture toughness of 8 mol% Ni-doped BSCF determined by micro-indentation method were 9.02 GPa, 121.5 GPa and 1.63 MPa·$m^{0.5}$, respectively.

6.3 Future Work

(1) Compare mechanical properties between undoped BSCF and Ni-doped BSCF between RT and high temperature.

In Chapter 4.2, BSCF shows an anomalous behaviour of Young's modulus between RT and 300 ℃ due to the Co^{3+} spin transition. When Co is partially substituted by Ni, it is still unknown what happens to Young's modulus of Ni-doped BSCF at elevated temperature. In addition, it should be noted that Ni doping positively affects mechanical properties of BSCF at RT. However, it is also unclear what happens to mechanical properties of Ni-doped BSCF at elevated temperature.

(2) Construct the modelling of pore size distribution of BSCF sintered under different conditions and predict the pore size distribution of BSCF

In Chapter 4.1, the microstructures of BSCF sintered under different conditions are observed, including grain size and pore size. Grain size and grain size distributions have been analysed. In future, the modelling of pore size distribution will be also constructed.

(3) Determine the secondary phase along grain boundary of fracture surface of BSCF by TEM

In Chapter 4.2, small particles along grain boundaries of fracture surfaces at high temperature are observed. However, it is still unknown what phase they are. In future, TEM will be applied to determine these small particles along grain boundary.

(4) Physical property tests

In Chapter 4.1 and Chapter 4.3, the microstructures of undoped and Ni-doped BSCF have been analysed. Since these functional materials mentioned can be applied in SOFC, it should be noted that physical properties such as impedance can be also assessed. In addition, these physical properties highly depend on microstructure.

References

[1] Conti J, Holtberg P, Doman L. International energy outlook 2011. US Energy Information Administration, Washington, DC, Paper No DOE/EIA-0484 2011.
[2] Conti JJ, Holtberg P, Beamon J, Schaal A, Ayoub J, Turnure J. Annual energy outlook 2011 with projections to 2035. United States of America Department of Energy Information Office of Integrated and International Energy Analysis Available at http://wwweia gov/neic/speeches/newell12162010 pdf2011.
[3] Bose AC. Inorganic membranes for energy and environmental applications. Pittsburgh, PA, USA: Springer; 2009.
[4] Colombo KE. Mixed-Conducting Membrane-based Gas Turbine Power Plant for CO_2 Capture: NTNU; 2009.
[5] Norman CJ. Synthesis and Characterisation of Barium Strontium Cobalt Iron Oxide Mixed Ionic and Electronic Conductors. PhD Thesis 2013.
[6] Santos J, Cruz P, Regala T, Magalhaes F, Mendes A. High-purity oxygen production by pressure swing adsorption. Industrial & Engineering Chemistry Research 2007;46:591-9.
[7] Smith A, Klosek J. A review of air separation technologies and their integration with energy conversion processes. Fuel Processing Technology 2001;70:115-34.
[8] Metz B, Davidson O, de Coninck H, Loos M, Meyer L. Carbon dioxide capture and storage. New York, USA: Cambridge University Press; 2005.
[9] Huang B. Thermo-mechanical properties of mixed ion electron conducting membrane materials: Forschungszentrum Jülich; 2011.
[10] Armstrong PA, Bennett DL, Foster E, Stein V. Ceramic membrane development for oxygen supply to gasification applications. Proceedings of the Gasification Technologies Conference, San Francisco, CA, USA2002.
[11] Repasky JM, Stein VE, Armstrong PA, Quintrell MS, Maxson A, Bartone LM. Ceramic and Coal: ITM Oxygen for Power Generation with Reduced CO_2-Emissions, Detailed Engineering Study Results. 2013.
[12] Sunarso J, Baumann S, Serra J, Meulenberg W, Liu S, Lin Y, et al. Mixed ionic-electronic conducting (MIEC) ceramic-based membranes for oxygen separation. Journal of Membrane Science 2008;320:13-41.
[13] Baumann S, Schulze-Küppers F, Roitsch S, Betz M, Zwick M, Pfaff E, et al. Influence of sintering conditions on microstructure and oxygen permeation of $Ba_{0.5}Sr_{0.5}Co_{0.8}Fe_{0.2}O_{3-\delta}$ (BSCF) oxygen transport membranes. Journal of Membrane Science 2010;359:102-9.
[14] Shao Z, Dong H, Xiong G, Cong Y, Yang W. Performance of a mixed-conducting ceramic membrane reactor with high oxygen permeability for methane conversion. Journal of Membrane Science 2001;183:181-92.
[15] Bouwmeester HJM, Burggraaf AJ. Dense ceramic membranes for oxygen separation. Membrane Science and Technology 1996;4:435-528.
[16] Kingery W, Bowen H, Uhlmann D. Introduction to ceramics 1976.
[17] Taroco H, Santos J, Domingues R, Matencio T. Ceramic Materials for Solid Oxide Fuel Cells: INTECH Open Access Publisher; 2011.
[18] Bhalla A, Guo R, Roy R. The perovskite structure–a review of its role in ceramic science and technology. Material Research Innovations 2000;4:3-26.

[19] Huang B, Malzbender J, Steinbrech R, Singheiser L. Discussion of the complex thermo-mechanical behavior of $Ba_{0.5}Sr_{0.5}Co_{0.8}Fe_{0.2}O_{3-\delta}$. Journal of Membrane Science 2010;359:80-5.
[20] Pena M, Fierro J. Chemical structures and performance of perovskite oxides. Chemical Reviews-Columbus 2001;101:1981-2018.
[21] Zhou W, Ran R, Shao Z. Progress in understanding and development of $Ba_{0.5}Sr_{0.5}Co_{0.8}Fe_{0.2}O_{3-\delta}$-based cathodes for intermediate-temperature solid-oxide fuel cells: A review. Journal of Power Sources 2009;192:231-46.
[22] Li C, Soh KCK, Wu P. Formability of ABO_3 perovskites. Journal of Alloys and Compounds 2004;372:40-8.
[23] McIntosh S, Vente JF, Haije WG, Blank DH, Bouwmeester HJ. Structure and oxygen stoichiometry of $SrCo_{0.8}Fe_{0.2}O_{3-\delta}$ and $Ba_{0.5}Sr_{0.5}Co_{0.8}Fe_{0.2}O_{3-\delta}$. Solid State Ionics 2006;177:1737-42.
[24] Shao Z, Yang W, Cong Y, Dong H, Tong J, Xiong G. Investigation of the permeation behavior and stability of a $Ba_{0.5}Sr_{0.5}Co_{0.8}Fe_{0.2}O_{3-\delta}$ oxygen membrane. Journal of Membrane Science 2000;172:177-88.
[25] Shao Z, Haile SM. A high-performance cathode for the next generation of solid-oxide fuel cells. Nature 2004;431:170-3.
[26] Deng Z, Yang W, Liu W, Chen C. Relationship between transport properties and phase transformations in mixed-conducting oxides. Journal of Solid State Chemistry 2006;179:362-9.
[27] Tai L, Nasrallah M, Anderson H. Thermochemical stability, electrical conductivity, and Seebeck coefficient of Sr-doped $LaCo_{0.2}Fe_{0.8}O_{3-\delta}$. Journal of Solid State Chemistry 1995;118:117-24.
[28] Kharton V, Yaremchenko A, Kovalevsky A, Viskup A, Naumovich E, Kerko P. Perovskite-type oxides for high-temperature oxygen separation membranes. Journal of Membrane Science 1999;163:307-17.
[29] Kruidhof H, Bouwmeester H, Doorn Rv, Burggraaf A. Influence of order-disorder transitions on oxygen permeability through selected nonstoichiometric perovskite-type oxides. Solid State Ionics 1993;63:816-22.
[30] Qiu L, Lee T, Liu L-M, Yang Y, Jacobson A. Oxygen permeation studies of SrCo 0.8 Fe 0.2 O 3− δ. Solid State Ionics 1995;76:321-9.
[31] Kharton V, Tikhonovich V, Shuangbao L, Naumovich E, Kovalevsky A, Viskup A, et al. Ceramic microstructure and oxygen permeability of $SrCo(Fe,M)O_{3-\delta}$ (M=Cu or Cr) perovskite membranes. Journal of the Electrochemical Society 1998;145:1363-73.
[32] Kovalevsky A, Kharton V, Tikhonovich V, Naumovich E, Tonoyan A, Reut O, et al. Oxygen permeation through $Sr(Ln)CoO_{3-\delta}$ (Ln=La, Nd, Sm, Gd) ceramic membranes. Materials Science and Engineering: B 1998;52:105-16.
[33] Teraoka Y, Zhang H-M, Furukawa S, Yamazoe N. Oxygen permeation through perovskite-type oxides. Chemistry Letters 1985;14:1743-6.
[34] Teraoka Y, Zhang H, Okamoto K, Yamazoe N. Mixed ionic-electronic conductivity of $La_{1-x}Sr_xCo_{1-y}Fe_yO_{3-\delta}$ perovskite-type oxides. Materials Research Bulletin 1988;23:51-8.
[35] Teraoka Y, Zhuang H, Furukawa S, Yamazoe N. Oxygen permeation through perovskite-type oxides. Chemistry Letters 1985:1743-6.
[36] McIntosh S, Vente JF, Haije WG, Blank DH, Bouwmeester HJ. Oxygen stoichiometry and chemical expansion of $Ba_{0.5}Sr_{0.5}Co_{0.8}Fe_{0.2}O_{3-\delta}$ measured by in situ neutron diffraction. Chemistry of Materials 2006;18:2187-93.
[37] Švarcová S, Wiik K, Tolchard J, Bouwmeester HJM, Grande T. Structural instability of cubic perovskite $Ba_xSr_{1-x}Co_{1-y}Fe_yO_{3-\delta}$. Solid State Ionics

2008;178:1787-91.
[38] Shao Z, Xiong G, Tong J, Dong H, Yang W. Ba effect in doped $Sr(Co_{0.8}Fe_{0.2})O_{3-\delta}$ on the phase structure and oxygen permeation properties of the dense ceramic membranes. Separation and Purification Technology 2001;25:419-29.
[39] Gellings PJ, Bouwmeester H. Handbook of Solid State Electrochemistry: CRC press; 1997.
[40] Badwal SPS, Ciacchi FT. Ceramic membrane technologies for oxygen separation. Advanced Materials 2001;13:993-6.
[41] Li X. Long Term Stability and Permeability of Mixed Ion Conducting Membranes under Oxyfuel Conditions: Forschungszentrum Jülich; 2014.
[42] Lee T, Yang Y, Jacobson A, Abeles B, Zhou M. Oxygen permeation in dense $SrCo_{0.8}Fe_{0.2}O_{3-\delta}$ membranes: surface exchange kinetics versus bulk diffusion. Solid State Ionics 1997;100:77-85.
[43] Sunarso J, Liu S, Lin Y, da Costa JD. Oxygen permeation performance of $BaBiO_{3-\delta}$ ceramic membranes. Journal of Membrane Science 2009;344:281-7.
[44] Lin YS, Wang W, Han J. Oxygen permeation through thin mixed‐conducting solid oxide membranes. AIChE journal 1994;40:786-98.
[45] Wang H, Tablet C, Feldhoff A, Caro J. Investigation of phase structure, sintering, and permeability of perovskite-type $Ba_{0.5}Sr_{0.5}Co_{0.8}Fe_{0.2}O_{3-\delta}$ membranes. Journal of Membrane Science 2005;262:20-6.
[46] Liu S, Gavalas GR. Oxygen selective ceramic hollow fiber membranes. Journal of Membrane Science 2005;246:103-8.
[47] Wang H, Tablet C, Feldhoff A, Caro J. A Cobalt‐Free Oxygen‐Permeable Membrane Based on the Perovskite‐Type Oxide $Ba_{0.5}Sr_{0.5}Zn_{0.2}Fe_{0.8}O_{3-\delta}$. Advanced Materials 2005;17:1785-8.
[48] Li K, Tan X, Liu Y. Single-step fabrication of ceramic hollow fibers for oxygen permeation. Journal of Membrane Science 2006;272:1-5.
[49] Teraoka Y, Nobunaga T, Yamazoe N. Effect of cation substitution on the oxygen semipermeability of perovskite-type oxides. Chemistry Letters 1988:503-6.
[50] Ishihara T, Yamada T, Arikawa H, Nishiguchi H, Takita Y. Mixed electronic–oxide ionic conductivity and oxygen permeating property of Fe-,Co-or Ni-doped $LaGaO_3$ perovskite oxide. Solid State Ionics 2000;135:631-6.
[51] Vente JF, McIntosh S, Haije WG, Bouwmeester HJ. Properties and performance of $Ba_xSr_{1-x}Co_{0.8}Fe_{0.2}O_{3-\delta}$ materials for oxygen transport membranes. Journal of Solid State Electrochemistry 2006;10:581-8.
[52] Wang B, Zydorczak B, Wu Z-T, Li K. Stabilities of $La_{0.6}Sr_{0.4}Co_{0.2}Fe_{0.8}O_{3-\delta}$ oxygen separation membranes—Effects of kinetic demixing/decomposition and impurity segregation. Journal of Membrane Science 2009;344:101-6.
[53] Liu Y, Tan X, Li K. Mixed conducting ceramics for catalytic membrane processing. Catalysis Reviews 2006;48:145-98.
[54] Coble R. A model for boundary diffusion controlled creep in polycrystalline materials. Journal of Applied Physics 1963;34:1679-82.
[55] Kuczynski GC. Self-diffusion in sintering of metallic particles. AIME TRANS 1949;185:169-78.
[56] Blendell J. Solid-state sintering. Journal of the American Ceramic Society 2001;70:339-43.
[57] Coble RL. Sintering crystalline solids. I. Intermediate and final state diffusion models. Journal of Applied Physics 1961;32:787-92.
[58] Kuczynski G. Physics and chemistry of sintering. Advances in Colloid and

Interface Science 1972;3:275-330.
[59] Bernard-Granger G, Monchalin N, Guizard C. Sintering of ceramic powders: Determination of the densification and grain growth mechanisms from the “grain size/relative density” trajectory. Scripta Materialia 2007;57:137-40.
[60] Johnson DL. Fundamentals of the sintering of ceramics. Processing of Crystalline Ceramics: Springer; 1978. p. 137-49.
[61] Chu M-Y. Sintering stress and microstructure in ceramic powder compacts. Lawrence Berkeley Lab., CA (USA); 1990.
[62] Raj R. Analysis of the sintering pressure. Journal of the American Ceramic Society 1987;70:C‐210-C‐1.
[63] Cocks AC. Constitutive modelling of powder compaction and sintering. Progress in Materials Science 2001;46:201-29.
[64] Chiang Y-M, Kingery WD, Birnie DP. Physical ceramics: principles for ceramic science and engineering: J. Wiley; 1997.
[65] Wong B, Pask JA. Models for kinetics of solid state sintering. Journal of the American Ceramic Society 1979;62:138-41.
[66] Burke J. Role of Grain Boundaries in Sintering. Journal of the American Ceramic Society 1957;40:80-5.
[67] Burke J, Turnbull D. Recrystallization and grain growth. Progress in Metal Physics 1952;3:220-92.
[68] Rupp JL, Infortuna A, Gauckler LJ. Microstrain and self-limited grain growth in nanocrystalline ceria ceramics. Acta Materialia 2006;54:1721-30.
[69] Chen PL, Chen IW. Grain boundary mobility in Y_2O_3: defect mechanism and dopant effects. Journal of the American Ceramic Society 1996;79:1801-9.
[70] Powers J, Glaeser A. Grain boundary migration in ceramics. Interface Science 1998;6:23-39.
[71] Baumann S, Serra J, Lobera M, Escolástico S, Schulze-Küppers F, Meulenberg W. Ultrahigh oxygen permeation flux through supported $Ba_{0.5}Sr_{0.5}Co_{0.8}Fe_{0.2}O_{3-\delta}$ membranes. Journal of Membrane Science 2011;377:198-205.
[72] Magnone E. A systematic literature review on BSCF-based cathodes for solid oxide fuel cell applications. Journal of Fuel Cell Science and Technology 2010;7:064001.
[73] Martynczuk J, Arnold M, Feldhoff A. Influence of grain size on the oxygen permeation performance of perovskite-type $(Ba_{0.5}Sr_{0.5})(Fe_{0.8}Zn_{0.2})O_{3-\delta}$ membranes. Journal of Membrane Science 2008;322:375-82.
[74] Mosadeghkhah A, Alaee MA, Mohammadi T. Effect of sintering temperature and dwell time and pressing pressure on $Ba_{0.5}Sr_{0.5}Co_{0.8}Fe_{0.2}O_{3-\delta}$ perovskite-type membranes. Materials & Design 2007;28:1699-706.
[75] Zhang X, Deces-Petit C, Yick S, Robertson M, Kesler O, Maric R, et al. A study on sintering aids for $Sm_{0.2}Ce_{0.8}O_{1.9}$ electrolyte. Journal of Power Sources 2006;162:480-5.
[76] Varela JA, Cerri J, Leite E, Longo E, Shamsuzzoha M, Bradt R. Microstructural evolution during sintering of CoO doped SnO_2 ceramics. Ceramics International 1999;25:253-6.
[77] Sakai N, Kawada T, Yokokawa H, Dokiya M, Kojima I. Liquid‐Phase‐Assisted Sintering of Calcium‐Doped Lanthanum Chromites. Journal of the American Ceramic Society 1993;76:609-16.
[78] Fang J, Thompson AM, Harmer MP, Chan HM. Effect of Yttrium and Lanthanum on the Final‐Stage Sintering Behavior of Ultrahigh‐Purity Alumina. Journal of the American Ceramic Society 1997;80:2005-12.
[79] Han J, Mantas P, Senos A. Densification and grain growth of Al-doped ZnO.

Journal of Materials Research 2001;16:459-68.
[80] Voytovych R, MacLaren I, Gülgün M, Cannon R, Rühle M. The effect of yttrium on densification and grain growth in α-alumina. Acta Materialia 2002;50:3453-63.
[81] Ran R, Guo Y, Gao D, Liu S, Shao Z. Effect of foreign oxides on the phase structure, sintering and transport properties of $Ba_{0.5}Sr_{0.5}Co_{0.8}Fe_{0.2}O_{3-\delta}$ as ceramic membranes for oxygen separation. Separation and Purification Technology 2011;81:384-91.
[82] Chen Y, Qian B, Li S, Jiao Y, Tade MO, Shao Z. The influence of impurity ions on the permeation and oxygen reduction properties of $Ba_{0.5}Sr_{0.5}Co_{0.8}Fe_{0.2}O_{3-\delta}$ perovskite. Journal of Membrane Science 2014;449:86-96.
[83] Pećanac G, Kiesel L, Kriegel R, Malzbender J. Comparison of thermo-mechanical characteristics of non-doped and 3mol% B-site Zr-doped $Ba_{0.5}Sr_{0.5}Co_{0.8}Fe_{0.2}O_{3-\delta}$. Ceramics International 2014;40:1843-50.
[84] Gong Z, Yin X, Hong L. Modification of B-site doping of perovskite $La_xSr_{1-x}Fe_{1-y-z}Co_yCr_zO_{3-\delta}$ oxide by Mg^{2+} ion. Solid State Ionics 2009;180:1471-7.
[85] Zhao J, Chen D, Shao Z, Liu S. Effect of CuO additive on the sintering and performance of niobium-doped strontium cobaltite as oxygen separation membranes. Separation and Purification Technology 2010;74:28-37.
[86] Chen PL, Chen IW. Grain growth in CeO_2: dopant effects, defect mechanism, and solute drag. Journal of the American Ceramic Society 1996;79:1793-800.
[87] Haworth P, Smart S, Glasscock J, Da Costa JD. Yttrium doped BSCF membranes for oxygen separation. Separation and Purification Technology 2011;81:88-93.
[88] Wu Z, Jin W, Xu N. Oxygen permeability and stability of Al_2O_3-doped $SrCo_{0.8}Fe_{0.2}O_{3-\delta}$ mixed conducting oxides. Journal of Membrane Science 2006;279:320-7.
[89] Senda T, Bradt RC. Grain Growth in Sintered ZnO and ZnO - Bi_2O_3 Ceramics. Journal of the American Ceramic Society 1990;73:106-14.
[90] Yan MF, Cannon RM, Bowen HK. Grain boundary migration in ceramics: Massachusetts Institute of Technology, Materials Processing Center; 1976.
[91] Klande T, Ravkina O, Feldhoff A. Effect of microstructure on oxygen permeation of $Ba_{0.5}Sr_{0.5}Co_{0.8}Fe_{0.2}O_{3-\delta}$ and $SrCo_{0.8}Fe_{0.2}O_{3-\delta}$ membranes. Journal of the European Ceramic Society 2013;33:1129-36.
[92] Park E. Grain growth of $BaTiO_3$. Journal of Materials Science Letters 1999;18:163-5.
[93] Valant M, Suvorov D, Pullar RC, Sarma K, Alford NM. A mechanism for low-temperature sintering. Journal of the European Ceramic Society 2006;26:2777-83.
[94] Sarma K, Farooq R, Jarman K, Pullar RC, Petrov PK, Alford NM. Sintering behaviour of $Ba_xSr_{1-x}TiO_3$. Integrated Ferroelectrics 2004;62:249-52.
[95] Burriel Mn, Peña-Martínez J, Chater RJ, Fearn S, Berenov AV, Skinner SJ, et al. Anisotropic oxygen ion diffusion in layered $PrBaCo_2O_{5+\delta}$. Chemistry of Materials 2012;24:613-21.
[96] Chang Y-S, Chang Y-H, Chen I-G, Chen G-J, Chai Y-L, Fang T-H, et al. Synthesis, formation and characterization of $ZnTiO_3$ ceramics. Ceramics International 2004;30:2183-9.
[97] Bäurer M, Weygand D, Gumbsch P, Hoffmann M. Grain growth anomaly in strontium titanate. Scripta Materialia 2009;61:584-7.
[98] Diethelm S, Sfeir J, Buffat P. Correlation between oxygen transport properties and microstructure in $La_{0.5}Sr_{0.5}FeO_{3-\delta}$. Journal of the European Ceramic Society 2005;25:2191-6.

[99] Xu Q, Huang D-p, Chen W, Lee J-h, Kim B-h, Wang H, et al. Influence of sintering temperature on microstructure and mixed electronic–ionic conduction properties of perovskite-type $La_{0.6}Sr_{0.4}Co_{0.8}Fe_{0.2}O_3$ ceramics. Ceramics International 2004;30:429-33.
[100] Salehi M, Clemens F, Pfaff EM, Diethelm S, Leach C, Graule T, et al. A case study of the effect of grain size on the oxygen permeation flux of BSCF disk-shaped membrane fabricated by thermoplastic processing. Journal of Membrane Science 2011;382:186-93.
[101] Yoon JS, Yoon MY, Lee EJ, Moon J-W, Hwang HJ. Influence of $Ce_{0.9}Gd_{0.1}O_{2-\delta}$ particles on microstructure and oxygen permeability of $Ba_{0.5}Sr_{0.5}Co_{0.8}Fe_{0.2}O_{3-\delta}$ composite membrane. Solid State Ionics 2010;181:1387-93.
[102] Ravkina O, Klande T, Feldhoff A. Investigation of Zr-doped BSCF perovskite membrane for oxygen separation in the intermediate temperature range. Journal of Solid State Chemistry 2013;201:101-6.
[103] Skinner S, Kilner J. Oxygen diffusion and surface exchange in $La_{2-x}Sr_xNiO_{4+\delta}$. Solid State Ionics 2000;135:709-12.
[104] Lein HL, Wiik K, Grande T. Kinetic demixing and decomposition of oxygen permeable membranes. Solid State Ionics 2006;177:1587-90.
[105] Lein HL, Wiik K, Einarsrud Ma, Grande T, Lara‐curzio E. High‐Temperature Creep Behavior of Mixed Conducting $La_{0.5}Sr_{0.5}Fe_{1-x}Co_xO_{3-\delta}$ ($0.5 \leqslant x \leqslant 1$) Materials. Journal of the American Ceramic Society 2006;89:2895-8.
[106] Pećanac G, Baumann S, Malzbender J. Mechanical properties and lifetime predictions for $Ba_{0.5}Sr_{0.5}Co_{0.8}Fe_{0.2}O_{3-\delta}$ membrane material. Journal of Membrane Science 2011;385:263-8.
[107] de With G. Structure, deformation, and integrity of materials, volume II: plasticity, visco-elasticity, and fracture. Wiley-VCH Berlin 2006:pp. 569-645.
[108] Fischer H, Dautzenberg G, Marx R. Nondestructive estimation of the strength of dental ceramic materials. Dental Materials 2001;17:289-95.
[109] Chanda A, Huang B, Malzbender J, Steinbrech R. Micro-and macro-indentation behaviour of $Ba_{0.5}Sr_{0.5}Co_{0.8}Fe_{0.2}O_{3-\delta}$ perovskite. Journal of the European Ceramic Society 2011;33:401-8.
[110] Rutkowski B. Mechanical properties and microstructure of dense ceramic membranes for oxygen separation in zero-emission power plants: Wydawnictwo Naukowe" Akapit"; 2013.
[111] Lipinska-Chwalek M, Schulze-Küppers F, Malzbender J. Stability aspects of porous $Ba_{0.5}Sr_{0.5}Co_{0.8}Fe_{0.2}O_{3-\delta}$. Ceramics International 2014;40:7395-9.
[112] Lipinska-Chwalek M, Malzbender J, Chanda A, Baumann S, Steinbrech R. Mechanical characterization of porous $Ba_{0.5}Sr_{0.5}Co_{0.8}Fe_{0.2}O_{3-\delta}$. Journal of the European Ceramic Society 2011.
[113] Malzbender J, Huang B, Mönch J, Steinbrech R. A comparison of results obtained using different methods to assess the elastic properties of ceramic materials exemplified for $Ba_{0.5}Sr_{0.5}Co_{0.8}Fe_{0.2}O_{3-\delta}$. Journal of Materials Science 2010;45:1227-30.
[114] Fossdal A, Einarsrud MA, Grande T. Mechanical properties of $LaFeO_3$ ceramics. Journal of the European Ceramic Society 2005;25:927-33.
[115] Orlovskaya N, Kleveland K, Grande T, Einarsrud MA. Mechanical properties of $LaCoO_3$ based ceramics. Journal of the European Ceramic Society 2000;20:51-6.
[116] Pathak S, Kuebler J, Payzant A, Orlovskaya N. Mechanical behavior and electrical conductivity of $La_{1-x}Ca_xCoO_3$ (x= 0, 0.2, 0.4, 0.55) perovskites. Journal of Power Sources 2010;195:3612-20.
[117] Lein HL, Wiik K, Grande T. Thermal and chemical expansion of mixed

conducting $La_{0.5}Sr_{0.5}Fe_{1-x}Co_xO_{3-\delta}$ materials. Solid State Ionics 2006;177:1795-8.
[118] Pathak S, Steinmetz D, Kuebler J, Payzant EA, Orlovskaya N. Mechanical behavior of $La_{0.8}Sr_{0.2}Ga_{0.8}Mg_{0.2}O_3$ perovskites. Ceramics International 2009;35:1235-41.
[119] Kim H-J, Kweon Y-G. Elastic modulus of plasma-sprayed coatings determined by indentation and bend tests. Thin Solid Films 1999;342:201-6.
[120] Giovan M, Sines G. Biaxial and uniaxial data for statistical comparisons of a ceramic's strength. Journal of the American Ceramic Society 1979;62:510-5.
[121] Shetty D, ROSENFIELD R, Bansal G, Duckworth W. Biaxial Fracture Studies of a Glass‐Ceramic. Journal of the American Ceramic Society 1981;64:1-4.
[122] Shetty DK, Rosenfield AR, McGuire P, Bansal G, Duckworth WH. Biaxial flexure tests for ceramics. American Ceramic Society Bulletin 1980;59:1193-7.
[123] Standard A. C1499–05: Standard test method for monotonic equibiaxial flexural strength of advanced ceramics at ambient temperature. Annual Book of ASTM Standards, ASTM, West Conshohocken, PA; 2003.
[124] Börger A, Supancic P, Danzer R. The ball on three balls test for strength testing of brittle discs: stress distribution in the disc. Journal of the European Ceramic Society 2002;22:1425-36.
[125] Pećanac G, Foghmoes S, Lipińska-Chwałek M, Baumann S, Beck T, Malzbender J. Strength degradation and failure limits of dense and porous ceramic membrane materials. Journal of the European Ceramic Society 2013;33:2689-98.
[126] Callister WD, Rethwisch DG. Materials science and engineering: an introduction: Wiley New York; 2007.
[127] Vuherer T, Godina A, Burzic Z, Gliha V. Fatigue crack initiation from microstructurally small Vickers indentations. Metalurgija 2007;45:237-43.
[128] Oliver WC, Pharr GM. An improved technique for determining hardness and elastic modulus using load and displacement sensing indentation experiments. Journal of Materials Research 1992;7:1564-83.
[129]Li N, Verma A, Singh P, Kim J-H. Characterization of $La_{0.58}Sr_{0.4}Co_{0.2}Fe_{0.8}O_{3-\delta}$–$Ce_{0.8}Gd_{0.2}O_2$ composite cathode for intermediate temperature solid oxide fuel cells. Ceramics International 2013;39:529-38.
[130] Huang B, Malzbender J, Steinbrech R, Singheiser L. Mechanical properties of $La_{0.58}Sr_{0.4}Co_{0.2}Fe_{0.8}O_{3-\delta}$ membranes. Solid State Ionics 2009;180:241-5.
[131] Asmani M, Kermel C, Leriche A, Ourak M. Influence of porosity on Young's modulus and Poisson's ratio in alumina ceramics. Journal of the European Ceramic Society 2001;21:1081-6.
[132] Boccaccini A, Fan Z. A new approach for the Young's modulus-porosity correlation of ceramic materials. Ceramics International 1997;23:239-45.
[133] Knudsen F. Effect of porosity on Young's modulus of alumina. Journal of the American Ceramic Society 1962;45:94-5.
[134] Phani KK, Niyogi S. Young's modulus of porous brittle solids. Journal of Materials Science 1987;22:257-63.
[135] Duckworth W. Discussion on compression strength of porous sintered Al_2O_3 and ZrO. Journal of the American Ceramic Society 1953;36:68.
[136] Watchman J. Mechanical properties of ceramics. . Wiley and Sons, New York; 1996.
[137] Cheng B, Gabbay M, Duffy Jr W, Fantozzi G. Mechanical loss and Young's modulus associated with phase transitions in barium titanate based ceramics. Journal of Materials Science 1996;31:4951-5.
[138] Huang B, Malzbender J, Steinbrech R, Grychtol P, Schneider C, Singheiser L.

Anomalies in the thermomechanical behavior of $Ba_{0.5}Sr_{0.5}Co_{0.8}Fe_{0.2}O_{3-\delta}$ ceramic oxygen conductive membranes at intermediate temperatures. Applied Physics Letters 2009;95:051901.
[139] Quinn JB, Quinn GD. Hardness and brittleness of ceramics. 20th Annual Conference on Composites, Advanced Ceramics, Materials, and Structures-A: Ceramic Engineering and Science Proceedings, Volume 17: John Wiley & Sons; 2009. pp. 59.
[140] Rice RW, Wu CC, Boichelt F. Hardness‐Grain‐Size Relations in Ceramics. Journal of the American Ceramic Society 1994;77:2539-53.
[141] Huang B. Thermo-mechanical Properties of Mixed Ion Electron Conducting Membrane Materials: Forschungszentrum Jülich; 2010.
[142] Chou YS, Stevenson JW, Armstrong TR, Pederson LR. Mechanical Properties of $La_{1-x}Sr_xCo_{0.2}Fe_{0.8}O_3$ Mixed-Conducting Perovskites Made by the Combustion Synthesis Technique. Journal of the American Ceramic Society 2000;83:1457-64.
[143] Stevenson JW, Armstrong TR, Pederson LR, Li J, Lewinsohn C, Baskaran S. Effect of A-site cation nonstoichiometry on the properties of doped lanthanum gallate. Solid State Ionics 1998;113:571-83.
[144] Chou YS, Kerstetter K, Pederson L, Williford R. Mechanical and thermal properties of combustion-synthesized. Journal of Material Research 2001;16:3545.
[145] Baskaran S, Lewinsohn CA, Chou Y, Qian M, Stevenson JW, Armstrong TR. Mechanical properties of alkaline earth-doped lanthanum gallate. Journal of materials science 1999;34:3913-22.
[146] Paulik S, Baskaran S, Armstrong T. Mechanical properties of calcium-substituted yttrium chromite. Journal of Materials Science Letters 1999;18:819-22.
[147] Manika I, Maniks J. Size effects in micro-and nanoscale indentation. Acta Materialia 2006;54:2049-56.
[148] Bull S, Page TF, Yoffe E. An explanation of the indentation size effect in ceramics. Philosophical Magazine Letters 1989;59:281-8.
[149] Gerberich W, Tymiak N, Grunlan J, Horstemeyer M, Baskes M. Interpretations of indentation size effects. Transactions-American Society of Mechanical Engineers Journal of Applied Mechanics 2002;69:433-42.
[150] Nix WD, Gao H. Indentation size effects in crystalline materials: a law for strain gradient plasticity. Journal of the Mechanics and Physics of Solids 1998;46:411-25.
[151] Shu J, Fleck N. The prediction of a size effect in microindentation. International Journal of Solids and Structures 1998;35:1363-83.
[152] Gao H, Huang Y, Nix W, Hutchinson J. Mechanism-based strain gradient plasticity—I. Theory. Journal of the Mechanics and Physics of Solids 1999;47:1239-63.
[153] Gane N, Cox J. The micro-hardness of metals at very low loads. Philosophical Magazine 1970;22:0881-91.
[154] Li H, Ghosh A, Han Y, Bradt R. The frictional component of the indentation size effect in low load microhardness testing. Journal of Materials Research 1993;8:1028-32.
[155] Babini G, Bellosi A, Galassi C. Characterization of hot-pressed silicon nitride-based materials by microhardness measurements. Journal of Materials Science 1987;22:1687-93.
[156] Gong J, Wu J, Guan Z. Examination of the indentation size effect in low-load Vickers hardness testing of ceramics. Journal of the European Ceramic Society 1999;19:2625-31.
[157] Wang PE, Chaki T. Sintering behaviour and mechanical properties of hydroxyapatite and dicalcium phosphate. Journal of Materials Science: Materials in Medicine 1993;4:150-8.

[158] Rice R. Evaluation and extension of physical property-porosity models based on minimum solid area. Journal of Materials Science 1996;31:102-18.
[159] Rice RW. Porosity of Ceramics: Properties and Applications: CRC Press; 1998.
[160] Hoepfner TP, Case E. The influence of the microstructure on the hardness of sintered hydroxyapatite. Ceramics International 2003;29:699-706.
[161] Liu D-M. Fabrication and characterization of porous hydroxyapatite granules. Biomaterials 1996;17:1955-7.
[162] Reynaud C, Thevenot F. Porosity dependence of mechanical properties of porous sintered SiC. Verification of the minimum solid area model. Journal of Materials Science Letters 2000;19:871-4.
[163] Anderson TL. Fracture mechanics: fundamentals and applications: CRC press; 2005.
[164] Quinn GD. Fractography of ceramics and glasses: US Department of Commerce, Technology Administration, National Institute of Standards and Technology; 2007.
[165] Green DJ. An introduction to the mechanical properties of ceramics. Cambridge: Cambridge University Press; 1998.
[166] Shetty DK, Rosenfield AR, Duckworth WH, Held P. A Biaxial‐Flexure Test for Evaluating Ceramic Strengths. Journal of the American Ceramic Society 1983;66:36-42.
[167] Junior SAR, Ferracane JL, Bona ÁD. Flexural strength and Weibull analysis of a microhybrid and a nanofill composite evaluated by 3-and 4-point bending tests. Dental Materials 2008;24:426-31.
[168] Weibull W. A statistical distribution function of wide applicability. Journal of Applied Mechanics 1951;18:293-7.
[169] Weil N, Daniel I. Analysis of fracture probabilities in nonuniformly stressed brittle materials. Journal of the American Ceramic Society 1964;47:268-74.
[170] Drennan J, Zelizko V, Hay D, Ciacchi FT, Rajendran S, Badwal SPS. Characterisation, conductivity and mechanical properties of theoxygen-ion conductor $La_{0.9}Sr_{0.1}Ga_{0.8}Mg_{0.2}O_{3-\delta}$
Journal of Materials Chemistry 1997;7:79-83.
[171] Lein HL, Andersen ØS, Vullum PE, Lara-Curzio E, Holmestad R, Einarsrud MA, et al. Mechanical properties of mixed conducting $La_{0.5}Sr_{0.5}Fe_{1-x}Co_xO_{3-\delta}$ ($0 \leqslant x \leqslant 1$) materials. Journal of Solid State Electrochemistry 2006;10:635-42.
[172] Paulik S, Baskaran S, Armstrong T. Mechanical properties of calcium-and strontium-substituted lanthanum chromite. Journal of Materials Science 1998;33:2397-404.
[173] Sammes N, Ratnaraj R. High-temperature mechanical properties of $La_{0.7}Sr_{0.3}Cr_{1-y}Co_yO_3$ in reducing environments. Journal of Materials Science 1997;32:687-92.
[174] Meixner DL, Cutler RA. Sintering and mechanical characteristics of lanthanum strontium manganite. Solid State Ionics 2002;146:273-84.
[175] Montross CS, Yokokawa H, Dokiya M, Bekessy L. Mechanical Properties of Magnesia‐Doped Lanthanum Chromite versus Temperature. Journal of the American Ceramic Society 1995;78:1869-72.
[176] Sammes N, Ratnaraj R, Fee M. The effect of sintering on the mechanical properties of SOFC ceramic interconnect materials. Journal of Materials Science 1994;29:4319-24.
[177] D'Souza CM, Sammes NM. Mechanical Properties of Strontium‐Doped Lanthanum Manganite. Journal of the American Ceramic Society 2000;83:47-52.
[178] Sammes NM, Keppeler FM, Näfe H, Aldinger F. Mechanical Properties of Solid‐State‐Synthesized Strontium‐and Magnesium‐Doped Lanthanum Gallate.

Journal of the American Ceramic Society 1998;81:3104-8.
[179] Huang B, Chanda A, Steinbrech R, Malzbender J. Indentation strength method to determine the fracture toughness of $La_{0.58}Sr_{0.4}Co_{0.2}Fe_{0.8}O_{3-\delta}$ and $Ba_{0.5}Sr_{0.5}Co_{0.8}Fe_{0.2}O_{3-\delta}$. Journal of Materials Science 2012;47:2695-9.
[180] Rice R. Grain size and porosity dependence of ceramic fracture energy and toughness at 22 ℃. Journal of Materials Science 1996;31:1969-83.
[181] Kim YW, Mitomo M, Hirotsuru H. Grain growth and fracture toughness of fine‐grained silicon carbide ceramics. Journal of the American Ceramic Society 1995;78:3145-8.
[182] Kawashima T, Okamoto H, Yamamoto H, Kitamura A. Grain size dependence of the fracture toughness of silicon nitride ceramics. Journal of the Japanese Ceramic Society 1991;99:320-3.
[183] Mussler B, Swain Mv, Claussen N. Dependence of fracture toughness of alumina on grain size and test technique. Journal of the American Ceramic Society 1982;65:566-72.
[184] Sikder B, Chanda A. Effect of Annealing on Fracture Toughness Evaluation of $Ba_{0.5}Sr_{0.5}Co_{0.8}Fe_{0.2}O_{3-\delta}$ (BSCF) at Different Temperatures. Applied Mechanics and Materials: Trans Tech Publ; 2014. pp. 816-20.
[185] Blamey J, Parry T. Strength and toughness of barium titanate ceramics. Journal of Materials Science 1993;28:4988-93.
[186] Orlovskaya N, Lugovy M, Pathak S, Steinmetz D, Lloyd J, Fegely L, et al. Thermal and mechanical properties of $LaCoO_3$ and $La_{0.8}Ca_{0.2}CoO_3$ perovskites. Journal of Power Sources 2008;182:230-9.
[187] Anstis G, Chantikul P, Lawn BR, Marshall D. A critical evaluation of indentation techniques for measuring fracture toughness: I, direct crack measurements. Journal of the American Ceramic Society 1981;64:533-8.
[188] Chantikul P, Anstis G, Lawn BR, Marshall D. A critical evaluation of indentation techniques for measuring fracture toughness: II, strength method. Journal of the American Ceramic Society 1981;64:539-43.
[189] Liu D-M, Lin B-W, Fu C-T. Porosity dependence of mechanical strengh and fracture toughness in SiC-Al_2O_3-Y_2O_3 ceramics. Nippon seramikkusu kyokai gakujutsu ronbunshi 1995;103:878-81.
[190] Atkinson A, Selcuk A. Mechanical behaviour of ceramic oxygen ion-conducting membranes. Solid State Ionics 2000;134:59-66.
[191] Lawn BR. Fracture of brittle solids: Cambridge university press; 1993.
[192] Wan K-T, Lathabai S, Lawn BR. Crack velocity functions and thresholds in brittle solids. Journal of the European Ceramic Society 1990;6:259-68.
[193] Szutkowska M, Boniecki M. Subcritical crack growth in zirconia-toughened alumina (ZTA) ceramics. Journal of Materials Processing Technology 2006;175:416-20.
[194] Munz D, Fett T. Ceramics: mechanical properties, failure behaviour, materials selection: Springer Verlag; 1999.
[195] Chevalier J, Olagnon C, Fantozzi G. Subcritical Crack Propagation in 3Y‐TZP Ceramics: Static and Cyclic Fatigue. Journal of the American Ceramic Society 1999;82:3129-38.
[196] Wiederhorn S. Subcritical crack growth in ceramics. Fracture Mechanics of Ceramics 1974:613-46.
[197] Choi SR, Salem JA, Holland FA. Estimation of slow crack growth parameters for constant stress-rate test data of advanced ceramics and glass by the individual data and arithmetic mean methods: Lewis Research Center, National Aeronautics and Space

Administration; 1997.
[198] Fett T, Hartlieb W, Keller K, Knecht B, Münz D, Rieger W. Subcritical crack growth in high-grade alumina. Journal of Nuclear Materials 1991;184:39-46.
[199] Dalgleish B, Rawlings RD. A comparison of the mechanical behavior of aluminas in air and simulated body environments. Journal of Biomedical Materials Research 1981;15:527-42.
[200] Rice RW. Mechanical properties of ceramics and composites: grain and particle effects: CRC Press; 2000.
[201] Newcomb SA, Tressler RE. Slow crack growth in sapphire fibers at 800 to 1500 °C. Journal of the American Ceramic Society 1993;76:2505-12.
[202] Choi SR, Salem J, Nemeth N. High-temperature slow crack growth of silicon carbide determined by constant-stress-rate and constant-stress testing. Journal of Materials Science 1998;33:1325-32.
[203] Evans A, Wiederhorn S. Crack propagation and failure prediction in silicon nitride at elevated temperatures. Journal of Materials Science 1974;9:270-8.
[204] Malzbender J, Pećanac G, Baumann S. Slow Crack Growth and Creep Rupture of $Ba_{0.5}Sr_{0.5}Co_{0.8}Fe_{0.2}O_{3-\delta}$. Key Engineering Materials 2012;488:303-6.
[205] Nagabhushana N, Nithyanantham T, Bandopadhyay S, Zhang J. Subcritical Crack Growth Behavior of A Perovskite‐Type Oxygen Transport Ceramic Membrane. International Journal of Applied Ceramic Technology 2009;8:390-7.
[206] Ogunkoya A, Eng M, Ukoba O, Eng B, Oyegunwa O, Idowu A, et al. Development of a Constant-Stress Creep Testing Equipment. 2011;12:82-6.
[207] Herring C. Diffusional viscosity of a polycrystalline solid. Journal of Applied Physics 1950;21:437-45.
[208] Wang J. An investigation of the deformation mechanism in grain size-sensitive Newtonian creep. Acta Materialia 2000;48:1517-31.
[209] Garofalo F. Fundamentals of creep and creep-rupture in metals: Macmillan; 1965.
[210] W.D.Kingery, Bowen HK, Uhlmann DR. Introduction to ceramics. New York Chichester;Wiley-Interscience; 1976.
[211] Wang ZC, Dupas-Bruzek C, Karato S. High temperature creep of an orthorhombic perovskite—$YAlO_3$. Physics of the Earth and Panetary Interiors 1999;110:51-69.
[212] Rutkowski B, Malzbender J, Beck T, Steinbrech R, Singheiser L. Creep behaviour of tubular $Ba_{0.5}Sr_{0.5}Co_{0.8}Fe_{0.2}O_{3-\delta}$ gas separation membranes. Journal of the European Ceramic Society 2011;31:493-9.
[213] Chokshi AH. Diffusion creep in oxide ceramics. Journal of the European Ceramic Society 2002;22:2469-78.
[214] Atkinson A, Ramos T. Chemically-induced stresses in ceramic oxygen ion-conducting membranes. Solid State Ionics 2000;129:259-69.
[215] Hendriksen PV, Larsen PH, Mogensen M, Poulsen FW, Wiik K. Prospects and problems of dense oxygen permeable membranes. Catalysis Today 2000;56:283-95.
[216] Yi J, Lein H, Grande T, Yakovlev S, Bouwmeester H. High-temperature compressive creep behaviour of the perovskite-type oxide $Ba_{0.5}Sr_{0.5}Co_{0.8}Fe_{0.2}O_{3-\delta}$. Solid State Ionics 2009;180:1564-8.
[217] Huanghai L. Preparation and Performance of BSCF-based Mixed Ionic-Electronic Conducting (MIEC) Ceramics: Univerisity of Manchester; 2015.
[218] ASTM. C1161-13 Standard test method for flexural strength of advanced ceramics at ambient temperature. 2008.
[219] Oliver WC, Pharr GM. Improved technique for determining hardness and elastic modulus using load and displacement sensing indentation experiments. Journal of materials research 1992;7:1564-83.

[220] Tanaka I, Pezzotti G. Evaluation of Slow Crack Growth Resistance in Ceramics for High‐Temperature Applications. Journal of the American Ceramic Society 1992;75:772-7.
[221] Tomkiewicz AC, Tamimi MA, Huq A, McIntosh S. Evidence for the low oxygen stoichiometry of cubic $Ba_{0.5}Sr_{0.5}Co_{0.5}Fe_{0.5}O_{3-\delta}$ from in-situ neutron diffraction. Solid State Ionics 2013;253:27-31.
[222] Standard ID. Fine ceramics (advanced ceramics, advanced technical ceramics) — Determination of density and apparent porosity. BSI; 2011.
[223] Koster H, Mertins FdrHB. Powder diffraction of the cubic perovskite $Ba_{0.5}Sr_{0.5}Co_{0.8}Fe_{0.2}O_{3-\delta}$. Powder Diffraction 2003;18:56-9.
[224] Shao Z, Yang W, Cong Y, Dong H, Tong J, Xiong G. Investigation of the permeation behavior and stability of. Journal of Membrane Science 2000;172:177-88.
[225] Huang B. Thermo-mechanical properties of mixed ion-electron conducting membrane materials 2010.
[226] Klande T, Ravkina O, Feldhoff A. Effect of microstructure on oxygen permeation of $Ba_{0.5}Sr_{0.5}Co_{0.8}Fe_{0.2}O_{3-\delta}$ and $SrCo_{0.8}Fe_{0.2}O_{3-\delta}$ membranes. Journal of the European Ceramic Society 2013;33:1129-36.
[227] Koster H, Mertins F. Powder diffraction of the cubic perovskite $Ba_{0.5}Sr_{0.5}Co_{0.8}Fe_{0.2}O_{3-\delta}$. Powder Diffraction 2003;18:56-9.
[228] Shao Z, Xiong G, Dong H, Yang W, Lin L. Synthesis, oxygen permeation study and membrane performance of a $Ba_{0.5}Sr_{0.5}Co_{0.8}Fe_{0.2}O_{3-\delta}$ oxygen-permeable dense ceramic reactor for partial oxidation of methane to syngas. Separation and Purification Technology 2001;25:97-116.
[229] Wei B, Lü Z, Li S, Liu Y, Liu K, Su W. Thermal and electrical properties of new cathode material $Ba_{0.5}Sr_{0.5}Co_{0.8}Fe_{0.2}O_{3-\delta}$ for solid oxide fuel cells. Electrochemical and Solid-State Letters 2005;8:A428-A31.
[230] Wang H, Tablet C, Feldhoff A, Caro J. Investigation of phase structure, sintering, and permeability of. Journal of Membrane Science 2005;262:20-6.
[231] Hillert M. On the theory of normal and abnormal grain growth. Acta Metallurgica 1965;13:227-38.
[232] Mendelson MI. Average grain size in polycrystalline ceramics. Journal of the American Ceramic Society 1969;52:443-6.
[233] Venkataraman KS, DiMilia RA. Predicting the Grain‐Size Distributions in High‐Density, High‐Purity Alumina Ceramics. Journal of the American Ceramic Society 1989;72:33-9.
[234] Averback R, Höfler H, Hahn H, Logas J. Sintering and grain growth in nanocrystalline ceramics. Nanostructured materials 1992;1:173-8.
[235] Baumann S, Schulze-Kuppers F, Roitsch S, Betz M, Zwick M, Pfaff E, et al. Influence of sintering conditions on microstructure and oxygen permeation of $Ba_{0.5}Sr_{0.5}Co_{0.8}Fe_{0.2}O_{3-delta}$ (BSCF) oxygen transport membranes. Journal of Membrane Science 2010;359:102-9.
[236] Standard B-. Advanced technical ceramics- Mechanical properties of monolithic ceramics at room temperature Part 6: Guidance for fractographic investigation: BSI; 2010.
[237] Batdorf S. Some approximate treatments of fracture statistics for polyaxial tension. International Journal of Fracture 1977;13:5-11.
[238] Breder K, Andersson T, Schoelin K. Fracture Strength of α-and β-SiAION Measured by Biaxial and Four-Point Bending. Journal of the American Ceramic Society 1990;73:2128-30.

[239] Quinn GD. Weibull strength scaling for standardized rectangular flexure specimens. Journal of the American Ceramic Society 2003;86:508-10.
[240] Chung S, Yap A, Chandra S, Lim C. Flexural strength of dental composite restoratives: Comparison of biaxial and three‐point bending test. Journal of Biomedical Materials Research Part B: Applied Biomaterials 2004;71:278-83.
[241] Hilpert K, Steinbrech R, Boroomand F, Wessel E, Meschke F, Zuev A, et al. Defect formation and mechanical stability of perovskites based on $LaCrO_3$ for solid oxide fuel cells (SOFC). Journal of the European Ceramic Society 2003;23:3009-20.
[242] McIntosh S, Vente JF, Haije WG, Blank DH, Bouwmeester HJ. Structure and oxygen stoichiometry of $SrCo_{0.8}Fe_{0.2}O_{3-\delta}$ and $Ba_{0.5}Sr_{0.5}Co_{0.8}Fe_{0.2}O_{3-\delta}$. Solid State Ionics 2006;177:1737-42.
[243] Green DJ. An introduction to the mechanical properties of ceramics: Cambridge Univ Pr; 1998.
[244] Chaim R, Hefetz M. Effect of grain size on elastic modulus and hardness of nanocrystalline ZrO_2-3 wt% Y_2O_3 ceramic. Journal of Materials Science 2004;39:3057-61.
[245] Kim H, Kim T. Measurement of hardness on traditional ceramics. Journal of the European Ceramic Society 2002;22:1437-45.
[246] Yang HG, Zeng HC. Preparation of hollow anatase TiO_2 nanospheres via Ostwald ripening. The Journal of Physical Chemistry B 2004;108:3492-5.
[247] Kawai C. Effect of grain size distribution on the strength of porous Si_3N_4 ceramics composed of elongated β-Si_3N_4 grains. Journal of Materials Science 2001;36:5713-7.
[248] Spriggs R, Brissette L, Vasilos T. Effect of porosity on elastic and shear moduli of polycrystalline magnesium oxide. Journal of the American Ceramic Society 1962;45:400-.
[249] Virkar AV, Huang JL, Cutler RA. Strengthening of Oxide Ceramics by Transformation‐Induced Stress. Journal of the American Ceramic Society 1987;70:164-70.
[250] Wang H, Tablet C, Yang W, Caro J. In situ high temperature X-ray diffraction studies of mixed ionic and electronic conducting perovskite-type membranes. Materials Letters 2005;59:3750-5.
[251] Zhang H, López‐Honorato E, Javed A, Shapiro I, Xiao P. A Study of the Microstructure and Vickers Indentation Fracture Toughness of Silicon Carbide Coatings on TRISO Fuel Particles. Journal of the American Ceramic Society 2012;95:1086-92.
[252] Jungk J, Boyce B, Buchheit T, Friedmann T, Yang D, Gerberich W. Indentation fracture toughness and acoustic energy release in tetrahedral amorphous carbon diamond-like thin films. Acta Materialia 2006;54:4043-52.
[253] Virkar AV, Matsumoto RL. Ferroelastic domain switching as a toughening mechanism in tetragonal zirconia. Journal of the American Ceramic Society 1986;69:C‐224-C‐6.
[254] Ebrahimi M, Chevalier J, Fantozzi G. Slow crack-growth behavior of alumina ceramics. Journal of Materials Research 2000;15:142-7.
[255] Deng Z-Y, She J, Inagaki Y, Yang J-F, Ohji T, Tanaka Y. Reinforcement by crack-tip blunting in porous ceramics. Journal of the European Ceramic Society 2004;24:2055-9.
[256] Ravi-Chandar K, Knauss W. An experimental investigation into dynamic fracture: III. On steady-state crack propagation and crack branching. International Journal of Fracture 1984;26:141-54.

[257] Ravi-Chandar K, Knauss W. An experimental investigation into dynamic fracture: II. Microstructural aspects. International Journal of Fracture 1984;26:65-80.
[258] Barsoum M, Barsoum M. Fundamentals of ceramics: CRC press; 2002.
[259] Pecanac G. Thermo-mechanical investigations and predictions for oxygen transport membrane materials: Forschungszentrum Jülich; 2013.
[260] Švarcová S, Wiik K, Tolchard J, Bouwmeester HJ, Grande T. Structural instability of cubic perovskite $Ba_xSr_{1-x}Co_{1-y}Fe_yO_{3-\delta}$. Solid State Ionics 2008;178:1787-91.
[261] Müller P, Störmer H, Dieterle L, Niedrig C, Ivers-Tiffée E, Gerthsen D. Decomposition pathway of cubic $Ba_{0.5}Sr_{0.5}Co_{0.8}Fe_{0.2}O_{3-\delta}$ between 700 °C and 1000 °C analyzed by electron microscopic techniques. Solid State Ionics 2012;206:57-66.
[262] Evans A, Lange F. Crack propagation and fracture in silicon carbide. Journal of Materials Science 1975;10:1659-64.
[263] Chou YS, Stevenson JW, Armstrong TR, Pederson LR. Mechanical Properties of $La_{1-x}Sr_xCo_{0.2}Fe_{0.8}O_3$ Mixed - Conducting Perovskites Made by the Combustion Synthesis Technique. Journal of the American Ceramic Society 2000;83:1457-64.
[264] Yang J, Zhao H, Liu X, Shen Y, Xua L. Bismuth doping effects on the structure, electrical conductivity and oxygen permeability of $Ba_{0.6}Sr_{0.4}Co_{0.7}Fe_{0.3}O_{3-\delta}$ ceramic membranes. International Journal of Hydrogen Energy 2012;37:e12699.
[265] Li Z, Wei B, Lü Z, Zhang Y, Chen K, Miao J, et al. Evaluation of $(Ba_{0.5}Sr_{0.5})_{0.85}Gd_{0.15}Co_{0.8}Fe_{0.2}O_{3-\delta}$ cathode for intermediate temperature solid oxide fuel cell. Ceramics International 2012;38:3039-46.
[266] Haworth P, Smart S, Glasscock J, Da Costa JD. High performance yttrium-doped BSCF hollow fibre membranes. Separation and Purification Technology 2012;94:16-22.
[267] Kang B-K, Lee H-C, Heo Y-W, Kim J-J, Kim JY, Lee J-H. Thermal expansion behavior of La-doped $Ba_{0.5}Sr_{0.5}Co_{0.8}Fe_{0.2}O_{3-\delta}$ cathode material. Ceramics International 2013;39:8267-71.
[268] Kharton V, Viskup A, Naumovich E, Tikhonovich V. Oxygen permeability of $LaFe_{1-x}Ni_xO_{3-\delta}$ solid solutions. Materials Research Bulletin 1999;34:1311-7.
[269] Wei B, Lü Z, Jia D, Huang X, Zhang Y, Su W. Thermal expansion and electrochemical properties of Ni-doped $GdBaCo_2O_{5+\delta}$ double-perovskite type oxides. International Journal of Hydrogen Energy 2010;35:3775-82.
[270] Yang J, Zhao H, Liu X, Shen Y, Xu L. Bismuth doping effects on the structure, electrical conductivity and oxygen permeability of $Ba_{0.6}Sr_{0.4}Co_{0.7}Fe_{0.3}O_{3-\delta}$ ceramic membranes. international journal of hydrogen energy 2012;37:12694-9.
[271] Stournari V, ten Donkelaar S, Malzbender J, Beck T, Singheiser L, Bouwmeester H. Creep behavior of perovskite-type oxides $Ba_{0.5}Sr_{0.5}(Co_{0.8}Fe_{0.2})_{1-x}Zr_xO_{3-\delta}$. Journal of the European Ceramic Society 2015;35:1841-6.
[272] Li F, Li J-F. Effect of Ni substitution on electrical and thermoelectric properties of $LaCoO_3$ ceramics. Ceramics International 2011;37:105-10.
[273] Kim J, Choi S, Jun A, Jeong HY, Shin J, Kim G. Chemically Stable Perovskites as Cathode Materials for Solid Oxide Fuel Cells: La-Doped $Ba_{0.5}Sr_{0.5}Co_{0.8}Fe_{0.2}O_{3-\delta}$. ChemSusChem 2014;7:1669-75.
[274] Garcia S, Font R, Portelles J, Quinones R, Heiras J, Siqueiros J. Effect of Nb doping on (Sr,Ba)TiO_3(BST) ceramic samples. Journal of Electroceramics 2001;6:101-8.
[275] Tzing W, Tuan W. Effect of NiO addition on the sintering and grain growth behaviour of $BaTiO_3$. Ceramics International 1999;25:69-75.
[276] Rahaman MN. Sintering of ceramics: CRC press; 2007.
[277] Brook R. Controlled grain growth. Treatise on Materials Science and Technology 1976;9:331-64.

[278] Olgaard DL, Evans B. Effect of second‐phase particles on grain growth in calcite. Journal of the American Ceramic Society 1986;69:C‐272-C‐7.
[279] Hazzledine P, Oldershaw R. Computer simulation of Zener pinning. Philosophical Magazine A 1990;61:579-89.
[280] Haroun N, Budworth D. Modifications to the Zener formula for limitation of grain size. Journal of Materials Science 1968;3:326-8.
[281] Gladman T. On the theory of the effect of precipitate particles on grain growth in metals. Proceedings of the Royal Society of London A: Mathematical, Physical and Engineering Sciences: The Royal Society; 1966. p. 298-309.
[282] Stearns LC, Harmer MP. Particle‐Inhibited Grain Growth in Al_2O_3‐SiC: II, Equilibrium and Kinetic Analyses. Journal of the American Ceramic Society 1996;79:3020-8.
[283] Bae IJ, Baik S. Abnormal grain growth of alumina. Journal of the American Ceramic Society 1997;80:1149-56.
[284] Bae SI, Baik S. Critical concentration of MgO for the prevention of abnormal grain growth in alumina. Journal of the American Ceramic Society 1994;77:2499-504.
[285] Horn DS, Messing GL. Anisotropic grain growth in TiO_2-doped alumina. Materials Science and Engineering: A 1995;195:169-78.
[286] Lee B-K, Chung S-Y, Kang S-JL. Grain boundary faceting and abnormal grain growth in $BaTiO_3$. Acta Materialia 2000;48:1575-80.
[287] Han J, Mantas P, Senos A. Grain growth in Mn-doped ZnO. Journal of the European Ceramic Society 2000;20:2753-8.
[288] Cho J, Harmer MP, Chan HM, Rickman JM, Thompson AM. Effect of yttrium and lanthanum on the tensile creep behavior of aluminum oxide. Journal of the American Ceramic Society 1997;80:1013-7.
[289] Watcharapasorn A, Jiansirisomboon S. Grain growth kinetics in Dy-doped $Bi_{0.5}Na_{0.5}TiO_3$ ceramics. Ceramics International 2008;34:769-72.
[290] Dutta S, Spriggs R. Grain growth in fully dense ZnO. Journal of the American Ceramic Society 1970;53:61-2.
[291] Dutta S, Spriggs R. Densification and grain growth in hot-pressed zinc oxide. Materials Research Bulletin 1969;4:797-806.
[292] Lindner R, Åkerström Å. Diffusion of nickel-63 in nickel oxide (NiO). Discussions of the Faraday Society 1957;23:133-6.
[293] Jud E, Huwiler CB, Gauckler LJ. Sintering analysis of undoped and cobalt oxide doped ceria solid solutions. Journal of the American Ceramic Society 2005;88:3013-9.
[294] Riege S, Thompson C, Frost H. Simulation of the influence of particles on grain structure evolution in two-dimensional systems and thin films. Acta Materialia 1999;47:1879-87.
[295] Ling H, Yan MF. Microhardness measurements on dopant modified superconducting $YBa_2Cu_3O_7$ ceramics. Journal of Applied Physics 1988;64:1307-11.
[296] Wang Y, Yang F, Xiao P. Rattlers or oxygen vacancies: Determinant of high temperature plateau thermal conductivity in doped pyrochlores. Applied Physics Letters 2013;102:141902.
[297] Wang Y, Yang F, Xiao P. Role and determining factor of substitutional defects on thermal conductivity: A study of $La_2(Zr_{1-x}B_x)_2O_7$ (B= Hf, Ce, $0 \leqslant x \leqslant 0.5$) pyrochlore solid solutions. Acta Materialia 2014;68:106-15.
[298] Pruneda J, Artacho E. First-principles study of structural, elastic, and bonding properties of pyrochlores. Physical Review B 2005;72:085107.
[299] Dean JA. Lange's handbook of chemistry. Properties of Atoms, Radicals, and

Bonds New York, NY: McGraw-Hill Professional; 1985.
[300] Xiang P-H, Dong X-L, Feng C-D, Zhong N, Guo J-K. Sintering behavior, mechanical and electrical properties of lead zirconate titanate/NiO composites from coated powders. Ceramics International 2004;30:765-72.
[301] Tromans D, Meech J. Fracture toughness and surface energies of minerals: theoretical estimates for oxides, sulphides, silicates and halides. Minerals Engineering 2002;15:1027-41.
[302] Nadeau J, Dickson J. Effects of Internal Stresses Due to a Dispersed Phase on the Fracture Toughness of Glass. Journal of the American Ceramic Society 1980;63:517-23.
[303] Faber K, Evans A. Crack deflection processes—I. Theory. Acta Metallurgica 1983;31:565-76.
[304] Selsing J. Internal stresses in ceramics. Journal of the American Ceramic Society 1961;44:419-.
[305] Green A. Determination of growth stresses in nickel oxide using X-ray diffraction. Materials Science and Technology 1992;8:159-62.
[306] Teraoka Y, Nobunaga T, Okamoto K, Miura N, Yamazoe N. Influence of constituent metal cations in substituted $LaCoO_3$ on mixed conductivity and oxygen permeability. Solid State Ionics 1991;48:207-12.
[307] Zhao L, He B, Zhang X, Peng R, Meng G, Liu X. Electrochemical performance of novel cobalt-free oxide $Ba_{0.5}Sr_{0.5}Fe_{0.8}Cu_{0.2}O_{3-\delta}$ for solid oxide fuel cell cathode. Journal of Power Sources 2010;195:1859-61.
[308] Zhang K, Ran R, Ge L, Shao Z, Jin W, Xu N. Systematic investigation on new $SrCo_{1-y}Nb_yO_{3-\delta}$ ceramic membranes with high oxygen semi-permeability. Journal of Membrane Science 2008;323:436-43.
[309] Fang S, Yoo C-Y, Bouwmeester H. Performance and stability of niobium-substituted $Ba_{0.5}Sr_{0.5}Co_{0.8}Fe_{0.2}O_{3-\delta}$ membranes. Solid State Ionics 2011;195:1-6.
[310] Kharton V, Viskup A, Naumovich E, Lapchuk N. Mixed electronic and ionic conductivity of $LaCo(M)O_3$ (M= Ga,Cr,Fe or Ni): I. Oxygen transport in perovskites $LaCoO_3$–$LaGaO_3$. Solid State Ionics 1997;104:67-78.
[311] Kharton V, Kovalevsky A, Tikhonovich V, Naumovich E, Viskup A. Mixed electronic and ionic conductivity of $LaCo(M)O_3$(M= Ga, Cr, Fe or Ni): II. Oxygen permeation through Cr-and Ni-substituted $LaCoO_3$. Solid State Ionics 1998;110:53-60.
[312] Kharton V, Viskup A, Bochkov D, Naumovich E, Reut O. Mixed electronic and ionic conductivity of $LaCo(M)O_3$ (M=Ga,Cr,Fe or Ni): III. Diffusion of oxygen through $LaCo_{1-x-y}Fe_xNi_yO_{3\pm\delta}$ ceramics. Solid State Ionics 1998;110:61-8.
[313] Koblischka-Veneva A, Koblischka MR, Simon P, Mücklich F, Murakami M. Electron backscatter diffraction study of polycrystalline $YBa_2Cu_3O_{7-\delta}$ ceramics. Physica C: Superconductivity 2002;382:311-22.
[314] Koblischka-Veneva A, Mücklich F, Koblischka M. A study of grain orientation of Alkali doped polycrystalline YBCO ceramics using an EBSD technique. Crystal Engineering 2002;5:411-8.
[315] Hurley P, Humphreys F. The application of EBSD to the study of substructural development in a cold rolled single-phase aluminium alloy. Acta Materialia 2003;51:1087-102.
[316] Humphreys F. Characterisation of fine-scale microstructures by electron backscatter diffraction (EBSD). Scripta Materialia 2004;51:771-6.
[317] Dingley DJ, Randle V. Microtexture determination by electron back-scatter diffraction. Journal of Materials Science 1992;27:4545-66.

Appendix A

Micro-indentation: ISO/DIS Standard 14577-1:2002

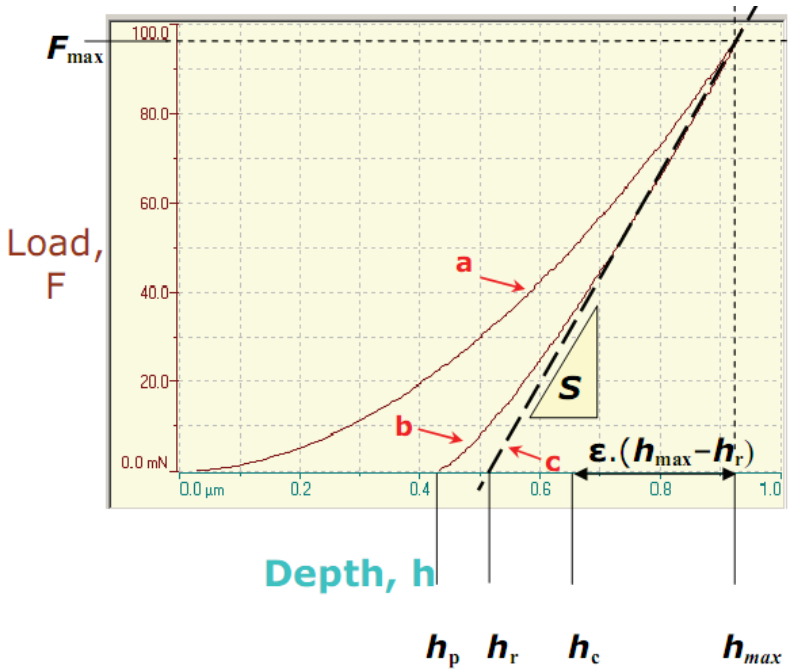

Figure 1. Typical indentation curve including loading and unloading process

a: Application of the test force

b: Removal of the test force

c: Tangent to curve b at F_{max}

$\boldsymbol{h_p}$ is the permanent indentation depth after removal of the test force

$\boldsymbol{h_r}$ is the point of the tangent c to curve b at F_{max} with the indentation depth-axis

$\boldsymbol{h_c}$ is the depth of contact of the indenter with the sample at F_{max}

$\boldsymbol{h_{max}}$ is the maximum indentation depth at F_{max}

$\boldsymbol{S}$ is the contact stiffness at F_{max}

$\boldsymbol{\varepsilon}$ is the geometric constant

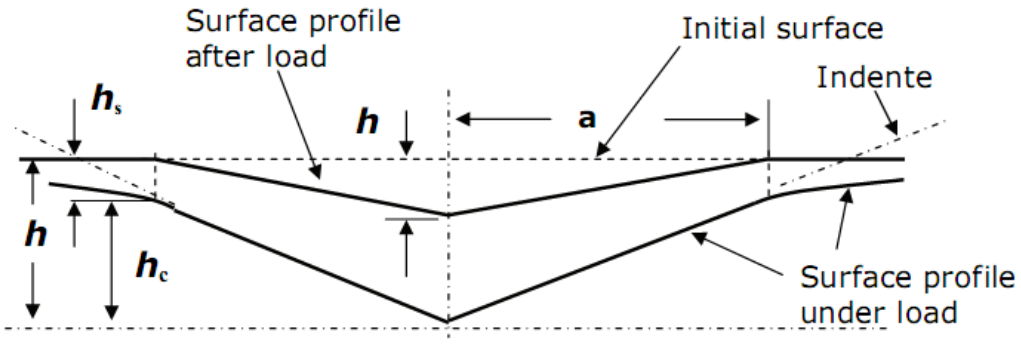

Figure 2. Schematic representation of the indenter-sample contact

***F**max* and ***h**max*:** Directly on curves (same acquisition point)

h_p: Linear fit: Fit start: 15% of F_{max} Fit end: 0% of F_{max}

End of load detection threshold: 0.5% of F_{max}

S (Tangent method): Tangent fit: Fit start: 95% of F_{max}

Fit end: 70% of F_{max}

$$S = \left(\frac{dF}{dh}\right)_m$$

m and **S** (O&P method): Power law fit of unloading curve:

Fit start: 98% of F_{max} Fit end: 40% of F_{max}

$$F = F_{max} \cdot \left(\frac{h - h_p}{h_{max} - h_p}\right)^m$$

Calculation of S: $$S = m \cdot F_{max} \cdot (h_{max} - h_p)^{-1}$$

h_r: Intercept of the tangent to the load-displacement data at the maximum load on unloading (S) with the depth axis.

$$h_r = h_{max} - F_{max}/S$$
$$h_c = h_{max} - \varepsilon \cdot (h_{max} - h_r)$$

ε: Depending on the diamond shape

Indenter Shape	m	ε
Flat Punch	1.0	1.0000
Cone	2.0	$2(\pi-2)/\pi=0.7268$
Sphere / Parabolo ïd	1.5	0.7500

In our case, ε is estimated using the m value!

(Table of ten values and linear extrapolation between two values)

Ref.: J. Woirgard and al../ Surface and coatings Technology 100-101 (1998) 103-109

β: Geometric factor (diamond shape dependant)

Circular $\beta = 1.000$

Triangular $\beta = 1.034$

Square $\beta = 1.012$

$\boldsymbol{A_p}$**:** Projected contact area (theoretical or calibrated)

$$A_p = f(h)$$

Indentation hardness is a measure of the resistance to permanent deformation or damage.

$$H_{IT} = \frac{F_{max}}{A_p} \text{ in Pascal}$$

$\boldsymbol{F_{max}}$ is the maximum Force

$\boldsymbol{A_p}$ is the projected contact area (theoretical or calibrated)

The deduced modulus is calculated from the following equation:

$$E_r = \frac{\sqrt{\pi}\cdot S}{2\cdot\beta\cdot\sqrt{A_p(h_c)}}$$

The Plane Strain Modulus $\boldsymbol{E^*}$ is calculated from the following equation:

$$E^* = \frac{1}{\frac{1}{E_r} - \frac{1-\nu_i^2}{E_i}}$$

With: E_i = Elastic modulus of the indenter (diamond 1141 GPa)

E_r = Reduced modulus of the indentation contact

V_i = Poisson's ratio of the indenter (0.07)

The indentation modulus is calculated from the Plane Strain modulus using an estimated sample Poisson's ratio:

$$E_{IT} = E^* \times (1 - \nu_s^{\,2})$$

As a reminder, typical values of Poisson's ratio are:

Ceramic: 0.1 to 0.3 Metal: 0.2 to 0.4 Polymer: 0.3 to 0.4

References

ISO/DIS Standard 14577-1:2002

DIN Standard 50359-1

*Meyer, E., Z. Ver. Dtsch. Ing. 52 (1908) 645

*Doerner, M.F., and Nix, W.D., "A method for interpreting the data from depth sensing indentation instruments", J. Mat. Res., 1, (1986), 601-609

*Oliver, W.C., Pharr, G.M., "An improved technique for determining hardness and elastic modulus using load and displacement sensing indentation experiments", J. Mat. Res., 7(6), June 1992, 1564-1583

*ISO/DIS Standard 14577-1, ISO/DIS 14577-2

*J. Woirgard *et al.*/ Surface and coatings Technology 100-101 (1998) 103-109.